

ULTRASOUND TRIGGERED DRUG DELIVERY OF TRANSFERRIN COUPLED
LIPOSOMES CARRYING THE DRUG DOXORUBICIN

By

Paul Said Kawak

A Thesis Presented to the Faculty of the
American University of Sharjah
College of Engineering
in Partial Fulfillment
of the Requirements
for the Degree of

Master of Science in
Chemical Engineering

Sharjah, United Arab Emirates

June 2020

Declaration of Authorship

I declare that this thesis is my own work and, to the best of my knowledge and belief, it does not contain material published or written by a third party, except where permission has been obtained and/or appropriately cited through full and accurate referencing.

Signed: Paul Said Kawak

Date: June 15th, 2020

The Author controls copyright for this report.
Material should not be reused without the consent of the author. Due
acknowledgement should be made where appropriate.

Approval Signatures

We, the undersigned, approve the Master's Thesis of Paul Said Kawak

Thesis Title: Ultrasound triggered drug delivery of transferrin coupled liposomes carrying the drug doxorubicin.

Date of Defense: 5-July-2020

Name, Title and Affiliation

Signature

Dr. Ghaleb Al Hussein
Professor,
Department of Chemical Engineering
Thesis Advisor

Dr. Rana Sabouni
Associate Professor,
Department of Chemical Engineering
Thesis Committee Member

Dr. Nahid Awad
Visiting Scholar
Thesis Committee Member

Dr. Sameer Al-Asheh
Interim Head
Department of Chemical Engineering

Dr. Lotfi Romdhane
Associate Dean for Graduate Studies and Research
College of Engineering

Dr. Sirin Tekinay
Dean
College of Engineering

Dr. Mohamed El-Tarhuni
Vice Provost for Graduate Studies
Office of Graduate Studies

Acknowledgments

Firstly, I am deeply grateful to my parents and brother for always being there to support me in all my endeavors. From my undergraduate to my graduate degree, my family has always been there to support and provide me with the guidance I needed.

My most heartfelt gratitude goes towards my thesis advisor and mentor Dr. Ghaleb Al Hussein, for his guidance throughout my masters and my thesis project. The positive attitude that he emits is a beacon of light through the darkest moments of stress and self-doubt. His knowledge and brilliance provide you with the urge to always become more knowledgeable. I would also like to thank Eng. Nour Al Sawafah and Eng. Vinod Paul for their help throughout this thesis and especially during the COVID 19 pandemic. Their help was imperative in finishing this thesis due to the lockdown. Dr. Nahid Awad was always available for guidance and help throughout the lab and I am deeply grateful for that. I would also like to thank Ms. Celine Moussa for her help around the lab during the summer of 2019.

I would also like to mention and thank my examiners Dr. Rana Sabouni and Dr. Nahid Awad for their comments during my proposal presentation. The comments you provided were important in enhancing my knowledge and this research thesis.

I would also like to thank the Chemical Engineering Department at the American University of Sharjah for the opportunity to pursue my goals and dreams and obtain a master's degree through a teaching assistantship. I would like to also thank all the professors who taught me throughout my years in AUS for all the knowledge they passed down and all the guidance they provided. Finally, my deepest gratitude goes to the director of the chemical engineering graduate program Dr. Sameer al-Asheh for his guidance and support.

Abstract

Cancer is one of the deadliest diseases of the 21st century. It is caused by the uncontrolled division of damaged and mutated cells. Several methods have been developed to combat cancer, including surgery, radiation, and chemotherapy. However, due to the nature of the disease and the cytotoxicity of the treatments, these treatments' effectiveness is limited. To mitigate the cytotoxicity of these treatments and improve efficacy, Smart Drug Delivery Systems are studied. These delivery systems contain nanoparticle that encapsulates a chemotherapeutic drug and delivers it selectively to the tumor site. This work will utilize a PEGylated liposome coupled with the protein Transferrin encapsulating the chemotherapeutic drug Doxorubicin. The PEG protects the vesicles from the human body's immune system. The vesicle can passively target the tumor site. Moreover, the transferrin ligand selectively binds to cancer cells, improving uptake chances. The liposomes were synthesized using the film hydration method. The averaged size of the control liposomes and Transferrin-targeted liposomes are 85.2 ± 5.83 nm, and 85.3 ± 7.15 nm, respectively. The lipid content of the liposomes is quantified, and the result for control liposomes is 8.024 ± 0.126 mg/ml, while the result for the Tf-targeted liposomes is 6.219 ± 1.109 mg/ml using the Stewart Assay. The conjugation of Transferrin proven using the BCA assay as the protein content was 2-fold higher than the control liposomes. Low-frequency ultrasound release is conducted using a 20-kHz US probe at three power densities, namely, 7.46, 9.85, 17.31 mW/cm², and the results showed an increase in the release of Doxorubicin from the transferrin coupled liposomes. The release results are fitted to nine different models, and the best-fitting model is the zero-order model. The second and third best-fitting models are Hixson-Crowell and Hopfenberg. Using three modalities of drug delivery targeting (passive, ligand, and acoustic triggered) may aid in curbing the unwanted side effects of conventional chemotherapy.

Search Terms: *Drug delivery, Ultrasound, Liposomes, Transferrin.*

Table of Contents

Abstract	5
List of Figures	9
List of Tables	13
Nomenclature	14
Chapter 1. Introduction	15
1.1 Overview	15
1.2 Research Contribution	15
1.3 Thesis Organization	15
1.4 Thesis Objectives	16
Chapter 2. Literature Review	17
2.1 Cancer	17
2.1.1 Treatment options.	18
2.2 SDDS - Smart Drug Delivery Systems	20
2.2.1 Passive targeting.	21
2.2.2 Active targeting.....	22
2.3 Different Types of Nanoparticles.....	23
2.3.1 Quantum dots (QDs).....	23
2.3.2 Carbon nanotubes.....	23
2.3.3 Dendrimers.....	24
2.3.4 Micelles.....	24
2.3.5 Liposomes.	25
2.4 Ligand-Targeting in Liposomal Drug Delivery	26
2.4.1 Trastuzumab.....	26
2.4.2 Folic acid.....	27
2.4.3 Transferrin.....	27

2.5 Trigger Mechanisms	28
2.5.1 pH.....	28
2.5.2 Temperature.	28
2.5.3 Light.....	29
2.5.3 Ultrasound.....	29
2.6 Previous Experimental <i>In Vitro</i> , <i>In Vivo</i> , and Release Studies.....	32
Chapter 3. Materials and Methods	36
3.1 Materials.....	36
3.2 Procedures.....	36
3.2.1 Preparation of ammonium sulfate control liposomes.	36
3.2.2 Preparation and addition of DOX.	37
3.2.2 Transferrin attachment.	38
3.2.3 Determination of liposome size using dynamic light scattering (DLS).....	38
3.2.4 Determination of liposomal phospholipid content using Stewart assay.	39
3.2.5 Determination of protein content using BCA assay.	41
3.2.6 Low-Frequency ultrasound release.	41
3.3 Modeling	43
3.3.1 Zero-order model & first-order model.	43
3.3.2 Higuchi model.....	45
3.3.3 Korsmeyer-Peppas model.	46
3.3.4 Hixson-Crowell model.....	47
3.3.5 Baker-Lonsdale model.	47
3.3.6 Gompertz model.....	48
3.3.7 Weibull model.....	48
3.3.8 Hopfenberg model.	48
Chapter 4. Results and Discussion.....	50
4.1 Characterization Test Results	50

4.1.1 DLS results.....	50
4.1.2 Stewart assay results.	50
4.1.3 BCA results.	52
4.2 LFUS Results	53
4.2.1 Control liposomes LFUS release results.....	53
4.2.2 Tf liposomes LFUS release results.	55
4.2.3 Comparison between control and Tf liposomes.....	57
4.2.4 Mechanical index results.....	63
4.3 Kinetic Modelling	64
4.3.1 Control liposomes kinetic modeling.	64
4.3.2 Tf-targeted liposomes kinetic modeling.	68
4.3.3 Kinetic modeling comparison between control and Tf liposomes.....	73
4.4 Discussion	76
Chapter 5. Conclusion and Future Work	79
References.....	80
Appendix A: Plots of Kinetic Models for Batches 2 & 3 of Control Liposomes at 7.46 mW/cm ²	88
Appendix B: Plots of Kinetic Models of Control Liposomes at 9.85 mW/cm ²	94
Appendix C: Plots of Kinetic Models of Control Liposomes at 17.31 mW/cm ²	103
Appendix D: Plots of Kinetic Models for Batches 2 & 3 of Tf-Liposomes at 7.46 mW/cm ²	112
Appendix E: Plots of Kinetic Models of Tf-Liposomes at 9.85 mW/cm ²	118
Appendix F: Plots of Kinetic Models of Tf-Liposomes at 17.31 mW/cm ²	127
Vita.....	136

List of Figures

Figure 1: Growth of a tumor [5]	17
Figure 2: Schematic showing the mechanism of passive targeting [24].....	21
Figure 3: Active targeting using different ligands [45]	22
Figure 4: Visual representation of a Dendrimer [35].....	24
Figure 5: Micelle Formation [39]	25
Figure 6: Liposome Structure [43].....	25
Figure 7: Ultrasound Induced Hyperthermia effect on the human tissue [68]	30
Figure 8: Stable and Inertial Cavitation [70]	31
Figure 9: Thin-film hydration method	37
Figure 10: Ultrasound probe placed in a cuvette filled with DOX Liposomes	42
Figure 11: Stewart Assay Calibration Curve	51
Figure 12: BCA Calibration Curve	52
Figure 13: Difference in protein content between control and Tf-targeted liposomes	53
Figure 14: Averaged CFR \pm standard deviation vs. Time for acoustic DOX release from control liposomes	54
Figure 15: CFR of DOX release from control liposomes at 6 pulses	54
Figure 16: CFR of DOX release from control liposomes at 6 pulses for 3 power densities	55
Figure 17: Averaged CFR \pm standard deviation vs. Time for the release of DOX from Tf-targeted liposomes	56
Figure 18: CFR of DOX release from Tf-liposomes at 6 acoustic pulses	57
Figure 19: CFR of DOX release from Tf-liposomes at 6 pulses for 3 power densities	57
Figure 20: Release of Dox from Tf-targeted liposomes compared to the control at 7.46 mW/cm ²	58
Figure 21: Release of DOX from Tf-targeted liposomes compared to the control liposomes at 9.85 mW/cm ²	58
Figure 22: Release of DOX from Tf-targeted liposomes compared to control liposomes at 17.31 mW/cm ²	59
Figure 23: Pulse wise comparison of the release of DOX from Tf-targeted and control liposomes at 7.46 mW/cm ²	62
Figure 24: Pulse wise comparison of the release of DOX from Tf-targeted and control liposomes at 9.85 mW/cm ²	62
Figure 25: Pulse wise comparison of the release of DOX from Tf-targeted and control liposomes at 17.31 mW/cm ²	63
Figure 26: Zero-order model fitting of DOX release from control liposomes at 7.46 mW/cm ² (Batch 1)	65
Figure 27: First order model fitting of DOX release from control liposomes at 7.46 mW/cm ² (Batch 1)	65
Figure 28: Higuchi model fitting of DOX release from control liposomes at 7.46 mW/cm ² (Batch 1)	66
Figure 29: Korsmeyer-Peppas model fitting of DOX release from control liposomes at 7.46 mW/cm ² (Batch 1)	66
Figure 30: Backer-Lonsdale model fitting of DOX release from control liposomes at 7.46 mW/cm ² (Batch 1)	66
Figure 31: Weibull model fitting of DOX release from control liposomes at 7.46 mW/cm ² (Batch 1)	67

Figure 32: Hixson-Crowell model fitting of DOX release from control liposomes at 7.46 mW/cm ² (Batch 1)	67
Figure 33: Hopfenberg model fitting of DOX release from control liposomes at 7.46 mW/cm ² (Batch 1)	67
Figure 34: Gompertz model fitting of DOX release from control liposomes at 7.46 mW/cm ² (Batch 1)	68
Figure 35: Zero-order model fitting of DOX release from Tf-targeted liposomes at 7.46 mW/cm ² (Batch 1)	70
Figure 36: First-order model fitting of DOX release from Tf-targeted liposomes at 7.46 mW/cm ² (Batch 1)	70
Figure 37: Higuchi model fitting of DOX release from Tf-targeted liposomes at 7.46 mW/cm ² (Batch 1)	70
Figure 38: Korsmeyer-Peppas model fitting of DOX release from Tf-targeted liposomes at 7.46 mW/cm ² (Batch 1)	71
Figure 39: Hixson-Crowell model fitting of DOX release from Tf-targeted liposomes at 7.46 mW/cm ² (Batch 1)	71
Figure 40: Baker-Lonsdale model fitting of DOX release from Tf-targeted liposomes at 7.46 mW/cm ² (Batch 1)	71
Figure 41: Weibull model fitting of DOX release from Tf-targeted liposomes at 7.46 mW/cm ² (Batch 1)	72
Figure 42: Hopfenberg model fitting of DOX release from Tf-targeted liposomes at 7.46 mW/cm ² (Batch 1)	72
Figure 43: Gompertz model fitting of DOX release from Tf-targeted liposomes at 7.46 mW/cm ² (Batch 1)	72
Figure 44: Zero-order (top), First-order (middle), and Higuchi (bottom) model fitting of DOX release from control liposomes at 7.46 mW/cm ² (Batch 2)	88
Figure 45: Korsmeyer-Peppas (top), Hixson-Crowell (middle), and Baker-Lonsdale (bottom) model fitting of DOX release from control liposomes at 7.46 mW/cm ² (Batch 2)	89
Figure 46: Weibull (top), Hopfenberg (middle), and Gompertz (bottom) model fitting of DOX release from control liposomes at 7.46 mW/cm ² (Batch 2)	90
Figure 47: Zero-order (top), First-order (middle), and Higuchi (bottom) model fitting of DOX release from control liposomes at 7.46 mW/cm ² (Batch 3)	91
Figure 48: Korsmeyer-Peppas (top), Hixson-Crowell (middle), and Baker-Lonsdale (bottom) model fitting of DOX release from control liposomes at 7.46 mW/cm ² (Batch 3)	92
Figure 49: Weibull (top), Hopfenberg (middle), and Gompertz (bottom) model fitting of DOX release from control liposomes at 7.46 mW/cm ² (Batch 3)	93
Figure 50: Zero-order (top), First-order (middle), and Higuchi (bottom) model fitting of DOX release from control liposomes at 9.85 mW/cm ² (Batch 1)	94
Figure 51: Korsmeyer-Peppas (top), Hixson-Crowell (middle), and Baker-Lonsdale (bottom) model fitting of DOX release from control liposomes at 9.85 mW/cm ² (Batch 1)	95
Figure 52: Weibull (top), Hopfenberg (middle), and Gompertz (bottom) model fitting of DOX release from control liposomes at 9.85 mW/cm ² (Batch 1)	96
Figure 53: Zero-order (top), First-order (middle), and Higuchi (bottom) model fitting of DOX release from control liposomes at 9.85 mW/cm ² (Batch 2)	97

Figure 54: Korsmeyer-Peppas (top), Hixson-Crowell (middle), and Baker-Lonsdale (bottom) model fitting of DOX release from control liposomes at 9.85 mW/cm ² (Batch 2)	98
Figure 55: Weibull (top), Hopfenberg (middle), and Gompertz (bottom) model fitting of DOX release from control liposomes at 9.85 mW/cm ² (Batch 2)	99
Figure 56: Zero-order (top), First-order (middle), and Higuchi (bottom) model fitting of DOX release from control liposomes at 9.85 mW/cm ² (Batch 3)	100
Figure 57: Korsmeyer-Peppas (top), Hixson-Crowell (middle), and Baker-Lonsdale (bottom) model fitting of DOX release from control liposomes at 9.85 mW/cm ² (Batch 3)	101
Figure 58: Weibull (top), Hopfenberg (middle), and Gompertz (bottom) model fitting of DOX release from control liposomes at 9.85 mW/cm ² (Batch 3)	102
Figure 59: Zero order (top), First Order (middle), and Higuchi (bottom) model fitting of DOX release from control liposomes at 17.31 mW/cm ² (Batch 1)	103
Figure 60: Korsmeyer-Peppas (top), Hixson-Crowell (middle), and Baker-Lonsdale (bottom) model fitting of DOX release from control liposomes at 17.31 mW/cm ² (Batch 1)	104
Figure 61: Weibull (top), Hopfenberg (middle), and Gompertz (bottom) model fitting of DOX release from control liposomes at 17.31 mW/cm ² (Batch 1)	105
Figure 62: Zero-order (top), First-order (middle), and Higuchi (bottom) model fitting of DOX release from control liposomes at 17.31 mW/cm ² (Batch 2)	106
Figure 63: Korsmeyer-Peppas (top), Hixson-Crowell (middle), and Baker-Lonsdale (bottom) model fitting of DOX release from control liposomes at 17.31 mW/cm ² (Batch 2)	107
Figure 64: Weibull (top), Hopfenberg (middle), and Gompertz (bottom) model fitting of DOX release from control liposomes at 17.31 mW/cm ² (Batch 2)	108
Figure 65: Zero-order (top), First-order (middle), and Higuchi (bottom) model fitting of DOX release from control liposomes at 17.31 mW/cm ² (Batch 3)	109
Figure 66: Korsmeyer-Peppas (top), Hixson-Crowell (middle), and Baker-Lonsdale (bottom) model fitting of DOX release from control liposomes at 17.31 mW/cm ² (Batch 3)	110
Figure 67: Weibull (top), Hopfenberg (middle), and Gompertz (bottom) model fitting of DOX release from control liposomes at 17.31 mW/cm ² (Batch 3)	111
Figure 68: Zero-order (top), First-order (middle), and Higuchi (bottom) model fitting of DOX release from Tf-targeted liposomes at 7.46 mW/cm ² (Batch 2)	112
Figure 69: Korsmeyer-Peppas (top), Hixson-Crowell (middle), and Baker-Lonsdale (bottom) model fitting of DOX release from Tf-targeted liposomes at 7.46 mW/cm ² (Batch 2)	113
Figure 70: Weibull (top), Hopfenberg (middle), and Gompertz (bottom) model fitting of DOX release from Tf-targeted liposomes at 7.46 mW/cm ² (Batch 2)	114
Figure 71: Zero-order (top), First-order (middle), and Higuchi (bottom) model fitting of DOX release from Tf-targeted liposomes at 7.46 mW/cm ² (Batch 3)	115
Figure 72: Korsmeyer-Peppas (top), Hixson-Crowell (middle), and Baker-Lonsdale (bottom) model fitting of DOX release from Tf-targeted liposomes at 7.46 mW/cm ² (Batch 3)	116
Figure 73: Weibull (top), Hopfenberg (middle), and Gompertz (bottom) model fitting of DOX release from Tf-targeted liposomes at 7.46 mW/cm ² (Batch 3)	117
Figure 74: Zero-order (top), First-order (middle), and Higuchi (bottom) model fitting of DOX release from Tf-targeted liposomes at 9.85 mW/cm ² (Batch 1)	118

Figure 75: Korsmeyer-Peppas (top), Hixson-Crowell (middle), and Baker-Lonsdale (bottom) model fitting of DOX release from Tf-targeted liposomes at 9.85 mW/cm ² (Batch 1).....	119
Figure 76: Weibull (top), Hopfenberg (middle), and Gompertz (bottom) model fitting of DOX release from Tf-targeted liposomes at 9.85 mW/cm ² (Batch 1)	120
Figure 77: Zero-order (top), First-order (middle), and Higuchi (bottom) model fitting of DOX release from Tf-targeted liposomes at 9.85 mW/cm ² (Batch 2)	121
Figure 78: Korsmeyer-Peppas (top), Hixson-Crowell (middle), and Baker-Lonsdale (bottom) model fitting of DOX release from Tf-targeted liposomes at 9.85 mW/cm ² (Batch 2).....	122
Figure 79: Weibull (top), Hopfenberg (middle), and Gompertz (bottom) model fitting of DOX release from Tf-targeted liposomes at 9.85 mW/cm ² (Batch 2)	123
Figure 80: Zero-order (top), First-order (middle), and Higuchi (bottom) model fitting of DOX release from Tf-targeted liposomes at 9.85 mW/cm ² (Batch 3)	124
Figure 81: Korsmeyer-Peppas (top), Hixson-Crowell (middle), and Baker-Lonsdale (bottom) model fitting of DOX release from Tf-targeted liposomes at 9.85 mW/cm ² (Batch 3).....	125
Figure 82: Weibull (top), Hopfenberg (middle), and Gompertz (bottom) model fitting of DOX release from Tf-targeted liposomes at 9.85 mW/cm ² (Batch 3)	126
Figure 83: Zero-order (top), First-order (middle), and Higuchi (bottom) model fitting of DOX release from Tf-targeted liposomes at 17.31 mW/cm ² (Batch 1)	127
Figure 84: Korsmeyer-Peppas (top), Hixson-Crowell (middle), and Baker-Lonsdale (bottom) model fitting of DOX release from Tf-targeted liposomes at 17.31 mW/cm ² (Batch 1).....	128
Figure 85: Weibull (top), Hopfenberg (middle), and Gompertz (bottom) model fitting of DOX release from Tf-targeted liposomes at 17.31 mW/cm ² (Batch 1)	129
Figure 86: Zero-order (top), First-order (middle), and Higuchi (bottom) model fitting of DOX release from Tf-targeted liposomes at 17.31 mW/cm ² (Batch 2)	130
Figure 87: Korsmeyer-Peppas (top), Hixson-Crowell (middle), and Baker-Lonsdale (bottom) model fitting of DOX release from Tf-targeted liposomes at 17.31 mW/cm ² (Batch 2).....	131
Figure 88: Weibull (top), Hopfenberg (middle), and Gompertz (bottom) model fitting of DOX release from Tf-targeted liposomes at 17.31 mW/cm ² (Batch 2)	132
Figure 89: Zero-order (top), First-order (middle), and Higuchi (bottom) model fitting of DOX release from Tf-targeted liposomes at 17.31 mW/cm ² (Batch 3)	133
Figure 90: Korsmeyer-Peppas (top), Hixson-Crowell (middle), and Baker-Lonsdale (bottom) model fitting of DOX release from Tf-targeted liposomes at 17.31 mW/cm ² (Batch 3).....	134
Figure 91: Weibull (top), Hopfenberg (middle), and Gompertz (bottom) model fitting of DOX release from Tf-targeted liposomes at 17.31 mW/cm ² (Batch 3)	135

List of Tables

Table 1: Amounts added to each centrifuge tube for the Stewart Assay	40
Table 2: Amounts added for BCA assay.....	41
Table 3: Ways of obtaining the exponent for the Korsmeyer-Peppas model based on the geometry [102].....	47
Table 4: The size of control and targeted liposome measured using DLS	50
Table 5: Stewart Assay Results.....	51
Table 6: BCA Results	52
Table 7: Heat map of p-values comparing the first pulse of DOX release from Tf-targeted and control liposomes	59
Table 8: Heat map of p-values comparing the second pulse of DOX release from Tf-targeted and control liposomes	60
Table 9: Heat map of p-values comparing the third pulse of DOX release from Tf-targeted and control liposomes	60
Table 10: Heat map of p-values comparing the fourth pulse of DOX release from Tf-targeted and control liposomes	60
Table 11: Heat map of p-values comparing the fifth pulse of DOX release from Tf-targeted and control liposomes	61
Table 12: Heat map of p-values comparing the sixth pulse of DOX release from Tf-targeted and control liposomes	61
Table 13: Coefficient of determination (R^2) analysis of DOX release from control liposome modeling.....	64
Table 14: Coefficient of determination (R^2) analysis of the DOX release from Tf-targeted liposome modeling.....	69
Table 15: Release constant values for the zero-order model	73
Table 16: Release constant values for Hixson-Crowell model.....	73
Table 17: Release constant values for Hopfenberg model.....	74
Table 18: ANOVA Two factor with replication on zero-order release constants	74
Table 19: ANOVA Two factor with replication on Hixson-Crowell release constants	75
Table 20: ANOVA Two factor with replication on Hopfenberg release constants	75
Table 21: Heat map of p-values comparing the release constants of the zero-order model for the release of DOX from Tf-targeted and control liposomes.....	75
Table 22: Heat map of p-values comparing the release constants of the Hixson-Crowell model for the release of DOX from Tf-targeted and control liposomes.....	76
Table 23: Heat map of p-values comparing the release constants of the Hopfenberg model for the release of DOX from Tf-targeted and control liposomes.....	76

Nomenclature

ANOVA- Analysis of Variance

DLS- Dynamic Light Scattering

DOX- Doxorubicin

DPPC- Dipalmitoylphosphatidylcholine

DSPE-PEG(200)-NH₂-1,2-distearoyl-sn-glycero-3-phosphoethanolamine-N-[amino(polyethylene glycol)-2000]

EPR- Enhanced permeability and Retention Effect

FDA- Food and Drug Administration

LFUS- Low-Frequency Ultrasound

MDR- Multi-Drug Resistance

PEG- Poly-ethylene Glycol

QD- Quantum Dot

RES- Reticuloendothelial System

SDDS- Smart Drug Delivery Systems

Tf- Transferrin

Chapter 1. Introduction

This chapter will focus on giving an overview of cancer and how to treat it. Moreover, it also contains the research contributions of this thesis and its organization.

1.1 Overview

Cancer is one of the deadliest diseases of the 21st century. In 2019 in the United States alone, it is reported that 1.7 million individuals have contracted the disease, and approximately 600 thousand individuals have died because of this ailment. Cancer is a disease that is caused by the uncontrolled division of cells in the host's body, adversely affecting several bodily functions in the process. The negative side effects are highly exacerbated by the spread of the malignant cells to the rest of the body [1]. Several methods can be used to treat cancer, including radiation, surgery, and the most important, which is chemotherapy. This method utilizes drugs that kill fast-growing cells in the body.

The chemotherapeutic drug doxorubicin will be encapsulated in a smart drug delivery system (SDDS). Adriamycin, the brand name of the anti-neoplastic drug doxorubicin, is commonly used in the treatment of many types of cancers like breast, lung, and stomach cancer [2]. Doxorubicin (DOX) encapsulated in liposomes, Doxil is approved by the United States of America's Food and Drug Administration (FDA). These liposomes will be conjugated to the protein Transferrin (Tf) for targeting. Furthermore, on the surface of these liposomes polyethylene glycol (PEG) will be added for stealth.

1.2 Research Contribution

This work will discuss the use of Liposomes (as DDS) coupled with PEG and the ligand Tf, which contain the chemotherapeutic drug DOX and will be released using ultrasound (US). The combination of these three drug delivery modalities, in conjunction with US, is novel and holds promise for future implementation in clinics.

1.3 Thesis Organization

The thesis starts with Chapter 1, which discusses the overview and the need for this experimental study. Chapter 2 continues with a deep dive into the theoretical background and the literature review that surrounds the topic of drug delivery. Chapter

3 explains the methods and materials used in the experimental study. Chapter 4 continues with presenting the results and discussing their significance. Finally, Chapter 5 lays out the conclusion for this piece of work and the future direction of this type of research.

1.4 Thesis Objectives

The objective of this research is to create and test an improved drug delivery system that carries doxorubicin into the HeLa cell line in hopes that it would reduce the agent's cytotoxicity to normal cells. This will be performed by coupling the liposomes to Tf and triggering the release of the drug using ultrasound. The objectives of this research are to:

- Synthesize both Tf-coupled and control liposomes that encapsulate doxorubicin.
- Characterize both liposomes using three different techniques:
 - Dynamic Light Scattering (DLS) to measure liposome size
 - Stuart Assay to measure phospholipid content
 - BCA Assay to measure ligand attachment
- Perform release experiments using 20-kHz low-frequency ultrasound (LFUS) at three different power densities.
- Model the kinetics of the release using nine different mathematical models.

Chapter 2. Literature Review

2.1 Cancer

The body is a complex structure that is composed of trillions of cells, which in turn make up multiple different tissues, organs, and organ systems. Normal healthy cells undergo division, and when their DNA gets damaged, they undergo apoptosis. Apoptosis is more commonly known as programmed cell death. Cancer develops when normal damaged cells do not undergo the latter process of death but instead start dividing uncontrollably. This results in the growth of a tumor made up of these damaged/diseased cells. A notable exception is the growth of the cancer of the blood, leukemia [3]. The process of tumor formation begins when the genes of the cells that are responsible for cell growth and cell death mutate. Two examples of these types of genes are tumor suppressor genes and proto-oncogenes. Proto-oncogenes are responsible for healthy cell growth, but when mutated, they allow cells to grow uncontrollably, giving rise to abnormal cells, which may turn cancerous. Tumor suppressor genes are responsible for regulating cell growth by either killing a cell that is mutated or repairing the damaged genes. When mutated, the tumor suppressor gene no longer performs its responsibilities and therefore gives way for cancerous cell behavior [4] [5]. Figure 1 shows the step-by-step growth of a tumor until it can undergo angiogenesis and create its own blood vessels [5].

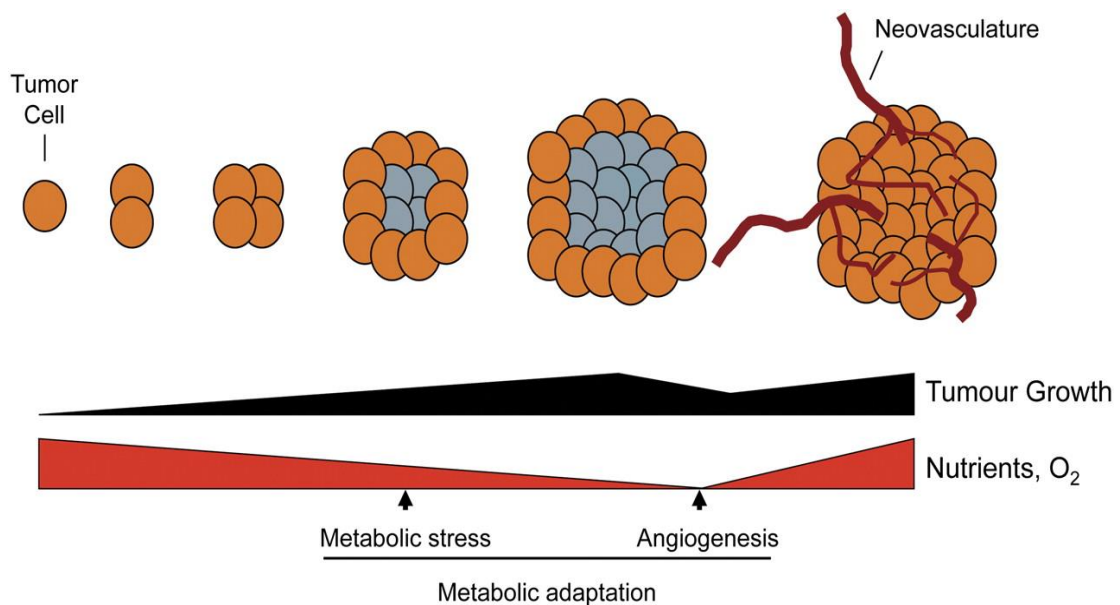


Figure 1: Growth of a tumor [5]

When a cell becomes abnormal and stops undergoing normal cell processes, they grow and divide without control, and these cells give rise to abnormal growth within the body, referred to as tumors. Tumors are not necessarily cancerous and normally fall into three categories: benign, premalignant, and malignant tumors. Benign tumors are localized growths that have not spread to the rest of the body. They are non-cancerous or not harmful unless they are located by nerves or blood vessels. However, benign tumors may potentially become malignant, and that is why it is imperative that they are checked out and regularly monitored by a doctor [6]. A prime example of a benign tumor is a Nevi, which is also known as a mole [6]. A premalignant tumor is a tumor that is not cancerous yet but is demonstrating some malignant properties. An example of premalignant tumors is Leukoplakia, which is the formation of white patches in the inside of the mouth. These types of tumors may cause serious harm to the body and have the potential to turn malignant. A malignant tumor is a tumor that has the ability to spread or metastasize throughout the body and is often associated with later, more lethal stages of cancer. This spreading of cancer cells is referred to as metastasis. These cancer cells utilize blood vessels and lymphatic vessels to invade other locations in the body and cause the growth of tumors in these new locations [7].

2.1.1 Treatment options. Over the years, several methods were developed to treat cancer, each wildly varying in efficacy and application. All treatment methods are, however, limited by cancer's complex nature. Because cancer cells are intertwined with the healthy cells of the body, killing them causes unnecessary body strain. Due to this, no panacea has been found for cancer, and all treatments are limited by the severity of their side effects. However, advancements in science continually introduce new solutions to old problems. Some examples of effective conventional treatment methods currently in use are surgery, chemotherapy, immunotherapy, and radiation therapy [8].

Surgery has been utilized in the treatment and diagnosis of cancer for several years. It can be used to obtain a sample of the tumor in a biopsy. This diagnostic method reveals essential details about the cancer, such as the type, progression level, and severity. Surgery can also be utilized to remove the tumor if the location of the tumor permits such an invasive procedure. Furthermore, surgery can be used as a preventative measure to prevent cancer by removing tissue or organs that may become cancerous. This procedure is usually done if there is a family history of cancer. An example of this

is a preventive mastectomy, where the breasts of an individual are removed if she carries gene mutations that increase the risk of developing breast cancer [9].

Radiation is a localized treatment that blasts radiation such as high energy electron beams, x-rays, and gamma rays to kill the cancer cells. Radiation can be administered internally or externally. The main objective of radiation therapy is to direct as much of the radiation as possible towards cancerous tissue. This radiation then destroys cells' DNA and stops them from proliferation. This treatment is not tumor-selective and may damage healthy cells. To avoid excessive damage to healthy tissue, the radiation beam is intentionally focused only on the tumor area. Short-term side effects include the same well-known side effects of chemotherapy like fatigue, hair loss, and nausea. Radiation therapy, similar to chemotherapy, might mutate cells and turn them cancerous [10], [11].

Immunotherapy utilizes the body's immune system to help kill cancer cells. It improves the body's immune system and provides the body with essential proteins, both of which help in killing cancers [8]. This method utilizes antibodies that are administered to a cancer patient, usually orally, in tablet form. These antibodies bind to antigens on the surface of tumor cells rendering these receptors ineffective. Without their function, they cannot help cancer growth, and this causes eventual cancer death. Herceptin immunotherapy involves administering Herceptin to a breast cancer patient to render the Human Epidermal Growth Factor 2 (HER2) receptor useless [12]. HER2 is a receptor that can be found on the surface of some breast cancer cells and is very important for the growth and proliferation of breast cancer cells. Herceptin can be utilized effectively against 25% of breast cancer cells [13].

Chemotherapy is a treatment procedure that utilizes drugs that are known for killing fast-growing cells. It is usually administered intravenously, which means that it is introduced into the bloodstream through a vein in the arm. Furthermore, it is usually used in conjunction with other methods such as surgery and radiation. This synergistic application usually involves complex combinations of treatment. For example, chemotherapy may be used to shrink a tumor before surgical removal and to rid the body of any remnants after. Despite its widespread use and efficacy, chemotherapy is infamous for its side effects ranging from mild to lethal, including vomiting, nausea, headaches, hair loss, cardiotoxicity, and death [14], [15]. Examples of chemotherapy drugs are Abraxane, DOX, Carboplatin, and Cytosan.

Drugs used in chemotherapy are called chemotherapeutics. DOX, a chemotherapeutic topoisomerase II inhibitor, works by attacking the cell's DNA or RNA and inhibiting its function. This, in turn, stops the cell from dividing and leads eventually to its demise. The most significant drawback to using doxorubicin is that it does not distinguish between healthy cells and cancerous cells. It is administered intravenously and shares many side effects with other chemotherapeutics with additional severity due to its cardiotoxicity, which causes the death of heart muscles, and may, in turn, cause heart failure. Doxorubicin is a carcinogen and, therefore, may also rarely cause the development of secondary cancers [16]. Some chemotherapeutic drugs are barely soluble and cytotoxic, which means that the more a human body is exposed to the treatment, the more at risk they are.

The treatments mentioned earlier are limited in efficacy and sometimes very hard to administer due to the location of the tumor. To overcome this limitation, researchers are actively trying to find better methods to treat cancer. This includes the development of Smart Drug Delivery Systems (SDDS). SDDS include a nanocarrier that is biocompatible, which can carry drugs. Furthermore, these nanocarriers can be coupled with ligands that have analogs overexpressed on the surface of cancerous cells. Finally, these carriers can be triggered using an external trigger such as light, ultrasound, heat, and magnetic triggers. These SDDS can reduce side effects because they contain the anti-neoplastic agent, effectively only releasing it specifically at the cancer site and preventing the death of healthy cells [17].

2.2 SDDS - Smart Drug Delivery Systems

Smart drug delivery systems (DDS) were designed using nanoparticles that encapsulate a therapeutic drug and use passive and active targeting to deliver the drug to the cancer site. Many types of nanoparticles are investigated in delivering chemotherapeutics, including liposomes, micelles, carbon nanotubes, and dendrimers. Nanoparticles should be in the size range of 1-150 nm in diameter to be classified as appropriate DDS. Sizes larger than this may be filtered by the body before the nanoparticles reach their destination. As a foreign object to the body, nanoparticles are also vulnerable to immune system attacks. For this reason, DDS are modified for stealth, which is achieved by PEGylation. PEGylation allows the nanoparticle to evade the reticuloendothelial system (RES), which removes foreign objects from the

bloodstream and deposits them in the liver or spleen. However, there are drawbacks to adding PEG as it lowers drug uptake by cells [18] [19]. There are three types of targeting methods: passive, active, and triggered targeting.

2.2.1 Passive targeting. Passive targeting is a phenomenon by which drug-encapsulating nanoparticles diffuse into cancer sites from the bloodstream. This is due to a phenomenon called the enhanced permeability and retention (EPR) effect [20]. The enhanced permeability is due to the blood vessels that surround the tumor cells. These blood vessels are usually more permeable than healthy cells due to the rapid growth of a tumor. The retention effect is due to the absence of lymphatic vessels around a tumor, which conventionally cleans excess water and accumulated substances. Passive targeting utilizes the EPR effect to allow for the accumulation of the nanocarriers at the tumor site [18], [21]. The EPR effect can take place typically when the SDDS is below 200 nm in diameter, corresponding to the vascular permeability around tumors [22]. This is beneficial because the gaps between cells that make-up normal blood vessels are between 5 and 10 nm allowing the nano-vehicles to target cancers preferentially [23]. Figure 2 below shows a representation of the concept of passive targeting. The figure illustrates how blood vessels around the cancer site are damaged and allow the nanoparticles to enter, while normal blood vessels do not allow the nanoparticles to exit the blood vessel.

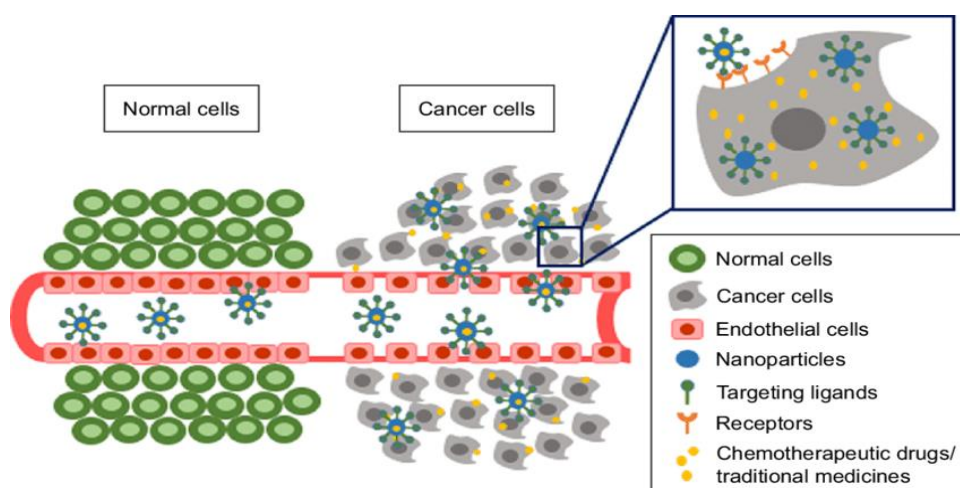


Figure 2: Schematic showing the mechanism of passive targeting [24]

Passive targeting is a powerful tool; however, it is limited due to several reasons. For example, the tumor may exhibit multiple drug resistance (MDR), which reduces

the cellular uptake of the drug. Furthermore, the EPR effect may not be as pronounced in some cancerous tumors. This is why this effect is more effective when coupled with other targeting modalities [21].

2.2.2 Active targeting. Cancerous tumors, when compared to normal cells, show an increased number of receptors for specific ligands overexpressed on their membrane. This occurs because these tumors need more nutrients due to their rapid cell growth, and this is largely mediated by receptor-mediated endocytosis. Each cancerous tumor overexpresses different receptors. Knowledge of this overexpression can help in choosing which ligand to conjugate to the nanoparticle when targeting each specific cancerous tumor. This mode of targeting is called active targeting. Some examples of effective ligands are Tf, Folic acid, and antibodies [18], [21]. When the ligand binds to the receptor, it is taken up by the cell (along with the nanoparticle and its contents) by receptor-mediated endocytosis. [24]. Figure 3 portrays the different types of ligand targeting.

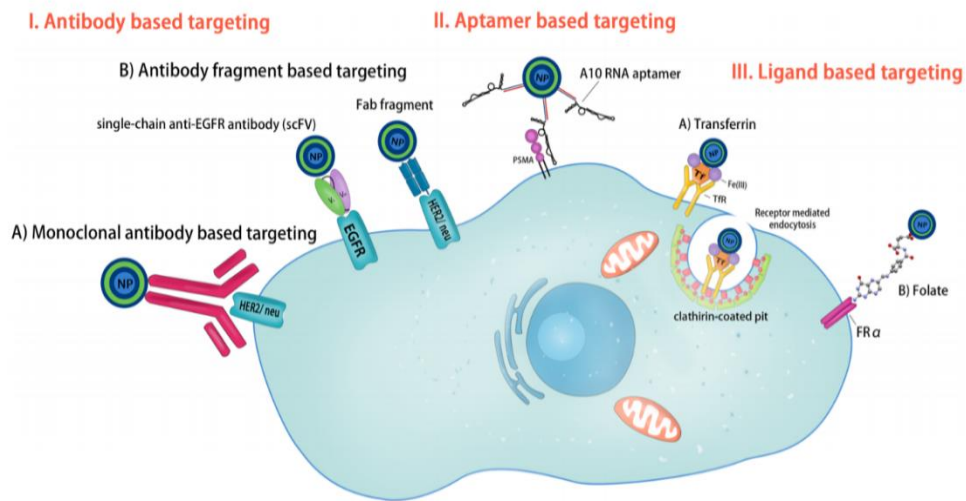


Figure 3: Active targeting using different ligands [45]

The nanocarrier accumulates preferentially at the tumor site due to EPR effects and is then taken up by the cell [25]. As seen in Figure 3, the ligand binds to the surface of the tumor and proceeds to be internalized by the receptor-mediated endocytosis process. Furthermore, active targeting could seamlessly be combined with elements of immunotherapy. Monoclonal Antibodies (mAbs) can be conjugated to the surface of DDS to efficiently transport the nanoparticle to the tumor location and provide a mode

of immunotherapy by blocking antigens that are required for the proliferation of cancer [26], [27]. Which ligand is used is dictated by the type of cancer that is present. For example, Herceptin and Estrone are used for the treatment of some breast cancer tumors as their receptors are overexpressed on the surface of these cells [12], [28].

2.3 Different Types of Nanoparticles

2.3.1 Quantum dots (QDs). Made up of a core, a shell, and a capping material, a quantum dot is an inorganic nanoparticle that is used in drug delivery. The core and the shell are usually made up of metals from the second and sixth group in the periodic table. QDs are fluorescent and can be used in many biomedical applications. Furthermore, the drug release process can be observed when using QDs due to their fluorescent nature. QDs emit traceable signals that can be observed and tracked to know its path [29]. A QD with a core made up of cadmium selenide, and a shell made up of zinc-sulfide is the most widely used [18], [30]. QDs can be extremely beneficial as they can be utilized for different pharmaceutical uses. They can be utilized in imaging, drug delivery, brain tumor diagnosis, and drug screening [31], [32]. This allows for better optimization of the QD. The fluorescence of QDs comes from their method of synthesis. They are formed by the addition of an organometallic substance to a hot trioctylphosphine. The QDs begin to form and change color as their size increases. This process can be stopped by the removal of heat to achieve and maintain the desired size [31]. Finally, as with all DDS, QDs can encapsulate a variety of different drugs for drug delivery purposes.

2.3.2 Carbon nanotubes. Carbon nanotubes are cylindrically shaped nanoparticles composed of benzene rings. They can either have a single wall or multiple walls. Carbon nanotubes without modifications are insoluble in any liquid; however, some changes to their chemistry can make them hydrophilic. They are more likely to be taken up by the cells when compared to free drugs [18], [21]. Furthermore, they can be utilized to encapsulate a variety of different chemotherapeutics for the treatment of cancer. They can also be used to deliver photodynamic therapy and photothermal therapy. These carbon tubes are stable at the nanoscale level, have high surface areas, and an excellent capacity for surface functionalization, which makes them extremely attractive to be used in cancer therapy [33]. One chemical recipe used to produce carbon nanotubes is a carbon monoxide reaction conducted at high pressure, [34].

2.3.3 Dendrimers. Dendrimers, named after the word tree, are made up of a polymer with a lot of branches. Its structure consists of a core and branches surrounding the core. Furthermore, it can be modified by conjugating active groups on its surface. These active groups are responsible for the hydrophilic or hydrophobic nature of the dendrimer. Like all other nanoparticles, modifications can be made to its surface to turn it into a stealth nanoparticle and allow it to target specific cancers using the active targeting method. Figure 4 illustrates the shape of a dendrimer [35]. Its size increases with the number of generations. Furthermore, they can be utilized in imaging and catalysis. They are highly favorable due to their high surface area and functionalization [18], [36], [37], [38].

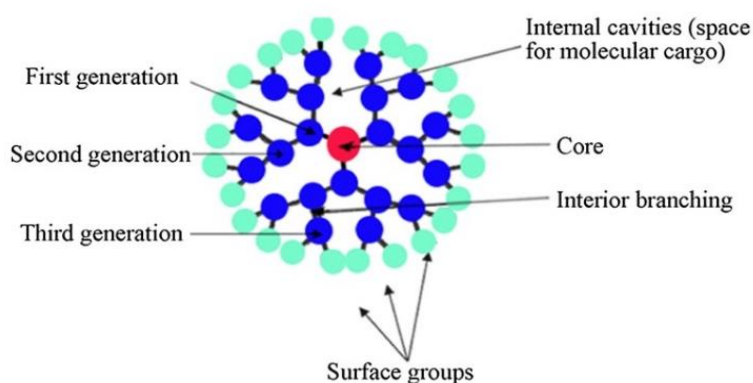


Figure 4: Visual representation of a Dendrimer [35]

2.3.4 Micelles. Micelles are nanoparticle structures composed of a hydrophilic head and a hydrophobic tail. These hydrophobic tails will aggregate when exposed to a water-based solvent forming an outer shell of hydrophilic heads, and a core made up of hydrophobic tails. The rearrangement is brought about by the driving forces pushing the hydrophobic part of these molecules away from the solvent and towards the core while bringing the hydrophilic side away from the core and towards the aqueous solvent. Drugs are often hydrophobic and, given that this is the case, will end up inside the micelle [18], [21]. Figure 5 below shows a visual representation of the process above [39].

Crosslinking of micelles is required for the journey throughout the body as it allows the micelle to retain the drug inside its core and does not allow it to release its cargo prematurely. Furthermore, like other nanoparticles, they can be PEGylated to turn them into stealth micelles, and a ligand can be conjugated to their surface to make sure they arrive at the right location in the body. Finally, a trigger can be used to ensure the

release of the contents upon demand [40], [41]. Micelles have been extensively studied for years; however, obtaining FDA approval has been a challenge, especially when compared with alternative nanoparticles like liposomes.

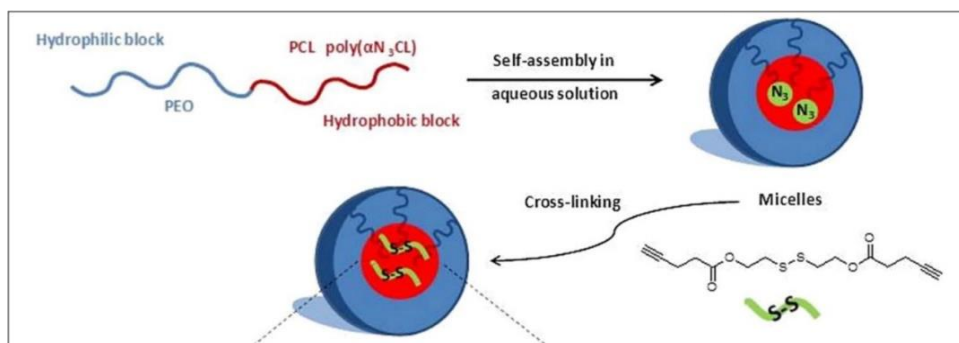


Figure 5: Micelle Formation [39]

2.3.5 Liposomes. Liposomes are one or multi-layered nanoparticles that are composed of a phospholipid bilayer. The phospholipid bilayer is composed of lipid molecules that have a phosphate group on their heads and a lipid group as their tail. The liposomal structure is unique, considering it can entrap both hydrophobic and hydrophilic drugs. The hydrophobic drugs can be trapped in the bilayer with the hydrophobic tails, and the hydrophilic drugs can be encapsulated inside the core of the liposome as it is hydrophilic. The liposome surface can be modified to convert the liposomes into both stealth and actively targeted liposomes. This is achieved by conjugating PEG and a ligand to the surface of the liposome [18], [28], [42]. Figure 6 shows a visual representation of a liposome [43].

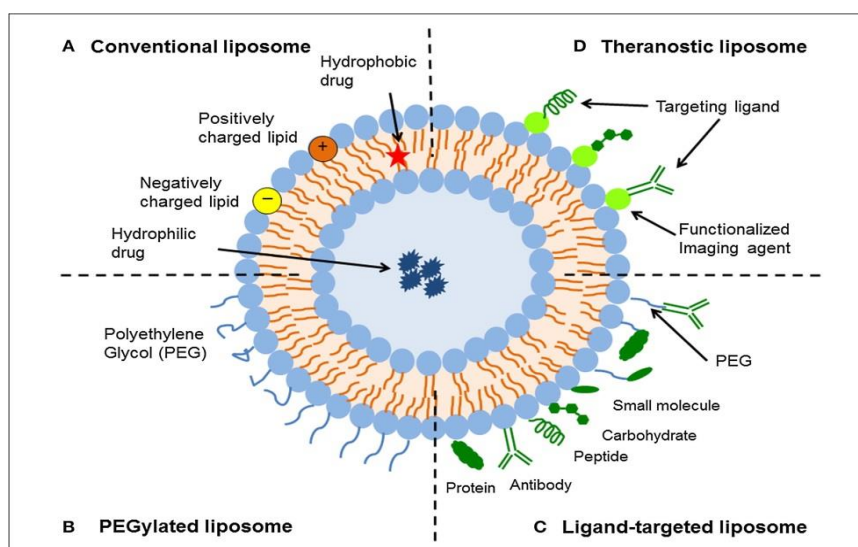


Figure 6: Liposome Structure [43]

As can be seen in Figure 6, a liposome can be functionalized in several ways. A liposome's composition is similar to that of a human cell membrane since it includes a phospholipid bilayer and cholesterol. Cholesterol, in cell membranes, is responsible for membrane fluidity and is added to the liposome for this purpose. Consequently, liposomes are made of structures that are already available in the body and are known to have little to no toxicity. Conventional liposomes encapsulating doxorubicin were approved by the FDA after successful clinical trials in 1995. One of the most used methods of making liposomes is the thin-film hydration method. This method relies on making a film of the lipids and then hydrating it with the solvent. The liposomes will form when exposed to the solvent, and some of the solvent will be encapsulated within the spaces inside the core of the liposome [18], [43].

2.4 Ligand-Targeting in Liposomal Drug Delivery

Several ligands can be used for targeting, and one of the most important criteria in choosing a ligand is the overexpression rate of the ligand's receptor on the surface of the targeted tumor. Common ligand types include antibodies, proteins, peptide chains, and carbohydrate groups, each of which has unique considerations. Tumors overexpress receptors for several ligands simultaneously, thus expanding the possible targeting options [44].

2.4.1 Trastuzumab. Trastuzumab, more well-known by its brand name Herceptin, is a monoclonal antibody that targets the Human Epidermal Growth Factor 2 (HER2) receptor. HER2 is a part of the Epidermal Growth Factor Receptor (EGFR) family. The HER2 receptor is extremely important for cancer cells as it helps in the process of growth and proliferation. When the antibody Herceptin binds to the HER2 receptor, it inhibits its function. Consequently, stopping the cancer cells from proliferation. This ligand is studied extensively because it provides not only an active targeting method for the nanoparticle to reach the cancerous tumor but also causes an immune response to occur that helps with killing the cancer cells. A phenomenon that happens when Herceptin reaches the targeted cancer cell is called antibody-dependent cellular cytotoxicity, and this inhibits the cell proliferation of cancer cells. The HER2 receptor is overexpressed in some forms of breast cancer. Furthermore, HER2 receptors can be found in some ovarian and uterine cancers. Since it preferentially binds to the chemical trastuzumab, trastuzumab can be used as a ligand in DDS. Furthermore, HER2

is scarcely found on normal human tissue, which empowers these DDS to specifically bind to cancerous tissue [45], [46], [47].

2.4.2 Folic acid. Folic acid, aka the folate moiety, is a relatively low-molecular-weight vitamin that targets the folate receptor [45]. Folate receptors are overexpressed on several cancerous tumors making folate a viable option in many situations. For example, Ross *et al.* found folate receptor expression in carcinomas to be around 200 times more than normal tissue [48]. The folate receptor mediates uptake of folate-brandishing liposomes into cancerous tumors. The instant that folate binds to its receptor, it is immediately internalized, along with the liposome, by receptor-mediated endocytosis and only detaches from the receptor at pH values lower than 5 [49]. Favorably, folate is relatively inexpensive and stable over a broad range of body temperatures. This availability and wide applicability make folate a very attractive and saturated research field [50]. Viable cancers for folate-modified treatment include breast, ovarian, and brain cancer.

2.4.3 Transferrin. Tf, a glycoprotein naturally secreted by the human liver, can be utilized as a ligand in a DDS. It has a molecular weight of 78 kDa and comprises 970 amino acids. Tf's main purpose in the body is to transport iron to cells to aid in cell growth. As expected for growth-enhancing proteins, its receptor is overexpressed in a wide variety of cancerous cells and tumors [51], [52], [53], [54], [55]. Tf-modified SDDS can utilize this matter and selectively bind to cancerous cells. Unfortunately, research has shown that the cytotoxicity of Tf-bound liposomes is higher than uncoupled liposomes [44]. To avoid this, the Tf receptor can also be targeted using mAbs and other ligands. The wide variety of potential ligands that can be utilized make the Tf receptor a very promising target for cancerous drug delivery. Once Tf, or other compatible ligands, binds to the receptor, it is internalized along with the nanocarrier using receptor-mediated endocytosis. Once inside the cell, the release of chemotherapeutics encapsulated inside the conjugated liposomes can begin killing the cancer cell. This happens because the cell tries to dissolve the capsule thereby releasing the contents. Tf-liposome conjugates have been utilized for the delivery of other cancer therapies like photodynamic, gene, and immunotherapy [56]. Furthermore, Tf-conjugated capsule-free chemotherapeutics were also studied thoroughly [57].

2.5 Trigger Mechanisms

An effective triggering mechanism ensures the contents of the liposomes are released specifically at the tumor site. The trigger can either be an internal trigger or an external trigger. An internal trigger is one that uses the cancerous cells' own hostile environment to damage the nanoparticle and release its contents into the cell. For example, quenched pH levels or higher temperatures may be used as possible triggers. An external mechanism utilizes external factors like light, heat, and ultrasound focused at the tumor site to provoke the nanoparticle to rupture and release its contents [58], [59].

2.5.1 pH. pH-responsive liposomes are stable at physiological pH, which is around 7.4, but when exposed to a different pH (usually, an acidic pH), they destabilize and lose their structure, releasing their contents in the process. The pH responsiveness of these liposomes is achieved with surface-modification by a pH-responsive substance. Often, this substance forms a stable bond at basic and physiological pH levels that deteriorates in other environments. Examples of such bonds include hydrazone, ester, amides, and ether bonds [60]. This is an advantageous feature because cancerous tumor environments have a lower acidic pH than normal, due to the Warburg effect [59]. The Warburg effect exists because of the rapid growth of cancerous tumors. Cancers grow faster by utilizing alternative, anaerobic routes of metabolism [58]. Among causing other destabilizing factors for cancer, anaerobic metabolism forms acids as a byproduct leaving behind a drastically acidic environment. The pH trigger is recognized as an internal trigger because the cancer's environment is utilized against it instead of an external trigger [61]. For liposomes specifically, the phospholipid bilayer is modified with a compound that changes phase in acidic pH. This causes the liposomes to selectively release at tumor sites because of their inherent acidic nature [62].

2.5.2 Temperature. The mechanism of this trigger relies on hyperthermia or inducing hyperthermia in the tumor. Although hyperthermia damages healthy tissue, it can be controlled to ensure that only the tumor and some surrounding tissue feel its effects. Tumor environments favor higher temperatures as that enhances growth. Tumor tissue grows faster at temperatures between 37 and 39 °C. However, it deteriorates at temperatures higher than 39 °C [63]. Heating the body must, therefore, take this into account to avoid aiding tumor growth. Any temperature-sensitive SDDS must take

advantage of this and trigger only at temperatures higher than approximately 39 °C. An example of such SDDSs is temperature-sensitive liposomes [64]. Liposomes are synthesized to be stable at body temperature (around 37°C). This effect is achieved by modifying the bilayer composition of the liposomes. This means that if a tumor site exhibits a higher temperature or a thermal effect is induced from an external source, these liposomes can become unstable and lose their structure. This effect can cause liposomes to release their contents, thereby inducing cell death [59].

2.5.3 Light. Focused light can cause hyperthermia or cause nanoparticle structure changes in the body. Therefore, it is used as a trigger for the release of drugs in tumors. Light can be precisely focused precisely and does not cause considerable unwanted tissue damage. However, there are problems with deep tissue penetration. The wavelength and intensity can be modified to efficiently harm cancer cells. Light is also used in cancer treatment; photothermal therapy and photodynamic therapy utilize light to damage cancerous cells. Photothermal therapy utilizes light's natural ability to induce hyperthermia, while photodynamic therapy creates reactive oxygen species that are harmful to cells. Nanoparticles can be designed to be vulnerable to light. The synergistic result is ruptured nanoparticles at the tumor site aided by light's ability to kill cancer cells [65], [66].

2.5.3 Ultrasound. Ultrasound is a safe imaging method that was adopted for medical purposes. Extensive studies show ultrasound waves can be benign to humans and are therefore routinely used for the imaging of fetuses in pregnant women. Ultrasound's biocompatibility means it adds no cytotoxicity to any SDDS [67]. Ultrasound is a mechanical wave classified by frequency, intensity, and pulse duration. The frequency of ultrasound is usually above the human hearing level (> 20 kHz). For imaging purposes, high-frequency ultrasound is used to create a high-resolution image. The high-frequency ultrasound used is usually around 1 MHz. However, as frequency increases, the penetration depth of ultrasound decreases significantly. For example, the penetration depth is around 10 cm at imaging frequencies. Ultrasound's mechanical nature means it travels faster in dense phases, which means it is better utilized on solid and liquid phases than gases. One downside to this phenomenon is the inability to use ultrasound for therapeutic or imaging purposes in the lungs. The power density of the

ultrasound is measured in units of W/cm^2 . It is the power of the wave applied to a unit area of tissue. It is calculated using Equation 1[68]:

$$I = \frac{P}{\rho * c} \quad (1)$$

where I is the intensity, P is the acoustic pressure, ρ is the density of the fluid, and c is ultrasound velocity in the fluid [68].

Ultrasound can be administered in two configurations for the sake of release. It can either be turned on and kept on for a continuous interval of time or pulsed at regular intervals. When it comes to biological applications, the continuous method is not preferred as ultrasound induces a thermal effect, and this can damage the tissue surrounding the tumor [68]. In contrast, pulsed ultrasound causes mild hyperthermia and is safer. Ultrasound can be applied at either high or low intensity. The choice of intensity depends on the area of application. Higher intensities deliver higher energies and cause tissue damage, while lower intensities can be too weak to trigger drug delivery response [68].

As mentioned previously, ultrasound can produce a thermal effect on the body. This thermal effect is due to the absorption of energy by the tissue where the ultrasound is applied [69]. If the absorption effect is too high, then the tissue's temperature will increase drastically, causing cell death. Furthermore, this could result in hyperthermia. Figure 7 below shows the effects of hyperthermia on the tissue [68]. Additionally, the tissues in the body are not homogenous, and this causes parts of the mechanical sound

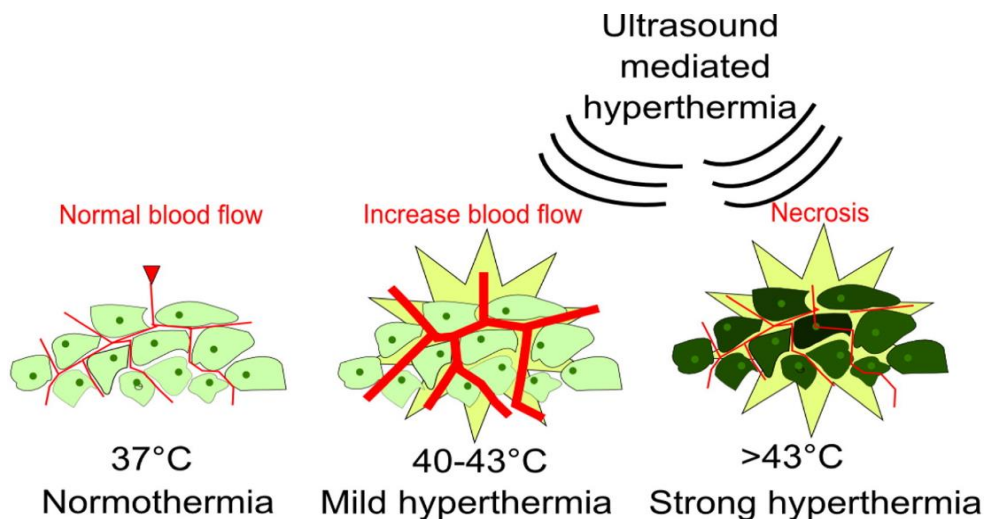


Figure 7: Ultrasound Induced Hyperthermia effect on the human tissue [68]

wave to disperse instead of being absorbed or continuing unaffected. The combination of both effects absorption and dispersion is called attenuation.

In addition to thermal effects, ultrasound applications can also cause mechanical effects. Waves generated by ultrasound have an acoustic pressure with a positive peak and a negative peak. At these two peaks, a phenomenon called cavitation occurs if there are bubbles in the surrounding fluid. There are two modes of ultrasound-induced cavitation, stable and collapse, each caused by different ultrasound parameters. Stable cavitation compresses and expands the bubbles at a stable rate, where they do not implode or cause disruptions in the surrounding fluid to a great extent. On the other hand, inertial or collapse cavitation causes these bubbles to explode and create a shockwave in the surrounding environment [69]. When dealing with liposomal release, collapse cavitation is desired as it allows the bubbles to shear the liposomes open, releasing their contents. Figure 8 below shows the effects of cavitation [70], [71].

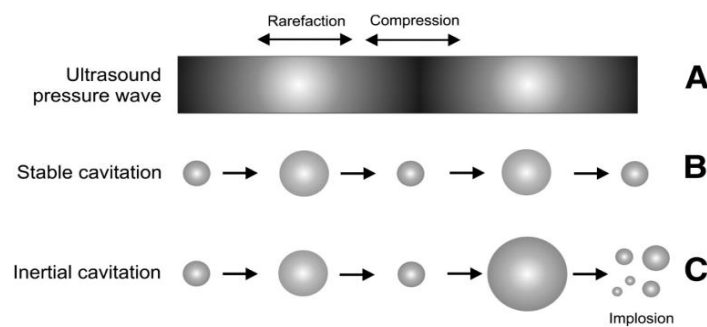


Figure 8: Stable and Inertial Cavitation [70]

When stable cavitation is introduced to a cell membrane, sonoporation takes place, which means blood vessels become more permeable. This phenomenon occurs because of the shear stress applied to the cell membrane because of the micro streams produced by stable cavitation. The micro streams allow for better uptake of drugs into cells by creating pores in the cell membrane. Research has shown that ultrasound causes sonoporation using both stable and inertial cavitation [70], [67].

While ultrasound has been deemed safe for use on humans, there are several configurations of ultrasonic waves that can cause damage to tissues. Ultrasound can excite dissolved air bubbles present in the lungs causing them to rupture due to cavitation. The application of ultrasound must be administered on a conductive gel-coated skin. This means that if the ultrasonic wave configuration is harmful, it can cause the skin to burn. To ensure the safe usage of ultrasound, two standards are utilized: the

thermal and mechanical indices. The thermal index demonstrates the rise in temperature that will occur due to the use of ultrasound, and Equation 2 shows how the thermal index is calculated [68].

$$TI = \frac{W_p}{W_{deg}} \quad (2)$$

where W_p is the acoustic power, and W_{deg} is the power required to raise the temperature of the targeted tissue by 1 °C. In other words, the thermal index is a measure of the increase in tissue temperature caused by the current configuration application. The hard limit is 6 °C everywhere on the body, but the eyes and neighboring skin. The mechanical index, on the other hand, defines how likely it is for collapse cavitation to occur. This depends on whether the location where the ultrasound is applied already has dissolved bubbles or not. The mechanical index is calculated using Equation 3 [72].

$$MI = \frac{P_{neg}}{\sqrt{f}} \quad (3)$$

where P_{neg} is the negative pressure of the ultrasound, and f is the frequency in MHz. The hard limit here is 0.7 [68]. For the sites in the body that have no microbubbles present or gas pockets, the mechanical index limit established by the FDA is 1.9. Stable cavitation happens at a mechanical index below 0.1. Between 0.1 and 0.5 stable cavitation occurs that produces nonlinear oscillations. Finally, collapse cavitation happens at mechanical indices higher than 0.5 [73].

2.6 Previous Experimental *In Vitro*, *In Vivo*, and Release Studies

Given the severe side effects of current cancer treatments, extensive research efforts are directed toward alleviating its side effects. Therefore, several researchers have used liposomes and other nanoparticles to deliver chemotherapeutic drugs and other cancer therapies to tumors with mostly promising results. We review some relevant studies here. *In vitro* experiments are experiments conducted on cells outside of a biological host to study the effect the therapy presented has on these cells. *In vivo* experiments are experiments conducted on animal hosts to gauge how safe and how effective the presented therapy is in a living organism.

Sriraman *et al.* produced folic acid- and Tf- conjugated DOX-containing liposomes and studied their effect on Hela cells and a tumor grown from Hela cells in mice [74]. The authors argue that the combination of two moieties is advantageous

because of the heterogeneity of their attachment on liposomal surfaces, which may enhance cellular uptake. The liposomes were made by making a lipid film through the drying of chloroform on a rotary evaporator and then freeze-drying the film for 4 hours. Subsequently, the freeze-dried lipid film was hydrated with ammonium sulfate forming the liposomes. These liposomes then underwent size reduction through extrusion. Untargeted DOX liposomes and single moiety targeted liposomes served as controls. The results showed that more Tf- and folic acid- conjugated liposomes were present in the Hela cell monolayer than single moiety liposomes. Furthermore, the dual-targeted DOX liposomes exhibited better cytotoxicity towards the Hela cells than both the control DOX liposomes and the single moiety liposomes.

The *in vivo* study was conducted on mice that were injected with Hela cells. The tumors were then given a growth period of around 11 days inside of the mice to ensure angiogenesis takes place. The mice were then split up into different groups and treated with the different liposome formulations. Consequently, the results showed better tumor growth inhibition by the folic acid and dual-targeted liposomes than the untreated and the other two controls. No signs of toxicity were shown on the animals because of the treatments used [74]. The *in vivo* results were less promising than the *in vitro* results but were favorable, nevertheless. This warrants further research as organisms are complex structures, and many reasons could have led to this.

Sakpakdeejaroen *et al.* conducted an *in vitro* and *in vivo* study on plumbagin-encapsulating Tf-conjugated liposomes [75]. Motivated by plumbagin's low solubility in blood, the authors' attempted to improve the agent's anti-cancer behavior by encapsulation. The Tf- and control liposomes were both made using probe sonication. The liposomes were then tested for stability, and both formulations showed stable behavior for at least 4 weeks. These liposomes were then tested for their anti-cancer efficiency on three different cell lines A431, B16-F10-luc-G5, and T98G. The cellular uptake of plumbagin was significantly higher for the targeted liposomes than the untargeted and free plumbagin. Furthermore, cell death was higher for all three cell lines when treated with the targeted liposomes than the control liposomes. The cell death was significantly higher for the B16-F10-luc-G5 cell line than the other two cell lines. Therefore, the cell line chosen for injection into the mice was the B16-F10-luc-G5 cell line. The tumors in the mice could grow before the mice were split into groups and treated with the liposome formulations and the free drug. The results showed slower

tumor growth when treated with the liposomal formulations than the free drug. The proposed treatment also led to the complete disappearance of the tumor in some and tumor regression in others. It is worth mentioning that the free drug treatment led to progressive tumor growth. Finally, the formulations showed no adverse side effects to the mice that were treated with them [75]. These results highly favor further exploration of this SDDS.

Jhaveri *et al.* conducted an *in vitro* and *in vivo* study on Tf- coupled liposomes encapsulating resveratrol [76]. The study set out to improve the delivery of resveratrol directly to cancer cells and avoid the rapid removal of the drug by the body. The liposomes were produced using the thin-film hydration method and freeze-dried after the organic solvent evaporated to ensure the complete removal of chloroform. The liposomes were then extruded to make them unilamellar and decrease their size. A human glioblastoma cell line called the U-87 cell line was used. The Tf-coupled liposomes showed better cell association and internalization than the plain liposomes. Furthermore, the Tf-coupled liposomes showed better cytotoxicity to the cancer cells than both the free drug and untargeted liposomes. The drug resveratrol increased the production of reactive oxygen species in cancer cells. The mice were then injected with the cancer cells and allowed time till the tumors grew to around 100 mm³. The mice were then treated with the Tf-coupled liposomes and the controls. The Tf-coupled liposomes showed better growth inhibition than both free drug and untargeted liposomes. It is interesting to note that the untargeted liposomes did not show significantly better growth inhibition than the free drug. The Tf-coupled liposomes treated group of mice also showed better survivability compared to the controls. Finally, no apparent toxicity was shown due to the treatments used [76].

Moghimipour *et al.* conducted an *in vitro* study using 5-Fluorouracil-encapsulating Tf liposomes [77]. The liposomes were made using the thin-film hydration method. Once the lipid film formed, a phosphate buffer solution (PBS) containing dissolved 5-Fluorouracil was added, and the solution was sonicated above the transition temperature of liposomes. The formed liposomes were then used on three different cell lines: HT-29 a human colorectal cancer cell line, CT26 a murine colon cancer, and Hu02 a fibroblast cell line. The *in vitro* study was conducted on the non-cancerous fibroblast cell line to test whether the Tf- liposome formulation was toxic to non-cancerous cells. Two controls were prepared: the normal liposomes and the free

drug. Cellular uptake in the cancerous cell lines was higher with the Tf-coupled liposomes than the untargeted liposomes, which ensures that the targeting is effective. Furthermore, the efficiency of anti-cancer activity by the Tfcoupled liposomes was higher than the two controls. Further confirming our assumption that encapsulation curbs side effects, the free drug caused higher cytotoxicity to the fibroblasts than both liposomal formulations [77].

Finally, the Ultrasound in Drug Delivery group at the American University of Sharjah has conducted several release studies on targeted liposomes encapsulating either DOX or calcein. The targeting ligands studied by this group are Tf [78], estrone [79] [80], RGD [81], lactose [82], albumin [83], and Herceptin [84].

The experimental studies presented above show that there is promise in the use of Tf as a targeting moiety for cancer. Although the first presented study shows more effective results using folic acid as a moiety, the overexpression of the Tf receptor on the surface of many different cancerous tumors also warrants further research.

Chapter 3. Materials and Methods

This chapter will discuss the materials that will be used, the procedures followed, and the modeling of the kinetics of the release.

3.1 Materials

The powders used for the preparation of liposomes are Dipalmitoyl phosphatidylcholine (DPPC) (1,2-dipalmitoyl-sn-glycerol-3-phosphocholine) and DSPE-PEG(2000)-Amine 1,2-distearoyl-sn-glycero-3-phosphoethanolamine-N-[amino(polyethylene glycol)-2000] (ammonium salt) were purchased from Avanti Polar Lipids Inc. (Alabaster, AL, USA). While the cholesterol, human holo Tf, ammonium sulfate salt, cyanuric chloride, Sephadex G-100, Sephadex G-25, phosphate buffer tablets, DOX, Triton X-100, HEPES sodium salt, L-ascorbic acid, and sucrose were all purchased from Sigma Aldrich and supplied by Labco. The bicinchoninic acid (BCA) kit was bought from Sigma50 Aldrich Chemie GmbH (Munich, Germany).

3.2 Procedures

3.2.1 Preparation of ammonium sulfate control liposomes. DSPE-PEG (2000), amine, DPPC, and cholesterol were used for the preparation of the control liposomes. The liposomes were prepared using the thin-film hydration method [85]. Briefly, the powders of DSPE and DPPC were mixed with cholesterol and dissolved in chloroform in a round bottom flask. Comprising the mixture was 5.58 mg of DSPE, 19.2 mg of DPPC, and 4.7 mg of cholesterol. These powders were placed in a 250-ml round bottom flask shown as step 1 in Figure 9. Then, 4 ml of chloroform were added to dissolve these organic compounds portrayed by step 2 in Figure 9. The round-bottom flask was placed in a rotary evaporator at vacuum pressure and 50 °C for fifteen minutes to form a lipid film by evaporating all the chloroform. The lipid film is the grey part on the bottom of the round bottom flask in step 3 of Figure 9. The thinner the lipid film, the better the liposomes formed. The thin-film hydration method was chosen as it is an easy and consistent method of making liposomes. While the lipid film formed, 29 mg of ammonium sulfate were added to 2 ml of distilled water and vortexed. The pH of the resultant solution is usually between 5.3 and 5.6. This solution was added to the round-bottom flask once the lipid film formed. The round-bottom flask was then connected to the rotary evaporator for 50 minutes at 60 °C, above the lipid's transition temperature.

The resulting solution is depicted in step 4 of Figure 9. It was then sonicated for two minutes in a sonication bath and extruded using an extrusion kit 31 times. The liposome solution was then placed in a column made of Sephadex G-25 and centrifuged for two minutes at a 1000 rpm to remove free ammonium sulfate. The Sephadex G-25 column was prepared by dissolving 1.5 grams of Sephadex powder in 20 ml of PBS and left to hydrate for a minimum of two hours. The resulting liposomes encapsulate ammonium sulfate and distilled water.

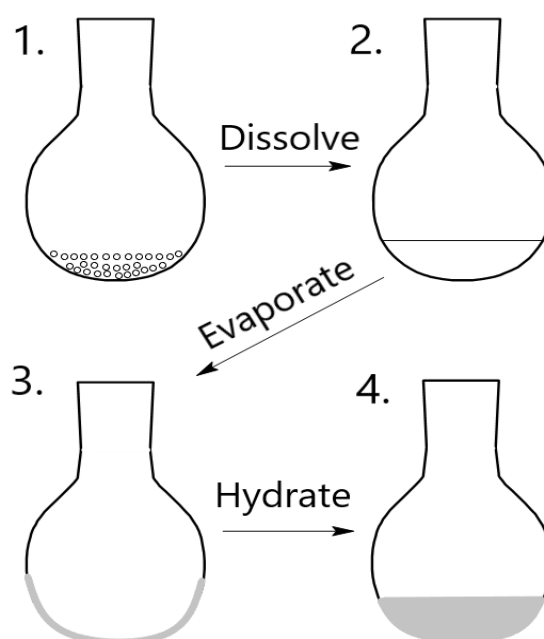
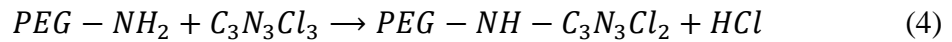


Figure 9: Thin-film hydration method

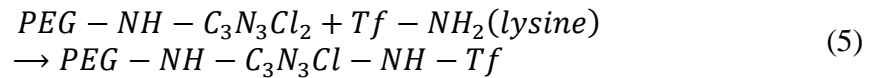
3.2.2 Preparation and addition of DOX. The encapsulation of DOX in liposomes is based on having a pH gradient between the inner liposomal solution and the outer solution [86], [87]. This pH gradient was maintained by dissolving DOX in the HEPES buffer solution. 16 mg of DOX was added to 1 ml of HEPES, a zwitterionic sulfonic acid buffering agent. The solution was then vortexed for around 30 minutes to ensure proper mixing. After adding 250 microliters of the DOX solution to the liposomes, the mixture was incubated in a water bath at 60°C for 40 minutes. The resulting solution was then passed through a column hydrated with PBS using the same steps as before. A slight adjustment was needed for the preparation of DOX liposomes, as outlined in section 3.2.1. The Sephadex powder will be hydrated in a HEPES buffer solution instead of PBS. In contrast to the ammonium sulfate solution inside the

liposomes that is acidic, the prepared DOX-HEPES buffer solution is of neutral pH. The pH gradient is self-maintaining because DOX is protonated inside the liposome.

3.2.2 Transferrin attachment. Prior to the attachment, these liposomes are passed through a borate-hydrated Sephadex column. The attachment is achieved by the conjugation of transferrin from the NH₂ terminal of lysine on a cyanuric chloride-modified PEG [88], [89]. Equation 4 shows the chemical reaction of conjugating PEG to cyanuric chloride.



Once the cyanuric chloride activated the PEG, Tf was added to the mixture. The solution is ready in 24 hours to ensure attachment as the process is slow [89], [90]. Equation 5 shows the attachment procedure of Tf to cyanuric chloride-activated PEG.



In this study, 10 mg of cyanuric chloride were first dissolved in 2.5 ml of deionized water and 0.5 ml of pure acetone. Then, the liposomes were placed in a vial and positioned in an ice bath. Then, 0.055 mL of the cyanuric chloride solution was added to the vial, and the reaction was left for 3 hours. While the solution reacted, 2 mg of Tf were added to 1 ml of borate buffer solution. After 3 hours, 0.125 ml of the Tf solution was added to the reaction vial, and the solution was left to react overnight. Once this concluded, the solution was passed through a Sephadex G-100 double-column prepared 24 hours before use. For the preparation of the double column, 1 gram of Sephadex G-100 powder was hydrated with 20 ml of PBS. The Sephadex G-100 column removes free Tf from the effluent liposomal solutions.

3.2.3 Determination of liposome size using dynamic light scattering (DLS). Size determination was performed using the DynaPro® NanoStar™, a DLS machine. DLS uses particle speed to estimate its size. This is based on dissolved colloids colliding with solvent particles due to random Brownian motion [91]. When dissolved particles and fluid particles collide, an energy transfer occurs between them and causes them to move [92]. A sample of 15 microliters of liposomes was dissolved and mixed properly in 1 ml of PBS. This sample was then transferred into a special DLS cuvette that was

then placed in the DLS machine. To ensure a proper measurement was made, a new DLS cuvette was used with every sample to avoid distortion by unclean or scratched used cuvettes. The DLS machine shines a laser through a filter that then passes through the sample, where the moving particles disperse and scatter the laser. These dispersed light particles are picked up by a light detector over a period. Finally, this signal is transferred to the computer application that processes it and calculates certain metrics based on these measurements. Among other metrics, the DLS machine computes the hydrodynamic radius and the polydispersity. Equation 6 is used to calculate the hydrodynamic radius based on the speed of the particles is the Stokes-Einstein equation [92].

$$D = \frac{K_B * T}{6 * \pi * \eta * R_H} \quad (6)$$

where D is the diffusion coefficient of the particles in m^2/s , T is the temperature in Kelvin, k_B is the Boltzmann's constant in $\text{m}^2\text{kg}/\text{K.s}^2$, η is the viscosity in Pa.s and R_H is the hydrodynamic radius in m . The polydispersity index portrays the particle size distribution. To ensure consistent sizes of liposomes, we used an upper limit of 20% polydispersity to define a good sample. The computer application marks samples that have a percent polydispersity index higher than 20% and does not include it in the averaged number it displays.

3.2.4 Determination of liposomal phospholipid content using Stewart assay.

The Stewart Assay is used to quantify the amount of phospholipid content present in a sample. It uses an inorganic reagent, namely ammonium ferrothiocyanate (FTC), to do this [93]. This compound creates a complex when combined with DPPC [94]. This complex is colored and dissolves in chloroform. To be able to quantify the amount of DPPC in the sample, a calibration curve is prepared to compare the absorbance at 485 nm, and the amount of DPPC added. This calibration curve can then be used to measure the amount of DPPC in a liposomal sample.

The procedure starts with adding 50 microliters of control liposomes into a 50 ml round bottom flask and 50 microliters of Tf liposomes into another 50 ml round bottom flask. Each flask is then placed on the rotary evaporator, kept at 45°C and under vacuum conditions for 15 minutes. After the liposomes dried up, 1 ml of chloroform is added to each flask to resuspend the sample. Each sample is then sealed properly to

avoid loss of chloroform and sonicated for 10 minutes in a sonication bath on its “delicate” setting. While the samples were sonicated, 14 centrifuge tubes are washed and dried properly. The tubes are labeled as 1, 1A, 2, 2A, 3, 3A, 4, 4A, 5, 5A, 6, 6A, B1, and B2. Centrifuge tubes B1 and B2 are blanks that contain no liposomes. These two are used to establish a baseline signal. Each tube will have a different concentration of liposomes added to it, according to Table 1. Every tube is labeled with a number, and an A is a replicate of the number. This way, each sample has a replicate to ensure that each sample’s result is accurate and not obtained because of dirt or a scratch on the cuvette used. Furthermore, samples from 1 to 3 are filled with control liposomes, and 4 to 6 are filled with transferrin liposomes.

Table 1: Amounts added to each centrifuge tube for the Stewart Assay

Tube number		Liposome solution (μL)	Chloroform (μL)	FTC (μL)	Total Amount (μL)
1	1A	75	1925	2000	4000
2	2A	125	1875	2000	4000
3	3A	200	1800	2000	4000
4	4A	75	1925	2000	4000
5	5A	125	1875	2000	4000
6	6A	200	1800	2000	4000
B1	B2	0	2000	2000	4000

Chloroform evaporates very quickly. Accordingly, special care was taken to keep the samples covered during preparation. After adding everything, each centrifuge tube was vortexed for 20 seconds to ensure that the reagent had enough contact time with the DPPC that is dissolved in the chloroform. This is required as FTC and chloroform are immiscible. These centrifuge tubes were then centrifuged for 10 minutes at 1000 rpm. Once the centrifuge concluded, a sample from the bottom of the tube was collected using a clean Pasteur pipette as it contains the colored complex of interest. Note that this chloroform layer should be placed in a quartz cuvette as a plastic cuvette would dissolve in chloroform. The absorbance at 485 nm is measured using an EvolutionTM 60S Ultraviolet-visible (UV-VIS) spectrophotometer (Thermo Fisher Scientific, Waltham, MA, USA) and using the calibration curve, the amount of DPPC was obtained. Finally, the inorganic reagent was disposed of in an inorganic waste bottle.

3.2.5 Determination of protein content using BCA assay. The BCA assay was used to quantify the number of proteins found in a sample by reducing copper from Cu^{+2} to Cu^{+1} . The reduction of copper happens more effectively when reacted with peptide bonds at 60°C [95]. This process involves two reactions. The first reaction involves the reduction of Cu^{+2} to Cu^{+1} by the amino acid residue called the biuret reaction. The second reaction is a reaction between the reduced Cu^{+1} and BCA. This reaction creates a purple color that is more noticeable at higher protein concentrations. A calibration curve with pure Tf was prepared at an absorbance of 562 nm [96]. The procedure starts with the addition of 7 ml of buffer QA to 7 ml of buffer QB and adding 0.28 ml of CuSO_4 to this mixture. Both buffers can be found in the BCA kit mentioned in Section 3.1. The mixture was gently mixed until it turned green. The mixture and liposomes were placed in 9 different Eppendorf tubes. Table 2 displays the amounts that were added to each Eppendorf tube. The Eppendorf tubes were labeled N1, N2, N3, N4, T1, T2, T3, T4, and B. N represents control liposomes, T represents Tf liposomes, and B represent blank.

Table 2: Amounts added for BCA assay

Eppendorf Tube		BCA mixture (μL)	PBS (μL)	Liposomes (μL)	Total amount (μL)
N1	N2	1000	600	400	2000
N3	N4	1000	800	200	2000
T1	T2	1000	600	400	2000
T3	T4	1000	800	200	2000
B1		1000	1000	0	2000

The Eppendorf tubes were placed in a 60 °C water bath for an hour. The samples were then garnished using a purple color with shading based on protein concentration. The Tf liposomes should have a darker purple color, and the control liposomes should be light purple. The blank sample was placed in a cuvette, and a baseline was established prior to this. The same spectrophotometer used in the Stewart assay was used to make these measurements.

3.2.6 Low-Frequency ultrasound release. The release of encapsulated DOX can be measured using a spectrofluorometer. This is because DOX is naturally fluorescent, and when excited with a laser, can produce a signal with a wavelength of 595 nm [97]. The laser wavelength should be around 470 nm to properly excite the

DOX [98]. Using this knowledge, the release profile can be measured by placing 75 microliters of the liposomal solution in 3 ml of PBS in a large 4-ml transparent cuvette. This cuvette is placed in QuantaMaster QM 30 Phosphorescence Spectrofluorometer (Photon Technology International, Edison NJ, USA). Baseline readings are done for 50 seconds on the unperturbed sample. After that, the collection is paused, and the ultrasound generating probe (model VC130PB, Sonics & Materials Inc., Newtown, CT) is placed inside of the sample. Figure 10 portrays how the probe should be positioned in the cuvette.

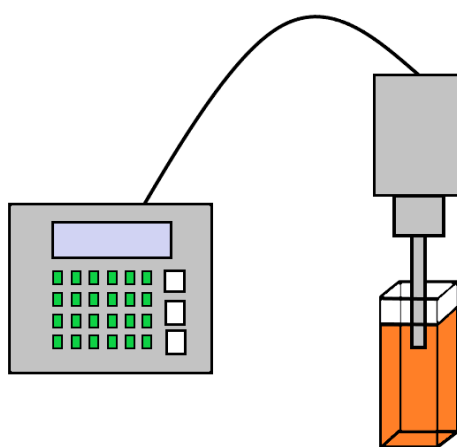


Figure 10: Ultrasound probe placed in a cuvette filled with DOX Liposomes

Once the probe is positioned correctly in the middle of the cuvette and not touching any side, the sample is subjected to ultrasound waves at 20 kHz. Data are collected for 10 more seconds, and then the ultrasound was turned on. The ultrasound waves are pulsed at 20 seconds on and 20 seconds off. Data is collected for a total of 300 seconds and six pulsed cycles of ultrasound. After this, 50 microliters of Triton X-100, a non-ionic surfactant, is added using a pipette to the sample to lyse the liposomes. After vigorous mixing, the sample is placed back into the spectrophotometer for 20 more seconds of data collection. The release is measured and replicated three times at three different power intensities: 7.46, 9.85, and 17.31 mW/cm². The spectrophotometer presents a final time profile of fluorescence intensity during the experiment. To calculate the amount of DOX released, the cumulative fraction release (CFR) profile is constructed using Equation 7.

$$CFR = \frac{f - f_0}{f_{Tri} - f_0} \quad (7)$$

where f is the fluorescence at time t , f_0 is the fluorescence at the beginning of sample collection before ultrasound is pulsed, and f_{Tri} is the fluorescence intensity after the addition of Triton X-100. The addition of Triton X-100 is important because it dissolves the liposomes and allows us to quantify the resultant maximum release of DOX.

3.3 Modeling

Kinetic modeling is needed to be able to predict how a drug is released. It can be used to predict important dynamic properties like the diffusion coefficient, which quantifies drug delivery behavior [99]. The kinetic models used in this research are the Zero-Order, First-Order, Higuchi, Korsmeyer-Peppas, Hixon-Corwell, Baker-Lonsdale, Gompertz, Weibull, and Hopfenberg models. These models are all either empirical or semi-empirical [99].

3.3.1 Zero-order model & first-order model. The zero-order model depends on Equation 8. It assumes the rate of release is slow and does not change with time [99].

$$\frac{dQ}{dt} = +K \quad (8)$$

where K is the release constant and has units of concentration per time. To obtain an equation for concentration as a function of time separation of variables is conducted on Equation 8, and the two sides are integrated, as seen in Equation 9.

$$\int_{Q_0}^{Q_1} dQ = \int_0^t K * dt \quad (9)$$

where Q_1 is the amount of drug dissolved at a certain time, Q_0 is the initial amount of the drug, which is usually zero because the release has not started, and K is the kinetic constant [99]. Furthermore, the final form of the zero-order model is given by Equation 10.

$$Q_1 = Q_0 + K * t \quad (10)$$

To be able to use this model to fit release data, it is transformed into CFR as a function of time in Equation 11.

$$\frac{Q_1 - Q_0}{Q_T} = CFR = \frac{K}{Q_T} * t \quad (11)$$

where Q_T is the total amount of the drug available, finally, the equation can be simplified further by the introduction of k_0 in Equation 12.

$$CFR = k_0 * t \quad (12)$$

This model can be used to describe drug delivery systems like transdermal delivery and matrix tablets [100]. The first-order model is given by Equation 13.

$$\frac{dc}{dt} = -k * c \quad (13)$$

where c is the temporal concentration while k is the first-order kinetic constant [99]. Equation 13's variables are separated and integrated, as shown in Equation 14.

$$\int_{c_0}^c \frac{dc}{c} = -k * \int_0^t dt \quad (14)$$

where c_0 is the initial concentration. After integration, Equation 15 is obtained.

$$\ln\left(\frac{c}{c_0}\right) = -k * t \quad (15)$$

Equation 15 is transformed to incorporate CFR into Equation 16 by taking the exponential of both sides then multiplying by c_0 .

$$c = c_0 * e^{-k*t} \quad (16)$$

Equation 16 is further modified by dividing both sides by the total concentration c_T and introducing CFR and obtaining Equation 17.

$$\frac{c - c_0}{c_T} = CFR = \frac{c_0}{c_T} * (e^{-k*t} - 1) \quad (17)$$

Finally, Equation 17 is linearized to obtain Equation 18, which can be directly applied to the obtained data with the assumption that c_0 is small compared to CFR.

$$\ln(CFR) = \ln\left(\frac{c_0}{c_T}\right) - k * t \quad (18)$$

Once release data are obtained, these models can be plotted versus time, and the constant can be obtained. This will aid us in predicting the kinetics of the release. The first-order model assumes the drug release rate is proportional to the amount of drug remaining inside of the matrix holding it. In the case of this research, that would be the

amount of DOX left inside of the liposome. This model is used to describe drugs that are enclosed in a porous matrix.

3.3.2 Higuchi model. In 1961, Higuchi proposed a model that was originally intended for planar systems, but it was extended to describe drug release kinetics [100]. This model is dependent on the assumptions that the drug concentration prior to release is higher than the solubility of the drug, the process of diffusion only happens in one dimension, the system thickness is larger than that of drug particles, the swelling of the matrix can be neglected, the drug diffusivity does not change, and the sink conditions are always ideal [99], [100]. The Higuchi concentration profile is shown in Equation 19.

$$\frac{Q}{A} = h \left(C_{cap} - \frac{C_s}{2} \right) \quad (19)$$

where the drug solubility in the matrix is C_s , Q is the drug released at time t , the concentration of the drug within the capsule or matrix is C_{cap} , the area is A , and the distance from the capsule surface is h [99], [101]. Equation 18 is differentiated with respect to time to obtain Equation 20.

$$J = \frac{1}{A} * \frac{dQ}{dt} = \frac{dh}{dt} * \left(C_{cap} - \frac{C_s}{2} \right) \quad (20)$$

where J is the mass flux. Then Fick's first law of diffusion can be used to simplify Equation 20 to Equation 21.

$$J = -D * \frac{dc}{dx} = \frac{dh}{dt} * \left(C_{cap} - \frac{C_s}{2} \right) = -D \left(\frac{-C_s}{h} \right) \quad (21)$$

where D is the drug diffusivity. Equation 21's variables are separated and integrated, as shown in Equation 22 and 23.

$$\left(C_{cap} - \frac{C_s}{2} \right) * \int_0^h h * dh = -D(-C_s) * \int_0^t dt \quad (22)$$

After integration Equation 23 is obtained.

$$\frac{h^2}{2} * \left(C_{cap} - \frac{C_s}{2} \right) = D * C_s * t \quad (23)$$

Equation 23 is manipulated to provide h on one side to be plugged back into Equation 19. The resulting equation is given by Equation 24.

$$\sqrt{\frac{2 * D * C_s * t}{C_{cap} - \frac{C_s}{2}}} = \frac{Q}{A * (C_{cap} - \frac{C_s}{2})} \quad (24)$$

Equation 24 is manipulated further to obtain Equation 24, and K_h is introduced as a release rate constant in Equation 25.

$$K_h = A * \sqrt{2 * D * C_s * (C_{cap} - \frac{C_s}{2})} \quad (25)$$

K_h from Equation 25 is plugged into Equation 24, and Equation 26 is obtained.

$$Q = K_h * \sqrt{t} \quad (26)$$

Finally, both sides of equation 24 are subtracted from Q_0 the initial concentration in the solution and divided by Q_T the total concentration of drug to obtain the model in terms of CFR. Equation 27 is utilized to model the release data.

$$\frac{Q - Q_0}{Q_T} = CFR = K_h * \sqrt{t} - \frac{Q_0}{Q_T} \quad (27)$$

This model has some limitations; it poorly applies to the end of drug release. Equation 28 is the Higuchi model used to portray heterogenous planar systems where drug diffusion occurs through a porous matrix, and the drug concentration before starting release is lower than the solubility of the drug.

$$Q = \sqrt{\frac{D * \delta}{\tau} * (2c_0 - \delta c_s) * c_s * t} \quad (28)$$

where δ is the porosity, τ is the tortuosity, and D is the diffusion coefficient [99]. This model can also be used to explain the release kinetics of transdermal drugs.

3.3.3 Korsmeyer-Peppas model. Korsmeyer-Peppas model is a relatively easy model to apply that is frequently used when modeling drug release kinetics [99]. The formula for this model is shown in Equation 29.

$$\frac{M_t}{M_\infty} = CFR = k * t^n \quad (29)$$

where M_t is the amount of drug released at time t and M_∞ is the amount of drug released at infinite time, k is the release rate constant, and n is the release exponent [102]. The release exponent can be obtained from Table 3 based on the drug transport mechanism and environment structure. Equation 27 is linearized and portrayed in Equation 30.

$$\log(CFR) = \text{Log}(k) + n * \log(t) \quad (30)$$

Table 3: Ways of obtaining the exponent for the Korsmeyer-Peppas model based on the geometry [102]

Release exponent (n)			Drug transport mechanism
Thin film	Cylinder	Sphere	
0.5	0.45	0.43	Fickian diffusion
$0.5 < n < 1$	$0.45 < n < 0.89$	$0.43 < n < 0.85$	Anomalous transport
1	0.89	0.85	Polymer swelling

3.3.4 Hixson-Crowell model. Hixson-Crowell model is used to describe systems where an alteration to the surface area or the radius of a structure occurs while release [99]. Equation 31 portrays this model.

$$W_t^{\frac{1}{3}} = W_0^{\frac{1}{3}} - \kappa * t \quad (31)$$

where W_0 is the initial drug in dosage form, W_t is the drug in dosage form at time t , and κ is the constant that includes the surface area to volume ratio. The drug in this model is assumed to dissolve in a manner where the geometric shape initially is always upheld until the whole tablet dissolves completely. For example, if the tablet/nanocarrier is spherical, the spherical shape does not change but gets smaller from all sides equally to maintain a spherical shape [102]. Equation 31 can be portrayed as Equation 2 by the division of Equation 31 by $W_0^{1/3}$.

$$(1 - CFR)^{\frac{1}{3}} = K_H * t \quad (32)$$

where K_H is the release rate constant, and CFR is obtained from Equation 7.

3.3.5 Baker-Lonsdale model. In 1976, Baker and Lonsdale developed a new model from the Higuchi model. This model assumes a spherical matrix [99]. It is depicted by Equation 33.

$$k * t = \frac{3}{2} * \left[1 - \left(1 - \frac{M_t}{M_\infty} \right)^{\frac{2}{3}} \right] - \frac{M_t}{M_\infty} \quad (33)$$

k for a homogenous spherical matrix is the diffusion coefficient multiplied by 3 and C_{ms} the drug solubility inside the matrix and divided by C_0 the initial concentration and r_0 the initial radius. The value of K , for a heterogeneous matrix, includes the porosity of the matrix and tortuosity factor.

3.3.6 Gompertz model. The Gompertz model is usually used to portray the dissolution in *in vitro* [99]. The model is given by Equation 34.

$$X(t) = X_{max} * e^{[-\alpha * e^{\beta * \log(t)}]} \quad (34)$$

The fraction of the dissolved drug at time t is given by $X(t)$, the maximum dissolution is given by X_{max} , the undissolved portion at time 1 is given by α and the shape parameter which has the units of the rate of dissolution per unit of time is given by β [99]. This model is beneficial because it can represent drug delivery systems that have good solubility and a release rate that is neither high nor low.

3.3.7 Weibull model. The Weibull model is given by Equation 35.

$$M = M_0 * \left(1 - e^{-\frac{(t-T)^b}{a}} \right) \quad (35)$$

The drug originally found is given by M_0 , the amount of drug dissolved as a function of time is M , the variable accounting for a time lag is given by T , the parameter accounting for the time dependence is given by a and parameter accounting for the shape of the curve is b [99]. This model is empirical, and therefore, cannot be used to make biological correlations and conclusions about drug behavior. The model parameters, a and b , can be obtained from the slope and intercept of the resultant linear log plot.

3.3.8 Hopfenberg model. This model was developed by Hopfenberg to find a correlation that best describes the kinetics of drug release from polymers whose surface erode over time as long as the surface area remains constant [99]. This model is portrayed in Equation 36.

$$\frac{M_t}{M_\infty} = 1 - \left(1 - \frac{k_0 * t}{C_L * a}\right)^n \quad (36)$$

where the rate constant is given by k_0 , the drug found in the mixture originally is given by C_L , the system's thickness divided by 2 is given by a , and the exponent n depends on the geometric shape of the polymer. It equals unity if the shape is flat, two if the shape is cylindrical, and three if the shape is spherical [99]. Since liposomes are spherical in shape, n is 3, and with some algebraic rearrangement, Equation 36 can be rewritten as Equation 37.

$$1 - \left(1 - \frac{M_t}{M_\infty}\right)^{\frac{1}{3}} = k * t \quad (37)$$

where k is the release constant and is k_0 divided by C_L and a .

Finally, all these models are going to be applied to the LFUS results to obtain the release rate constants. The coefficient of determination (R^2) of each model will be analyzed, and whichever model gives the best R^2 will be the one that best represents the drug release kinetics of the liposomes being used in this study.

Chapter 4. Results and Discussion

4.1 Characterization Test Results

4.1.1 DLS results. The liposome size was obtained using the DLS machine, and the results obtained are shown in Table 4.

Table 4: The size of control and targeted liposome measured using DLS

	Batch number	Liposome size (nm) (Radius)	Average liposome size \pm Standard Deviation (nm)	Percent polydispersity index (%)
Control	1	80.2	85.2 \pm 5.83	13.6
	2	83.6		12.3
	3	91.5		11.2
Tf	1	80.3	85.3 \pm 7.15	16.2
	2	82.1		11.0
	3	93.5		9.69

The sizes of both types of liposomes were found to be similar (statistically insignificant, p-value = 0.98). This is expected as the size of the Tf molecule does not significantly alter the liposome size, and that can be observed in another research conducted on Tf liposomes by Nour AlSawftah in [78]. The Tf liposomes obtained by that study are slightly larger than the control liposomes. However, like this research, the difference was statistically insignificant. These liposomes under 150 nm in size can utilize the EPR effect to accumulate at the tumor site. This means that these liposomes can effectively target cancer cells *in vivo* and *in vitro* experiments using passive methods. Furthermore, the percent polydispersity index was lower than 20% for all batches, which indicates that the synthesized liposomes were monodispersed.

4.1.2 Stewart assay results. The calibration curve that relates the phospholipid content to the absorbance is portrayed in Figure 11.

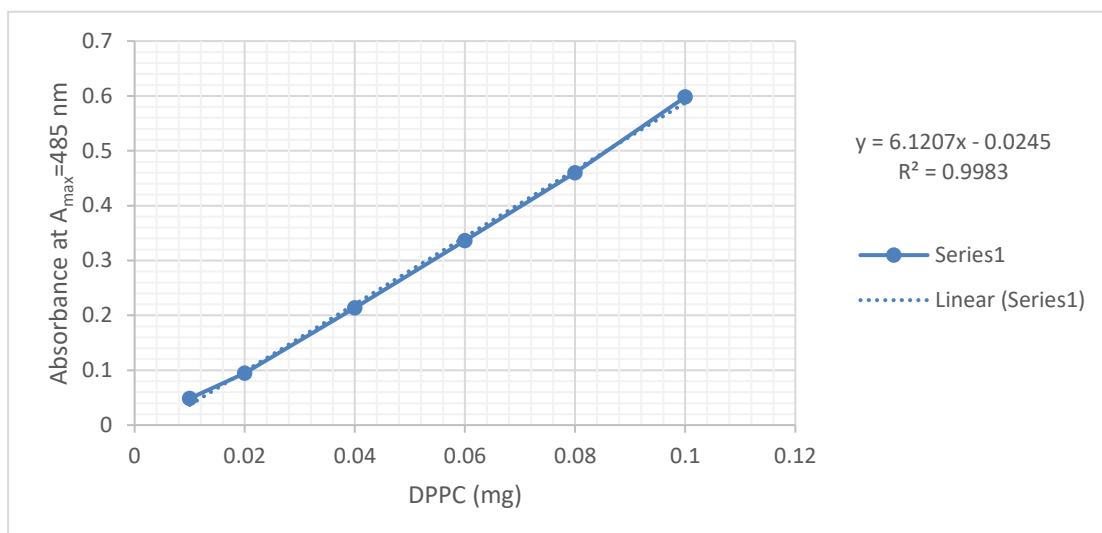


Figure 11: Stewart Assay Calibration Curve

The calibration curve obtained has a regression R^2 value of 0.9983; hence this linear relationship can be used to obtain the DPPC concentration in mg directly by plugging in the absorbance of the samples into the above equation. This calibration curve was obtained by measuring the absorbance of different levels of DPPC and can be used to measure the phospholipid content of the liposomes produced in this study. The amount of DPPC is found in Table 5.

Table 5: Stewart Assay Results

	Sample	Absorbance Average	DPPC (mg)	Average (mg)	DPPC (mg/ml) in the tube	Average (mg/ml)
Control	1	0.228	0.041	0.046	8.153	8.024
	1A	0.285	0.050			
	2	0.380	0.066	0.074	7.901	
	2A	0.477	0.082			
	3	0.701	0.119	0.120	8.019	
	3A	0.722	0.122			
Tf double column	4	0.152	0.029	0.028	5.033	6.219
	4A	0.146	0.028			
	5	0.348	0.061	0.060	6.395	
	5A	0.337	0.059			
	6	0.668	0.113	0.108	7.230	
	6A	0.610	0.104			

As can be seen in Table 5, the amount of lipids in the control liposomes is 8.024 ± 0.126 mg/ml, while in the Tf-targeted liposomes, it is 6.219 ± 1.109 mg/ml. This difference is statistically significant with a p-value of 0.049. This difference can be explained by the extra preparation steps that Tf-targeted liposomes undergo before they are characterized. Specifically, the double Sephadex G-100 column purification step, as this step dilutes the liposomes significantly. The control liposomes are 1.29 times more concentrated than the Tf-targeted liposomes.

4.1.3 BCA results. The BCA results can be seen in Table 6 for both control and Tf liposomes and their averages.

Table 6: BCA Results

	Recalculated Protein Content ($\mu\text{g/ml}$)	
	Control	Tf
Batch 1	0.0180	0.0396
Batch 2	0.0161	0.0327
Batch 3	0.0159	0.0311
Average	0.0167	0.0345

As can be seen in Table 6, the amount of proteins found in the Tf liposomes is ≈ 2 -fold higher compared to control liposomes. The results were tested using a two-tailed t-test, and the p-value was found to be 0.0028, indicating statistical significance. This result proves the conjugation of Tf molecules to the surface of the produced liposomes. The BCA assay relies on the calibration curve shown in Figure 12 to calculate protein content. This calibration curve is produced using different concentrations of Tf and recording the absorbance at 562 nm.

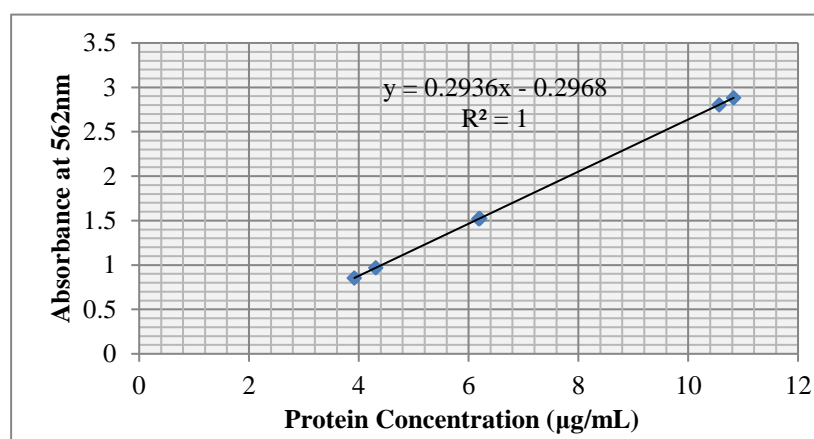


Figure 12: BCA Calibration Curve

As observed in Figure 12, the absorbance is linearly correlated to protein concentration; hence the equation shown can be utilized by plugging in the absorbance as y and obtaining the protein content as x. Finally, the Tf results are corrected by multiplying by 1.29 to account for the extra lipid content in the control liposomes. Figure 13 shows the difference \pm the standard deviation between the control and Tf liposomes in terms of protein content.

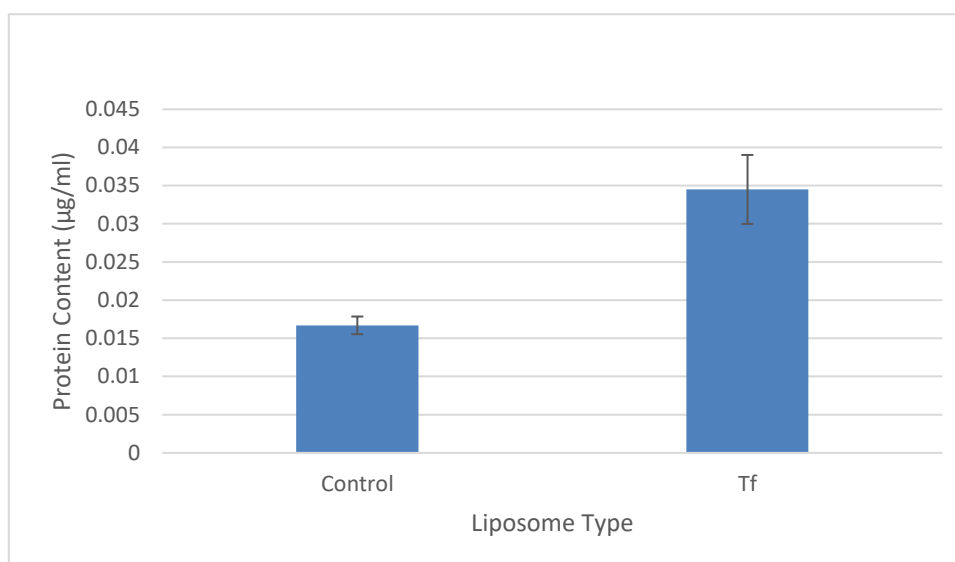


Figure 13: Difference in protein content between control and Tf-targeted liposomes

4.2 LFUS Results

4.2.1 Control liposomes LFUS release results. LFUS release studies were conducted on three batches of control liposomes at three different power densities, and the averaged results are presented in Figure 14.

Figure 14 portrays the results of the LFUS release study, and as expected, the fraction of the drug released is increasing with time, indicating that every time the ultrasound is pulsed (turned on) an increase in the fluorescence is observed. Furthermore, there is none or minimal increase or decrease at the off pulses of the ultrasound, which means that the liposomes are relatively stable (not releasing the anti-neoplastic agent) when not subjected to ultrasonic power. All six pulses of the 7.46 and 9.85 mW/cm² are similar (p-values in Tables 7 to 12 are higher than 0.05, showing statistical insignificance). This lack of statistical significance could be due to the extension of the off-pulse time by 10 more seconds compared to previous experiments, which led to the removal of the effect of hyperthermia due to the ultrasonic pulses [78],

[103]. Moreover, when comparing the release data at 17.31 mW/cm^2 with the two other power densities, for the first four pulses no statistical significance is observed as portrayed in Tables 7 to 10. However, statistical significance can be observed in the 5th and 6th pulse of the 17.31 mW/cm^2 . Figures 15 and 16 show the release of control liposomes at different pulses in two unique ways.

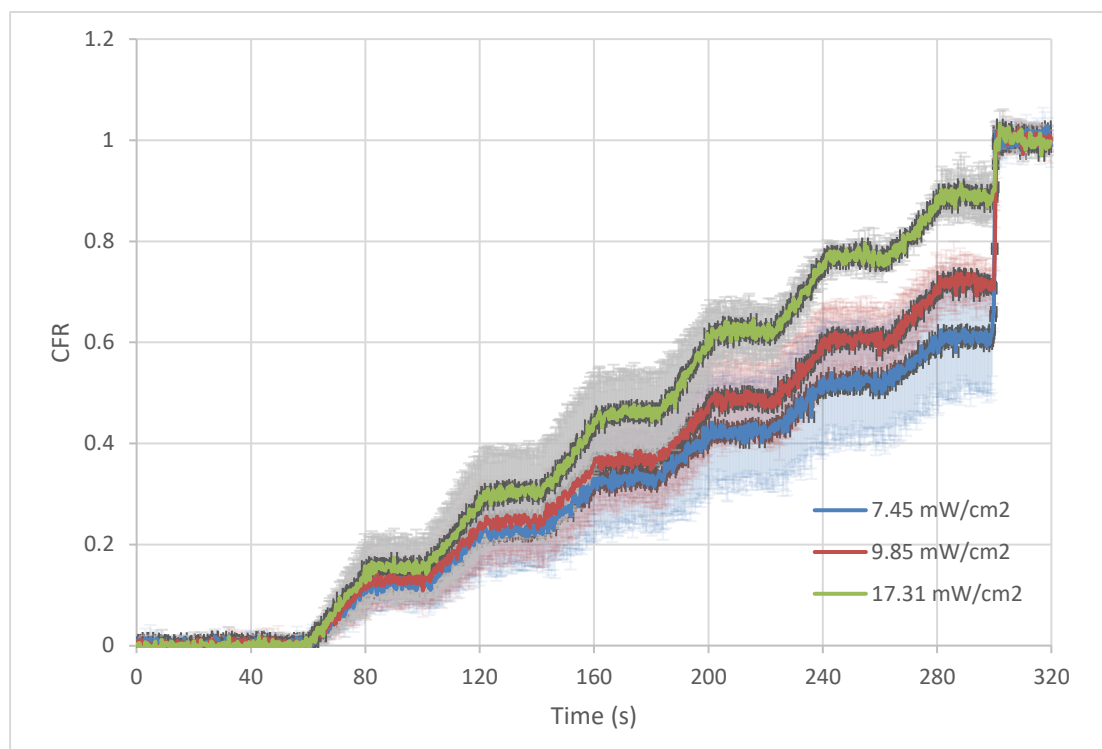


Figure 14: Averaged CFR \pm standard deviation vs. Time for acoustic DOX release from control liposomes

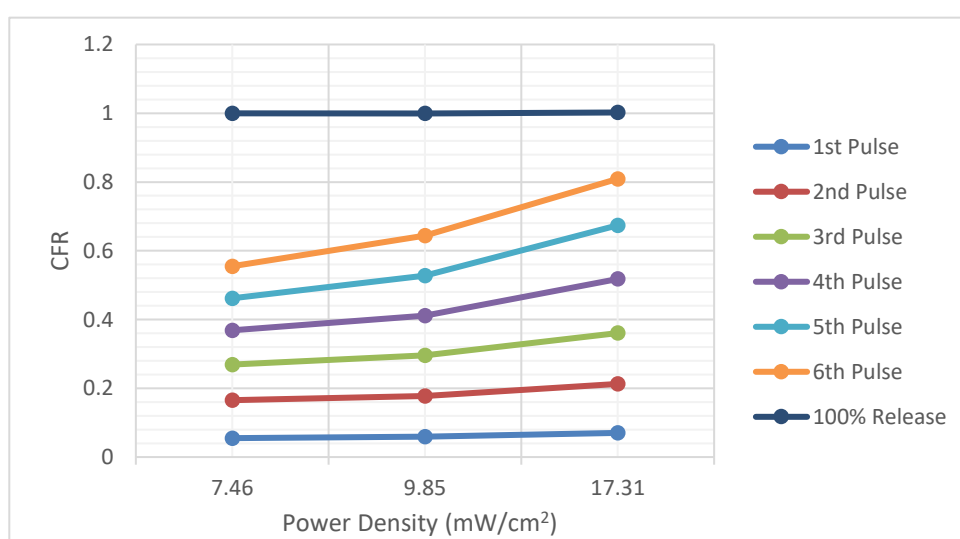


Figure 15: CFR of DOX release from control liposomes at 6 pulses

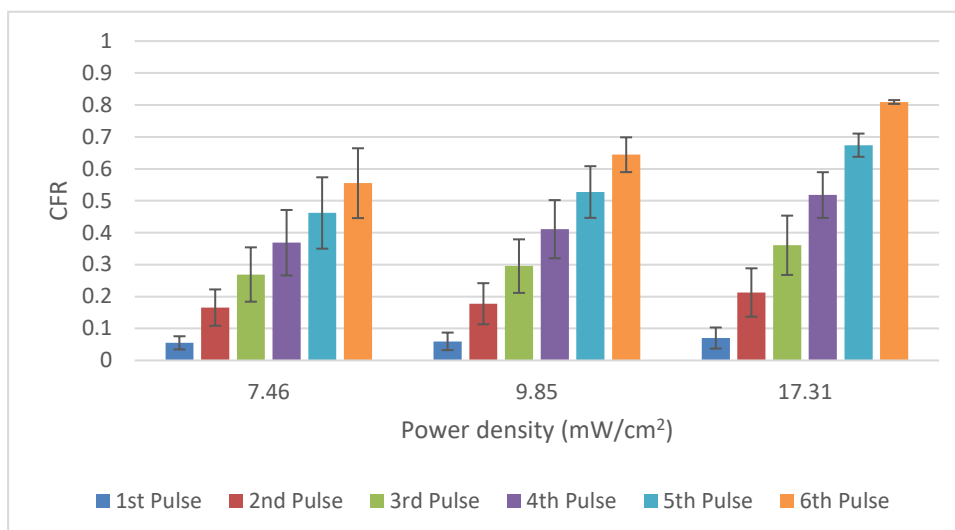


Figure 16: CFR of DOX release from control liposomes at 6 pulses for 3 power densities

Figure 15 portrays the increase in release at different power densities at every pulse, while Figure 16 portrays the increase in release at different pulses at the three power densities investigated.

The lack of statistical significance could be attributed to the low amount of DOX encapsulated inside the liposomes. Therefore, when comparing release at 7.46 and 9.85 mW/cm², the p-values for all pulses are statistically insignificant. However, as can be seen in Figure 16 there seems to be a steady increase between every pulse at different power densities. Finally, all maximum release values (after the addition of Triton X-100) correspond to a CFR of 1 or close to it which means that there is no statistical significance between the maximum release between different batches.

4.2.2 Tf liposomes LFUS release results. LFUS release experiments were conducted on three batches of Tf conjugated liposomes, and the release results are presented in Figure 17.

Figure 17 shows that at every pulse, the CFR increases steadily with time at somewhat of a constant slope. Furthermore, the standard deviation shown in the graph is within the acceptable range. Also, at the off pulses, little to no increase is observed in the CFR, which means that without ultrasonic waves, the liposomes do not release their contents. The release at 9.85 mW/cm² is higher than that at 7.46 mW/cm²; however, a statistically significant increase in the release is only observed in pulses four, five, and six. This can be observed in Tables 10 to 12. Moreover, when comparing

the 17.31 mW/cm² release to the 7.46 and 9.85 mW/cm² a statistically significant increase in release can be observed from the third pulse till the sixth pulse. Furthermore, at the fourth, fifth, and sixth pulses, a statistically significant release is observed in the 9.85 mW/cm² power density release compared to the 7.46 mW/cm² power density release, which proves that at higher power densities the liposomes release faster than at lower densities. At first and second pulses, the liposome's environment is subjected to a change through the pulsation of ultrasound, which causes a disturbance, and the liposomes start to release their contents. Therefore, there is no statistically significant release at the beginning, as can be observed in both Figure 17 and Tables 7 - 9.

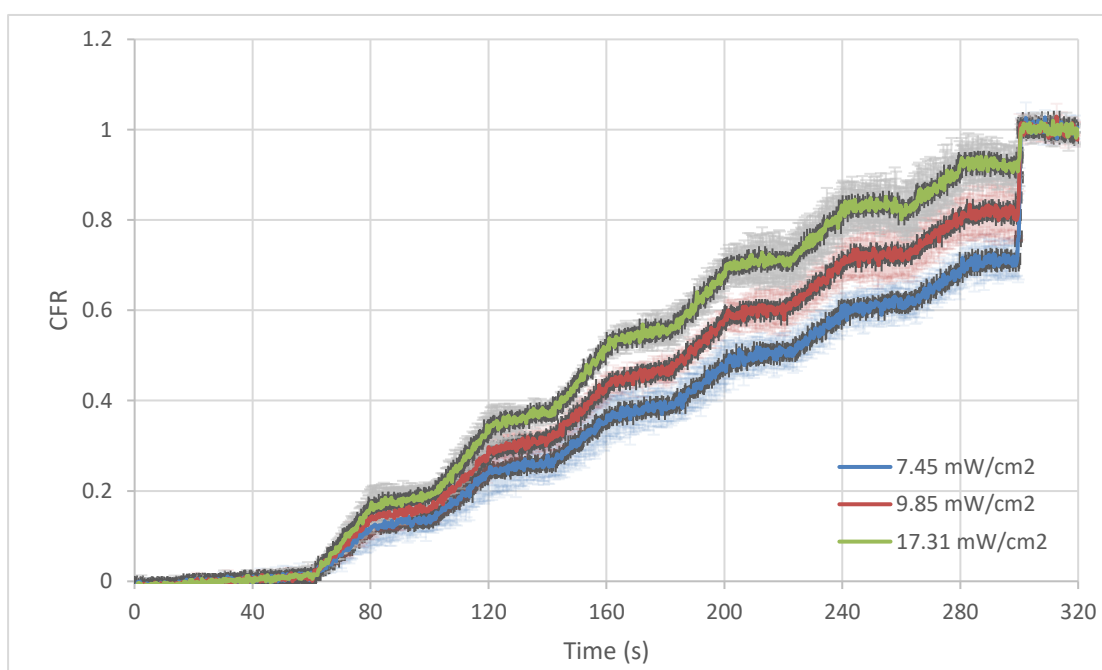


Figure 17: Averaged CFR \pm standard deviation vs. Time for the release of DOX from Tf-targeted liposomes

Figures 18 and 19 show the release of DOX from Tf liposomes at different pulses in two unique ways. Figure 18 portrays the increase in release at different power densities at every pulse. On the other hand, Figure 19 portrays the increase in release at different pulses at every power density. The results in Figure 18 show that there is an increase in the amount released at the third, fourth, fifth, and sixth pulse when the power density increases. This means there is a direct relationship between the amount released and the power density of the pulsed ultrasound. In Figure 19, the results portray that at every consecutive ultrasonic pulse, more DOX is released. The Tf liposomes seem to show more sensitivity to ultrasonic pulsation based on statistical significance.

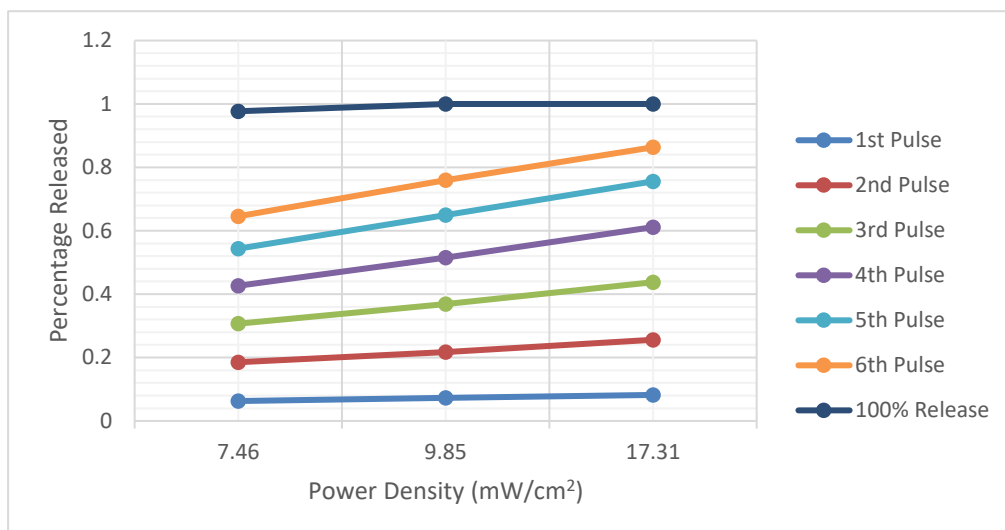


Figure 18: CFR of DOX release fromTf-liposomes at 6 acoustic pulses

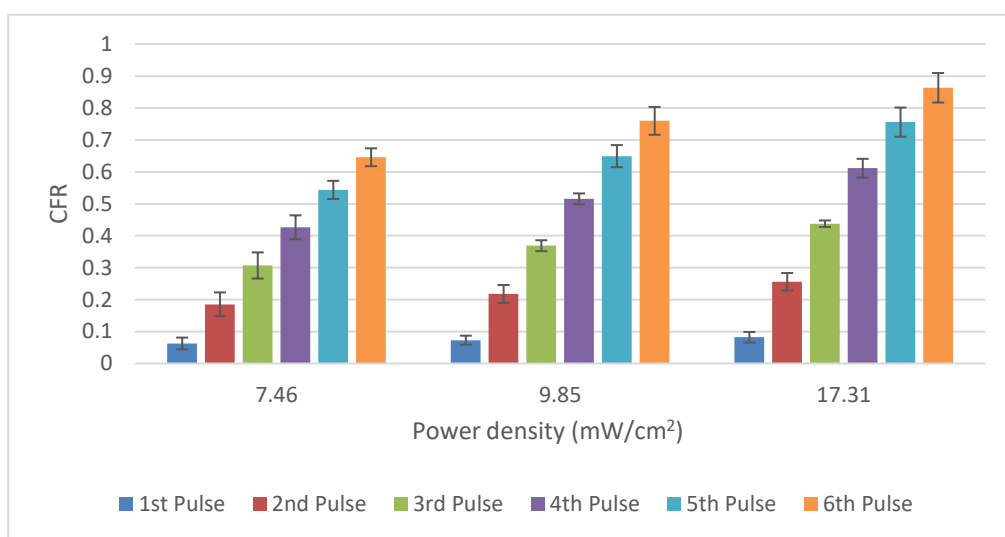


Figure 19: CFR of DOX release fromTf-liposomes at 6 pulses for 3 power densities

4.2.3 Comparison between control and Tf liposomes. The 7.46, 9.85, and 17.31 mW/cm² release results for both Tf and control are shown in Figures 20, 21, and 22, respectively.

Figures 27, 31, and 39 show that the Tf liposomes release more DOX (most of the time) and that both liposomes cease to release in the “off” portion of the pulses. This means that the liposomes are stable under normal conditions. Furthermore, the p values for both sets of data are shown in the heat maps in Tables 7 to 12. The first and second pulses show no statistical significance in the difference between runs at all power densities and carrier types, which corroborates the data plots seen in Figures 14,

17, 20, 21, and 22 as the first pulse shows a minimal to no increase in release in all of these plots at all power densities

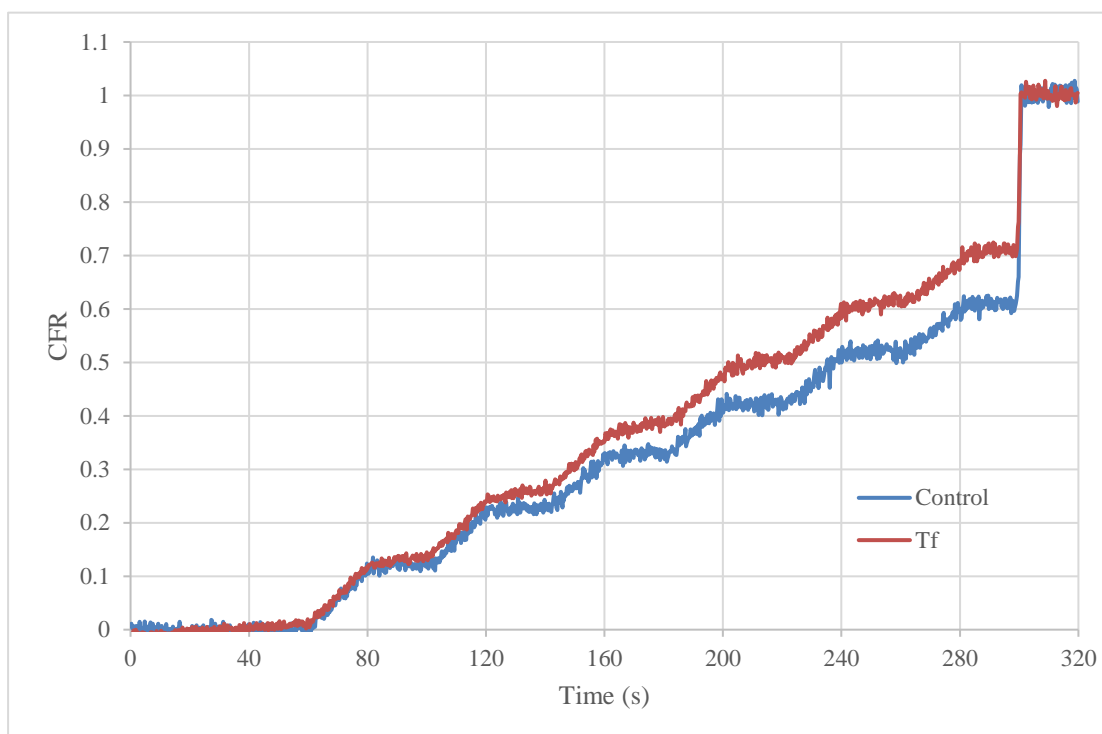


Figure 20: Release of Dox from Tf-targeted liposomes compared to the control at 7.46 mW/cm²

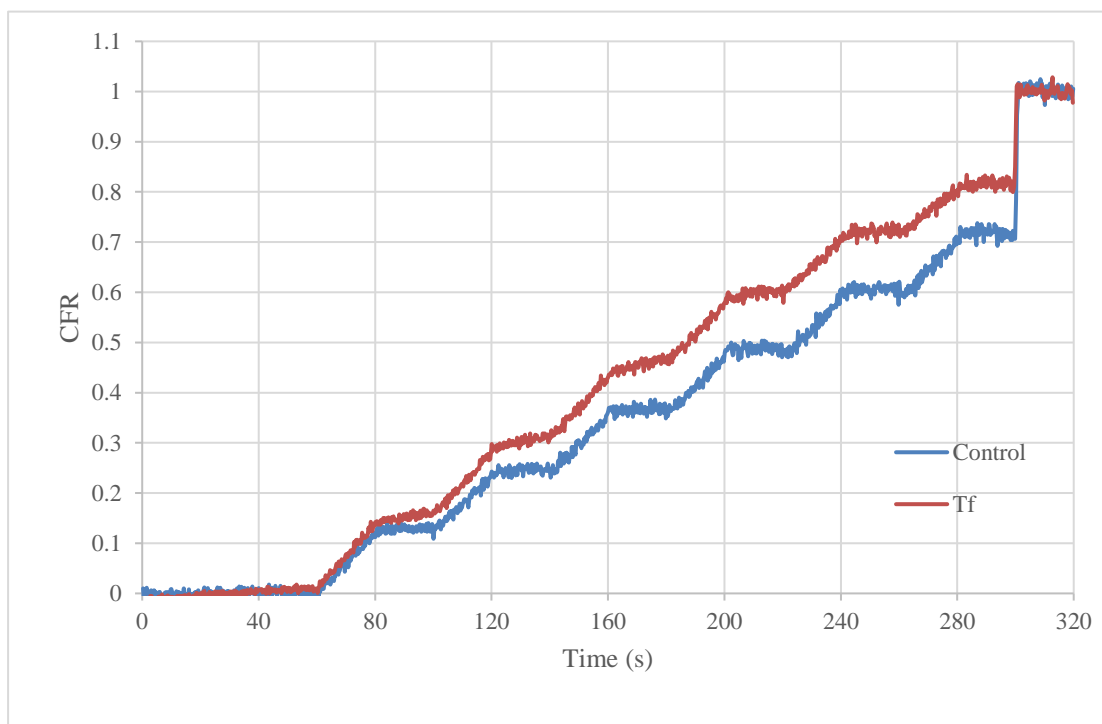


Figure 21: Release of DOX from Tf-targeted liposomes compared to the control liposomes at 9.85 mW/cm²

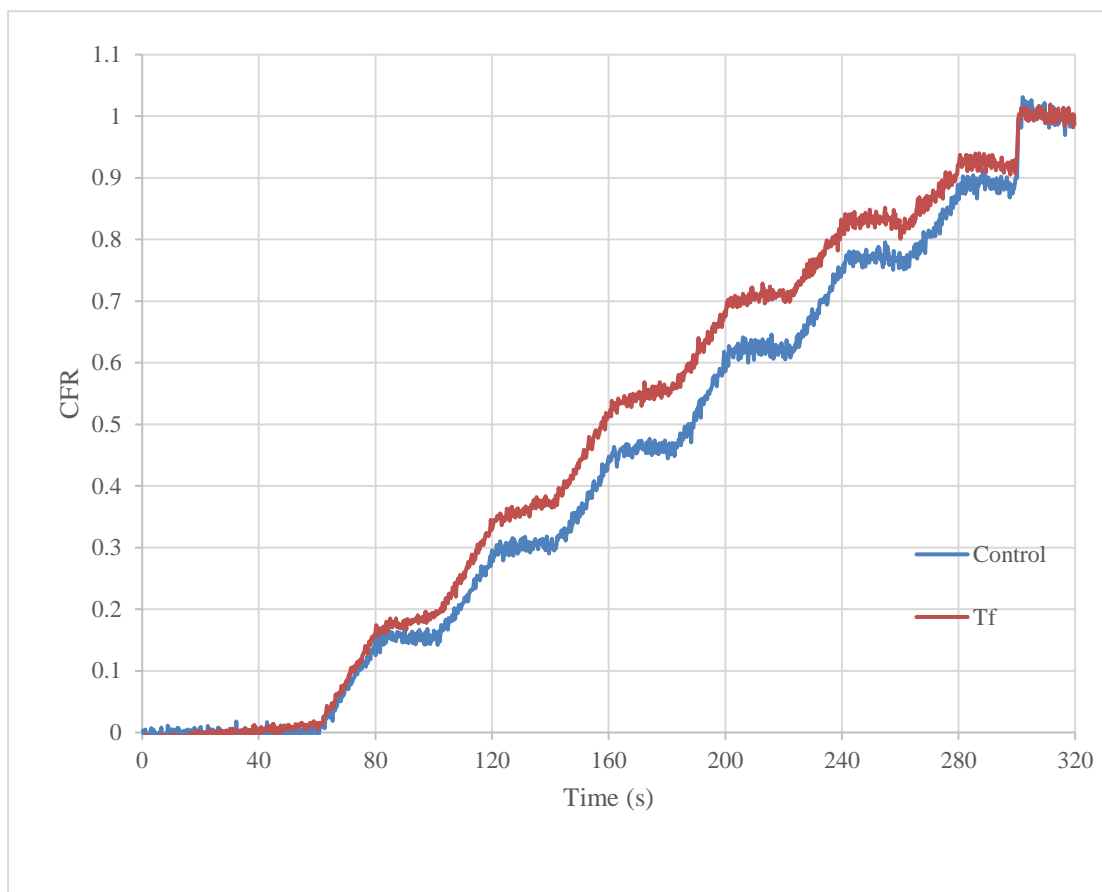


Figure 22: Release of DOX from Tf-targeted liposomes compared to control liposomes at 17.31 mW/cm²

Table 7: Heat map of p-values comparing the first pulse of DOX release from Tf-targeted and control liposomes

First Pulse						
Power Density (mW/cm ²)	7.46-control	9.85-control	17.31-control	7.46- Tf	9.85- Tf	17.31- Tf
7.46-control	1	0.825	0.537	0.654	0.280	0.152
9.85-control	0.825	1	0.694	0.881	0.497	0.295
17.31-control	0.537	0.694	1	0.750	0.898	0.608
7.46- Tf	0.654	0.881	0.750	1	0.485	0.248
9.85- Tf	0.280	0.497	0.898	0.485	1	0.511
17.31- Tf	0.152	0.295	0.608	0.248	0.511	1

p≥0.05	0.05≥p≥0.04	0.04≥p≥0.03	0.03≥p≥0.02	0.02≥p≥0.01	p≤0.01
--------	-------------	-------------	-------------	-------------	--------

Table 8: Heat map of p-values comparing the second pulse of DOX release from Tf-targeted and control liposomes

Second Pulse						
Power Density (mW/cm ²)	7.46-control	9.85-control	17.31-control	7.46- Tf	9.85- Tf	17.31-Tf
7.46- control	1	0.820	0.436	0.641	0.228	0.067
9.85- control	0.820	1	0.573	0.866	0.379	0.123
17.31- control	0.436	0.573	1	0.603	0.921	0.403
7.46- Tf	0.641	0.866	0.603	1	0.296	0.056
9.85- Tf	0.228	0.379	0.921	0.296	1	0.164
17.31- Tf	0.067	0.123	0.403	0.056	0.164	1

p≥0.05	0.05≥p≥0.04	0.04≥p≥0.03	0.03≥p≥0.02	0.02≥p≥0.01	p≤0.01
--------	-------------	-------------	-------------	-------------	--------

Table 9: Heat map of p-values comparing the third pulse of DOX release from Tf-targeted and control liposomes

Third Pulse						
Power Density (mW/cm ²)	7.46-control	9.85-control	17.31-control	7.46- Tf	9.85- Tf	17.31- Tf
7.46- control	1	0.722	0.276	0.526	0.117	0.027
9.85- control	0.722	1	0.418	0.842	0.211	0.043
17.31- control	0.276	0.418	1	0.411	0.888	0.226
7.46- Tf	0.526	0.842	0.411	1	0.073	0.006
9.85- Tf	0.117	0.211	0.888	0.073	1	0.004
17.31- Tf	0.027	0.043	0.226	0.006	0.004	1

p≥0.05	0.05≥p≥0.04	0.04≥p≥0.03	0.03≥p≥0.02	0.02≥p≥0.01	p≤0.01
--------	-------------	-------------	-------------	-------------	--------

Table 10: Heat map of p-values comparing the fourth pulse of DOX release from Tf-targeted and control liposomes

Fourth Pulse						
Power Density (mW/cm ²)	7.46-control	9.85-control	17.31-control	7.46-Tf	9.85-Tf	17.31-Tf
7.46- control	1	0.621	0.108	0.411	0.071	0.017
9.85- control	0.621	1	0.185	0.799	0.122	0.022
17.31- control	0.108	0.185	1	0.121	0.959	0.104
7.46- Tf	0.411	0.799	0.121	1	0.020	0.003
9.85- Tf	0.071	0.122	0.959	0.020	1	0.008
17.31- Tf	0.017	0.022	0.104	0.003	0.008	1

p≥0.05	0.05≥p≥0.04	0.04≥p≥0.03	0.03≥p≥0.02	0.02≥p≥0.01	p≤0.01
--------	-------------	-------------	-------------	-------------	--------

Table 11: Heat map of p-values comparing the fifth pulse of DOX release from Tf-targeted and control liposomes

Fifth Pulse						
Power Density (mW/cm ²)	7.46-control	9.85-control	17.31-control	7.46- Tf	9.85-Tf	17.31-Tf
7.46- control	1	0.456	0.035	0.287	0.050	0.014
9.85- control	0.456	1	0.046	0.761	0.074	0.013
17.31- control	0.035	0.046	1	0.008	0.440	0.073
7.46- Tf	0.287	0.761	0.008	1	0.015	0.002
9.85- Tf	0.050	0.074	0.440	0.015	1	0.032
17.31- Tf	0.014	0.013	0.073	0.002	0.032	1

p≥0.05	0.05≥p≥0.04	0.04≥p≥0.03	0.03≥p≥0.02	0.02≥p≥0.01	p≤0.01
--------	-------------	-------------	-------------	-------------	--------

Table 12: Heat map of p-values comparing the sixth pulse of DOX release from Tf-targeted and control liposomes

Sixth Pulse						
Power Density (mW/cm ²)	7.46-control	9.85-control	17.31-control	7.46-Tf	9.85-Tf	17.31-Tf
7.46- control	1	0.275	0.016	0.236	0.039	0.011
9.85- control	0.275	1	0.006	0.967	0.045	0.006
17.31- control	0.016	0.006	1	0.001	0.123	0.115
7.46- Tf	0.236	0.967	0.001	1	0.019	0.002
9.85- Tf	0.039	0.045	0.123	0.019	1	0.048
17.31- Tf	0.011	0.006	0.115	0.002	0.048	1

p≥0.05	0.05≥p≥0.04	0.04≥p≥0.03	0.03≥p≥0.02	0.02≥p≥0.01	p≤0.01
--------	-------------	-------------	-------------	-------------	--------

The heat maps shown in Tables 9 through 12 highlight some important release trends. In particular, it shows the effect of adding Tf and changing the ultrasound power density on the release of DOX. According to the literature, adding Tf to liposomes increases the release [78]. This statistically significant increase can be seen in the release of DOX at the 9.85 mW/cm² power density from Tf liposomes compared to the control at the sixth pulse. However, at 17.31 and 7.46 mW/cm², there is no statistically significant difference between the release profiles obtained by Tf and control liposomes. Figures 23 to 25 show the pulse-wise difference in release between the Tf

and control liposomes by the 7.46, 9.85, and 17.31 mW/cm² power densities, respectively. Interestingly, all figures show a higher average release fraction from the Tf liposomes versus their control at all pulses. However, as explained above this increase in release is not always statistically significant. Visually, the control liposomal release error bars sometimes exceed the averaged Tf release fraction and even the upper Tf error bar. This is especially prominent in Figure 23 sometimes even exceeding the positive error bar Tf release. At 9.85 mW/cm², or in Figure 26, this effect is less visible.

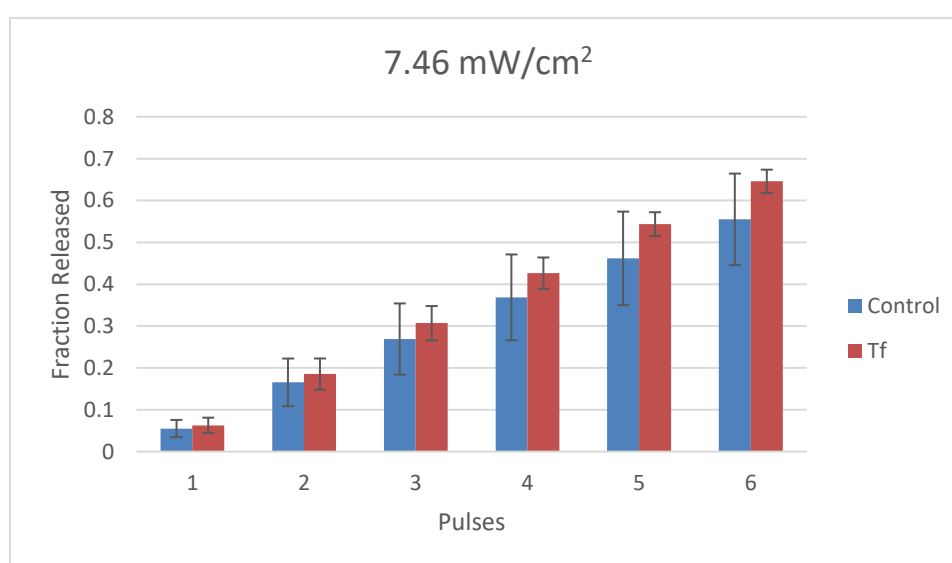


Figure 23: Pulse wise comparison of the release of DOX from Tf-targeted and control liposomes at 7.46 mW/cm²

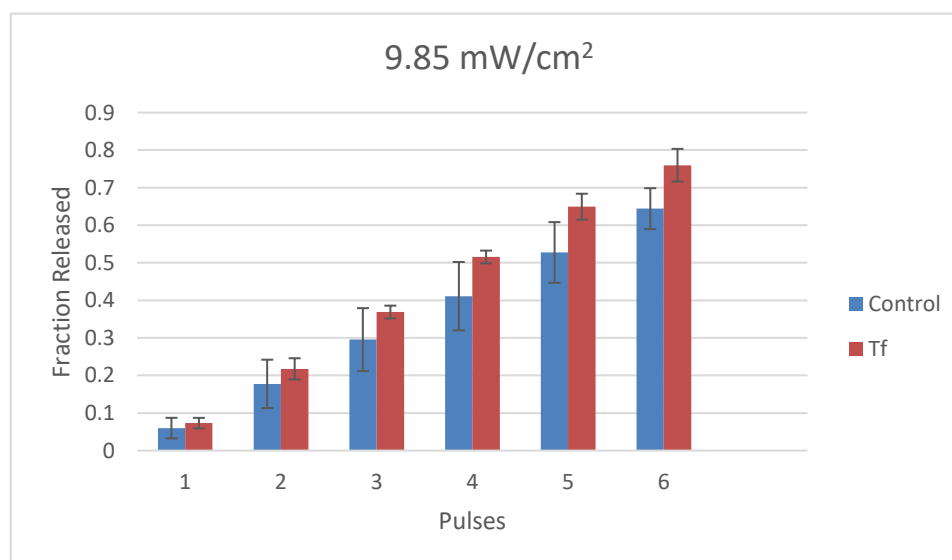


Figure 24: Pulse wise comparison of the release of DOX from Tf-targeted and control liposomes at at 9.85 mW/cm²

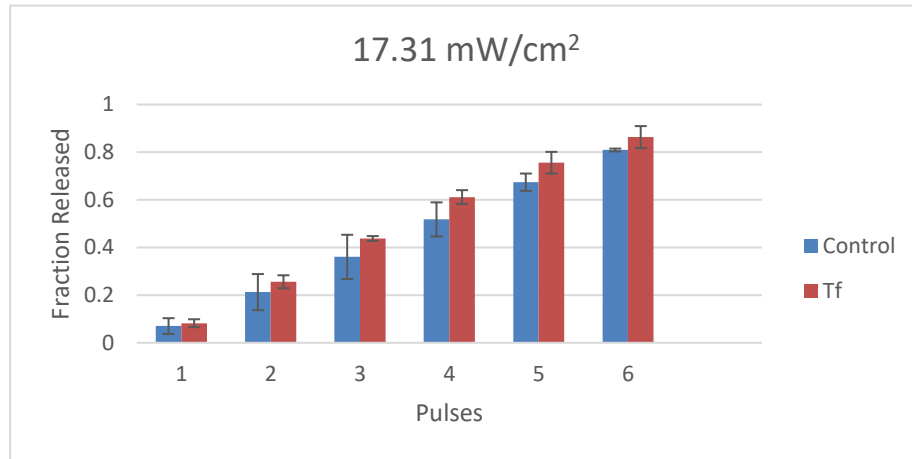


Figure 25: Pulse wise comparison of the release of DOX from Tf-targeted and control liposomes at at 17.31 mW/cm²

The evidence presented shows a higher release of DOX from the Tf-conjugated liposomes compared to the control liposomes, as previously reported, where the release from protein conjugated liposomes is known to make the liposomes more sonosensitive [28], [42], [104], [105].

4.2.4 Mechanical index results. The mechanical index is calculated using Equation 3 in section 2.4.3. It is a measure that indicates whether collapse cavitation is occurring or stable cavitation. The P_{neg} is reliant on the power density of the ultrasound and the impedance of the body, which is very close to the impedance of water. The calculated mechanical indices for the ultrasound intensities 7.46, 9.85, and 17.31 mW/cm² are 0.105, 0.120, and 0.160, which are well below the collapse cavitation limits introduced in section 2.4.3. Collapse cavitation occurs above 0.3, the threshold of biological effects is 0.7, and the threshold of tissue damage is 1.0. All calculated mechanical indices are below these threshold values. Thus, we postulate that the release reported in sections 5.2.1 and 5.2.2 is due to stable cavitation. This means that the ultrasound is causing micro streams that penetrate the walls of the liposomes, causing the release of the drug. From a release point of view, a more efficient drug delivery method is to increase the mechanical index to above 0.3 and allowing for collapse cavitation events to occur. However, the use of collapse cavitation on the human body could have its own detrimental effects. For example, the use closer to regions in the body that have pockets of air in which the use of collapse cavitation could cause these pockets of air to damage body tissue. The 17.31 mW/cm² power density ultrasound releases around 80% to 85% after 120 seconds (6 pulses). Hypothetically speaking, the

patient would need to be subjected to pulsed ultrasound for 5 minutes only to release most of the DOX at the tumor location.

4.3 Kinetic Modelling

4.3.1 Control liposomes kinetic modeling. As explained in section 3.3, nine kinetic models were applied to the LFUS results by eliminating the starting CFR, the off-pulse CFR, and the maximum release. The equations utilized were derived and presented in CFR terms in section 3.3. A regression analysis was conducted by excel to test how close the experimental data are to the best fit line generated by excel. The results of R^2 can be observed in Table 13.

Table 13: Coefficient of determination (R^2) analysis of DOX release from control liposome modeling

Liposome + Power density	Model Name	Batch #			Average
		1	2	3	
Control – 7.46 mW/cm ²	Zero-order	0.988	0.989	0.982	0.986
	First-order	0.754	0.768	0.860	0.794
	Higuchi	0.985	0.968	0.926	0.960
	Korsmeyer-Peppas	0.993	0.945	0.946	0.961
	Hixson-Crowell	0.997	0.987	0.971	0.985
	Baker-Lonsdale	0.949	0.913	0.864	0.909
	Weibull	0.993	0.956	0.941	0.963
	Hopfenberg	0.997	0.987	0.971	0.985
	Gompertz	0.903	0.918	0.872	0.898
Control – 9.85 mW/cm ²	Zero-order	0.989	0.994	0.981	0.988
	First-order	0.742	0.784	0.870	0.799
	Higuchi	0.985	0.967	0.911	0.954
	Korsmeyer-Peppas	0.993	0.969	0.958	0.973
	Hixson-Crowell	0.996	0.986	0.955	0.979
	Baker-Lonsdale	0.943	0.900	0.817	0.887
	Weibull	0.993	0.976	0.948	0.972
	Hopfenberg	0.996	0.986	0.955	0.979
	Gompertz	0.896	0.908	0.834	0.879
Control – 17.31 mW/cm ²	Zero-order	0.984	0.995	0.984	0.988
	First-order	0.696	0.742	0.841	0.760
	Higuchi	0.988	0.960	0.904	0.950
	Korsmeyer-Peppas	0.991	0.951	0.957	0.966
	Hixson-Crowell	0.996	0.970	0.938	0.968
	Baker-Lonsdale	0.944	0.869	0.808	0.874
	Weibull	0.992	0.975	0.935	0.967
	Hopfenberg	0.996	0.970	0.938	0.968
	Gompertz	0.859	0.834	0.741	0.811

The R^2 results observed in Table 13 clearly show that the release clearly follows the zero-order model for release. This is embodied by having the closest R^2 to one in all three runs at all three power densities obtaining an average R^2 for 7.46, 9.85, and 17.31 mW/cm² of 0.986, 0.988, and 0.988. The second-best fits were obtained using Hixon-Crowell and Hopfenberg models. All nine models' fitting for the first batch at 7.46 mW/cm² power density are presented in Figures 26 to 34. All other modeling data for control liposomes can be found in Appendix A to C.

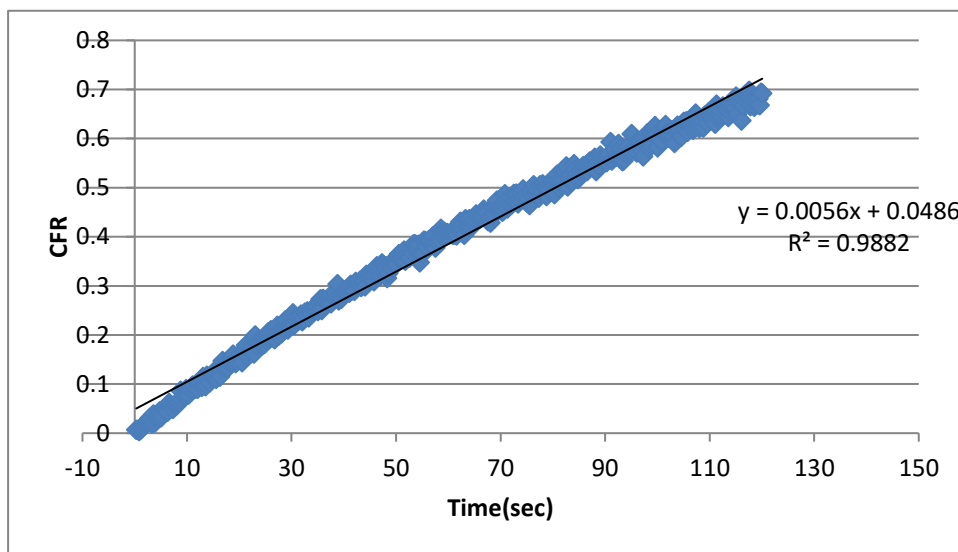


Figure 26: Zero-order model fitting of DOX release from control liposomes at 7.46 mW/cm² (Batch 1)

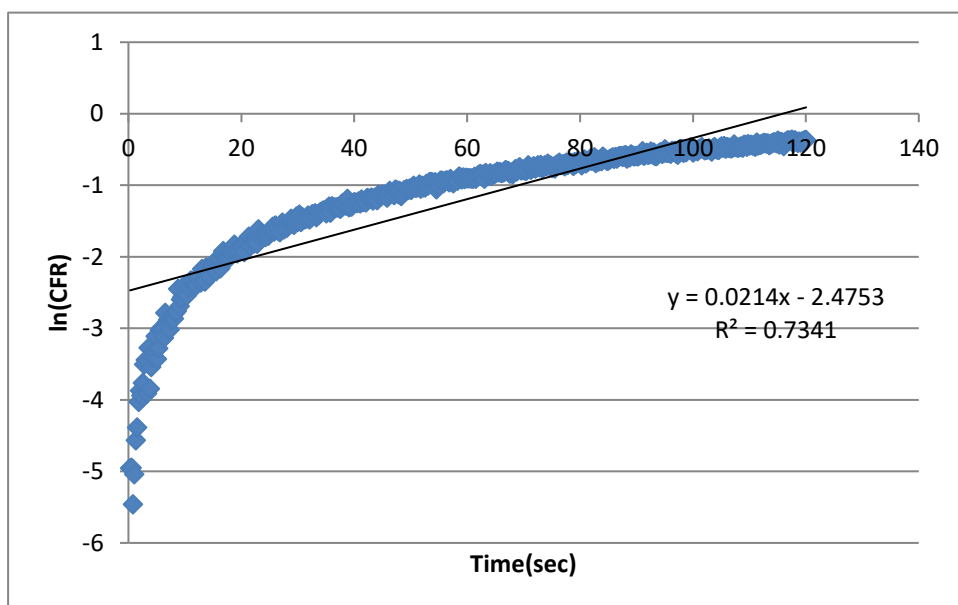


Figure 27: First order model fitting of DOX release from control liposomes at 7.46 mW/cm² (Batch 1)

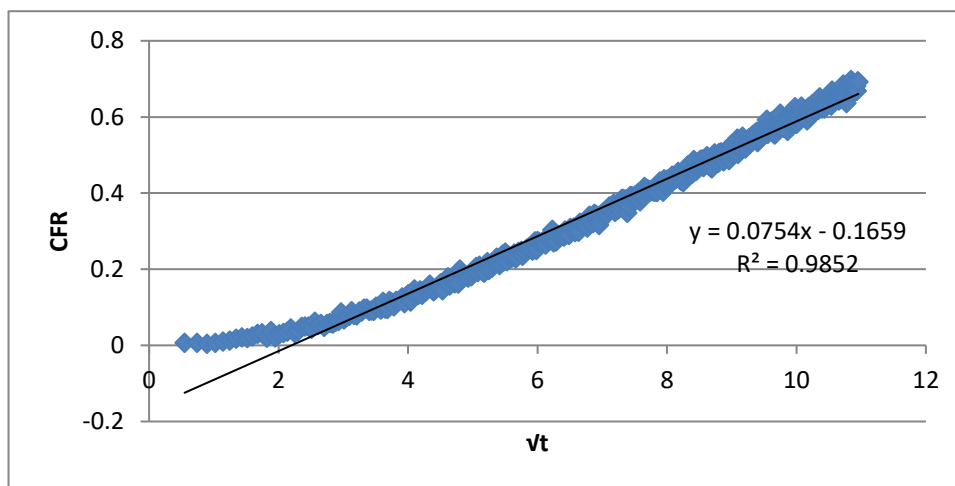


Figure 28: Higuchi model fitting of DOX release from control liposomes at 7.46 mW/cm² (Batch 1)

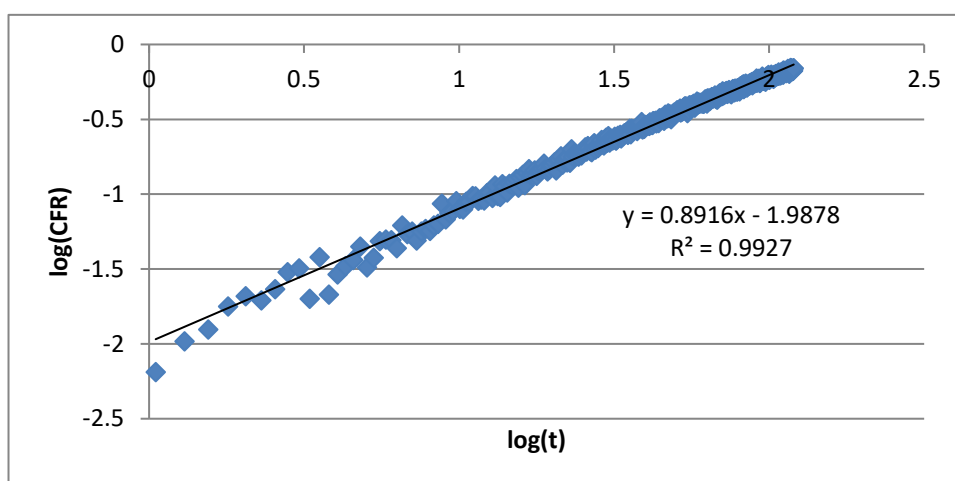


Figure 29: Korsmeyer-Peppas model fitting of DOX release from control liposomes at 7.46 mW/cm² (Batch 1)

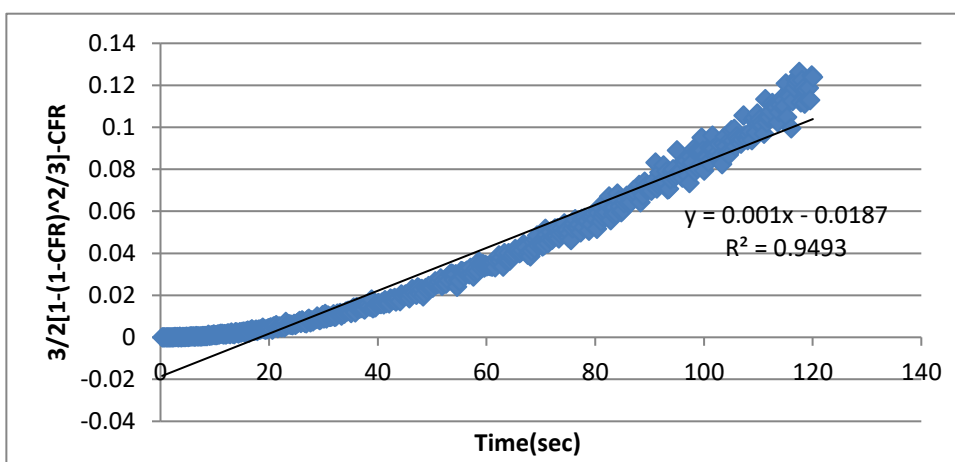


Figure 30: Backer-Lonsdale model fitting of DOX release from control liposomes at 7.46 mW/cm² (Batch 1)

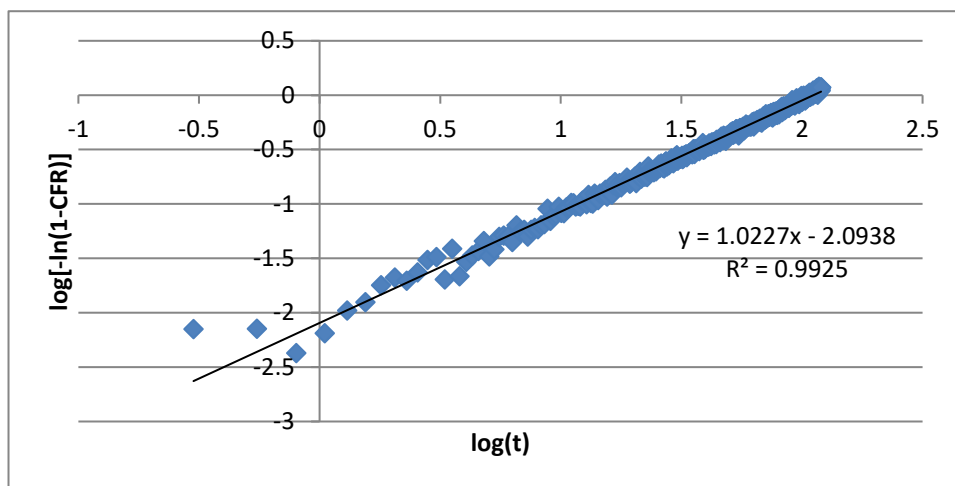


Figure 31: Weibull model fitting of DOX release from control liposomes at 7.46 mW/cm² (Batch 1)

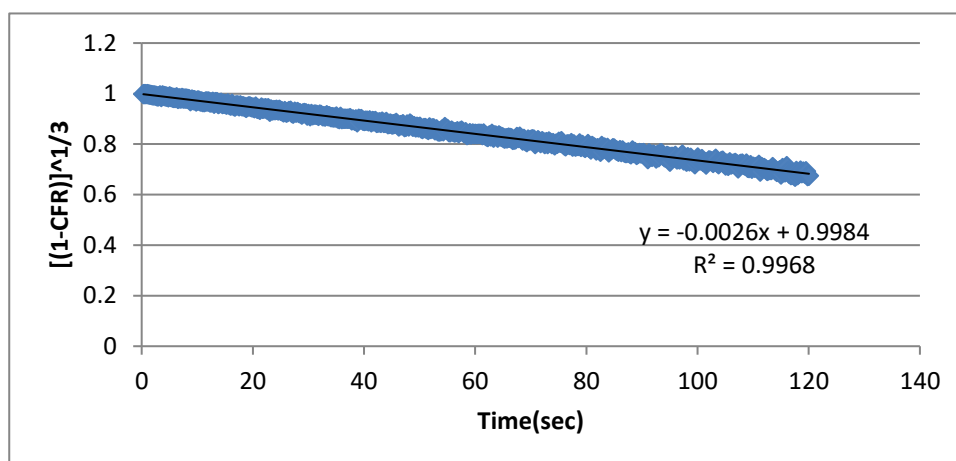


Figure 32: Hixson-Crowell model fitting of DOX release from control liposomes at 7.46 mW/cm² (Batch 1)

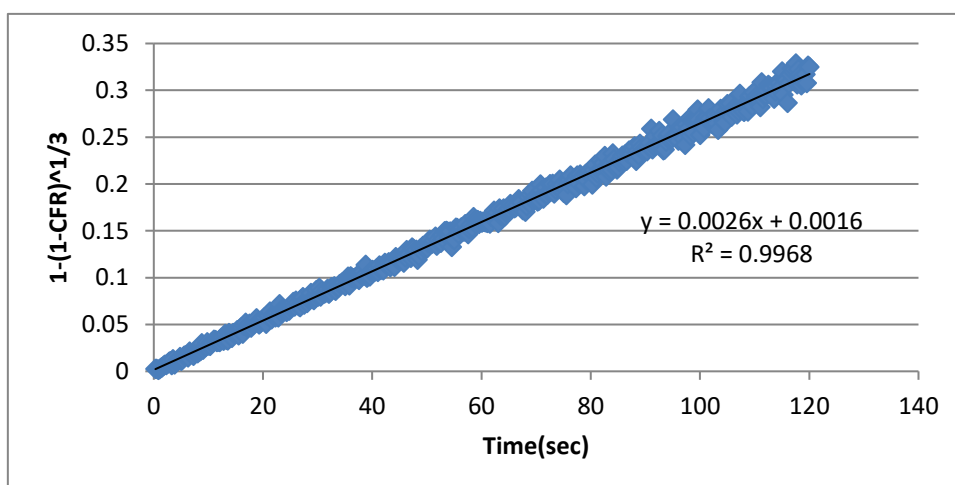


Figure 33: Hopfenberg model fitting of DOX release from control liposomes at 7.46 mW/cm² (Batch 1)

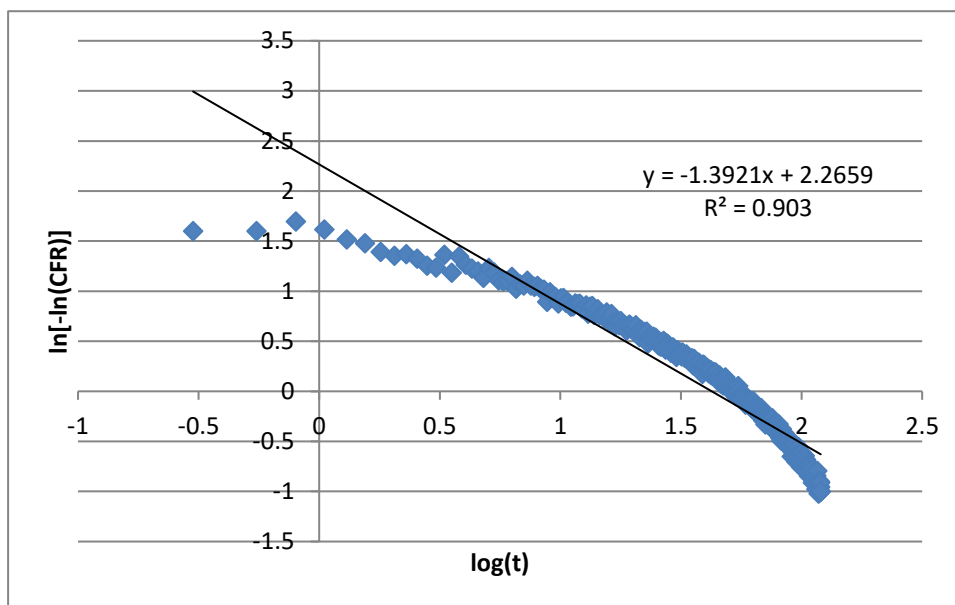


Figure 34: Gompertz model fitting of DOX release from control liposomes at 7.46 mW/cm² (Batch 1)

The release from the models can be best described by three different models accordingly. The zero-order model assumes that the drug release is slow and is constant and independent of drug concentration. This can be observed in Figure 14 where the slope of the pulses seems to be constant and not changing over time. The Hixson-Crowell and Hopfenberg models both assume that the surface of the matrix is being altered in some way or another, which corroborates the assumption that the ultrasound is affecting the stability of the liposomal structure. The rest of the modeling figures are available in Appendix A to C.

4.3.2 Tf-targeted liposomes kinetic modeling. The same nine models were used to analyze/fit the release results for the Tf liposomes. The CFR is plotted vs. time in the zero-order model, and linearization is used to check the fit. Three R² are obtained for each condition, and these values are presented in Table 14. The results mirror the results of acoustic release from the control liposomes, where the best fitting model is zero-order with R² values equal to 0.991, 0.992, and 0.989 R² for the 7.46, 9.85 and 17.31 mW/cm² power density release. The two other models with the highest R² are Hixson-Crowell and Hopfenberg. The R² values for those 2 models are equal and are 0.988, 0.988, and 0.983 R² for the 7.46, 9.85, and 17.31 mW/cm² power density release. The fitted models can be observed in Figures 35 to 43. All other model fitting data for Tf liposomes can be found in Appendix D to E

Table 14: Coefficient of determination (R^2) analysis of the DOX release from Tf-targeted liposome modeling

Liposome	R^2	Batch #			Average
	Batch #	1	2	3	
Tf – 7.46 mW/cm ²	Zero-order	0.991	0.991	0.994	0.991
	First-order	0.711	0.846	0.796	0.784
	Higuchi	0.982	0.934	0.967	0.961
	Korsmeyer-Peppas	0.982	0.951	0.980	0.971
	Hixson-Crowell	0.997	0.977	0.992	0.988
	Baker-Lonsdale	0.946	0.876	0.920	0.914
	Weibull	0.989	0.939	0.972	0.966
	Hopfenberg	0.997	0.977	0.992	0.988
	Gompertz	0.909	0.819	0.856	0.861
Tf – 9.85 mW/cm ²	Zero-order	0.992	0.992	0.994	0.992
	First-order	0.724	0.838	0.771	0.778
	Higuchi	0.984	0.947	0.969	0.967
	Korsmeyer-Peppas	0.994	0.948	0.954	0.965
	Hixson-Crowell	0.996	0.977	0.990	0.988
	Baker-Lonsdale	0.936	0.889	0.918	0.914
	Weibull	0.995	0.940	0.974	0.970
	Hopfenberg	0.996	0.977	0.990	0.988
	Gompertz	0.888	0.853	0.795	0.846
Tf – 17.31 mW/cm ²	Zero-order	0.990	0.988	0.988	0.989
	First-order	0.713	0.805	0.726	0.748
	Higuchi	0.983	0.959	0.975	0.972
	Korsmeyer-Peppas	0.992	0.964	0.970	0.975
	Hixson-Crowell	0.992	0.970	0.987	0.983
	Baker-Lonsdale	0.926	0.890	0.921	0.912
	Weibull	0.994	0.941	0.969	0.968
	Hopfenberg	0.992	0.970	0.987	0.983
	Gompertz	0.844	0.746	0.801	0.797

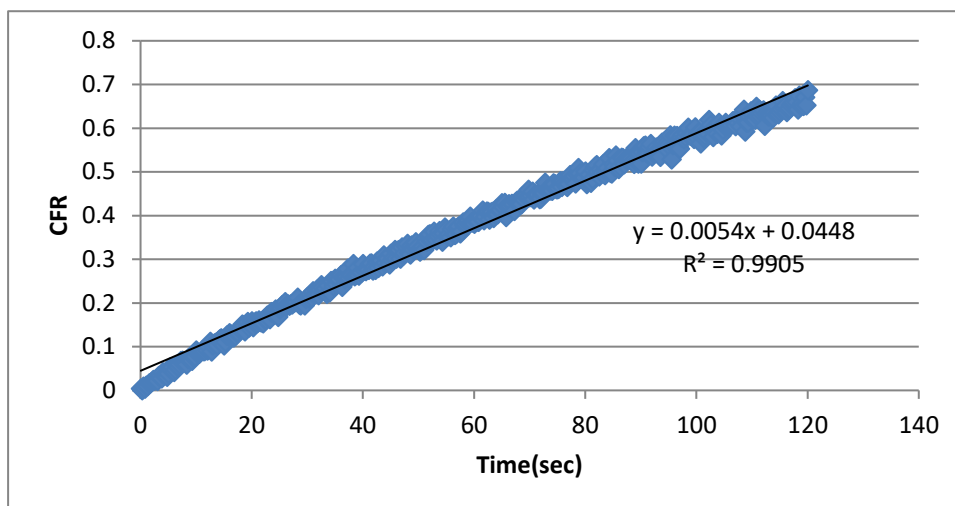


Figure 35: Zero-order model fitting of DOX release from Tf-targeted liposomes at 7.46 mW/cm² (Batch 1)

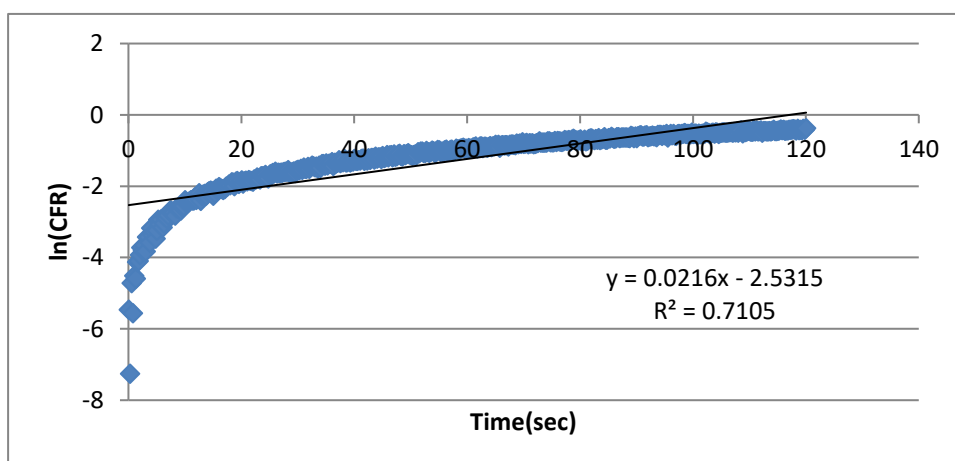


Figure 36: First-order model fitting of DOX release from Tf-targeted liposomes at 7.46 mW/cm² (Batch 1)

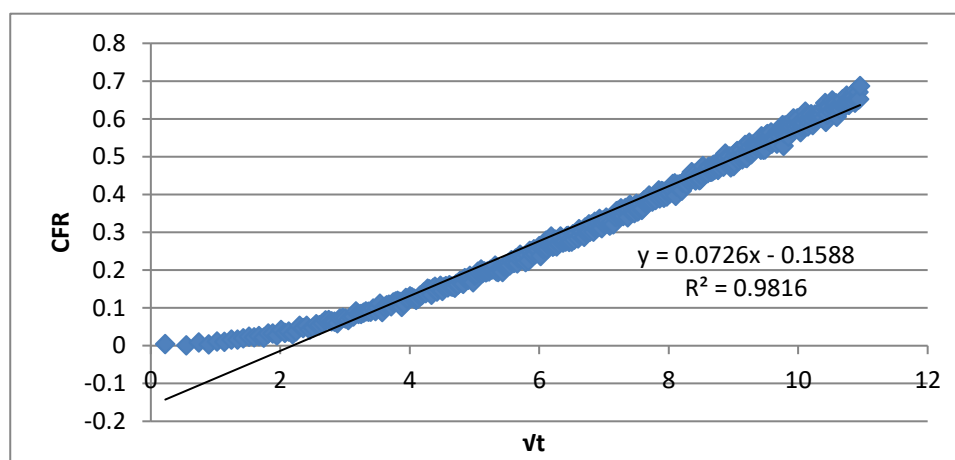


Figure 37: Higuchi model fitting of DOX release from Tf-targeted liposomes at 7.46 mW/cm² (Batch 1)

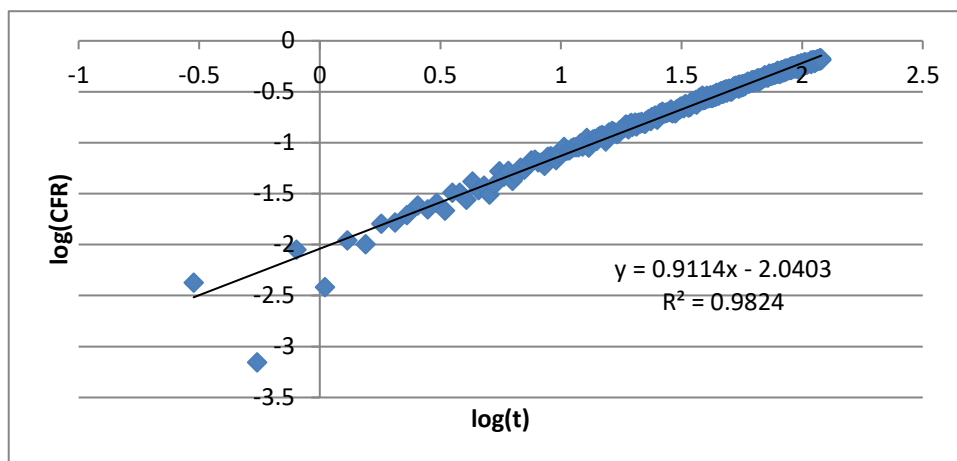


Figure 38: Korsmeyer-Peppas model fitting of DOX release from Tf-targeted liposomes at 7.46 mW/cm² (Batch 1)

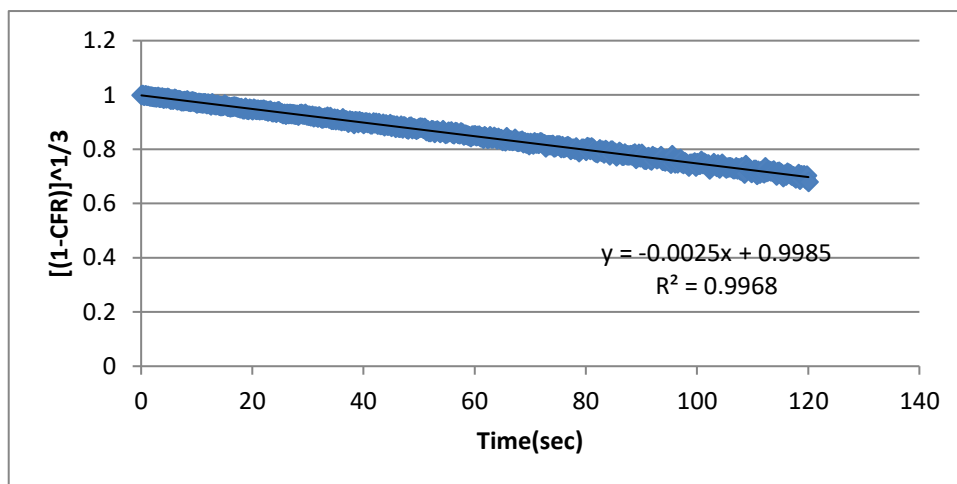


Figure 39: Hixson-Crowell model fitting of DOX release from Tf-targeted liposomes at 7.46 mW/cm² (Batch 1)

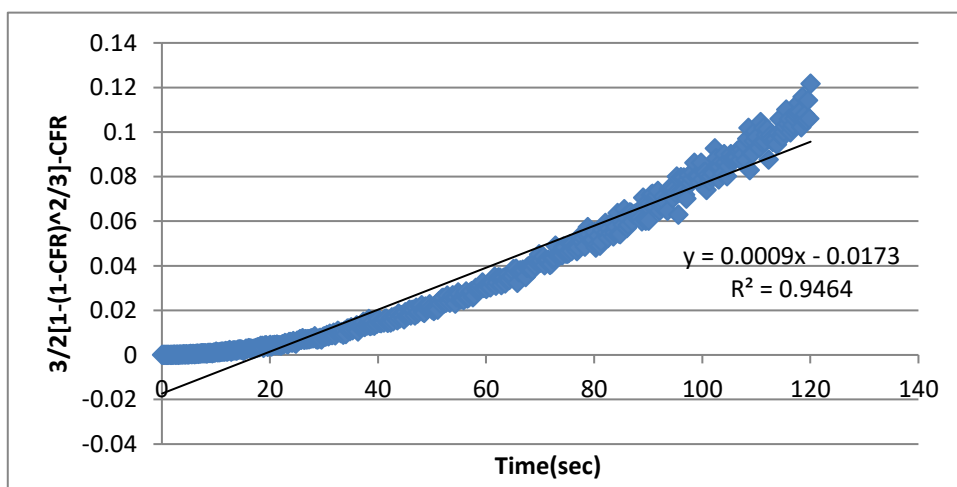


Figure 40: Baker-Lonsdale model fitting of DOX release from Tf-targeted liposomes at 7.46 mW/cm² (Batch 1)

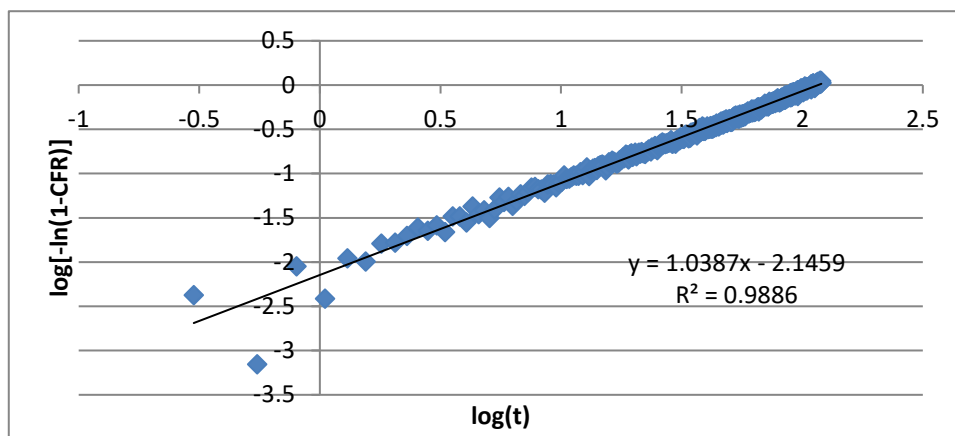


Figure 41: Weibull model fitting of DOX release from Tf-targeted liposomes at 7.46 mW/cm² (Batch 1)

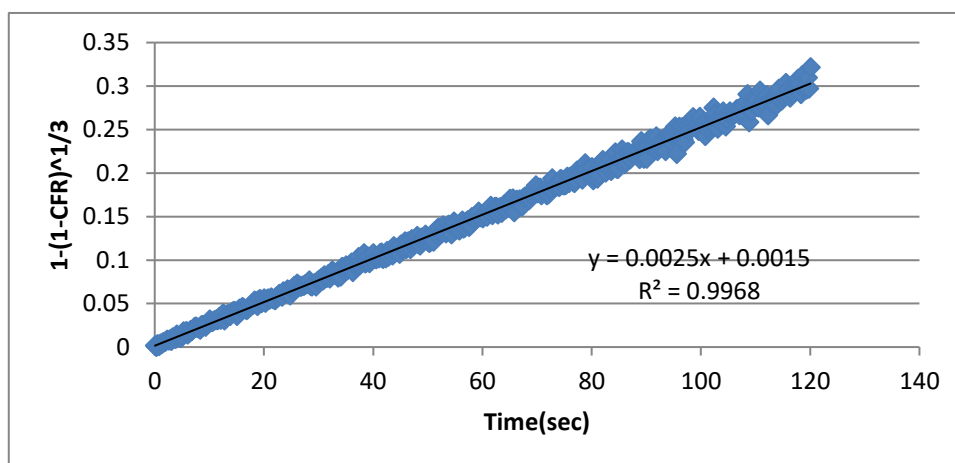


Figure 42: Hopfenberg model fitting of DOX release from Tf-targeted liposomes at 7.46 mW/cm² (Batch 1)

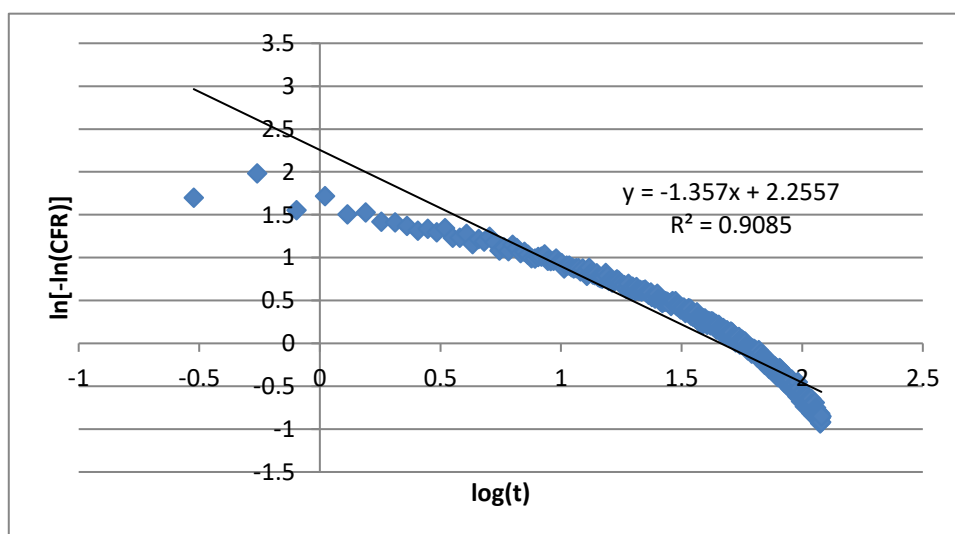


Figure 43: Gompertz model fitting of DOX release from Tf-targeted liposomes at 7.46 mW/cm² (Batch 1)

The fitting of the release data most closely resembles a straight line in the zero-order, Hixson-Crowell, and Hopfenberg models. Thus, we conclude that the release is slow and constant and not dependent on the concentration of the DOX, and this can be observed in Figure 17. Furthermore, the other two models indicate that the surface of the liposomes is being affected.

4.3.3 Kinetic modeling comparison between control and Tf liposomes. The kinetic modeling done on both the control and Tf liposomes presents three models that can be used to describe both liposomal formulations. This may indicate that the attachment does not affect the method of release. This assumption will be investigated further in this section. The release constant values for the zero-order, Hixson-Crowell, and Hopfenberg models are shown in Tables 15 to 17.

Table 15: Release constant values for the zero-order model

Lip	Batch #	Power density (mW/cm ²)		
		7.46	9.85	17.31
Control	Batch 1	0.0056	0.006	0.007
	Batch 2	0.0054	0.0061	0.0076
	Batch 3	0.0039	0.0055	0.0078
	Standard deviation	0.000929	0.000321	0.000416
Tf	Batch 1	0.0054	0.0062	0.0072
	Batch 2	0.006	0.0075	0.0087
	Batch 3	0.0061	0.007	0.008
	Standard deviation	0.000379	0.000656	0.000751

Table 16: Release constant values for Hixson-Crowell model

Lip	Batch #	Power density (mW/cm ²)		
		7.46	9.85	17.31
Control	Batch 1	-0.0026	-0.0029	-0.0039
	Batch 2	-0.0024	-0.0028	-0.0041
	Batch 3	-0.0016	-0.0024	-0.0041
	Standard deviation	0.000529	0.000265	0.00011547
Tf	Batch 1	-0.0025	-0.0031	-0.004
	Batch 2	-0.0027	-0.0039	-0.0053
	Batch 3	-0.0029	-0.0037	-0.0047
	Standard deviation	0.0002	0.000416	0.000650641

Table 17: Release constant values for Hopfenberg model

Lip	Batch #	Power density (mW/cm ²)		
		7.46	9.85	17.31
Control	Batch 1	0.0026	0.0029	0.0039
	Batch 2	0.0024	0.0028	0.0041
	Batch 3	0.0016	0.0024	0.0041
	Standard deviation	0.000529	0.000265	0.000115
Tf	Batch 1	0.0025	0.0031	0.004
	Batch 2	0.0027	0.0039	0.0053
	Batch 3	0.0029	0.0037	0.0047
	Standard deviation	0.0002	0.000416	0.000651

These release constants were compared using the ANOVA: Two factors with Replication in the Data Analysis tool pack in excel. This analysis requires two independent variables and one dependent variable. The independent variables are the variables in this study that are controlled and varied, which are the power density of the ultrasound and whether the liposomes are conjugated to Tf or not (targeted vs. non-targeted). The dependent variable is the variable obtained through modeling, which is the release constant k. Furthermore, three null hypotheses are required to be able to analyze the data obtained from the data analysis software. The first hypothesis is that the dependent variable, k, portrays no significant difference between the control and Tf liposomes. The second hypothesis is that the different power densities do not show a significant difference in release constants. Finally, the third hypothesis states that the two independent variables are independent of each other. For these hypotheses to be rejected, the p-value should be below 0.05. The results of the ANOVA test are reported Tables 18 to 20.

Table 18: ANOVA Two factor with replication on zero-order release constants

ANOVA						
Source of Variation	SS	df	MS	F	P-value	F crit
Sample	2.88E-06	1	2.88E-06	7.590044	0.01744	4.747225
Columns	1.62E-05	2	8.11E-06	21.37775	0.000111	3.885294
Interaction	2.23E-07	2	1.12E-07	0.29429	0.750286	3.885294
Within	4.55E-06	12	3.79E-07			
Total	2.39E-05	17				

Table 19: ANOVA Two factor with replication on Hixson-Crowell release constants

ANOVA						
Source of Variation	SS	df	MS	F	P-value	F crit
Sample	0.000002	1	0.000002	12	0.004682	4.747225
Columns	1.11E-05	2	5.56E-06	33.34333	1.26E-05	3.885294
Interaction	1.03E-07	2	5.17E-08	0.31	0.739148	3.885294
Within	0.000002	12	1.67E-07			
Total	1.52E-05	17				

Table 20: ANOVA Two factor with replication on Hopfenberg release constants

ANOVA						
Source of Variation	SS	df	MS	F	P-value	F crit
Sample	0.000002	1	0.000002	12	0.004682	4.747225
Columns	1.11E-05	2	5.56E-06	33.34333	1.26E-05	3.885294
Interaction	1.03E-07	2	5.17E-08	0.31	0.739148	3.885294
Within	0.000002	12	1.67E-07			
Total	1.52E-05	17				

The results from all three tests show that the first two hypotheses can be rejected as both the F is higher than the F crit for all three tests. Furthermore, the p-values are lower than 0.05. This is an expected result as the power density and the type of liposome are supposed to affect the release constants. The third null hypothesis cannot be rejected as the F is lower than the F crit and the p-value is higher than 0.05 at around 0.745 for all three tests. This means that the independent variables do not depend on each other and hence are truly independent. Finally, the heat maps for the release constants of all three models are shown below.

Table 21: Heat map of p-values comparing the release constants of the zero-order model for the release of DOX from Tf-targeted and control liposomes

Zero-order model						
Power Density (mW/cm ²)	7.46- Control	9.85- Control	17.31- Control	7.46- Tf	9.85- Tf	17.31- Tf
7.46- Control	1	0.188	0.013	0.209	0.042	0.012
9.85- Control	0.188	1	0.006	0.913	0.070	0.011
17.31- Control	0.013	0.006	1	0.007	0.275	0.370
7.46- Tf	0.209	0.913	0.007	1	0.071	0.012
9.85- Tf	0.042	0.070	0.275	0.071	1	0.137
17.31- Tf	0.012	0.011	0.370	0.012	0.137	1

p≥0.05	0.05≥p≥0.04	0.04≥p≥0.03	0.03≥p≥0.02	0.02≥p≥0.01	p≤0.01
--------	-------------	-------------	-------------	-------------	--------

Table 22: Heat map of p-values comparing the release constants of the Hixson-Crowell model for the release of DOX from Tf-targeted and control liposomes

Hixson-Crowell						
Power Density (mW/cm ²)	7.46- Control	9.85- Control	17.31- Control	7.46- Tf	9.85- Tf	17.31- Tf
7.46- Control	1	0.217	0.004	0.201	0.025	0.007
9.85- Control	0.217	1	0.001	1	0.038	0.008
17.31- Control	0.004	0.001	1	0.001	0.135	0.172
7.46- Tf	0.201	1	0.001	1	0.031	0.007
9.85- Tf	0.025	0.038	0.135	0.031	1	0.069
17.31- Tf	0.007	0.008	0.172	0.007	0.069	1

p≥0.05	0.05≥p≥0.04	0.04≥p≥0.03	0.03≥p≥0.02	0.02≥p≥0.01	p≤0.01
--------	-------------	-------------	-------------	-------------	--------

Table 23: Heat map of p-values comparing the release constants of the Hopfenberg model for the release of DOX from Tf-targeted and control liposomes

Hopfenberg						
Power Density (mW/cm ²)	7.46- Control	9.85- Control	17.31- Control	7.46- Tf	9.85- Tf	17.31- Tf
7.46- Control	1	0.217	0.004	0.201	0.025	0.007
9.85- Control	0.217	1	0.001	1.000	0.038	0.008
17.31- Control	0.004	0.001	1	0.001	0.135	0.172
7.46- Tf	0.201	1.000	0.001	1	0.031	0.007
9.85- Tf	0.025	0.038	0.135	0.031	1	0.069
17.31- Tf	0.007	0.008	0.172	0.007	0.069	1

p≥0.05	0.05≥p≥0.04	0.04≥p≥0.03	0.03≥p≥0.02	0.02≥p≥0.01	p≤0.01
--------	-------------	-------------	-------------	-------------	--------

4.4 Discussion

Six batches of liposomes were synthesized, three of which are control and three Tf- targeted liposomes. The characterization tests conducted in section 5.1 were performed to determine whether the liposomes are affected by the conjugation of Tf to these novel drug delivery carriers. The results of the size analysis did not concur with the literature because no statistical significance was observed between Tf and control liposomes. The important aspect was that both liposomes have a size lower than 200 nm, which means that they can pass through the pores in the vascular portion around cancerous cells (via the EPR effect). The results of the Stewart assay showed that the difference in lipid content was significant. This means that the conjugation procedure is diluting the liposomes, and this might occur when passing the liposomes from a

double-column for the purification from free Tf. Further experiments may be conducted to ensure that the difference in lipid content was not significant by passing the control liposomes through a double column too. This ensures that the lipid content was, in fact, not affecting anything else in the experiments. Finally, the BCA assay showed a significant difference in the protein content between the control and Tf liposomes. This was an expected result due to the addition of Tf to the conjugated liposomes.

The LFUS release profiles shown in section 5.2 shows how the pulsation of low-frequency ultrasound can effectively release DOX from liposomes. The pulsation of ultrasound for 20 s ON 20 s OFF prevented heating the tissues by hyperthermia. Previously, the AUS drug delivery Lab used to pulse the US at 20 s ON 10 s OFF, and at the 17.31 mW/cm² power density; however, this used to overheat the liposomes. This meant that the release could be due to hyperthermia and cavitation or both. Furthermore, the drug release profiles also showed that at higher power densities, the release is more prominent. The Tf liposomes released more significantly at the fifth and sixth pulse compared to the control liposomes. This follows similar trends in literature, whereby the conjugation of Tf to the surface of liposomes renders these nanocarriers more echogenic. Unfortunately, the background light in the lab caused an increase in the noise level of release experiments. Additionally, when the ultrasound probe is overused, the samples overheat when they are subjected to acoustic energy. This may have caused the control liposomes to release as much as the Tf liposomes. Finally, at the 17.31 mW/cm² power density, it is observed that no statistical significance in Dox release is observed when the control and Tf liposomes. This may be due to the higher intensity of the ultrasound, which destabilizes the liposomal structure regardless of whether it is more echogenic or not. Lastly, both control and Tf liposomes were stable under normal conditions.

The kinetics modeling showed consistent results for both types of liposomes and different power densities. The zero-order, Hixson-Crowell, and Hopfenberg models provided the best fitting for both 3 control liposomes and 3 Tf liposomes batches. This showed that the method of release does not change upon the conjugation of Tf to the liposomes. An ANOVA test was conducted on the release constants for the three models showed an R² value close to 1. The zero-order model is the simplest model and describes the release of liposomes almost perfectly. This is because the amount of DOX encapsulated inside the liposomes does not affect the release profile. This result is

expected as the ultrasound is reported to create pores in the liposomal bilayer and may not be affected by the amount of DOX available.

DOX was chosen as the anti-neoplastic agent for this study because it is naturally fluorescent, which meant that no dye was needed to track its release from liposomes. However, the most important reason for choosing to encapsulate DOX is that it is one of the most widely used chemotherapeutic drugs due to its effectiveness in treating solid as well as blood cancers.

Finally, these results need to be replicated in *in vitro* and *in vivo* experiments in the hopes they will reach the clinical trial phase. Eventually, the goal is to create the ability of mass production and appropriate human use to alleviate the side effects of cancer and properly target cancer and avoid MDR.

Chapter 5. Conclusion and Future Work

Cancer is the second deadliest disease in the world, second only to heart disease. The reason cancer is such a challenging disease is in its very nature; your own mutated body cells growing uncontrollably and spreading throughout your body. The only way to eliminate these cells is by using methods that may kill healthy as well as diseased cells. Chemotherapy is one such method where chemotherapeutic agents that destroy fast-growing cells are injected into the bloodstream to wreak havoc around the body. The objective of this research is to effectively deliver the chemotherapeutics in liposomal capsules, target them passively utilizing their size, actively using Tf to the site of the tumor, and release the DOX using ultrasound at the cancer site, thereby reducing the side effects that famously accompany chemotherapy.

The objective was achieved by synthesizing the liposomes using the thin-film hydration method. The size of these liposomes was tested using a DLS machine, and no statistical significance was observed between the Tf-targeted liposomes and control liposomes. The lipid content was quantified and used to calculate the protein content. The Stewart assay confirmed the attachment of Tf to the surface of liposomes. LFUS release studies were conducted to measure the release as a function of time for six ultrasound pulses. The results showed a higher release of DOX from the Tf-coupled liposomes when compared to the control liposomes. Zero-order, Hixson-Crowell, and Hopfenberg models were the models that provided the best fit to release data.

In conclusion, the results reported in this thesis are promising, which warrants further investigation were favorable. High-frequency ultrasound studies should be performed to measure the release of Dox from these targeted nano-vehicles when subjected to megahertz levels of ultrasound. *In vitro* studies should be conducted to measure the effectiveness of these liposomes on cells and their safety. *In vivo* should be conducted after *in vitro experiments* to prove the safety of using these liposomes is in animal hosts. Finally, if all of the aforementioned tests show promise, the final step is to pursue clinical trials to obtain FDA approval and move onto mass production and treatment of patients.

References

- [1] R. L. Siegel, K. D. Miller, and A. Jemal, "Cancer statistics, 2019," *CA: A Cancer Journal for Clinicians*, vol. 69, no. 1, pp. 7-34, 2019.
- [2] "Doxorubicin (Adriamycin) | Cancer drugs | Cancer Research UK," [Online]. Available: <https://www.cancerresearchuk.org/about-cancer/cancer-in-general/treatment/cancer-drugs/drugs/doxorubicin>. [Accessed: 20-Apr-2019].
- [3] "What Is Cancer? - National Cancer Institute," [Online]. Available: <https://www.cancer.gov/about-cancer/understanding/what-is-cancer>. [Accessed: 20-Apr-2019].
- [4] "Oncogenes and tumor suppressor genes | American Cancer Society," [Online]. Available: <https://www.cancer.org/cancer/cancer-causes/genetics/genes-and-cancer/oncogenes-tumor-suppressor-genes.html>. [Accessed: 20-Apr-2019].
- [5] R. G. Jones and C. B. Thompson, "Tumor suppressors and cell metabolism: a recipe for cancer growth," *Genes & Development*, vol. 23, no. 5, pp. 537-548, 2009.
- [6] "Benign Tumors: Causes, Symptoms & Diagnosis," [Online]. Available: <https://www.healthline.com/health/benign>. [Accessed: 30-Apr-2020].
- [7] Y. Brazier, "Tumors: Benign, premalignant, and malignant," 2019. [Online]. Available: <https://www.medicalnewstoday.com/articles/249141.php>. [Accessed: 15-Apr-2020].
- [8] "Types of Cancer Treatment | American Cancer Society," [Online]. Available: <https://www.cancer.org/treatment/treatments-and-side-effects/treatment-types.html>. [Accessed: 10-Apr-2019].
- [9] "Prophylactic Mastectomy | Breastcancer.org," [Online]. Available: https://www.breastcancer.org/treatment/surgery/prophylactic_mast. [Accessed: 25-May-2020].
- [10] D. Abshire and M. K. Lang, "The Evolution of Radiation Therapy in Treating Cancer," *Seminars in Oncology Nursing*, vol. 34, no. 2, pp. 151-157, 2018.
- [11] "Radiation therapy: Uses, types, and side effects," [Online]. Available: <https://www.medicalnewstoday.com/articles/158513>. [Accessed: 27-Mar-2019].
- [12] R. O. Dillman, "Cancer Immunotherapy," *Cancer Biotherapy & Radiopharmaceuticals*, vol. 26, no. 1, pp. 1-64, 2011.
- [13] M. L. Disis, *Immunotherapy of Cancer*, Totowa, NJ: Humana Press, 2006, p. 435.
- [14] American Cancer Society, "Chemotherapy," [Online]. Available: <https://www.cancer.org/treatment/treatments-and-side-effects/treatment-types/chemotherapy.html>. [Accessed: 18-Apr-2019].
- [15] P. J. Hesketh, "Chemotherapy-Induced Nausea and Vomiting," *The New England Journal of Medicine*, vol. 358, no. 23, pp. 2482-2494, 2008.
- [16] "Side effects of doxorubicin (Adriamycin) | Cancer drugs | Cancer Research UK," [Online]. Available: <https://www.cancerresearchuk.org/about->

cancer/cancer-in-general/treatment/cancer-drugs/drugs/doxorubicin/side-effects. [Accessed: 18-Apr-2019].

- [17] A. Prasanna, R. Pooja, V. Suchithra, A. Ravikumar, P. Kumar Gupta, and V. Niranjana, "Smart Drug Delivery Systems for Cancer Treatment Using Nanomaterials," *Materials Today: Proceedings*, vol. 5, no. 10, pp. 21047-21054, 2018.
- [18] S. Hossen, M. K. Hossain, M. Basher, M. Mia, M. Rahman, and M. J. Uddin, "Smart nanocarrier-based drug delivery systems for cancer therapy and toxicity studies: A review," *Journal of Advanced Research*, vol. 15, pp. 1-18, 2019.
- [19] M. Morales-Cruz, Y. Delgado, B. Castillo, C. M. Figueroa, A. M. Molina, A. Torres, M. Milián, and K. Griebenow, "Smart Targeting To Improve Cancer Therapeutics," *Drug Design, Development and Therapy*, vol. 13, pp. 3753-3772, 2019.
- [20] H. Maeda, "Tumor-Selective Delivery of Macromolecular Drugs via the EPR Effect: Background and Future Prospects," *Bioconjugate Chemistry*, vol. 21, no. 5, pp. 797-802, 2010.
- [21] A. Dadwal, A. Baldi, and R. Kumar Narang, "Nanoparticles as carriers for drug delivery in cancer," *Artificial Cells, Nanomedicine, and Biotechnology*, vol. 46, no. 2, pp. 295-305, 2018.
- [22] Qu-Hong, J. A. Nagy, D. R. Senger, H. F. Dvorak, and A. M. Dvorak, "Ultrastructural localization of vascular permeability factor/vascular endothelial growth factor (VPF/VEGF) to the abluminal plasma membrane and vesiculovacuolar organelles of tumor microvascular endothelium," *The Journal of Histochemistry and Cytochemistry*, vol. 43, no. 4, pp. 381-389, 1995.
- [23] B. Haley and E. Frenkel, "Nanoparticles for drug delivery in cancer treatment," *Urologic Oncology: Seminars and Original Investigations*, vol. 26, no. 1, pp. 57-64, 2008.
- [24] N. Muhamad, T. Plengsuriyakarn, and K. Na-Bangchang, "Application of active targeting nanoparticle delivery system for chemotherapeutic drugs and traditional/herbal medicines in cancer therapy: a systematic review," *International Journal of Nanomedicine*, vol. Volume 13, pp. 3921-3935, 2018.
- [25] J. D. Byrne, T. Betancourt, and L. Brannon-Peppas, "Active targeting schemes for nanoparticle systems in cancer therapeutics," *Advanced Drug Delivery Reviews*, vol. 60, no. 15, pp. 1615-1626, 2008.
- [26] R. R. Sawant, A. M. Jhaveri and V. P. Torchilin, "Immunomicelles for advancing personalized therapy," *Advanced Drug Delivery Reviews*, vol. 64, no. 13, pp. 1436-1446, 2012.
- [27] J. O. Eloy, R. Petrilli, L. N. F. Trevizan and M. Chorilli, "Immunoliposomes: A review on functionalization strategies and targets for drug delivery," *Colloids and Surfaces B: Biointerfaces*, vol. 159, pp. 454-467, 2017.
- [28] N. M. Salkho, V. Paul, P. Kawak, R. F. Vitor, A. M. Martins, M. Al Sayah, and G. A. Hussein, "Ultrasonically controlled estrone-modified liposomes for estrogen-positive breast cancer therapy," *Artificial Cells, Nanomedicine & Biotechnology*, vol. 46, pp. 462-472, 2018.
- [29] L. Qi and X. Gao, "Emerging application of quantum dots for drug delivery and therapy," *Expert Opinion on Drug Delivery*, vol. 5, no. 3, pp. 263-267, 2008.

- [30] C. Núñez, S. V. Estévez and M. del Pilar Chantada, "Inorganic nanoparticles in diagnosis and treatment of breast cancer," *Journal of Biological Inorganic Chemistry*, vol. 23, no. 3, pp. 331-345, 2018.
- [31] S. Jha, P. Mathur, S. Ramteke and N. K. Jain, "Pharmaceutical potential of quantum dots," *Artificial Cells, Nanomedicine & Biotechnology*, vol. 46, no. 1, pp. 57-65, 2018.
- [32] M.-X. Zhao and B.-J. Zhu, "The Research and Applications of Quantum Dots as Nano-Carriers for Targeted Drug Delivery and Cancer Therapy," *Nanoscale Research Letters*, vol. 11, no. 1, pp. 1-9, 2016.
- [33] K. H. Son, J. H. Hong, and J. W. Lee, "Carbon nanotubes as cancer therapeutic carriers and mediators," *International Journal of Nanomedicine*, vol. 11, pp. 5163-5185, 2016.
- [34] M. Sheikhpour, A. Golbabaie and A. Kasaeian, "Carbon nanotubes: A review of novel strategies for cancer diagnosis and treatment," *Materials Science and Engineering: C*, vol. 76, pp. 1289-1304, 2017.
- [35] K. Jain, P. Kesharwani, U. Gupta, and N. K. Jain, "Dendrimer toxicity: Let's meet the challenge," *International Journal of Pharmaceutics*, vol. 394, no. 1, pp. 122-142, 2010.
- [36] S. Rawal and M. M. Patel, "Threatening cancer with nanoparticle aided combination oncotherapy," *Journal of Controlled Release*, vol. 301, pp. 76-109, 2019.
- [37] R. S. Ambekar, M. Choudhary, and B. Kandasubramanian, "Recent advances in dendrimer-based nanoplatfrom for cancer treatment: A review," *European Polymer Journal*, vol. 126, pp. 1-15, 2020.
- [38] H. Yang, "Targeted nanosystems: Advances in targeted dendrimers for cancer therapy," *Nanomedicine: Nanotechnology, Biology and Medicine*, vol. 12, no. 2, pp. 309-316, 2016.
- [39] S. Cajot, D. Schol, F. Danhier, V. Preat, M.-C. Pauw, and C. Jérôme, "In Vitro Investigations of Smart Drug Delivery Systems Based on Redox-Sensitive Cross-Linked Micelles," *Macromolecular bioscience*, vol. 13, no. 12, pp. 1661-1670, 2013.
- [40] Y. Yi, G. Lin, S. Chen, J. Liu, H. Zhang, and P. Mi, "Polyester micelles for drug delivery and cancer theranostics: Current achievements, progresses and future perspectives," *Materials Science and Engineering: C*, vol. 83, pp. 218-232, 2018.
- [41] G. Yu, Q. Ning, Z. Mo and S. Tang, "Intelligent polymeric micelles for multidrug co-delivery and cancer therapy," *Artificial Cells, Nanomedicine & Biotechnology*, vol. 47, no. 1, pp. 1476-1487, 2019.
- [42] N. S. Awad, V. Paul, M. S. Mahmoud, N. M. Al Sawaftah, P. S. Kawak, M. H. Al Sayah, and G. A. Hussein, "Effect of Pegylation and Targeting Moieties on the Ultrasound-Mediated Drug Release from Liposomes," *ACS Biomaterials Science & Engineering*, vol. 6, no. 1, pp. 48-57, 2020.
- [43] L. Sercombe, T. Veerati, F. Moheimani, S. Y. Wu, A. K. Sood and S. Hua, "Advances and Challenges of Liposome Assisted Drug Delivery," *Frontiers in Pharmacology*, vol. 6, pp. 286-299, 2015.

- [44] M. Riaz, M. Riaz, X. Zhang, C. Lin, K. Wong, X. Chen, G. Zhang, A. Lu, and Z. Yang, "Surface Functionalization and Targeting Strategies of Liposomes in Solid Tumor Therapy: A Review," *International Journal of Molecular Sciences*, vol. 19, no. 1, pp. 195-222, 2018.
- [45] R. Bazak, M. Houri, S. El Achy, S. Kamel, and T. Refaat, "Cancer active targeting by nanoparticles: a comprehensive review of literature," *Journal of Cancer Research and Clinical Oncology*, vol. 141, no. 5, pp. 769-784, 2015.
- [46] S. Goodall, M. L. Jones, and S. Mahler, "Monoclonal antibody-targeted polymeric nanoparticles for cancer therapy – future prospects," *Journal of Chemical Technology & Biotechnology*, vol. 90, no. 7, pp. 1169-1176, 2015.
- [47] A. I. Fraguas-Sánchez, C. Martín-Sabroso, A. Fernández-Carballido and A. I. Torres-Suárez, "Current status of nanomedicine in the chemotherapy of breast cancer," *Cancer Chemotherapy and Pharmacology*, vol. 84, no. 4, pp. 689-706, 2019.
- [48] J. F. Ross, P. K. Chaudhuri, and M. Ratnam, "Differential regulation of folate receptor isoforms in normal and malignant tissues in vivo and in established cell lines. Physiologic and clinical implications," *Cancer*, vol. 73, no. 9, pp. 2432-2443, 1994.
- [49] A. Béduneau, P. Saulnier, and J.-P. Benoit, "Active targeting of brain tumors using nanocarriers," *Biomaterials*, vol. 28, no. 33, pp. 4947-4967, 2007.
- [50] G. L. Zwicke, G. Ali Mansoori and C. J. Jeffery, "Utilizing the folate receptor for active targeting of cancer nanotherapeutics," *Nano Reviews*, vol. 3, no. 1, pp. 1-11, 2012.
- [51] J. A. Habeshaw, T. A. Lister, A. G. Stansfeld and M. F. Greaves, "Correlation of transferrin receptor expression with histological class and outcome in non-hodgkin lymphoma," *The Lancet*, vol. 321, no. 8323, pp. 498-501, 1983.
- [52] D. Yang, F. Wang, R. Elliott, and J. Head, "Expression of transferrin receptor and ferritin H-chain mRNA are associated with clinical and histopathological prognostic indicators in breast cancer," *Anticancer Research*, vol. 21, pp. 541-549, 2001.
- [53] K. Kondo, M. Noguchi, K. Mukai, Y. Matsuno, Y. Sato, Y. Shimosato and Y. Monden, "Transferrin receptor expression in adenocarcinoma of the lung as a histopathologic indicator of prognosis," *Chest*, vol. 97, no. 6, pp. 1367-1371, 1990.
- [54] R. Prior, G. Reifenberger and W. Wechsler, "Transferrin receptor expression in tumours of the human nervous system: relation to tumour type, grading and tumour growth fraction," *Virchows Archiv A Pathological Anatomy and Histopathology*, vol. 416, no. 6, pp. 491-496, 1990.
- [55] G. J. Seymour, M. D. Walsh, M. F. Lavin, G. Strutton, and R. A. Gardiner, "Transferrin receptor expression by human bladder transitional cell carcinomas," *Urological Research*, vol. 15, no. 6, pp. 341-344, 1987.
- [56] T. R. Daniels, E. Bernabeu, J. A. Rodríguez, S. Patel, M. Kozman, D. A. Chiappetta, E. Holler, J. Y. Ljubimova, G. Helguera, and M. L. Penichet, "The transferrin receptor and the targeted delivery of therapeutic agents against cancer," *Biochimica et Biophysica Acta (BBA) - General Subjects*, vol. 1820, no. 3, pp. 291-317, 2012.

- [57] S. Tortorella and T. C. Karagiannis, "Transferrin Receptor-Mediated Endocytosis: A Useful Target for Cancer Therapy," *Journal of Membrane Biology*, vol. 247, no. 4, pp. 291-307, 2014.
- [58] F. Movahedi, R. G. Hu, D. L. Becker, and C. Xu, "Stimuli-responsive liposomes for the delivery of nucleic acid therapeutics," *Nanomedicine: Nanotechnology, Biology and Medicine*, vol. 11, no. 6, pp. 1575-1584, 2015.
- [59] L. L. Tayo, "Stimuli-responsive nanocarriers for intracellular delivery," *Biophysical Reviews*, vol. 9, no. 6, pp. 931-940, 2017.
- [60] S. J. Sonawane, R. S. Kalhapure and T. Govender, "Hydrazone linkages in pH responsive drug delivery systems," *European Journal of Pharmaceutical Sciences*, vol. 99, pp. 45-65, 2017.
- [61] H. B. Ruttala, T. Ramasamy, T. Madeshwaran, T. T. Hiep, U. Kandasamy, K. T. Oh, H.-G. Choi, C. S. Yong, and J. O. Kim, "Emerging potential of stimulus-responsive nanosized anticancer drug delivery systems for systemic applications," *Archives of Pharmacal Research*, vol. 41, no. 2, pp. 111-129, 2018.
- [62] Z. Cao, W. Li, R. Liu, X. Li, H. Li, L. Liu, Y. Chen, C. Lv, and Y. Liu, "pH- and enzyme-triggered drug release as an important process in the design of anti-tumor drug delivery systems," *Biomedicine & Pharmacotherapy*, vol. 118, pp. 1-12, 2019.
- [63] Y. Dou, K. Hynynen, and C. Allen, "To heat or not to heat: Challenges with clinical translation of thermosensitive liposomes," *Journal of Controlled Release*, vol. 249, pp. 63-73, 2017.
- [64] E. Mazzotta, L. Tavano, and R. Muzzalupo, "Thermo-Sensitive Vesicles in Controlled Drug Delivery for Chemotherapy," *Pharmaceutics*, vol. 10, no. 3, pp. 150-170, 2018.
- [65] S. J. Leung and M. Romanowski, "Light-Activated Content Release from Liposomes," *Theranostics*, vol. 2, no. 10, pp. 1020-1036, 2012.
- [66] N. V. Rao, H. Ko, J. Lee, and J. H. Park, "Recent Progress and Advances in Stimuli-Responsive Polymers for Cancer Therapy," *Frontiers in Bioengineering and Biotechnology*, vol. 6, pp. 1-15, 2018.
- [67] G. Canavese, A. Ancona, L. Racca, M. Canta, B. Dumontel, F. Barbaresco, T. Limongi, and V. Cauda, "Nanoparticle-assisted ultrasound: A special focus on sonodynamic therapy against cancer," *Chemical Engineering Journal*, vol. 340, pp. 155-172, 2018.
- [68] T. Boissenot, A. Bordat, E. Fattal, and N. Tsapis, "Ultrasound-triggered drug delivery for cancer treatment using drug delivery systems: From theoretical considerations to practical applications," *Journal of Controlled Release*, vol. 241, pp. 144-163, 2016.
- [69] W. G. Pitt, G. A. Hussein and B. J. Staples, "Ultrasonic drug delivery – a general review," *Expert Opinion on Drug Delivery*, vol. 1, no. 1, pp. 37-56, 2004.
- [70] I. Lentacker, I. De Cock, R. Deckers, S. De Smedt and C. Moonen, "Understanding ultrasound induced sonoporation: Definitions and underlying mechanisms," *Advanced Drug Delivery Reviews*, vol. 72, pp. 49-64, 2014.

- [71] A. Schroeder, J. Kost, and Y. Barenholz, "Ultrasound, liposomes, and drug delivery: principles for using ultrasound to control the release of drugs from liposomes," *Chemistry and Physics of Lipids*, vol. 162, no. 1, pp. 1-16, 2009.
- [72] R. E. Apfel and C. K. Holland, "Gauging the likelihood of cavitation from short-pulse, low-duty cycle diagnostic ultrasound," *Ultrasound in Medicine & Biology*, vol. 17, no. 2, pp. 179-185, 1991.
- [73] S. Son, H. S. Min, D. G. You, B. S. Kim, and I. C. Kwon, "Echogenic nanoparticles for ultrasound technologies: Evolution from diagnostic imaging modality to multimodal theranostic agent," *Nano Today*, vol. 9, no. 4, pp. 525-540, 2014.
- [74] S. K. Sriraman, G. Salzano, C. Sarisozen, and V. Torchilin, "Anti-cancer activity of doxorubicin-loaded liposomes co-modified with transferrin and folic acid," *European Journal of Pharmaceutics and Biopharmaceutics*, vol. 105, pp. 40-49, 2016.
- [75] I. Sakpakdeejaroen, S. Somani, P. Laskar, M. Mullin, and C. Dufès, "Transferrin-bearing liposomes entrapping plumbagin for targeted cancer therapy," *Journal of Interdisciplinary Nanomedicine*, vol. 4, no. 2, pp. 54-71, 2019.
- [76] A. Jhaveri, P. Deshpande, B. Pattni and V. Torchilin, "Transferrin-targeted, resveratrol-loaded liposomes for the treatment of glioblastoma," *Journal of Controlled Release*, vol. 277, pp. 89-101, 2018.
- [77] E. Moghimipour, M. Rezaei, M. Kouchak, Z. Ramezani, M. Amini, K. Ahmadi Angali, S. Saremy, F. Abedin Dorkoosh, and S. Handali, "A mechanistic study of the effect of transferrin conjugation on cytotoxicity of targeted liposomes," *Journal of Microencapsulation*, vol. 35, no. 6, pp. 548-558, 2018.
- [78] N. AlSawaftah, "The Use of Transferrin and Ultrasound in Cancer Treatment," M.S. thesis, Dept. Chem. Eng. American Univ., Sharjah, UAE, 2019.
- [79] N. Mohammad, "Acoustically activated release of estrone-targeted liposomes used for breast cancer treatment," M.S. thesis, Dept. Chem. Eng. American Univ., Sharjah, UAE, 2016.
- [80] P. Kawak, "Ultrasound Triggered Release of Estrone- Targeted Liposomes," M.S. thesis, Dept. Chem. Eng., American Univ., Sharjah, UAE, 2017.
- [81] M. Mahmoud, "The Effect of Ultrasound on the Drug Delivery of RGD-Targeted Liposomes," M.S. thesis, Dept. Chem. Eng. American Univ., Sharjah, UAE, 2018.
- [82] R. Abusamra, "Using Lactose and Ultrasound to deliver chemotherapeutics," M.S. thesis, Dept. Chem. Eng. American Univ., Sharjah, UAE, 2019.
- [83] A. Farooq, "Doxorubicin-encapsulated Albumin liposomes with acoustic triggering for cancer treatment," M.S. thesis, Dept. Chem. Eng. American Univ., Sharjah, UAE, 2019.
- [84] A. Ahmed, "Ultrasound triggered release of Trastuzumab-conjugated immunoliposomes targeting breast cancer," M.S. thesis, Dept. Chem. Eng. American Univ., Sharjah, UAE, 2018.
- [85] L. Al-Zubaidi, M. Al-Rubaie and T. Abdullah, "Multi Lamellar Vesicles (MLVs) Liposomes Preparation by Thin Film Hydration Technique," *Eng. & Tech. Journal*, vol. 32, no. 3, pp. 550-560, 2014.

- [86] Y. Barenholz, "Doxil® — The first FDA-approved nano-drug: Lessons learned," *Journal of Controlled Release*, vol. 160, no. 2, pp. 117-134, 2012.
- [87] A. Fritze, F. Hens, A. Kimpfler, R. Schubert, and R. Peschka-Süss, "Remote loading of doxorubicin into liposomes driven by a transmembrane phosphate gradient," *Biochimica et Biophysica Acta (BBA) - Biomembranes*, vol. 1758, no. 10, pp. 1633-1640, 2006.
- [88] V. Damodaran and C. Fee, "Protein PEGylation: An overview of chemistry and process considerations," *European Pharmaceutical Review*, vol. 15, pp. 18-26, 2010.
- [89] J. M. Harris, "Laboratory Synthesis of Polyethylene Glycol Derivatives," *Journal of Macromolecular Science, Part C*, vol. 25, no. 3, pp. 325-373, 1985.
- [90] J. L. and W. J. Kao*, "Synthesis of Polyethylene Glycol (PEG) Derivatives and PEGylated–Peptide Biopolymer Conjugates," *Biomacromolecules*, vol. 4, no. 4, pp. 1055-1067, 2003.
- [91] W. I. Goldberg, "Dynamic light scattering," *American Journal of Physics*, vol. 67, no. 12, pp. 1152-1160, 1999.
- [92] "The principles of dynamic light scattering :: Anton Paar Wiki," [Online]. Available: <https://wiki.anton-paar.com/en/the-principles-of-dynamic-light-scattering/>. [Accessed: 15-May-2019].
- [93] "The Stewart Assay | Liposome: Encapsula's Scientific Blog," [Online]. Available: <http://www.liposomes.org/2009/01/stewart-assay.html>. [Accessed: 15-May-2019].
- [94] J. C. M. Stewart, "Colorimetric determination of phospholipids with ammonium ferrothiocyanate," *Analytical Biochemistry*, vol. 104, no. 1, pp. 10-14, 1980.
- [95] P. K. Smith, R. I. Krohn, G. T. Hermanson, A. K. Mallia, F. H. Gartner, M. D. Provenzano, E. K. Fujimoto, N. M. Goeke, B. J. Olson, and D. C. Klenk, "Measurement of protein using bicinchoninic acid," *Analytical Biochemistry*, vol. 150, no. 1, pp. 76-85, 1985.
- [96] F. He, "BCA (Bicinchoninic Acid) Protein Assay," *Bio-Protocol*, vol. 1, no. 5, 2011.
- [97] X. Dai, Z. Yue, M. E. Eccleston, J. Swartling, N. K. H. Slater and C. F. Kaminski, "Fluorescence intensity and lifetime imaging of free and micellar-encapsulated doxorubicin in living cells," *Nanomedicine: Nanotechnology, Biology and Medicine*, vol. 4, no. 1, pp. 49-56, 2008.
- [98] S. Shah, A. Chandra, A. Kaur, N. Sabnis, A. Lacko, Z. Gryczynski, R. Fudala, and I. Gryczynski, "Fluorescence properties of doxorubicin in PBS buffer and PVA films," *Journal of Photochemistry And Photobiology. B, Biology*, vol. 170, pp. 65-69, 2017.
- [99] S. Dash, P. N. Murthy, L. Nath and P. Chowdhury, "Kinetic modeling on drug release from controlled drug delivery systems," *Acta Poloniae Pharmaceutica*, vol. 67, no. 3, pp. 217-23, 2010.
- [100] P. Costa and J. M. Sousa Lobo, "Modeling and comparison of dissolution profiles," *European Journal of Pharmaceutical Sciences*, vol. 13, no. 2, pp. 123-133, 2001.

- [101] J. Siepmann and N. A. Peppas, "Higuchi equation: Derivation, applications, use and misuse," *International Journal of Pharmaceutics*, vol. 418, no. 1, pp. 6-12, 2011.
- [102] J. Siepmann and F. Siepmann, "Mathematical modeling of drug delivery," *International Journal of Pharmaceutics*, vol. 364, no. 2, pp. 328-343, 2008.
- [103] H. Moussa, "Liposomal drug release using ultrasound and modeling release dynamics for model predictive controller design," M.S. thesis, Dept. Chem. Eng. American Univ., Sharjah, UAE, 2015.
- [104] N. S. Awad, V. Paul, M. H. Al-Sayah, and G. A. Hussein, "Ultrasonically controlled albumin-conjugated liposomes for breast cancer therapy," *Artificial Cells, Nanomedicine, and Biotechnology*, vol. 47, no. 1, pp. 705-714, 2019.
- [105] A. Wadi, M. Abdel-Hafez, G. Hussein, and V. Paul, "Multi-Model Investigation and Adaptive Estimation of the Acoustic Release of a Model Drug From Liposomes," *IEEE Transactions on NanoBioscience*, vol. 19, no. 1, pp. 68-77, 2019.

Appendix A: Plots of Kinetic Models for Batches 2 & 3 of Control Liposomes at 7.46 mW/cm²

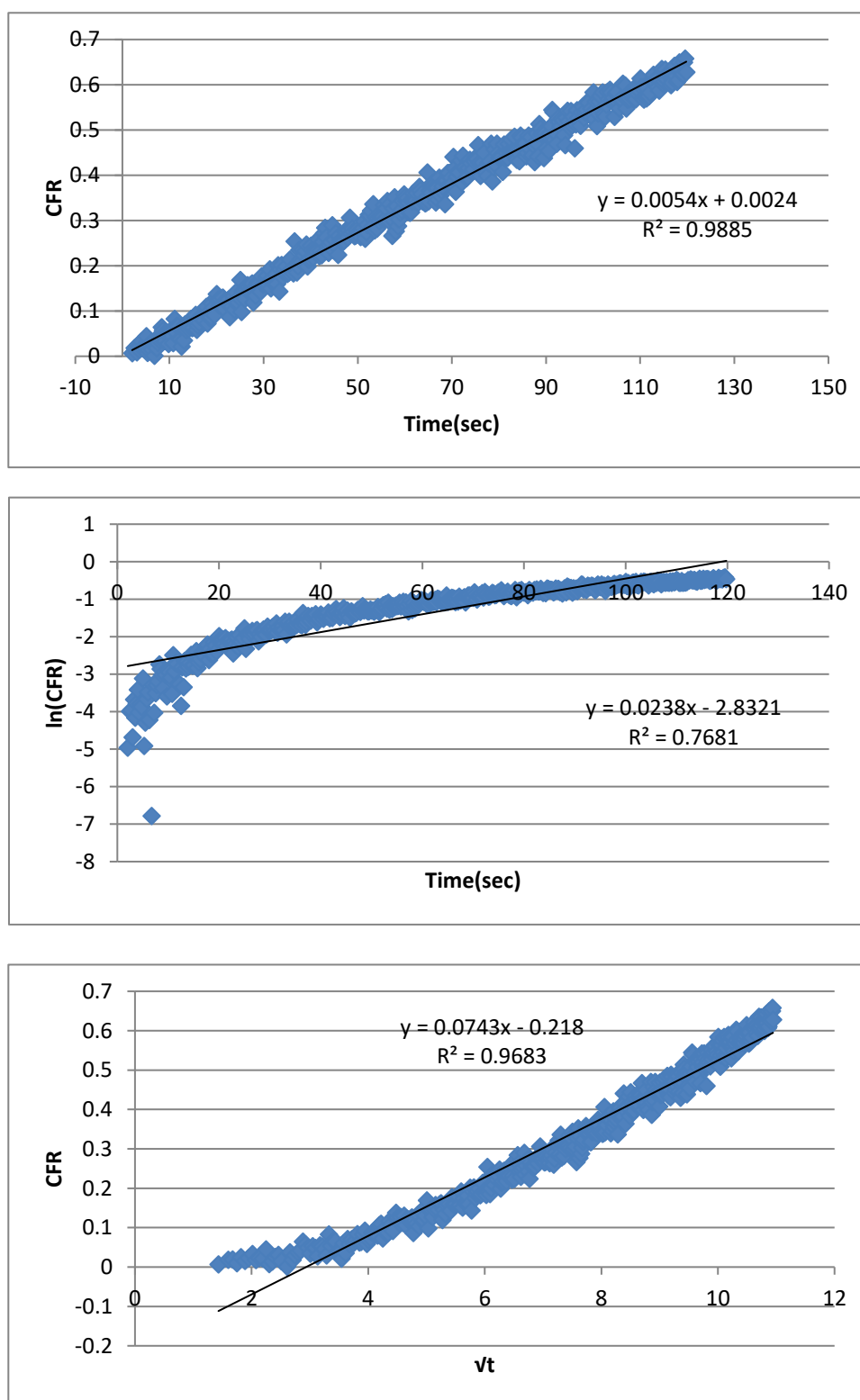


Figure 44: Zero-order (top), First-order (middle), and Higuchi (bottom) model fitting of DOX release from control liposomes at 7.46 mW/cm² (Batch 2)

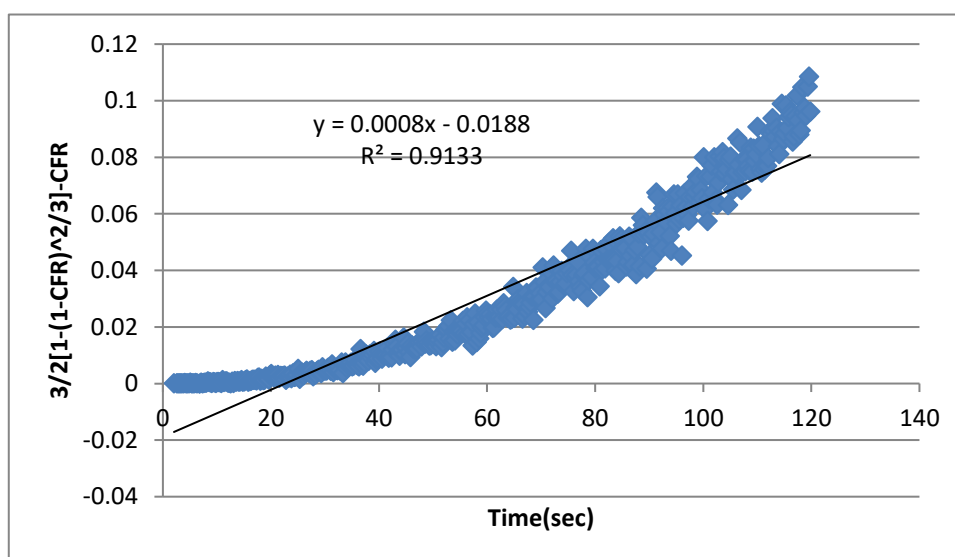
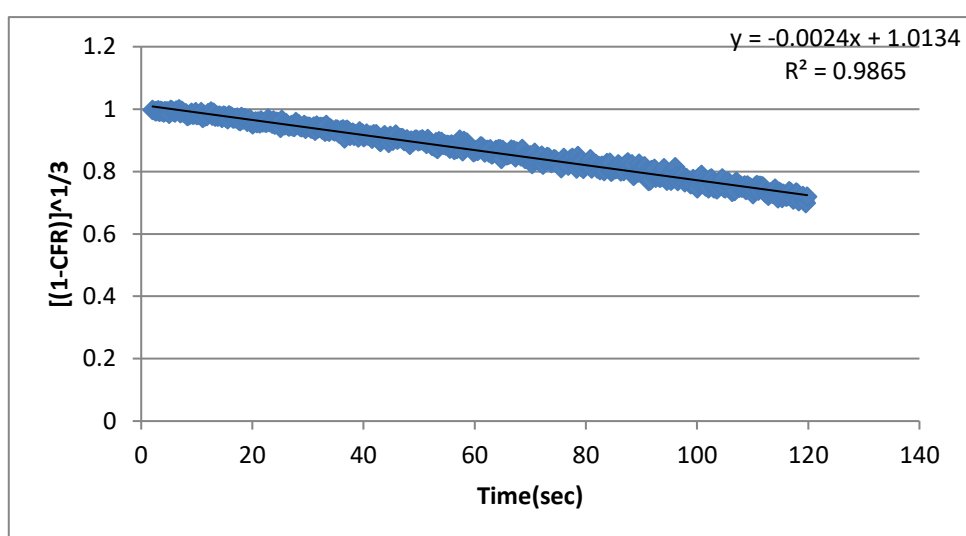
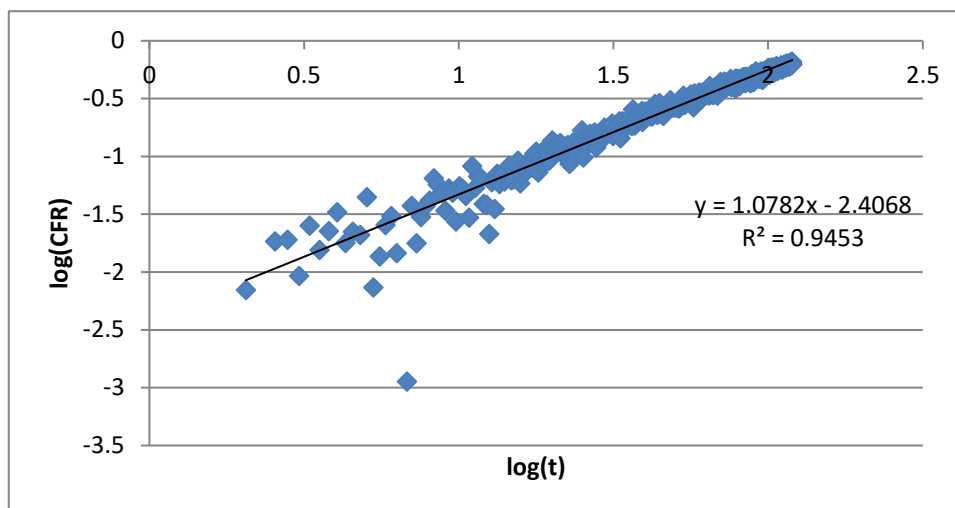


Figure 45: Korsmeyer-Peppas (top), Hixson-Crowell (middle), and Baker-Lonsdale (bottom) model fitting of DOX release from control liposomes at 7.46 mW/cm^2 (Batch 2)

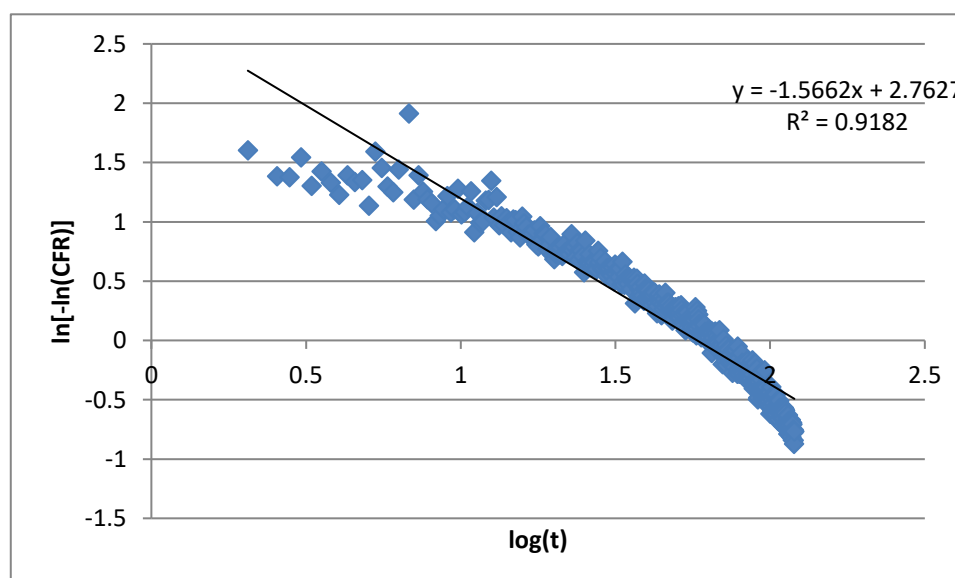
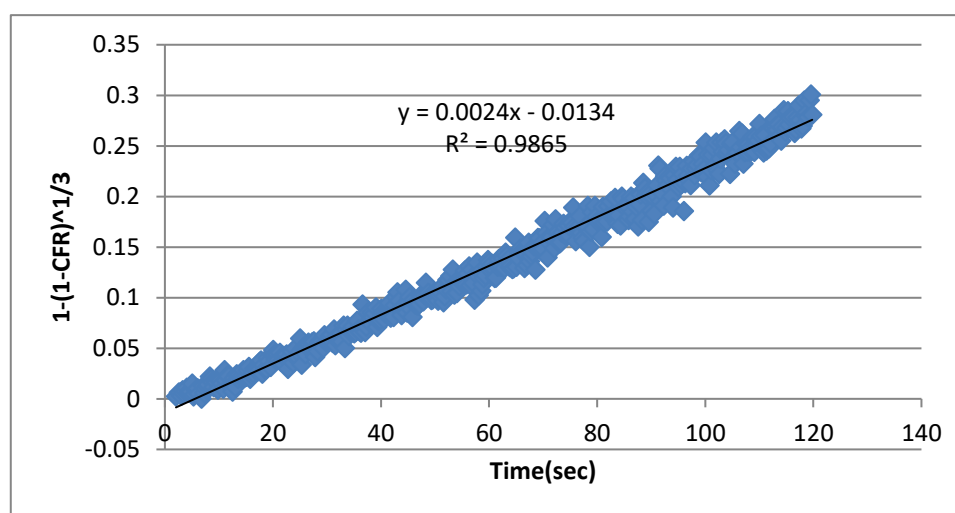
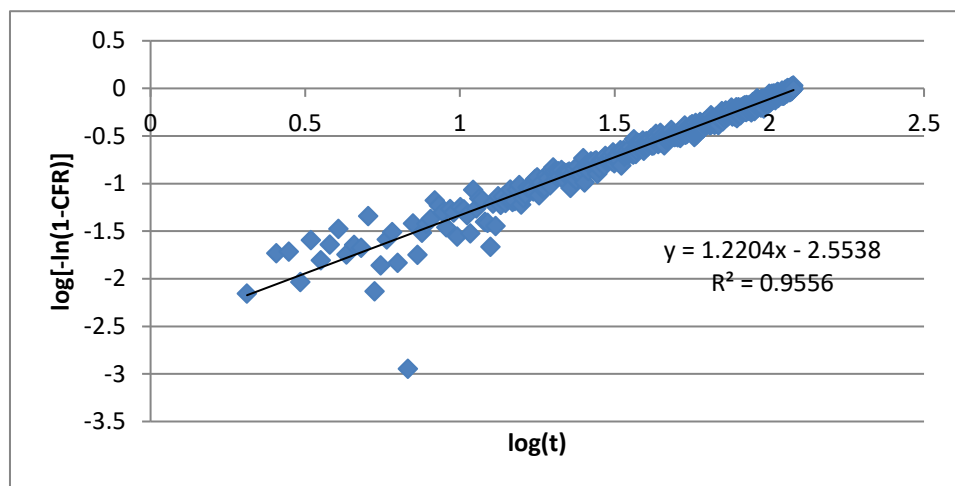


Figure 46: Weibull (top), Hopfenberg (middle), and Gompertz (bottom) model fitting of DOX release from control liposomes at 7.46 mW/cm² (Batch 2)

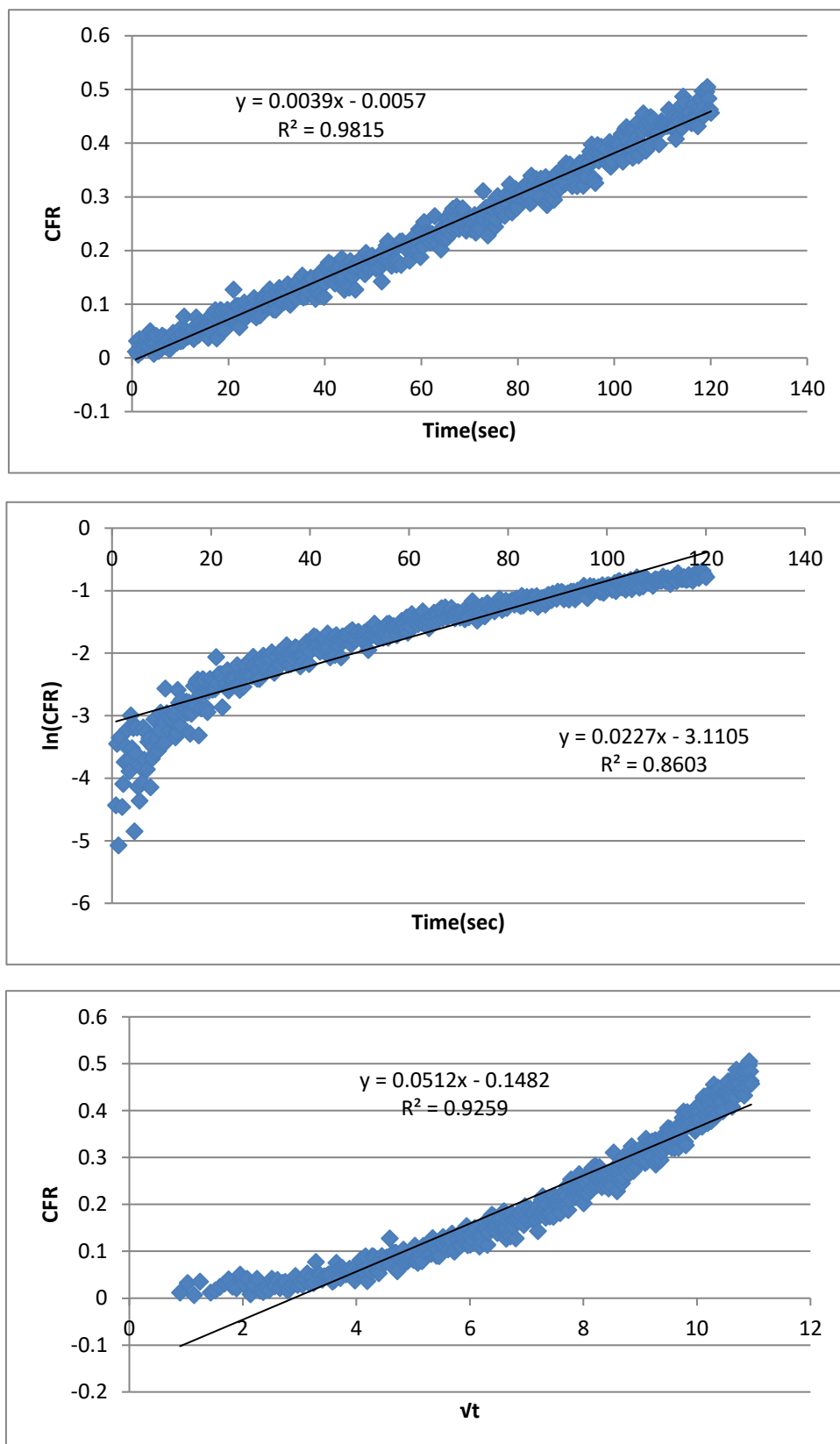


Figure 47: Zero-order (top), First-order (middle), and Higuchi (bottom) model fitting of DOX release from control liposomes at 7.46 mW/cm² (Batch 3)

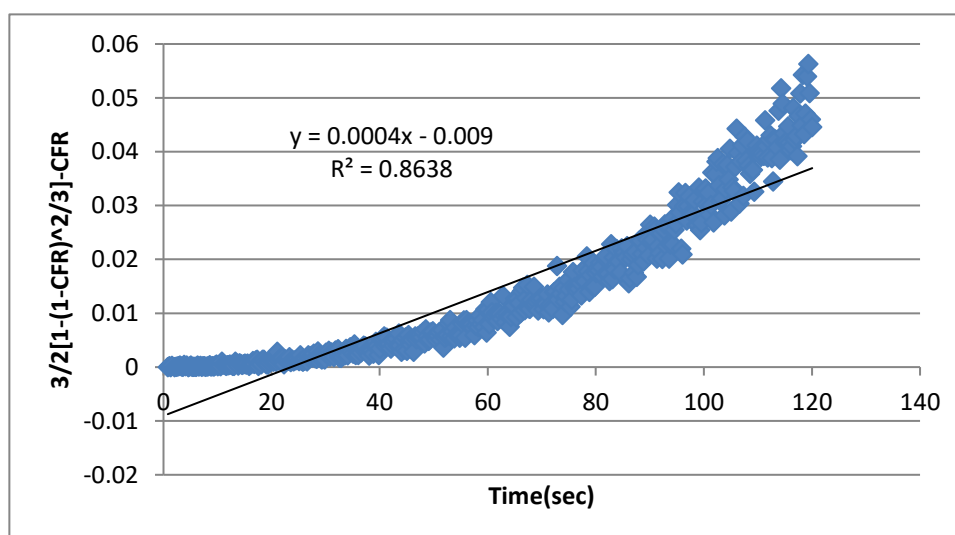
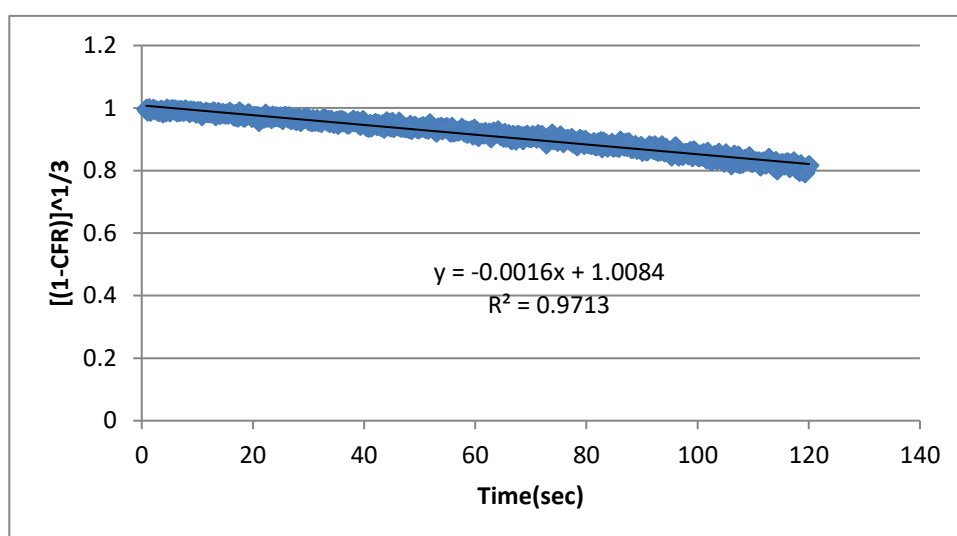
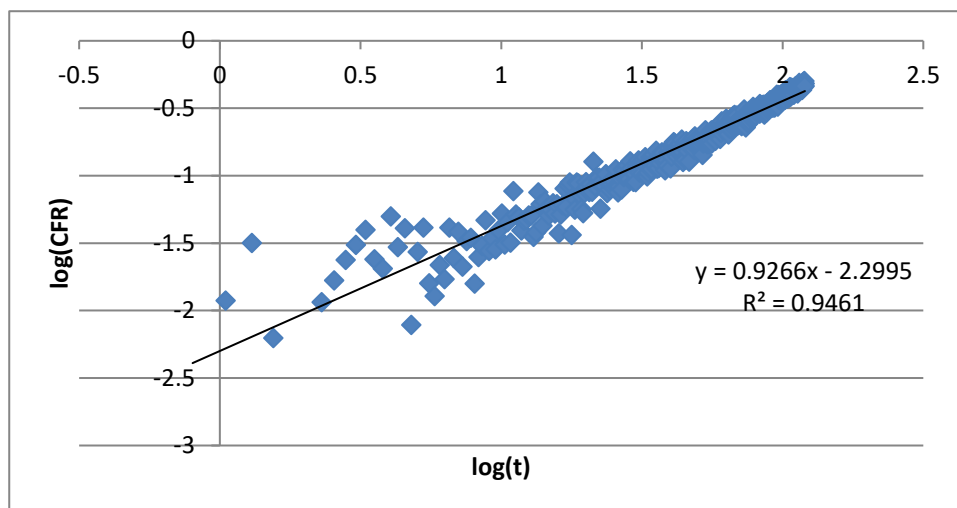


Figure 48:Korsmeyer-Peppas (top), Hixson-Crowell (middle), and Baker-Lonsdale (bottom) model fitting of DOX release from control liposomes at 7.46 mW/cm² (Batch 3)

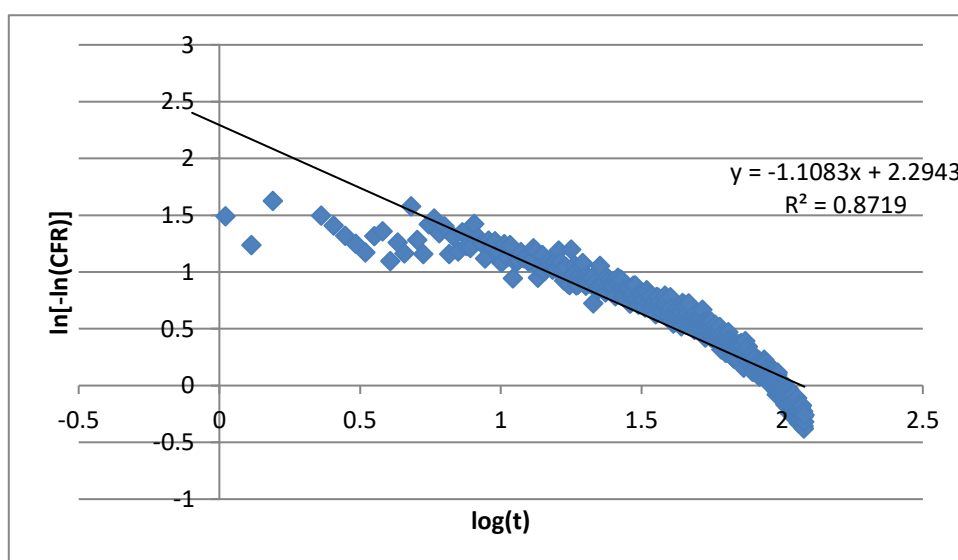
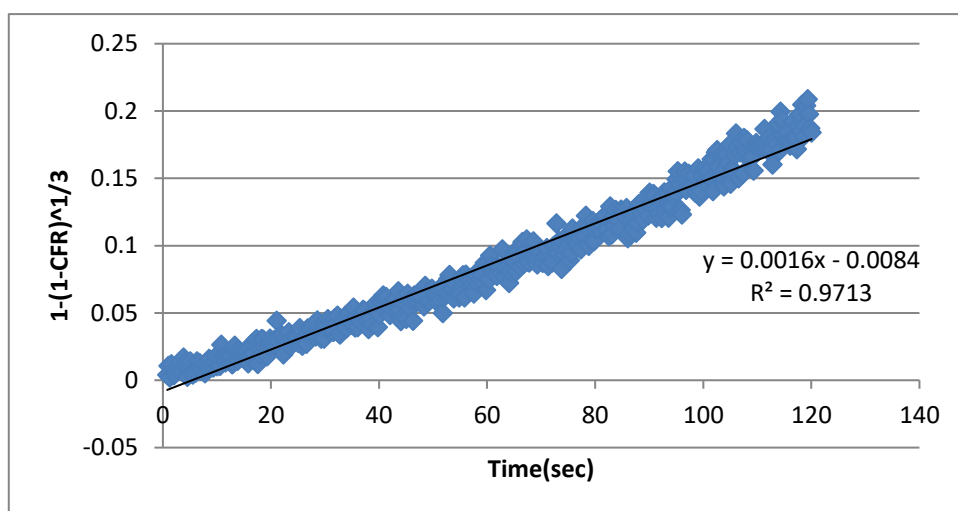
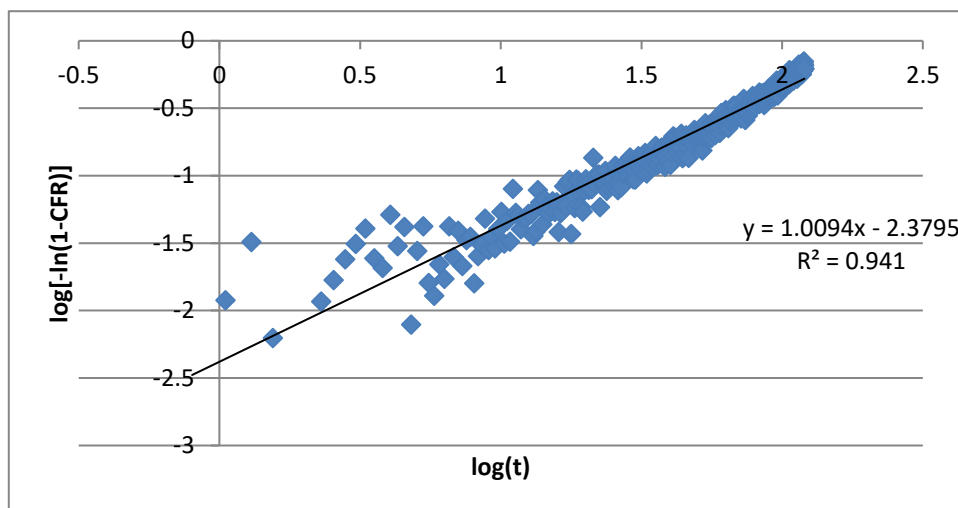


Figure 49: Weibull (top), Hopfenberg (middle), and Gompertz (bottom) model fitting of DOX release from control liposomes at 7.46 mW/cm² (Batch 3)

Appendix B: Plots of Kinetic Models of Control Liposomes at 9.85 mW/cm²

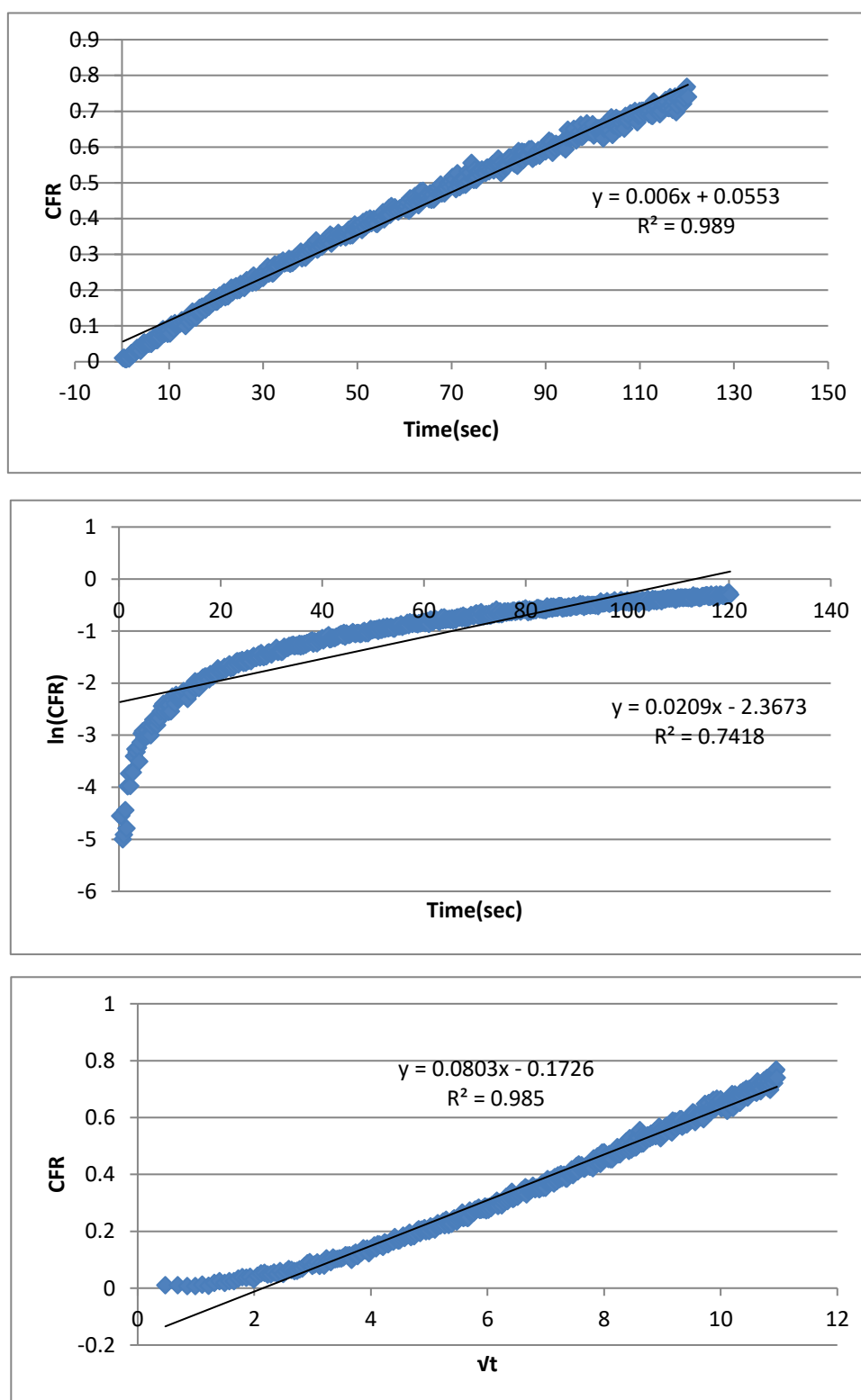


Figure 50: Zero-order (top), First-order (middle), and Higuchi (bottom) model fitting of DOX release from control liposomes at 9.85 mW/cm² (Batch 1)

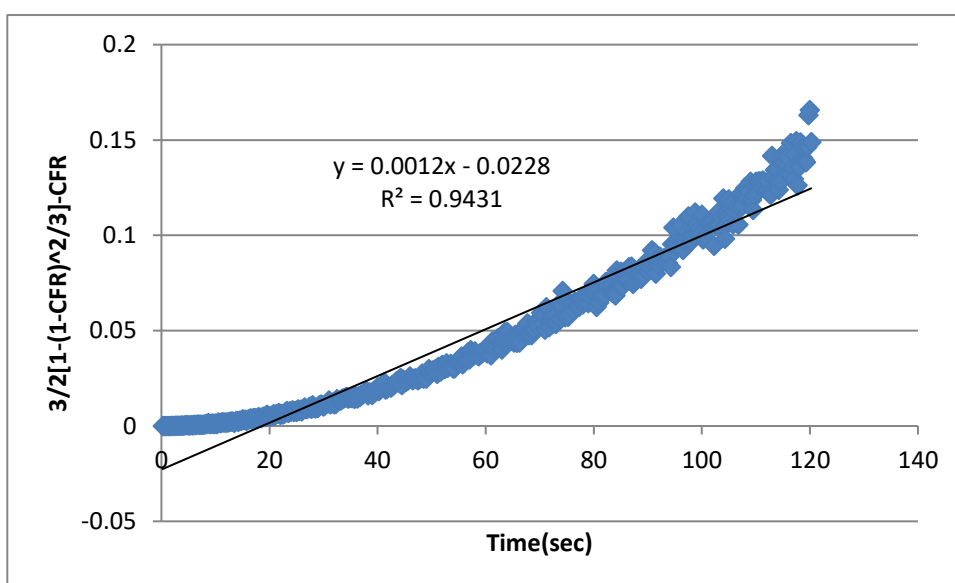
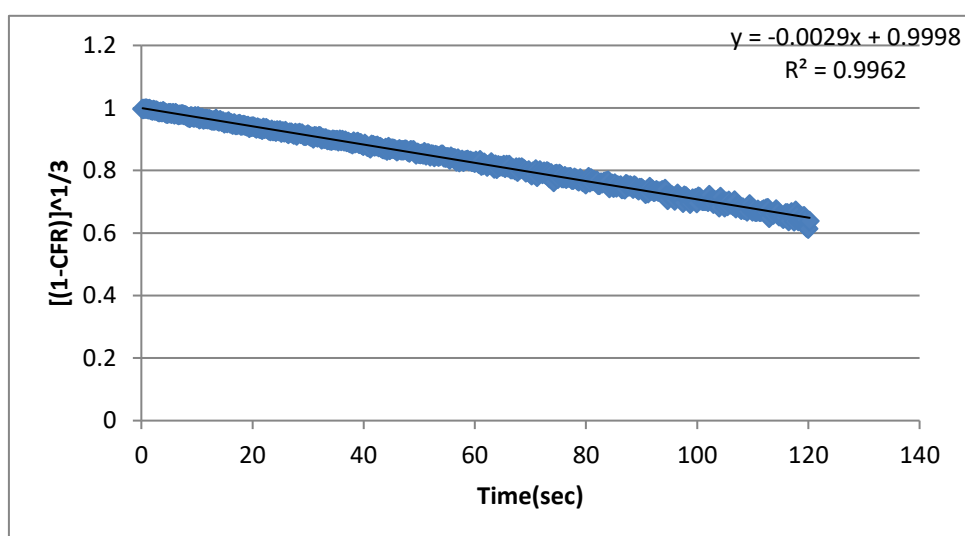
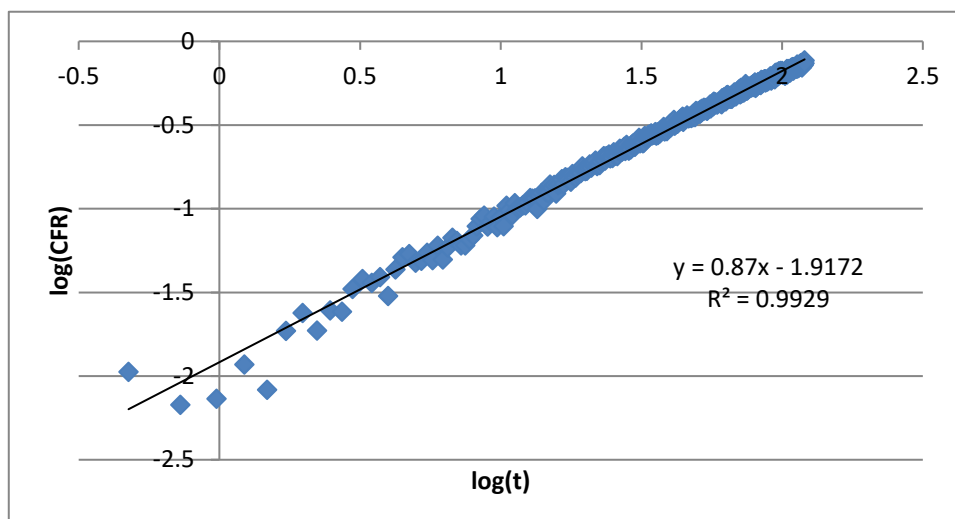


Figure 51: Korsmeyer-Peppas (top), Hixson-Crowell (middle), and Baker-Lonsdale (bottom) model fitting of DOX release from control liposomes at 9.85 mW/cm^2 (Batch 1)

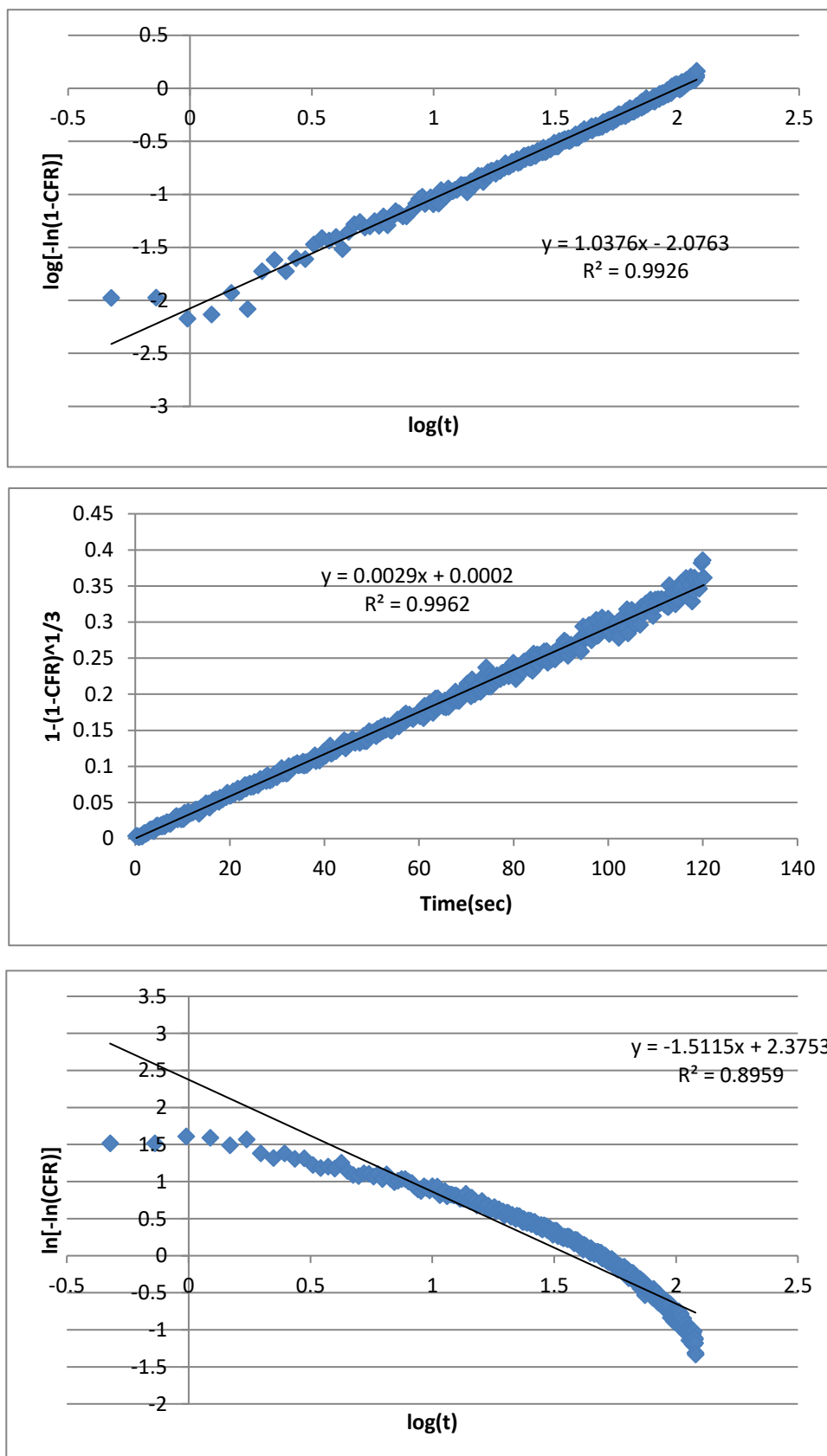


Figure 52: Weibull (top), Hopfenberg (middle), and Gompertz (bottom) model fitting of DOX release from control liposomes at 9.85 mW/cm² (Batch 1)

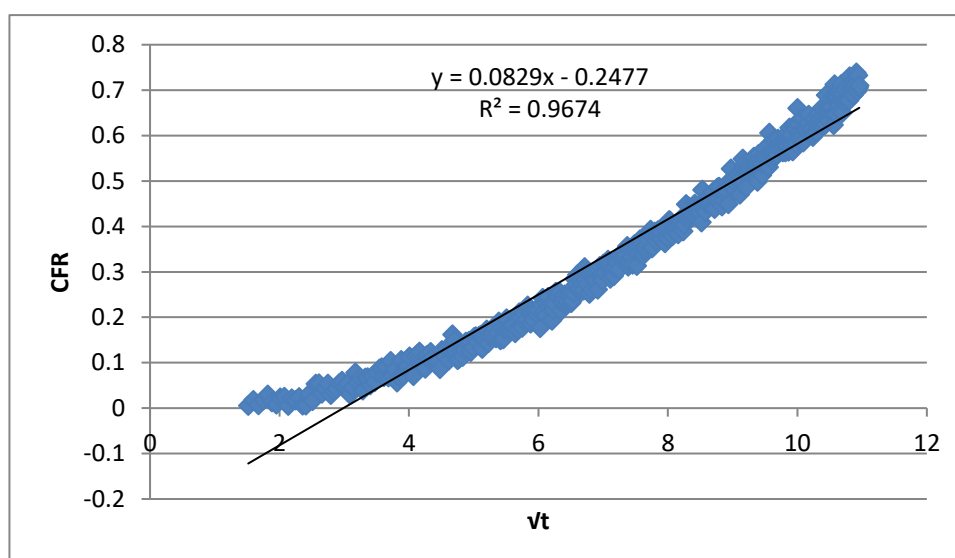
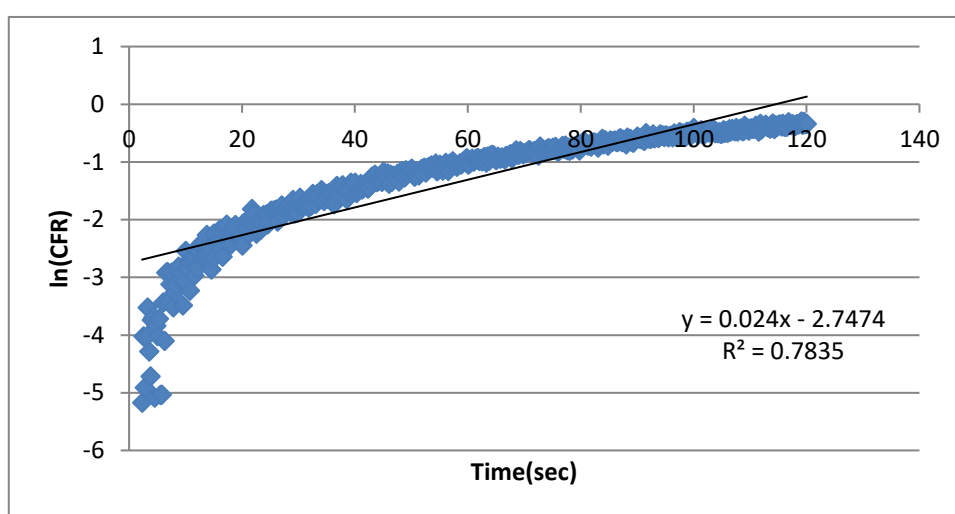
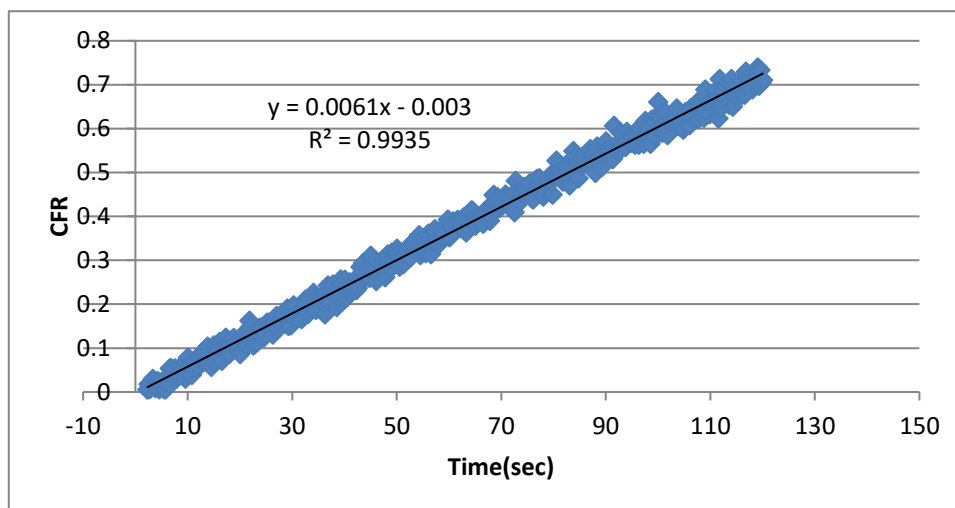


Figure 53: Zero-order (top), First-order (middle), and Higuchi (bottom) model fitting of DOX release from control liposomes at 9.85 mW/cm² (Batch 2)

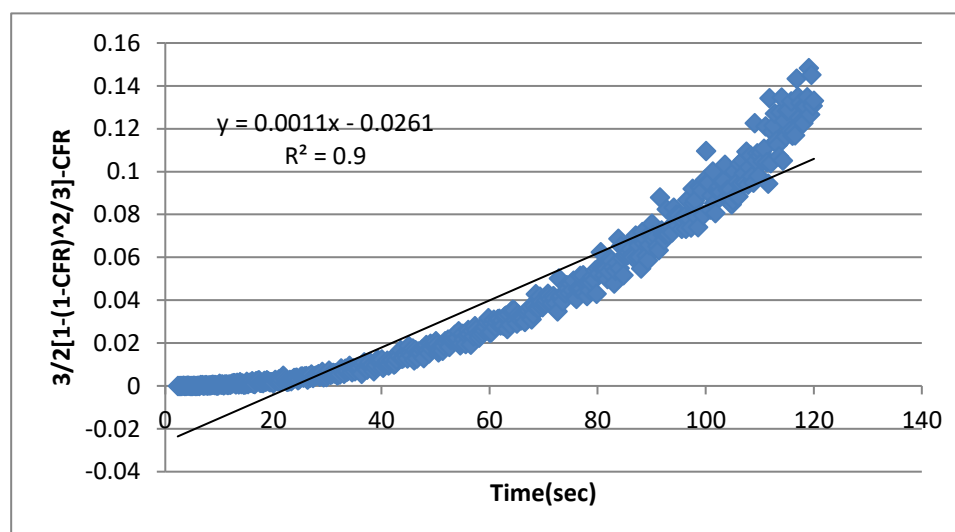
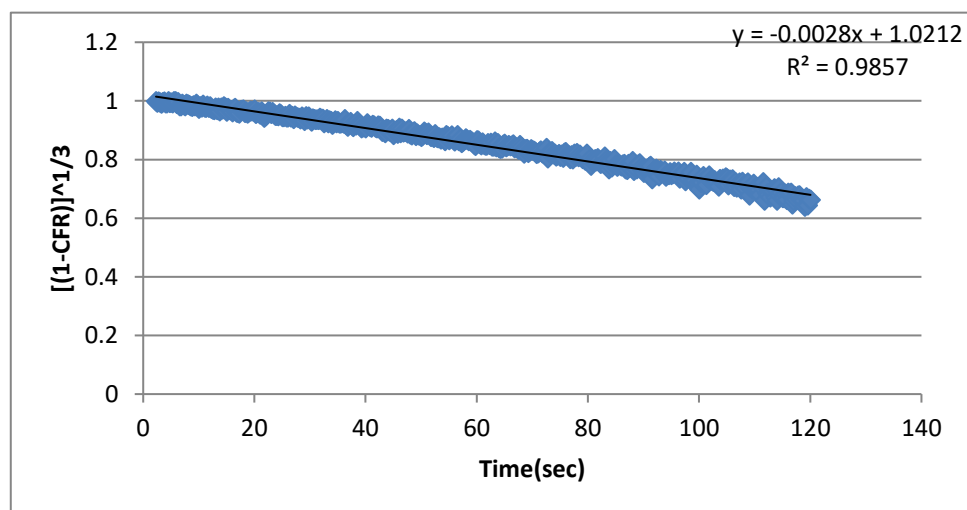
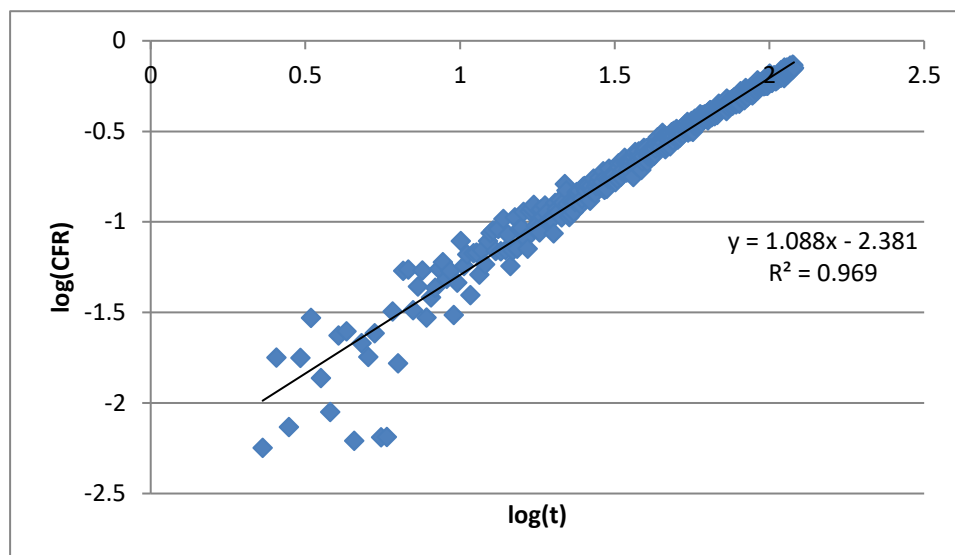


Figure 54: Korsmeyer-Peppas (top), Hixson-Crowell (middle), and Baker-Lonsdale (bottom) model fitting of DOX release from control liposomes at 9.85 mW/cm^2 (Batch 2)

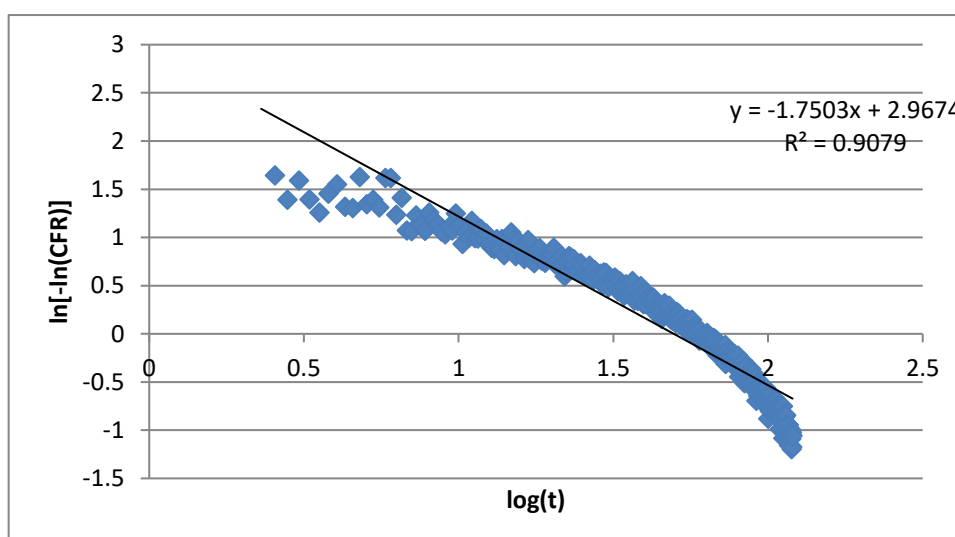
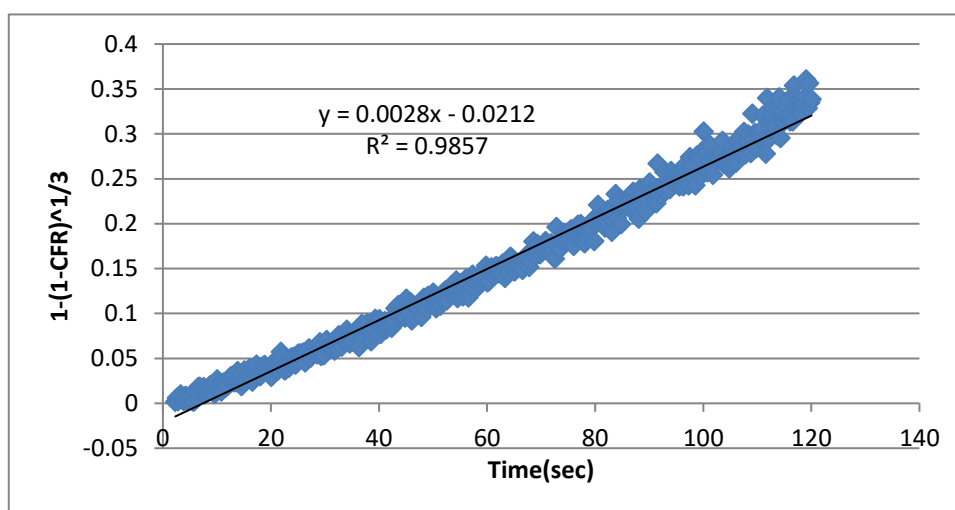
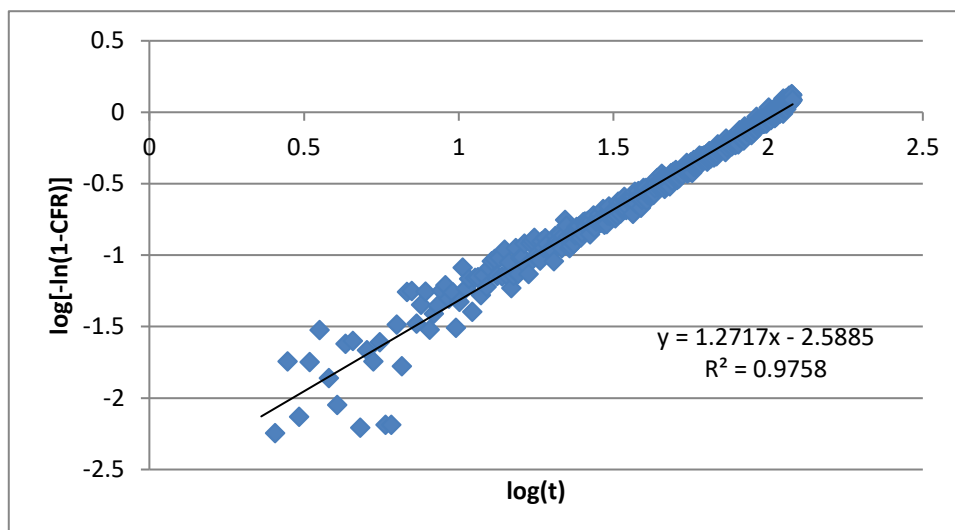


Figure 55: Weibull (top), Hopfenberg (middle), and Gompertz (bottom) model fitting of DOX release from control liposomes at 9.85 mW/cm² (Batch 2)

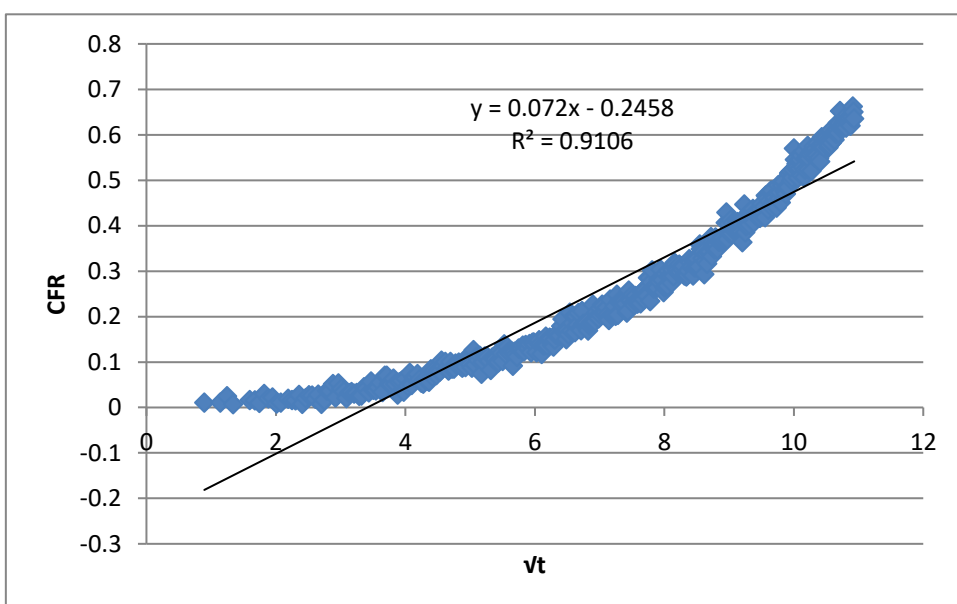
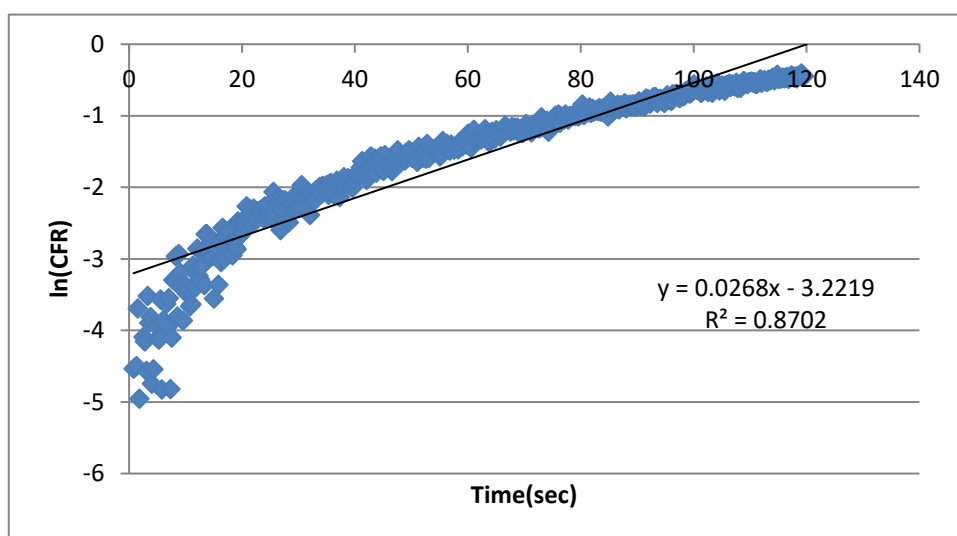
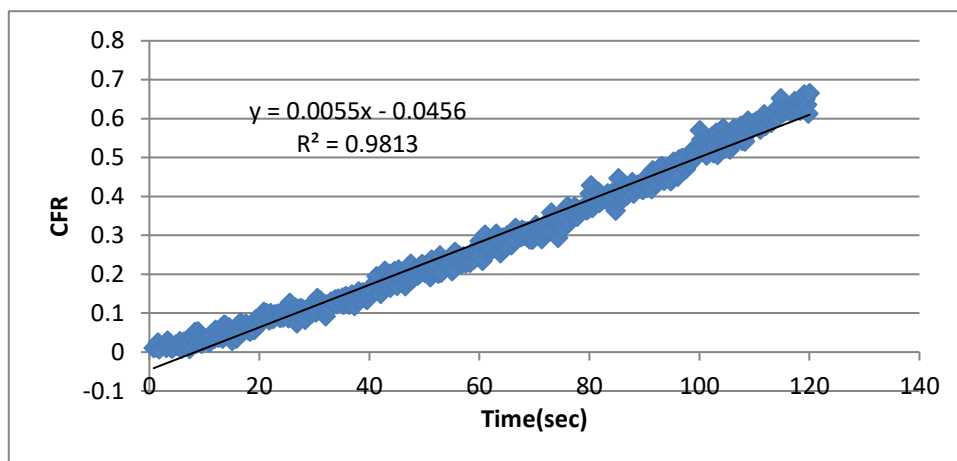


Figure 56: Zero-order (top), First-order (middle), and Higuchi (bottom) model fitting of DOX release from control liposomes at 9.85 mW/cm² (Batch 3)

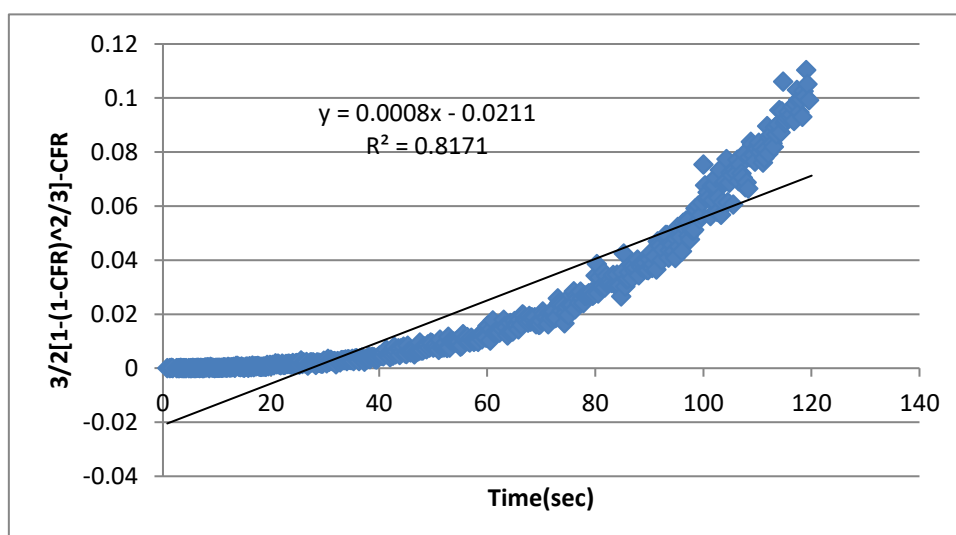
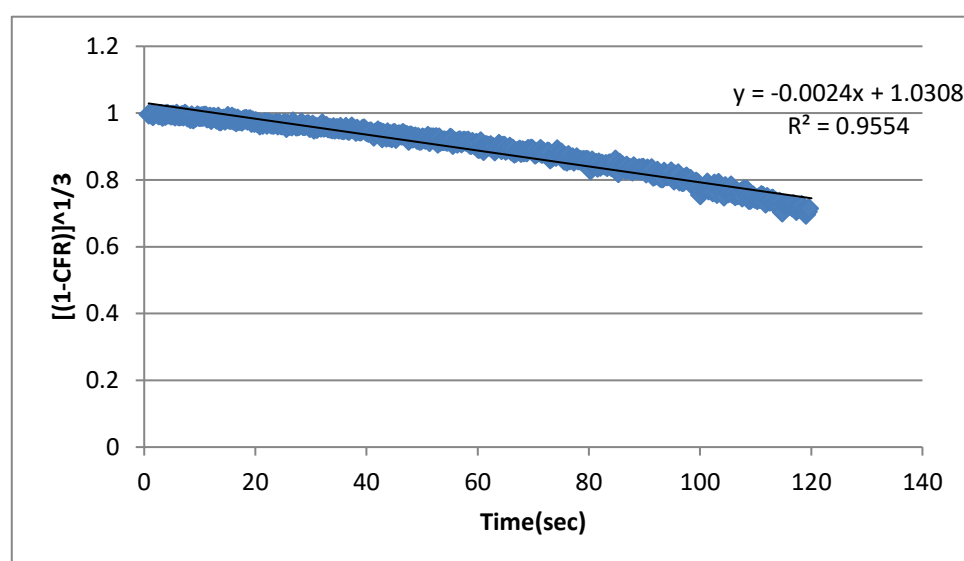
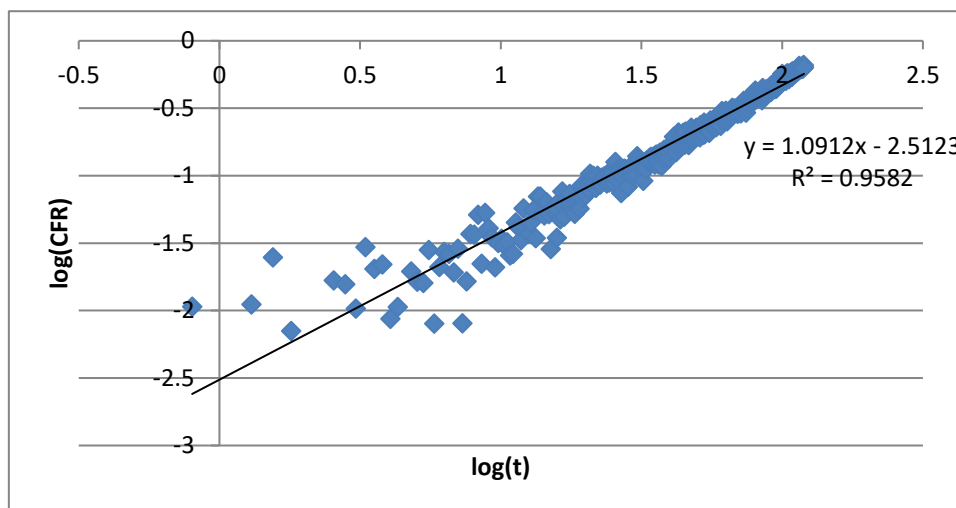


Figure 57: Korsmeyer-Peppas (top), Hixson-Crowell (middle), and Baker-Lonsdale (bottom) model fitting of DOX release from control liposomes at 9.85 mW/cm² (Batch 3)

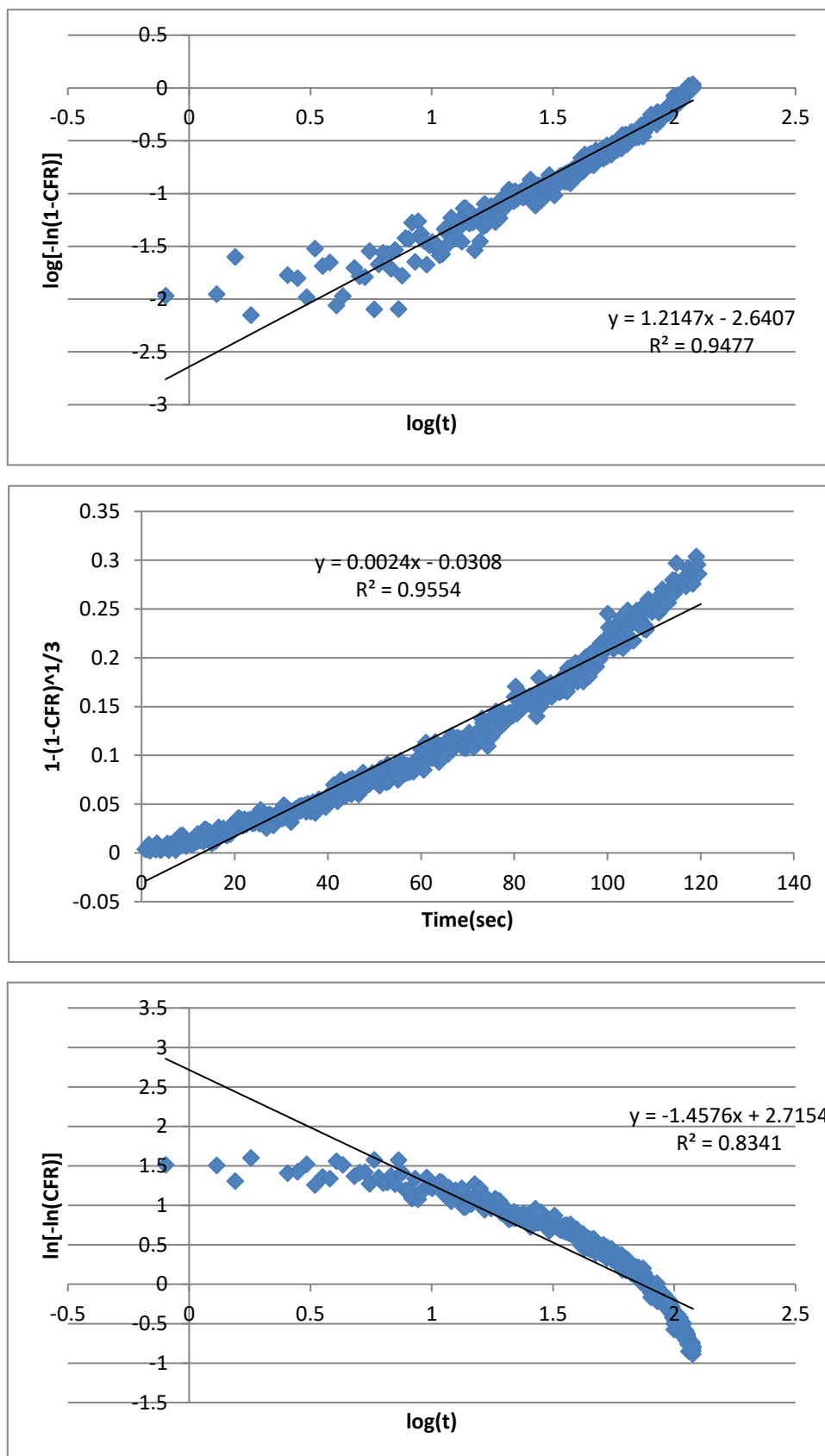


Figure 58: Weibull (top), Hopfenberg (middle), and Gompertz (bottom) model fitting of DOX release from control liposomes at 9.85 mW/cm² (Batch 3)

Appendix C: Plots of Kinetic Models of Control Liposomes at 17.31 mW/cm²

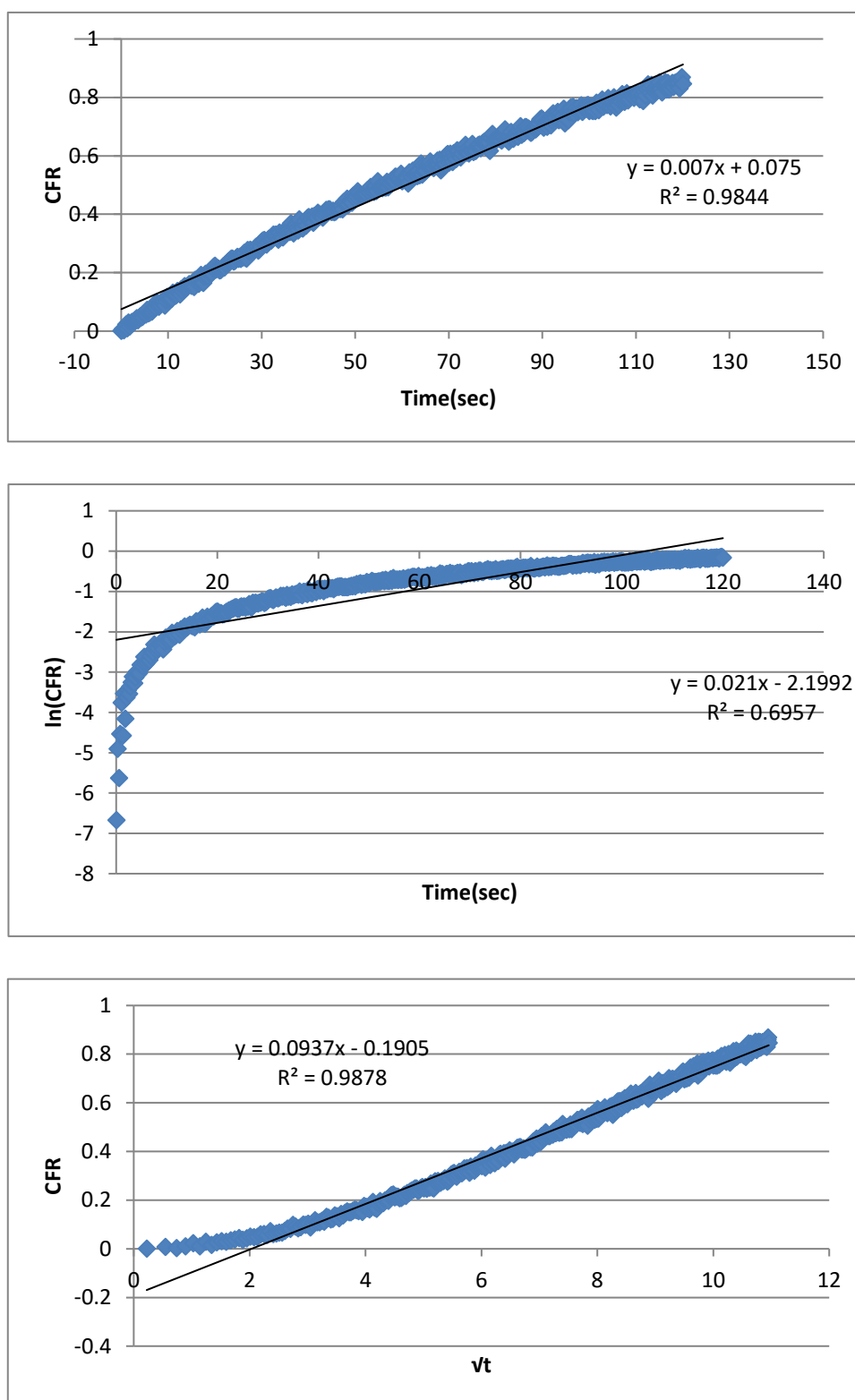


Figure 59: Zero order (top), First Order (middle), and Higuchi (bottom) model fitting of DOX release from control liposomes at 17.31 mW/cm² (Batch 1)

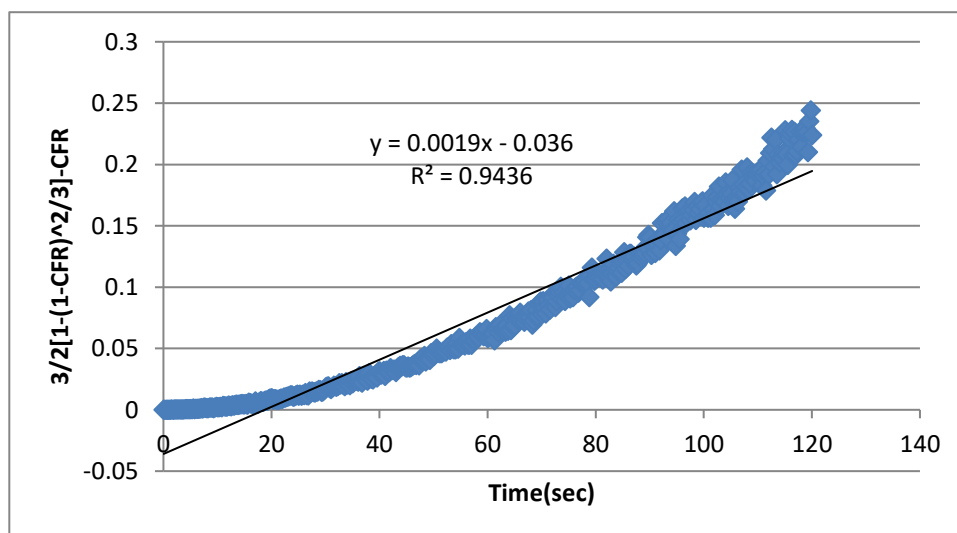
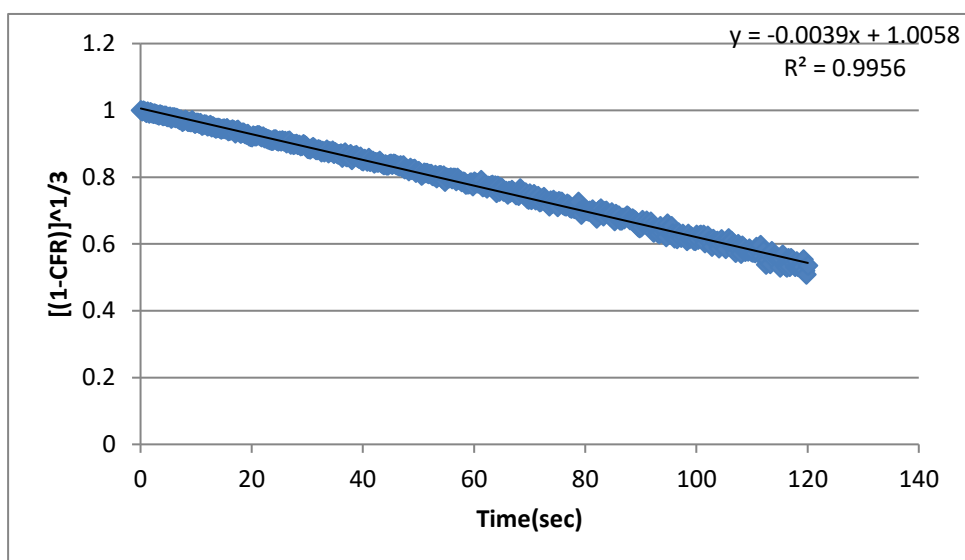
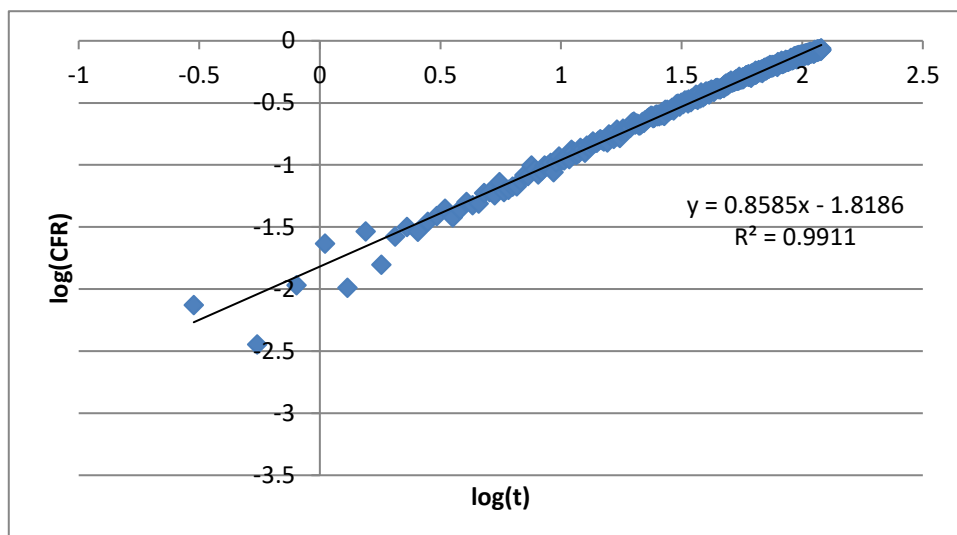


Figure 60: Korsmeyer-Peppas (top), Hixson-Crowell (middle), and Baker-Lonsdale (bottom) model fitting of DOX release from control liposomes at 17.31 mW/cm² (Batch 1)

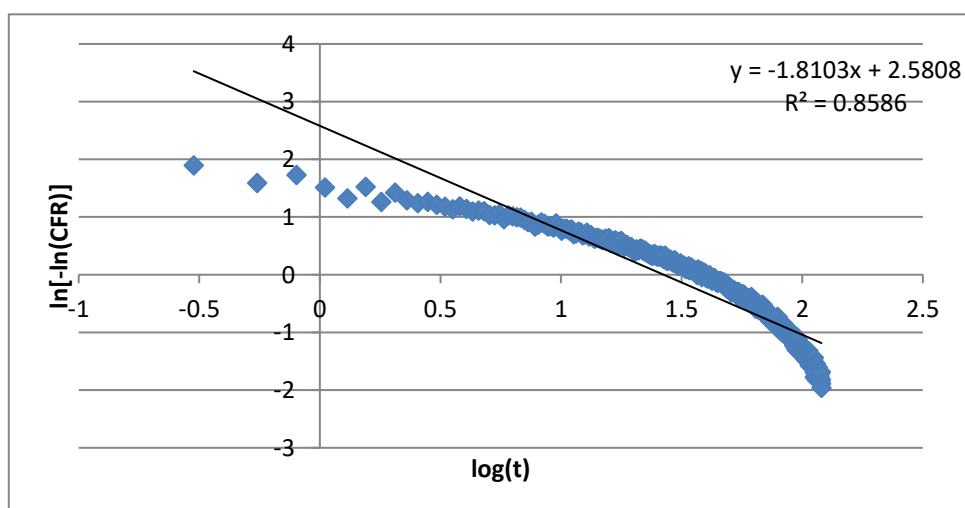
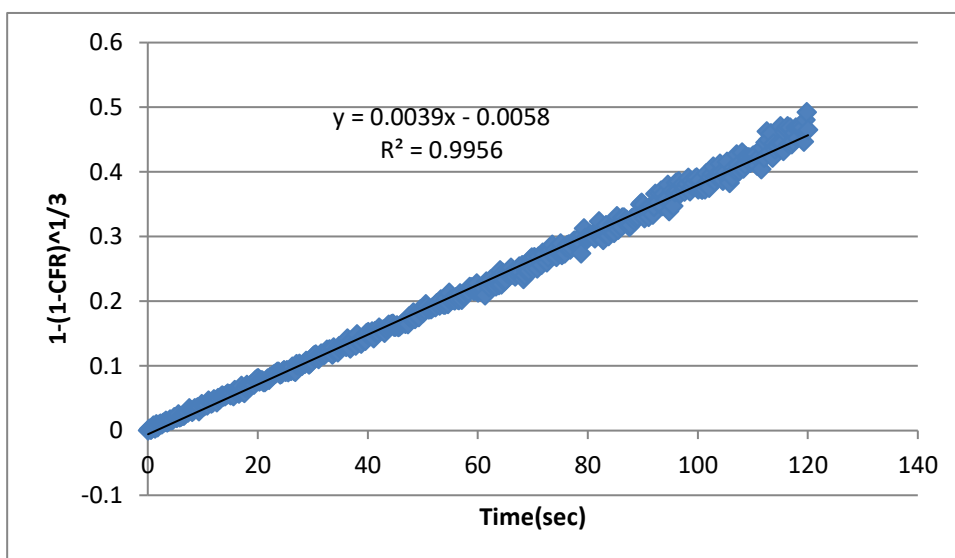
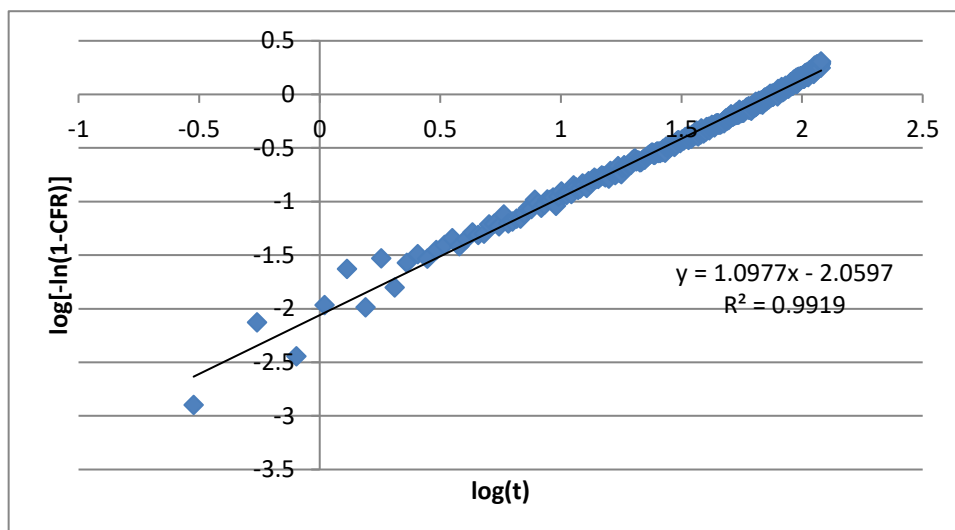


Figure 61: Weibull (top), Hopfenberg (middle), and Gompertz (bottom) model fitting of DOX release from control liposomes at 17.31 mW/cm² (Batch 1)

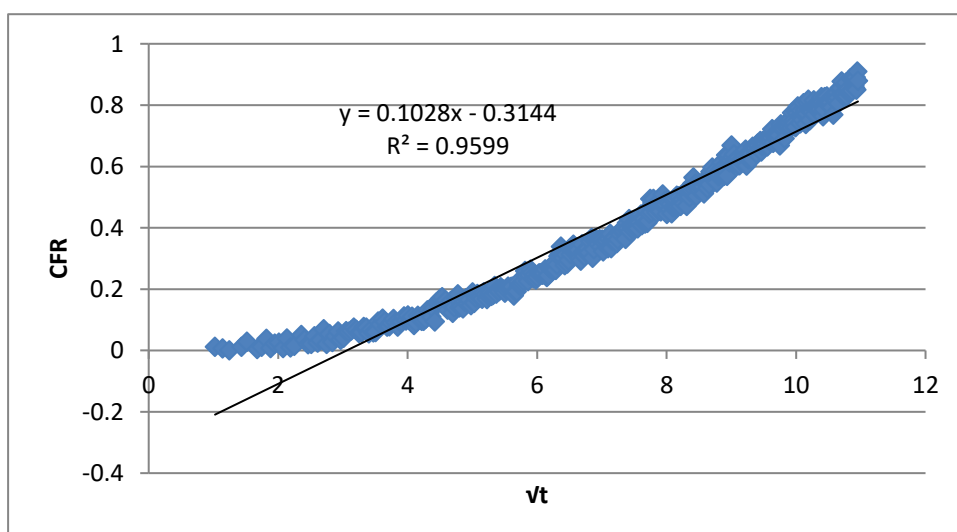
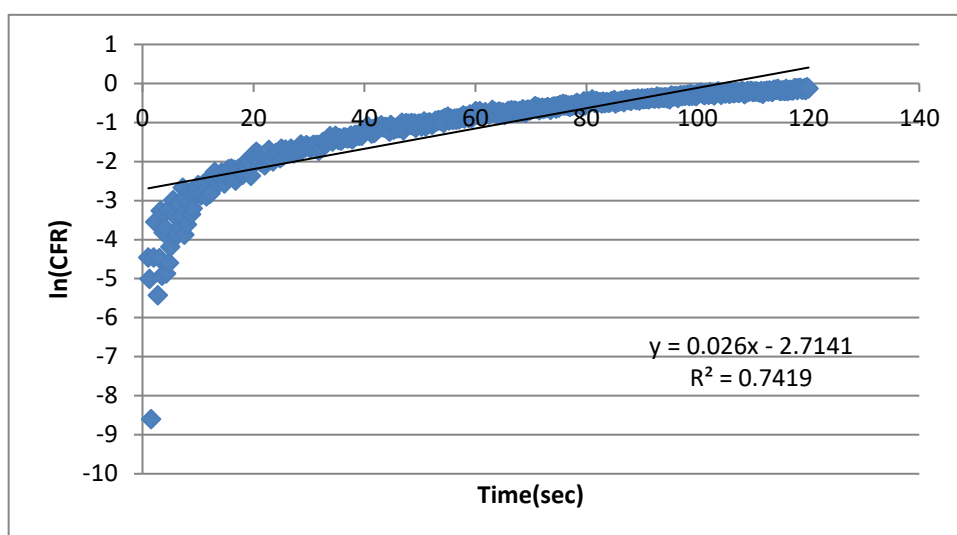
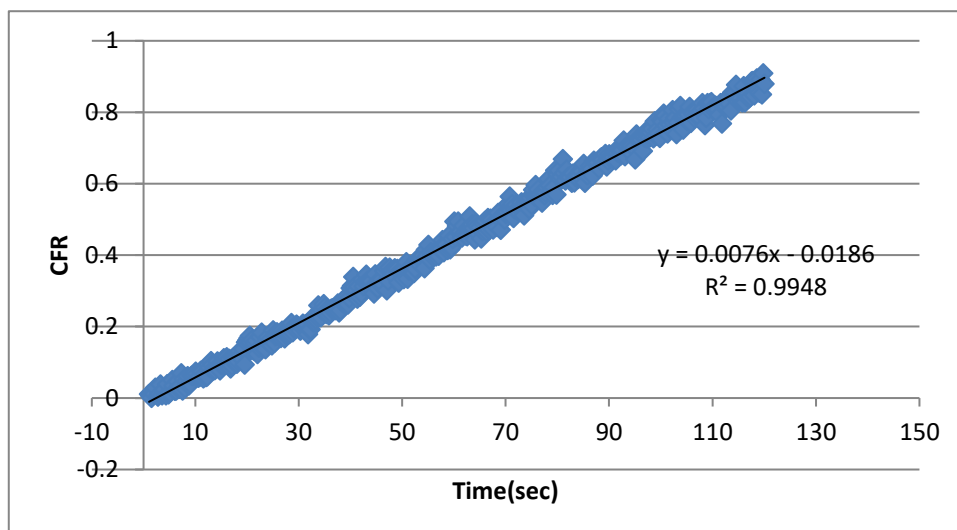


Figure 62: Zero-order (top), First-order (middle), and Higuchi (bottom) model fitting of DOX release from control liposomes at 17.31 mW/cm² (Batch 2)

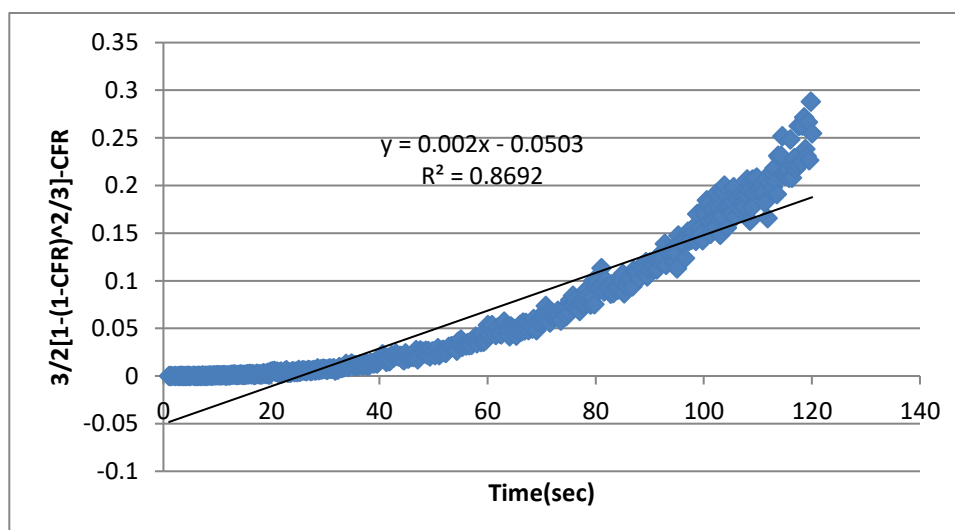
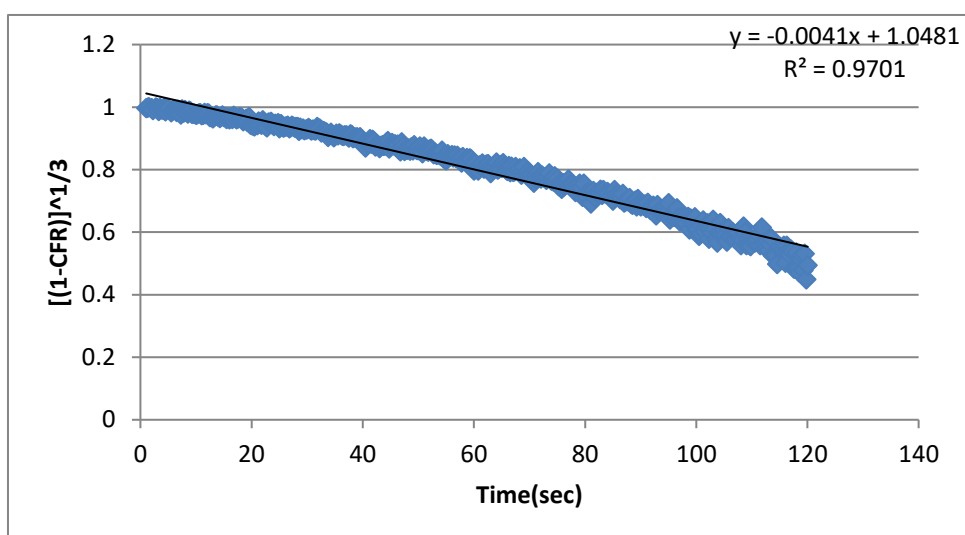
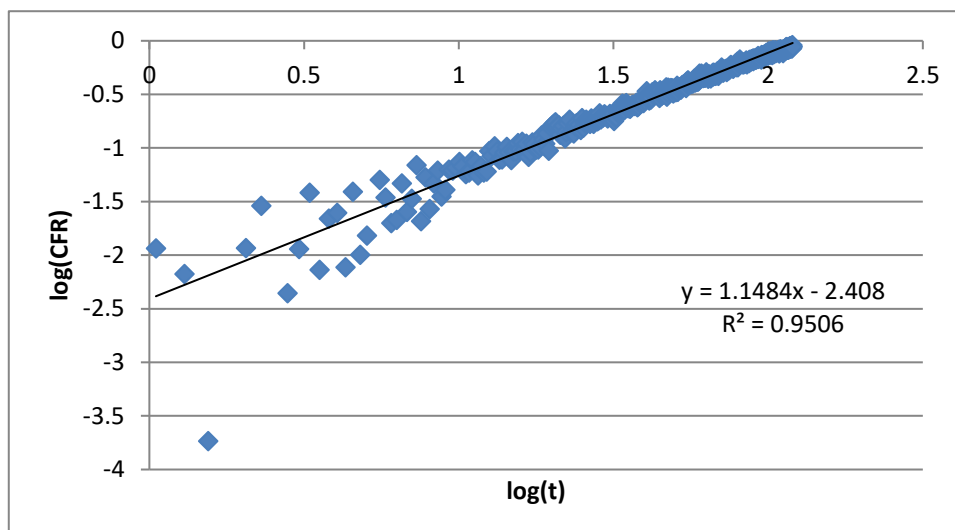


Figure 63: Korsmeyer-Peppas (top), Hixson-Crowell (middle), and Baker-Lonsdale (bottom) model fitting of DOX release from control liposomes at 17.31 mW/cm² (Batch 2)

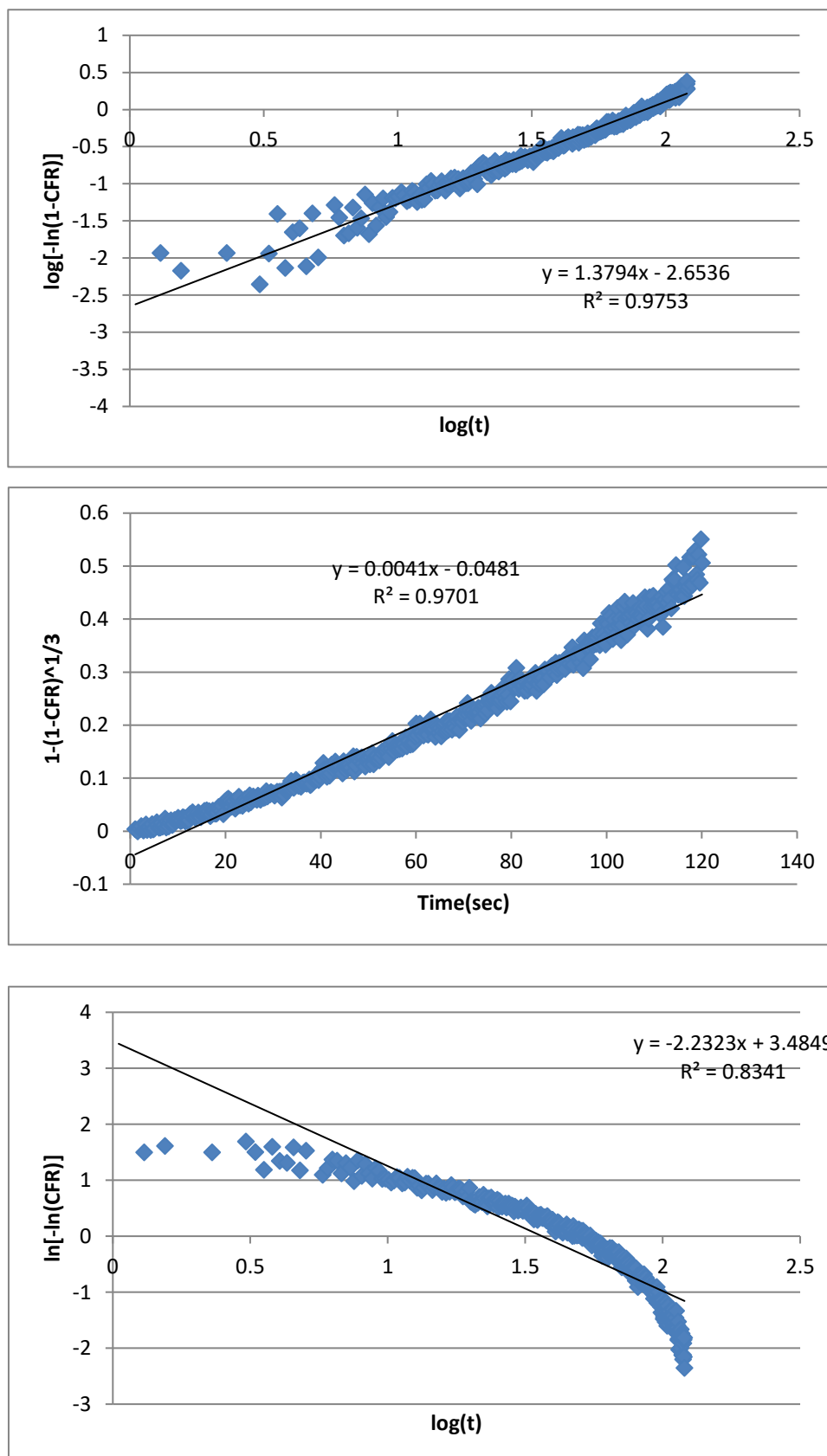


Figure 64: Weibull (top), Hopfenberg (middle), and Gompertz (bottom) model fitting of DOX release from control liposomes at 17.31 mW/cm² (Batch 2)

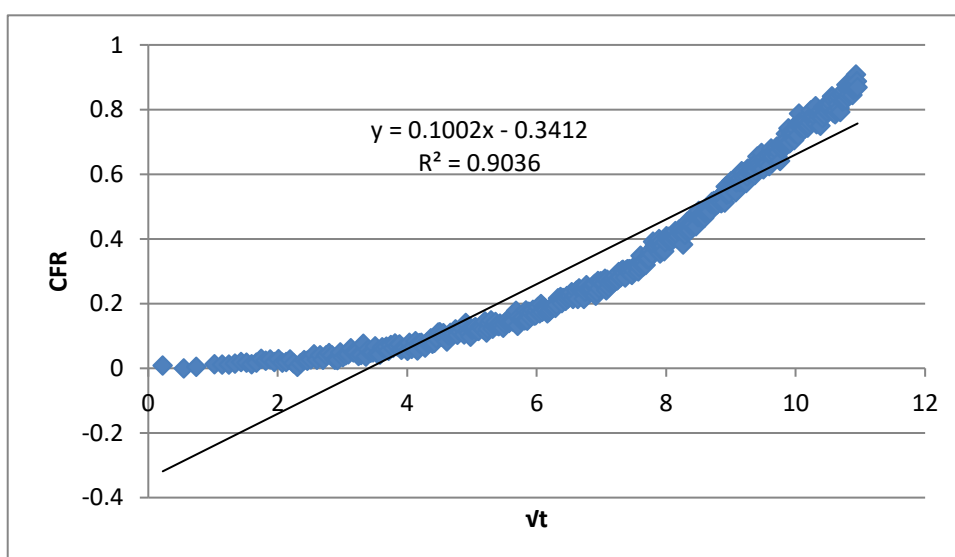
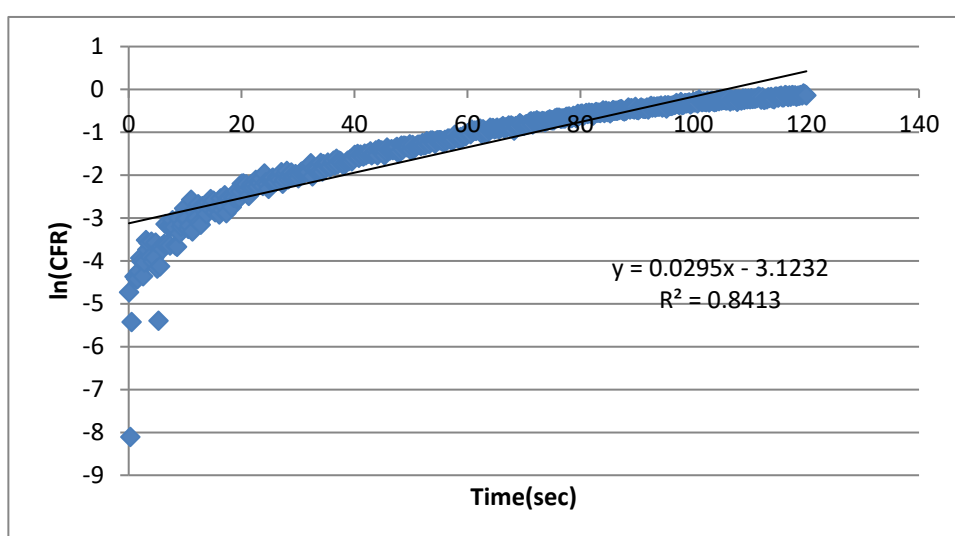
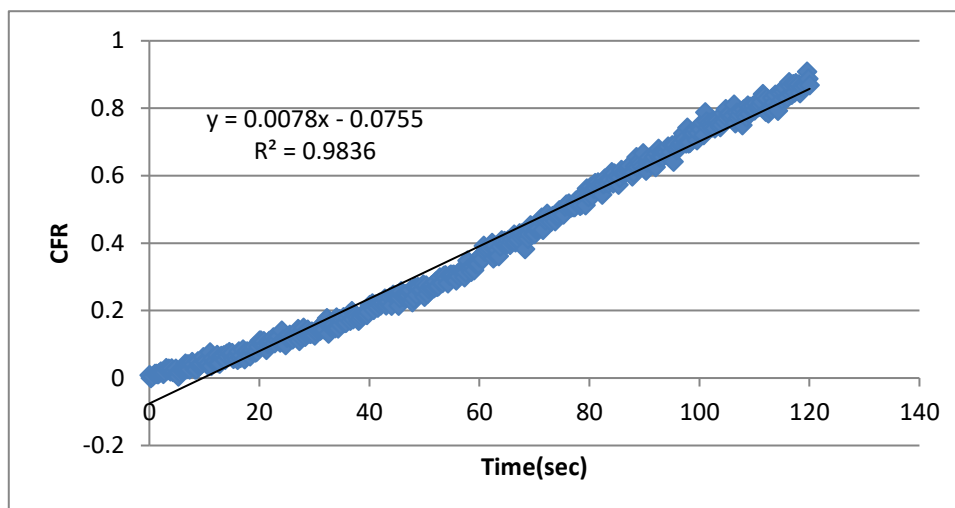


Figure 65: Zero-order (top), First-order (middle), and Higuchi (bottom) model fitting of DOX release from control liposomes at 17.31 mW/cm² (Batch 3)

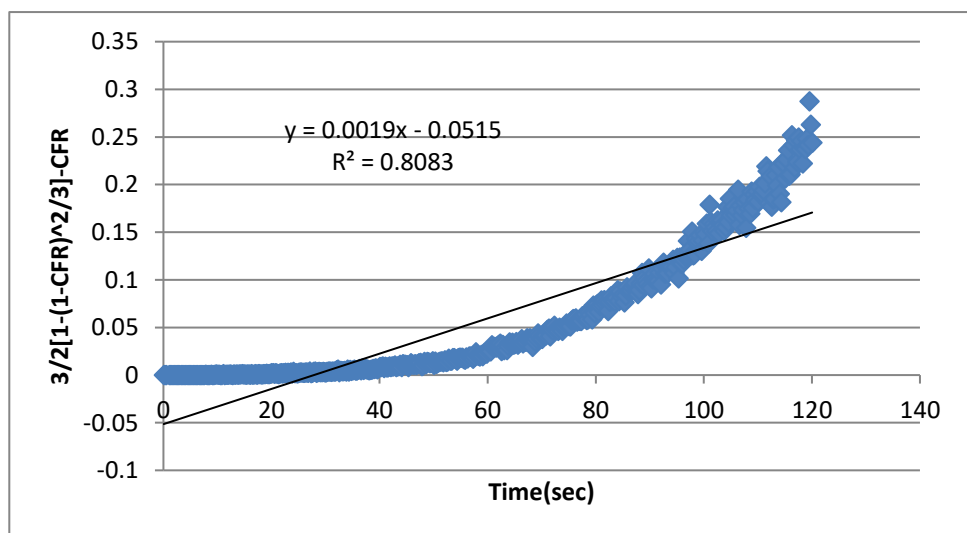
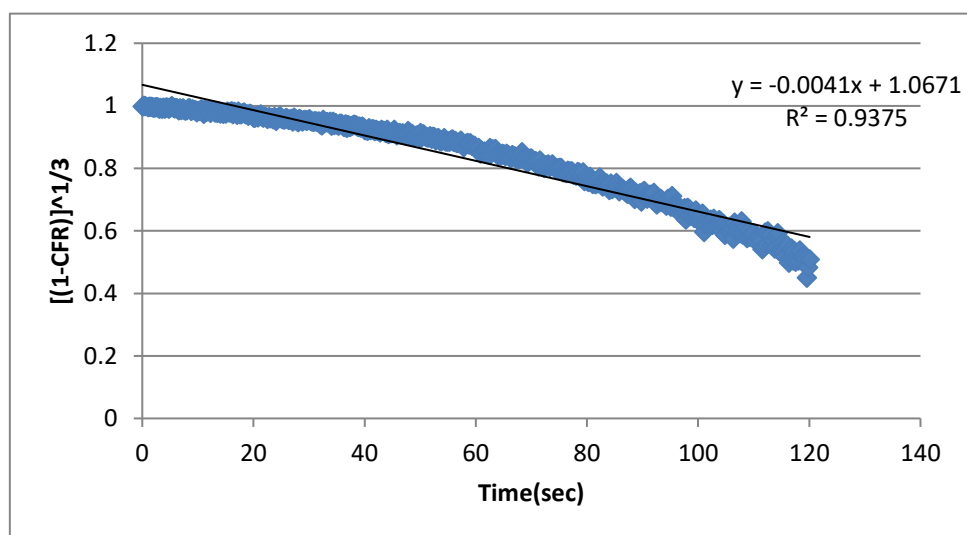
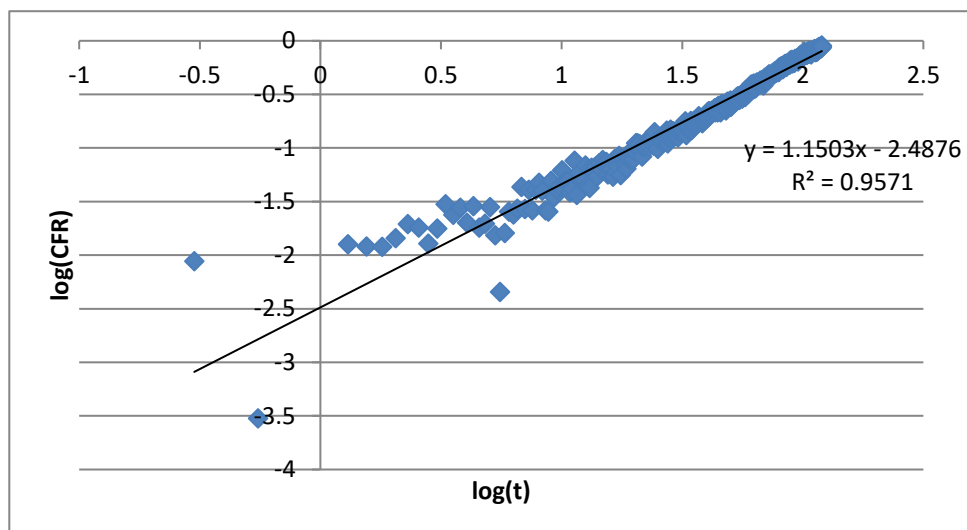


Figure 66: Korsmeyer-Peppas (top), Hixson-Crowell (middle), and Baker-Lonsdale (bottom) model fitting of DOX release from control liposomes at 17.31 mW/cm^2 (Batch 3)

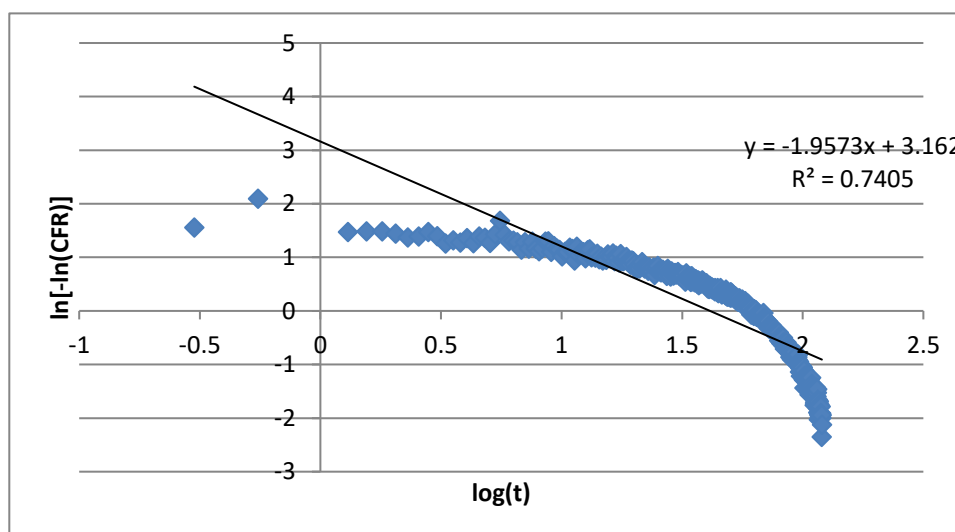
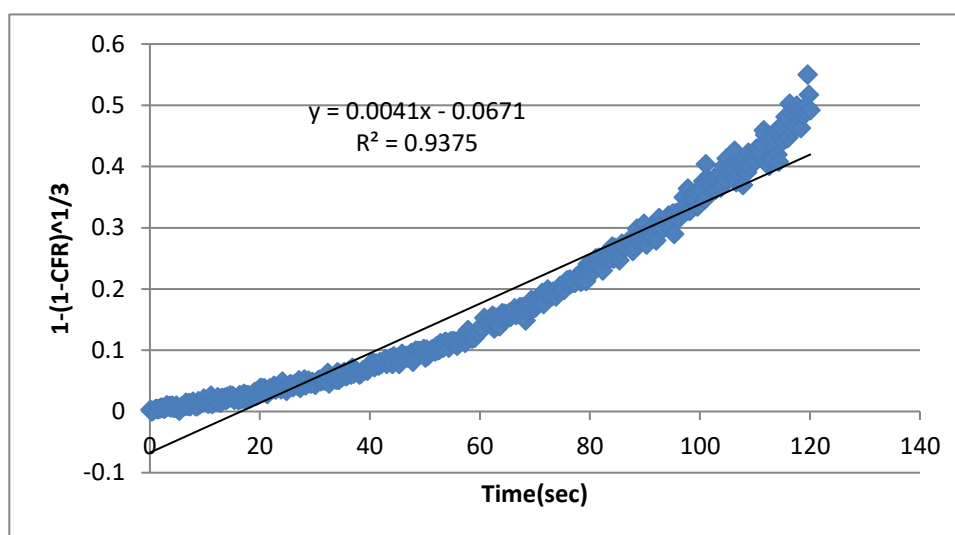
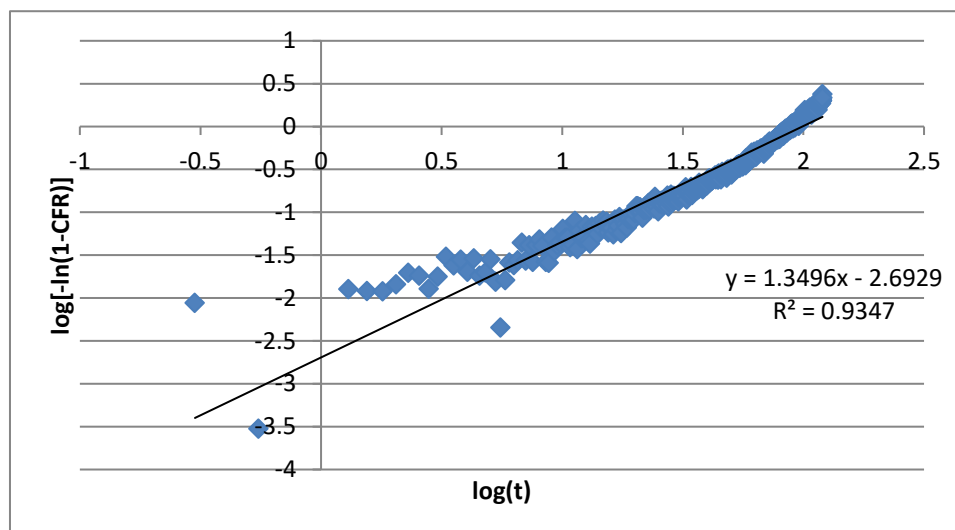


Figure 67: Weibull (top), Hopfenberg (middle), and Gompertz (bottom) model fitting of DOX release from control liposomes at 17.31 mW/cm^2 (Batch 3)

Appendix D: Plots of Kinetic Models for Batches 2 & 3 of Tf-Liposomes at 7.46 mW/cm²

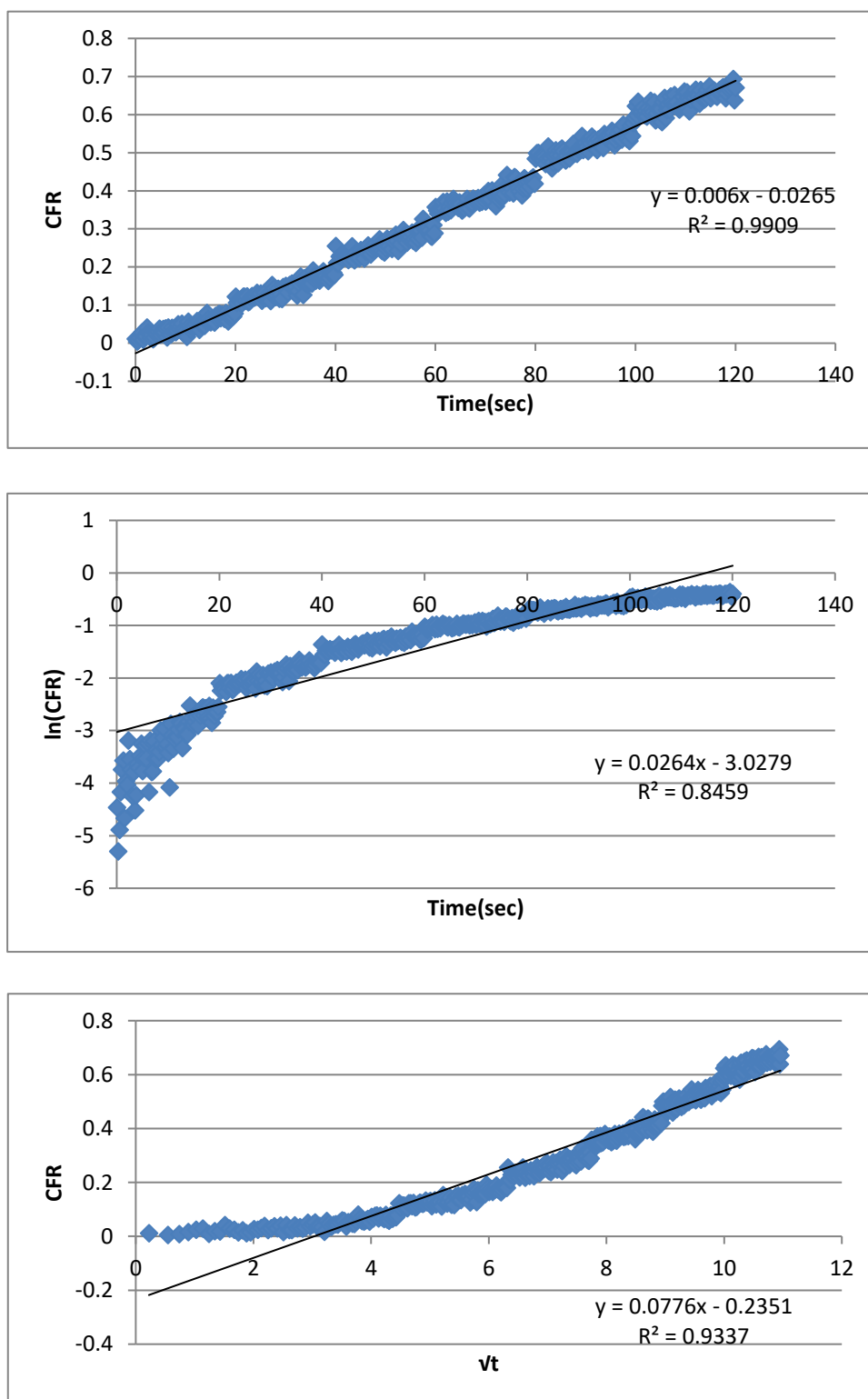


Figure 68: Zero-order (top), First-order (middle), and Higuchi (bottom) model fitting of DOX release from Tf-targeted liposomes at 7.46 mW/cm² (Batch 2)

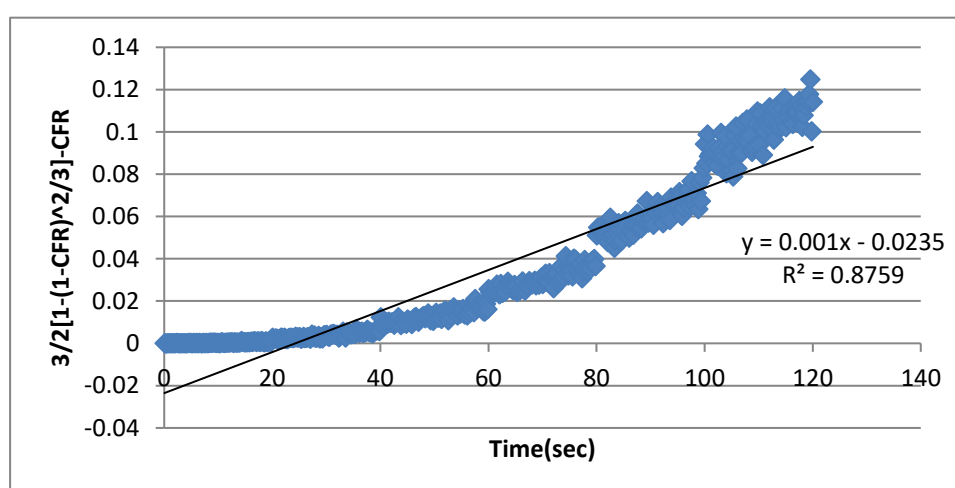
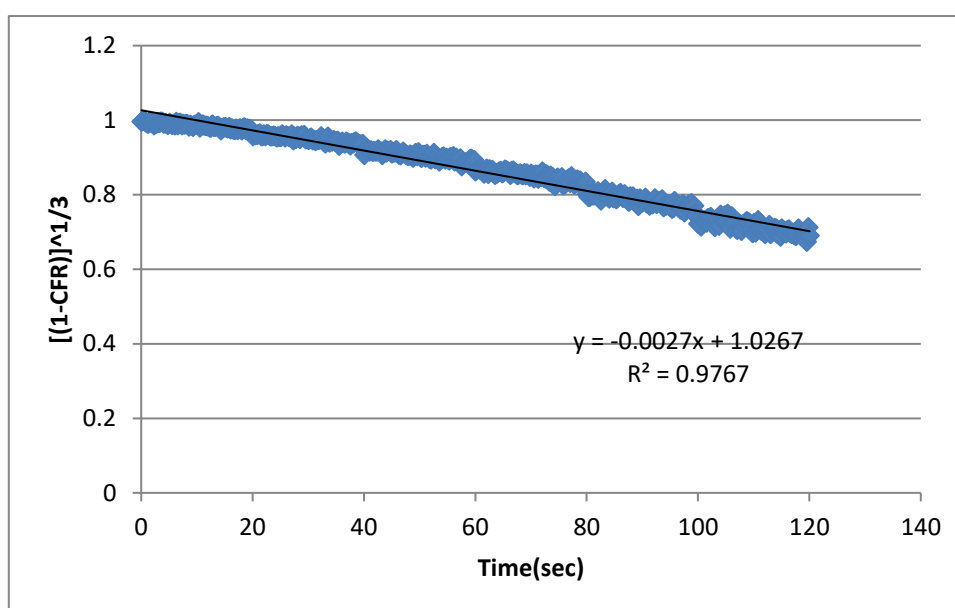
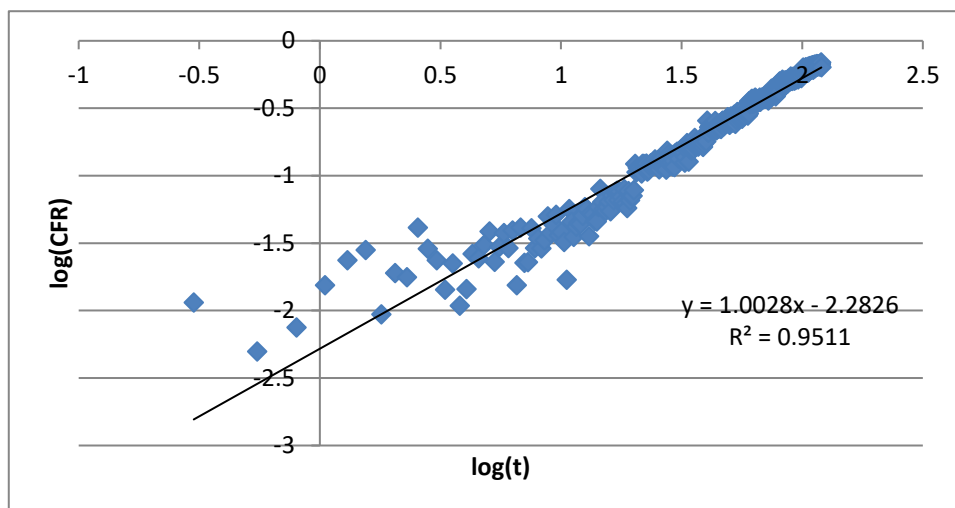


Figure 69: Korsmeyer-Peppas (top), Hixson-Crowell (middle), and Baker-Lonsdale (bottom) model fitting of DOX release from Tf-targeted liposomes at 7.46 mW/cm² (Batch 2)

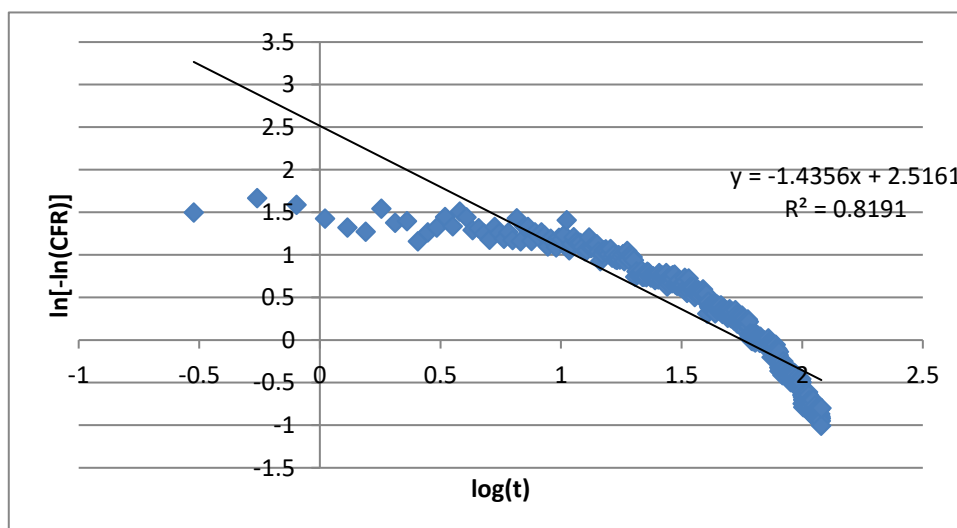
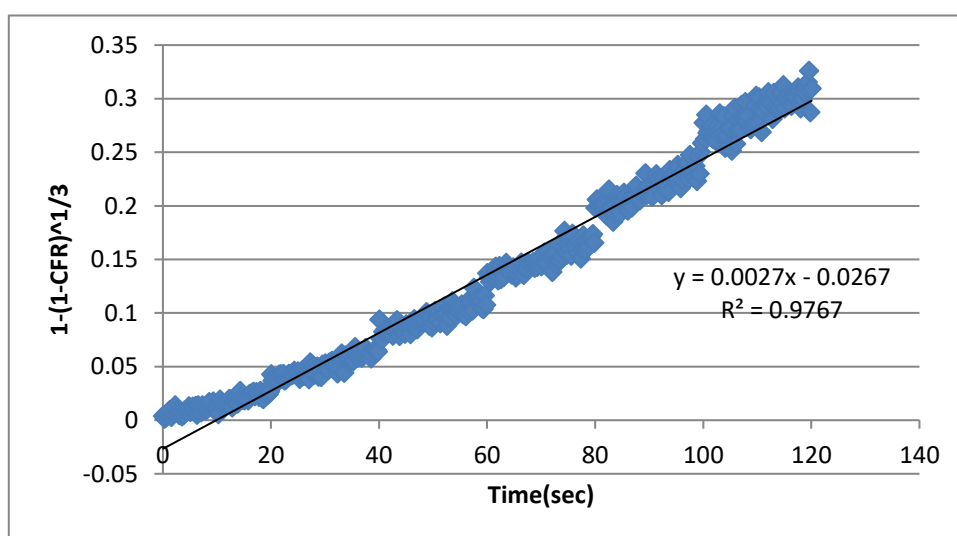
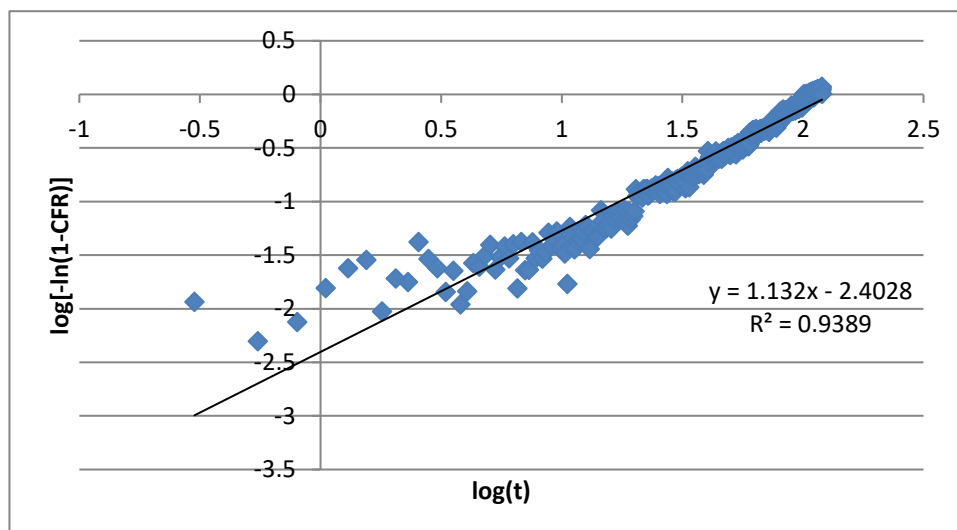


Figure 70: Weibull (top), Hopfenberg (middle), and Gompertz (bottom) model fitting of DOX release from Tf-targeted liposomes at $7.46 \text{ mW}/\text{cm}^2$ (Batch 2)

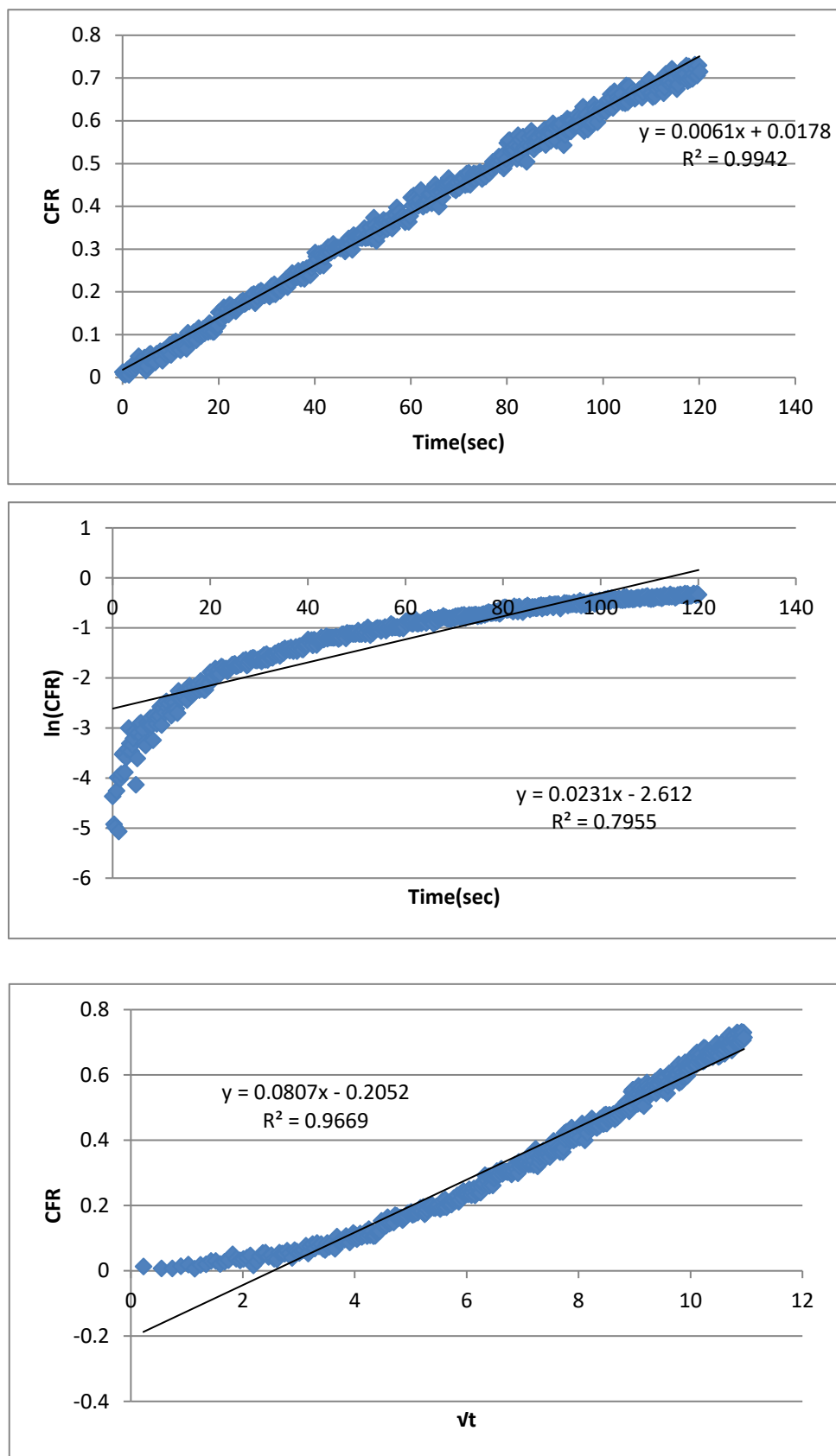


Figure 71: Zero-order (top), First-order (middle), and Higuchi (bottom) model fitting of DOX release from Tf-targeted liposomes at 7.46 mW/cm² (Batch 3)

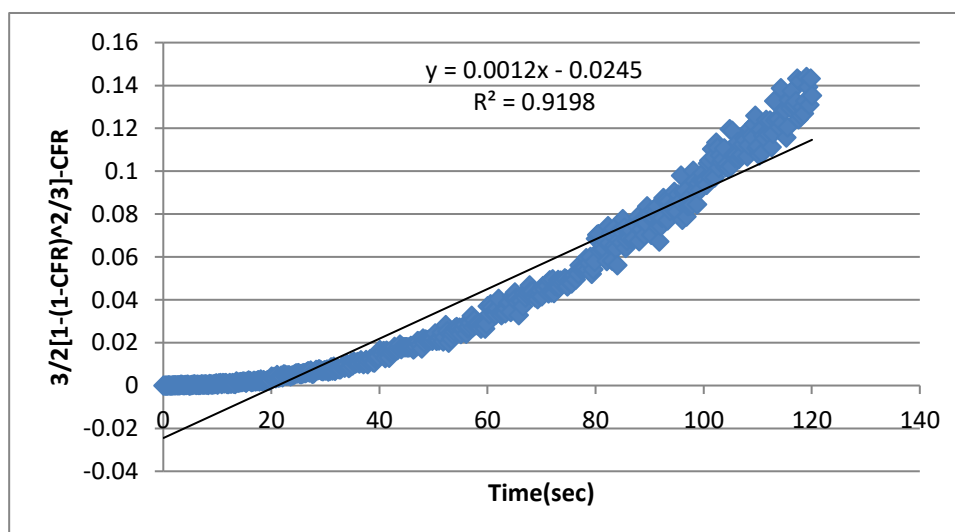
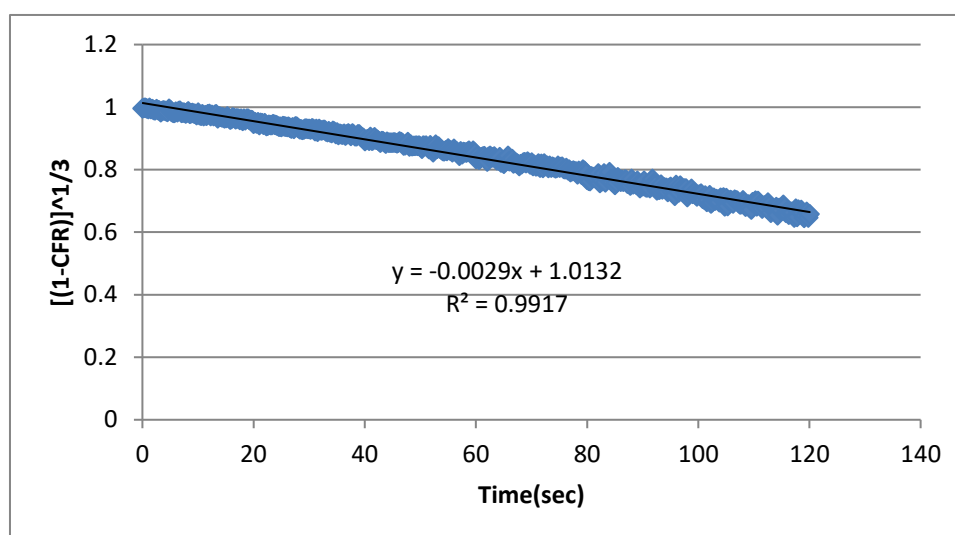
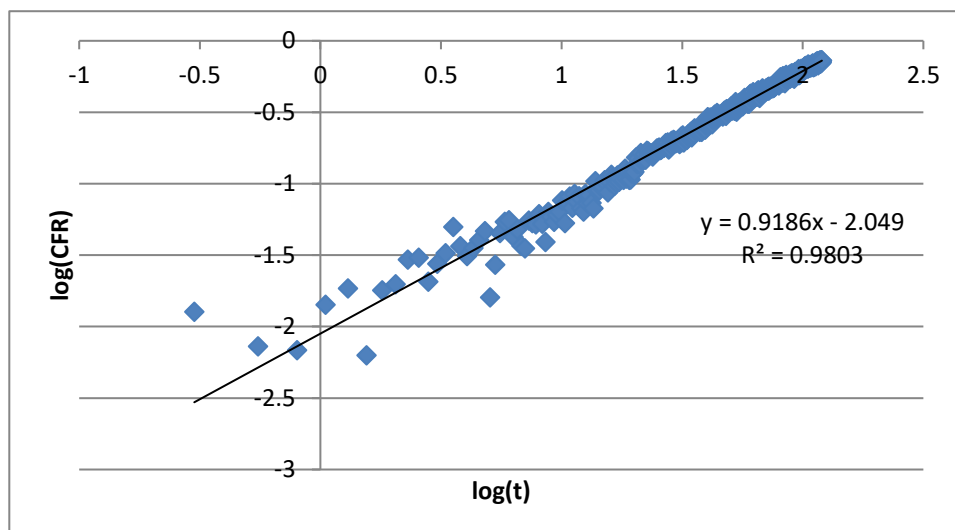


Figure 72: Korsmeyer-Peppas (top), Hixson-Crowell (middle), and Baker-Lonsdale (bottom) model fitting of DOX release from Tf-targeted liposomes at 7.46 mW/cm² (Batch 3)

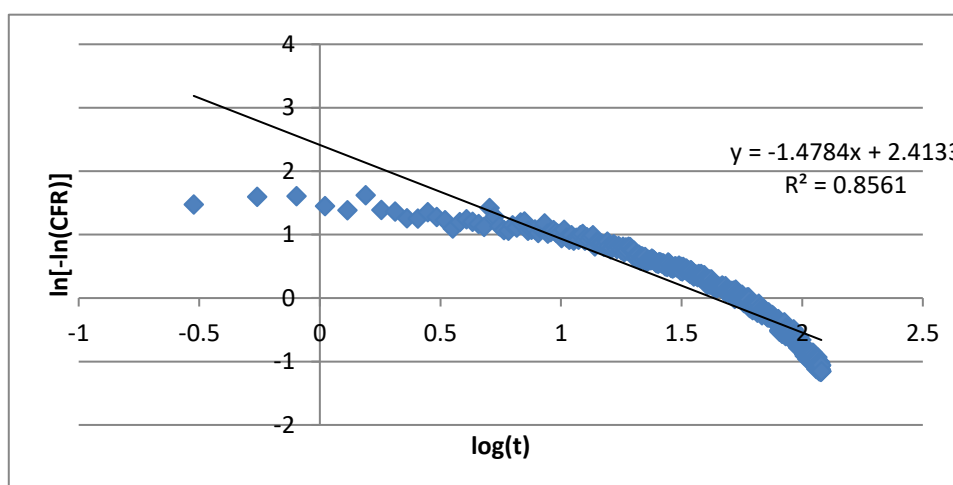
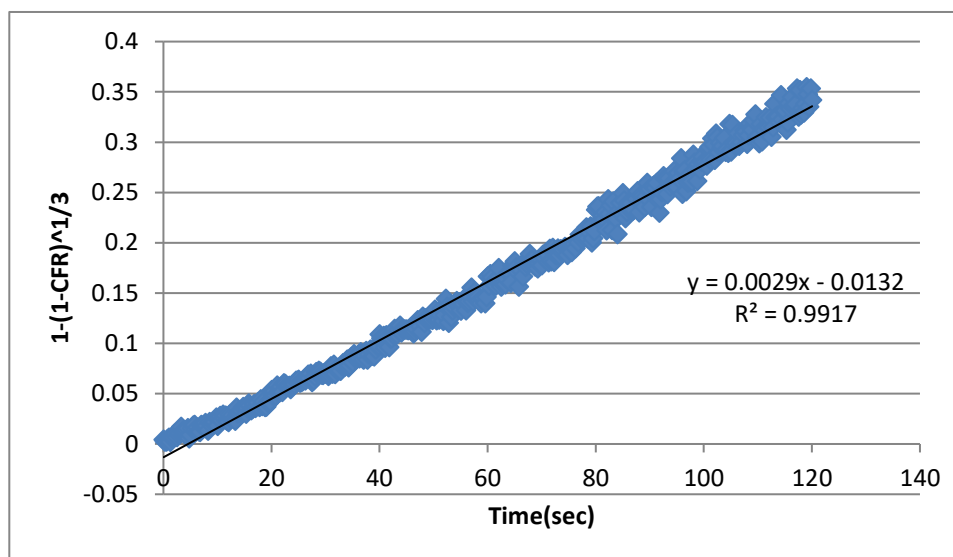
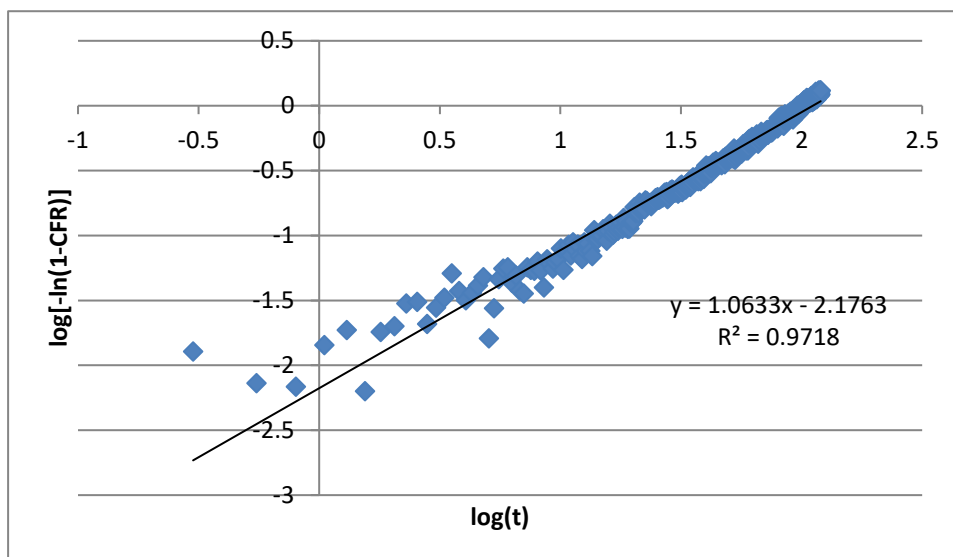


Figure 73: Weibull (top), Hopfenberg (middle), and Gompertz (bottom) model fitting of DOX release from Tf-targeted liposomes at 7.46 mW/cm² (Batch 3)

Appendix E: Plots of Kinetic Models of Tf-Liposomes at 9.85 mW/cm²

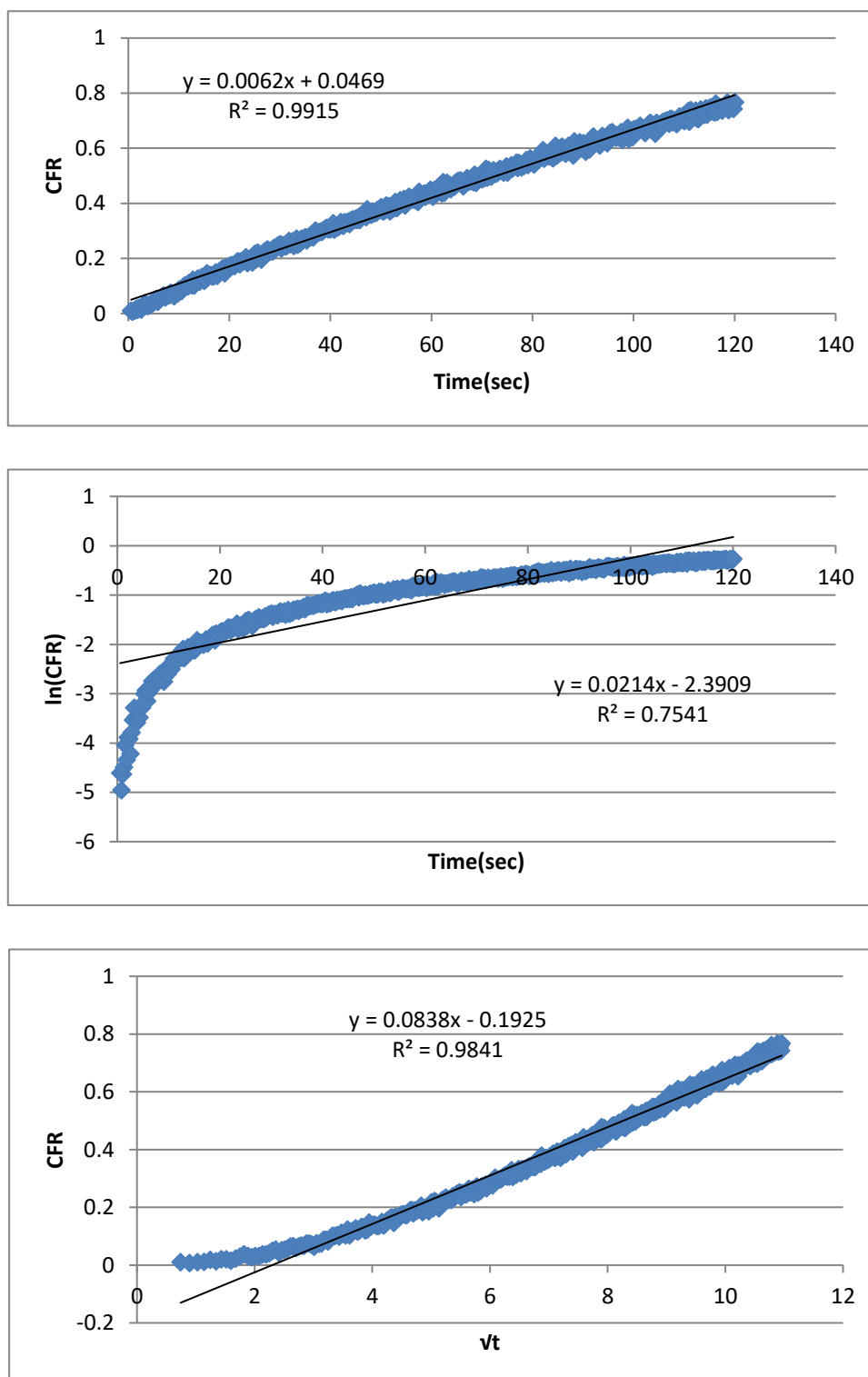


Figure 74: Zero-order (top), First-order (middle), and Higuchi (bottom) model fitting of DOX release from Tf-targeted liposomes at 9.85 mW/cm² (Batch 1)

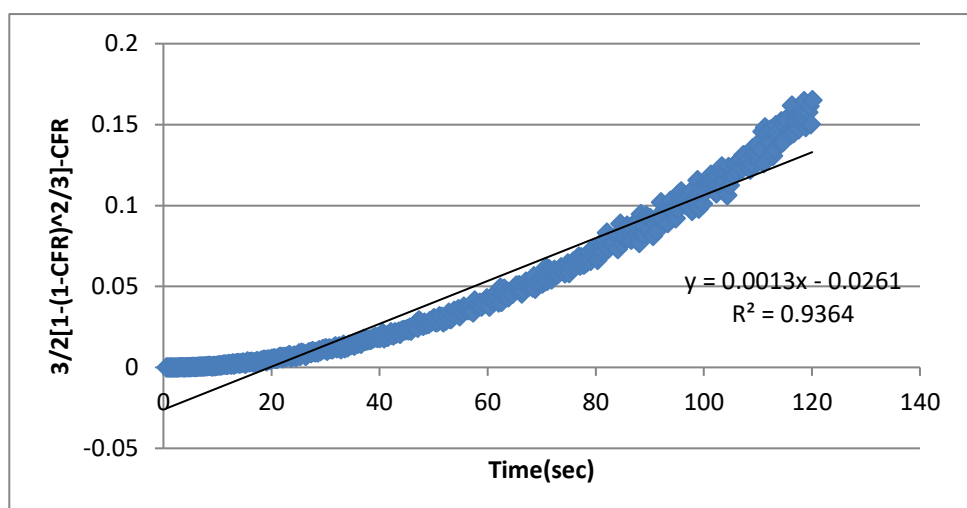
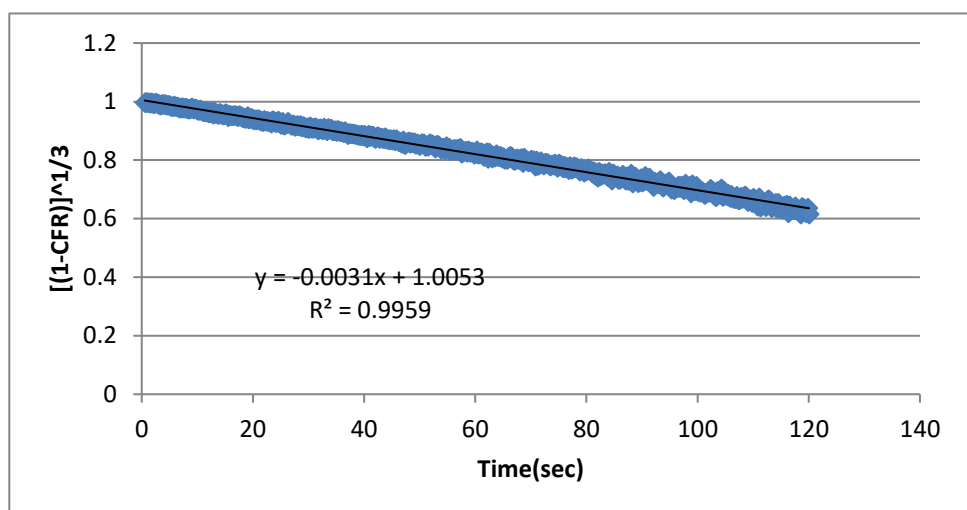
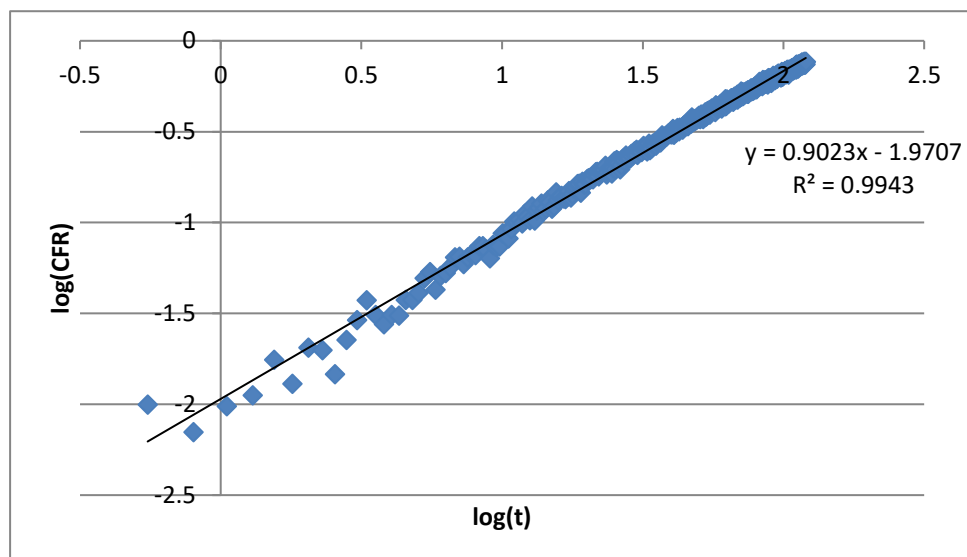


Figure 75: Korsmeyer-Peppas (top), Hixson-Crowell (middle), and Baker-Lonsdale (bottom) model fitting of DOX release from Tf-targeted liposomes at 9.85 mW/cm² (Batch 1)

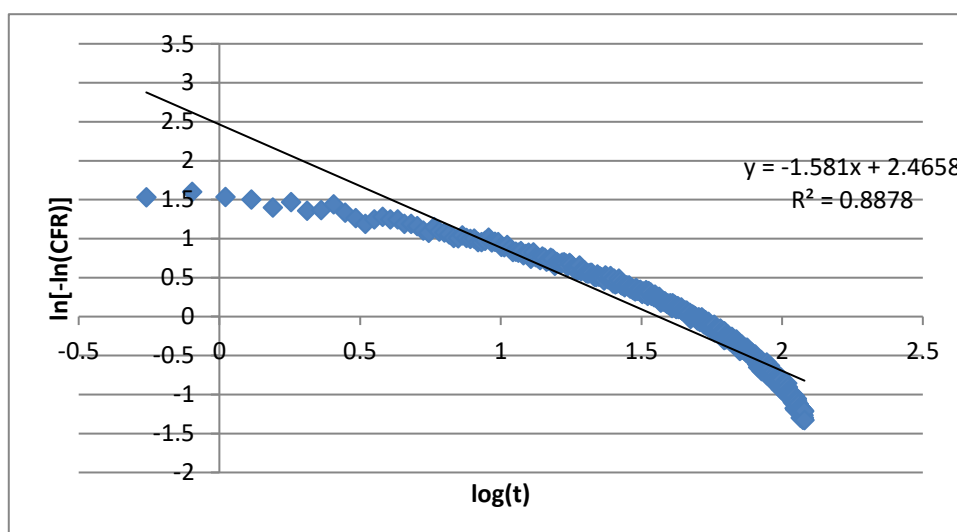
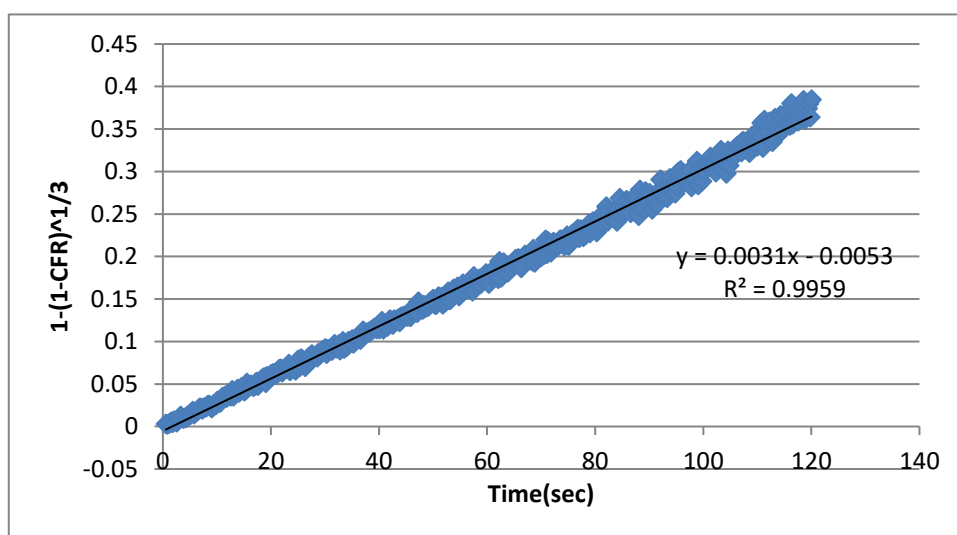
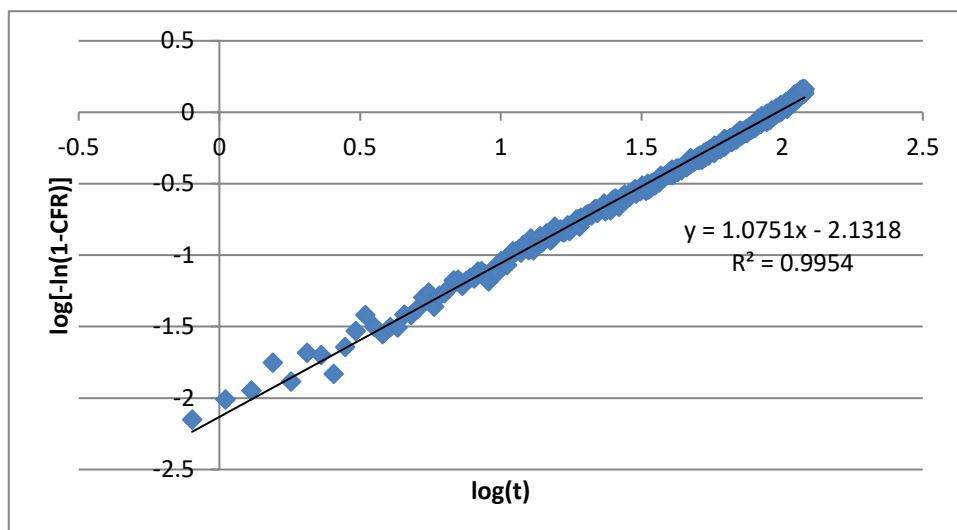


Figure 76: Weibull (top), Hopfenberg (middle), and Gompertz (bottom) model fitting of DOX release from Tf-targeted liposomes at 9.85 mW/cm² (Batch 1)

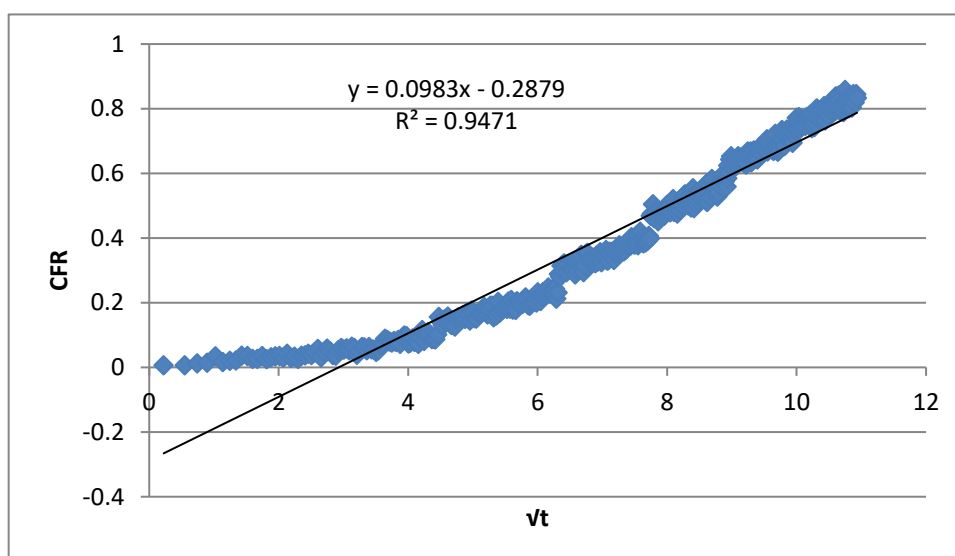
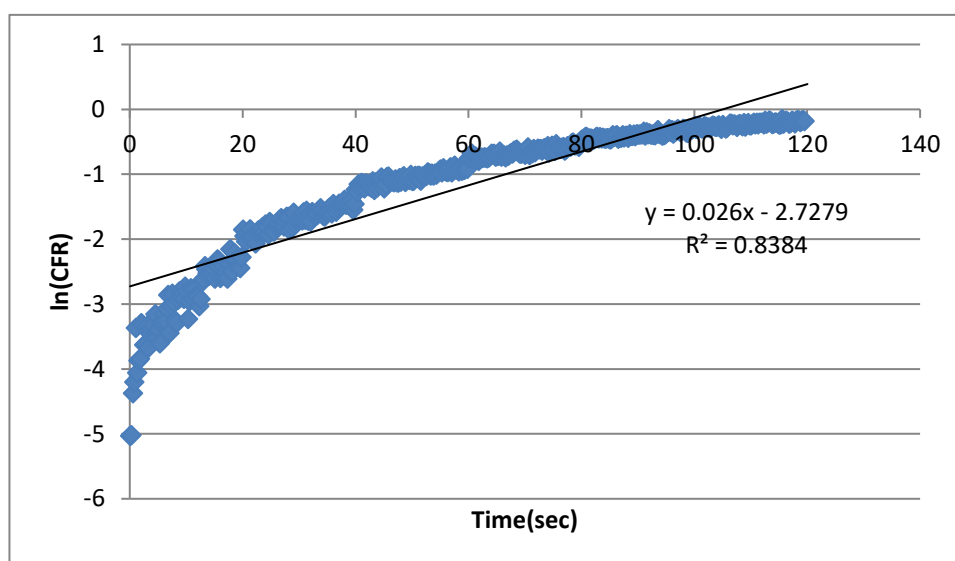
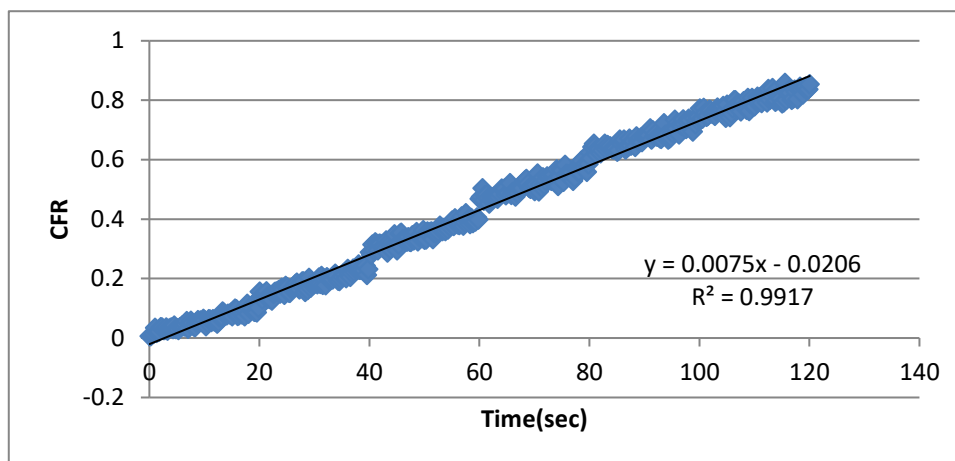


Figure 77: Zero-order (top), First-order (middle), and Higuchi (bottom) model fitting of DOX release from Tf-targeted liposomes at 9.85 mW/cm² (Batch 2)

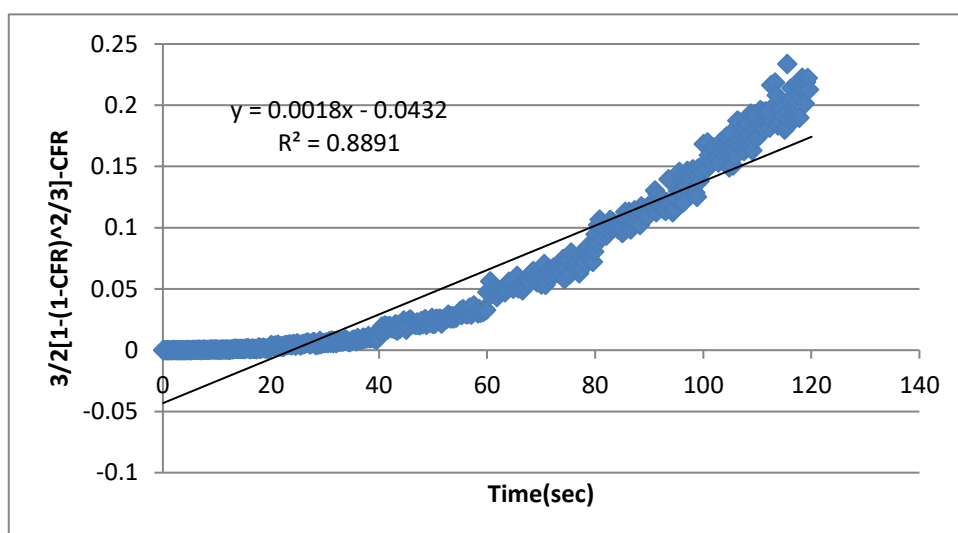
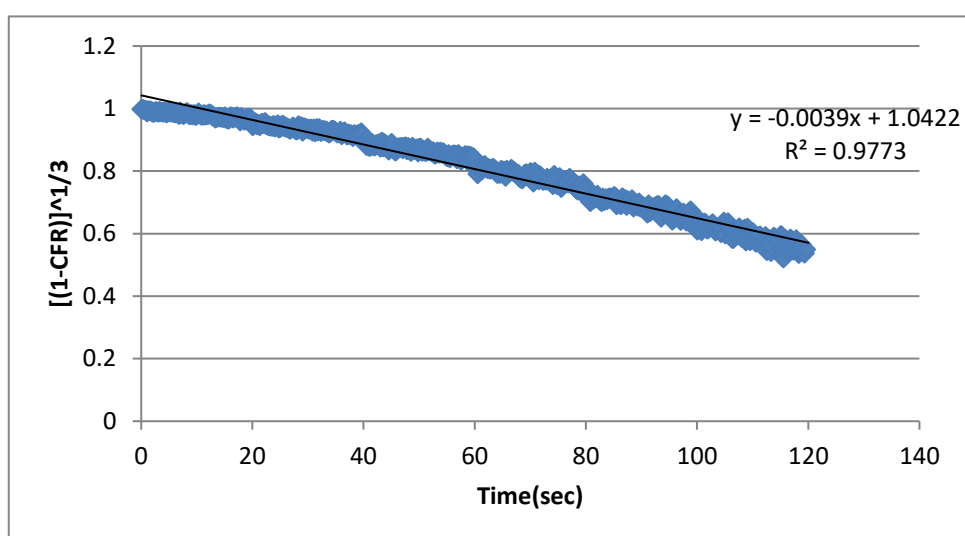
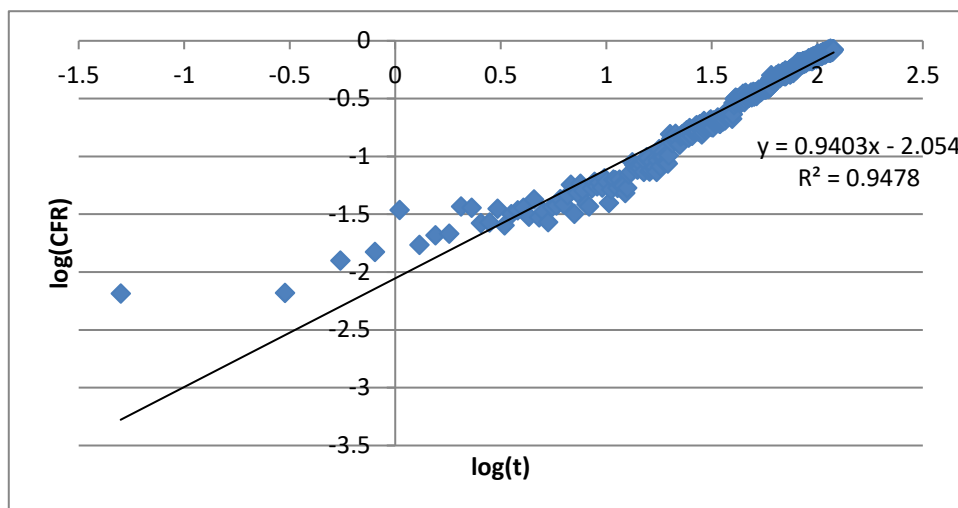


Figure 78: Korsmeyer-Peppas (top), Hixson-Crowell (middle), and Baker-Lonsdale (bottom) model fitting of DOX release from Tf-targeted liposomes at 9.85 mW/cm^2 (Batch 2)

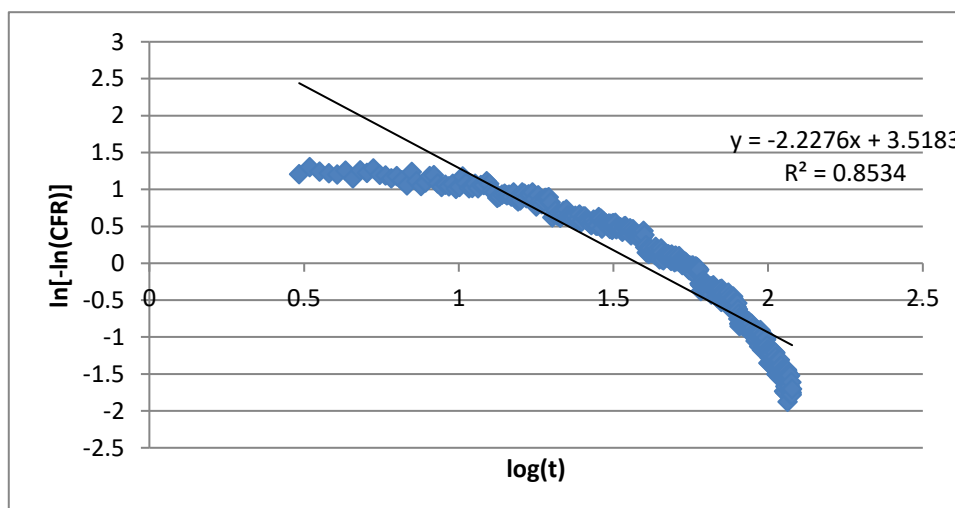
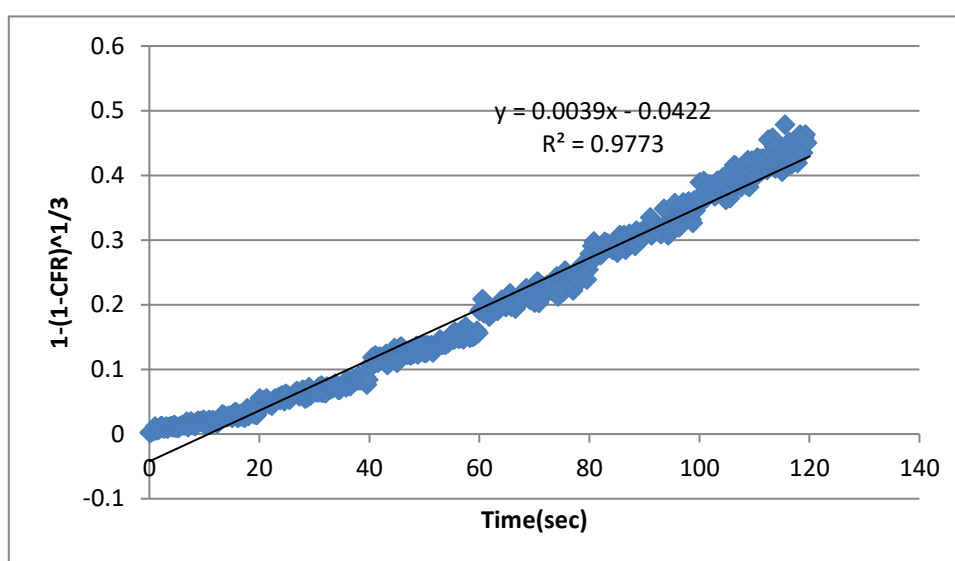
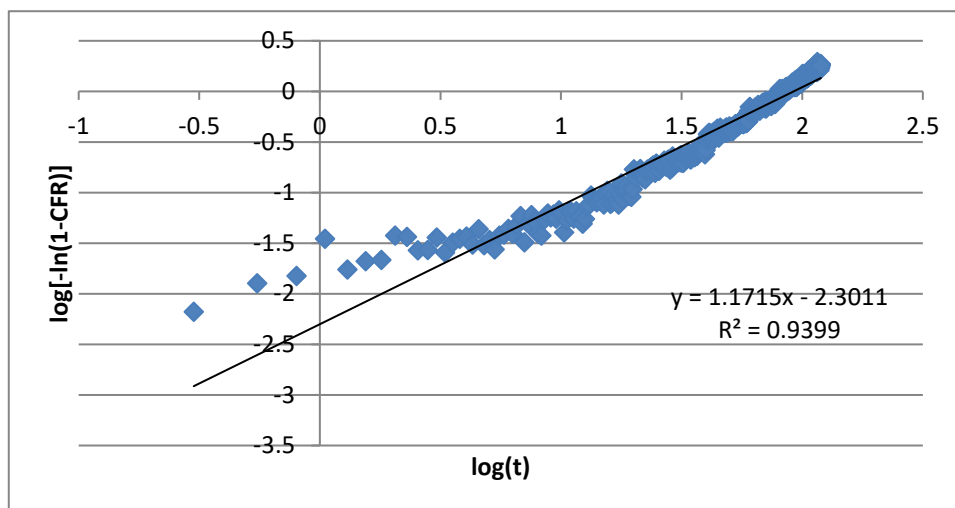


Figure 79: Weibull (top), Hopfenberg (middle), and Gompertz (bottom) model fitting of DOX release from Tf-targeted liposomes at 9.85 mW/cm² (Batch 2)

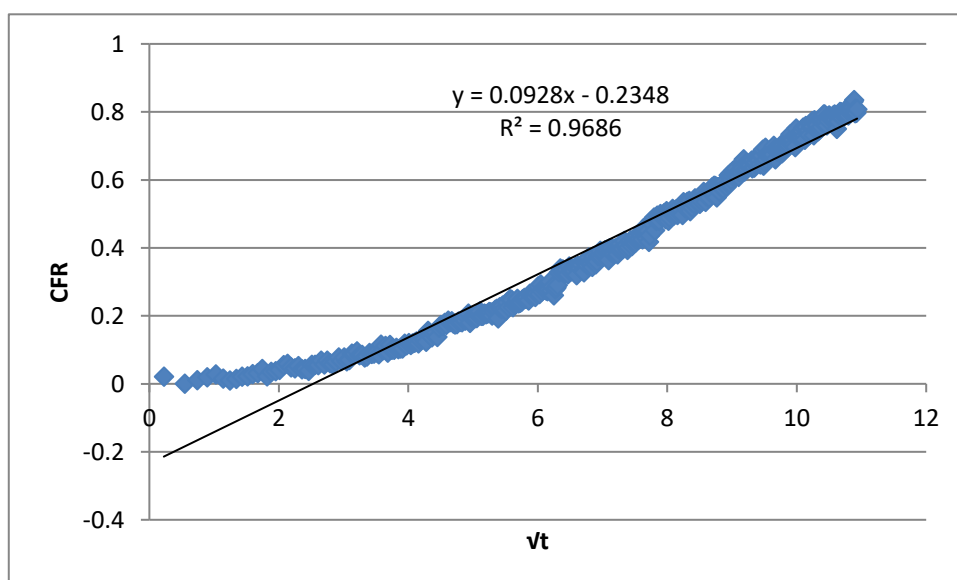
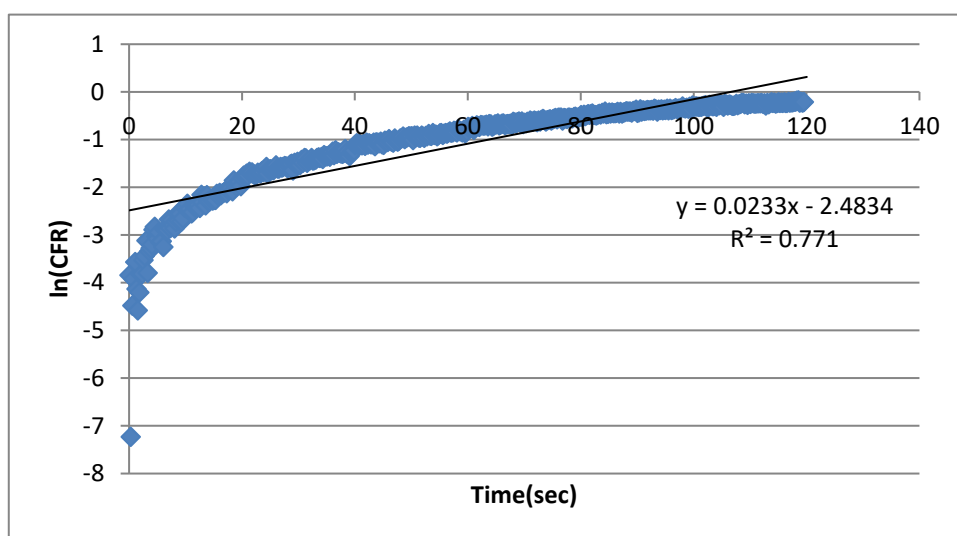
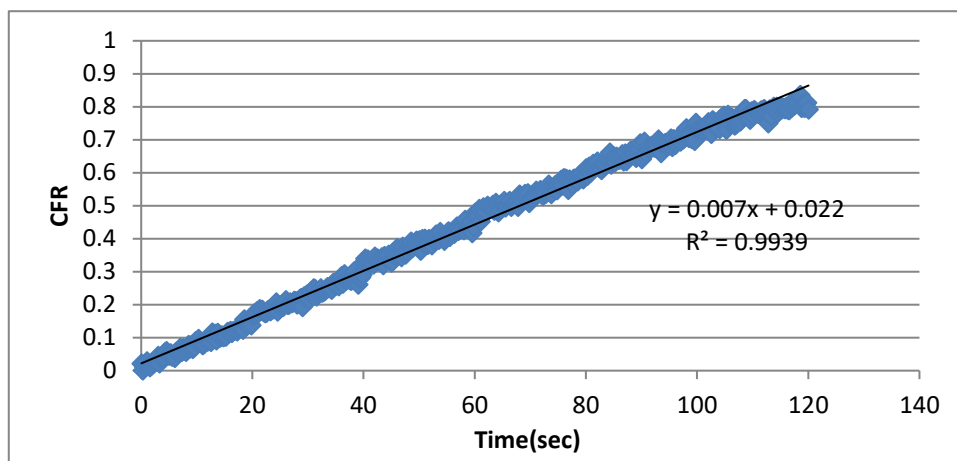


Figure 80: Zero-order (top), First-order (middle), and Higuchi (bottom) model fitting of DOX release from Tf-targeted liposomes at 9.85 mW/cm² (Batch 3)

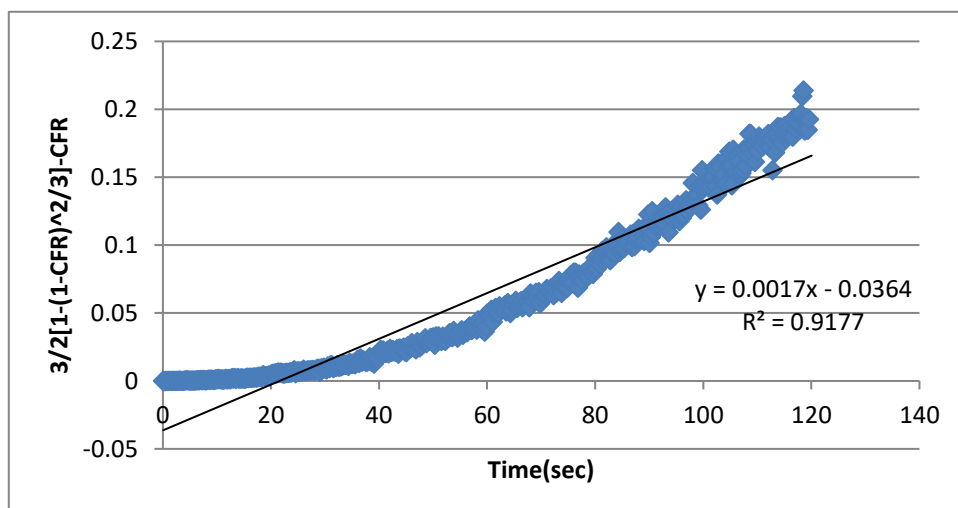
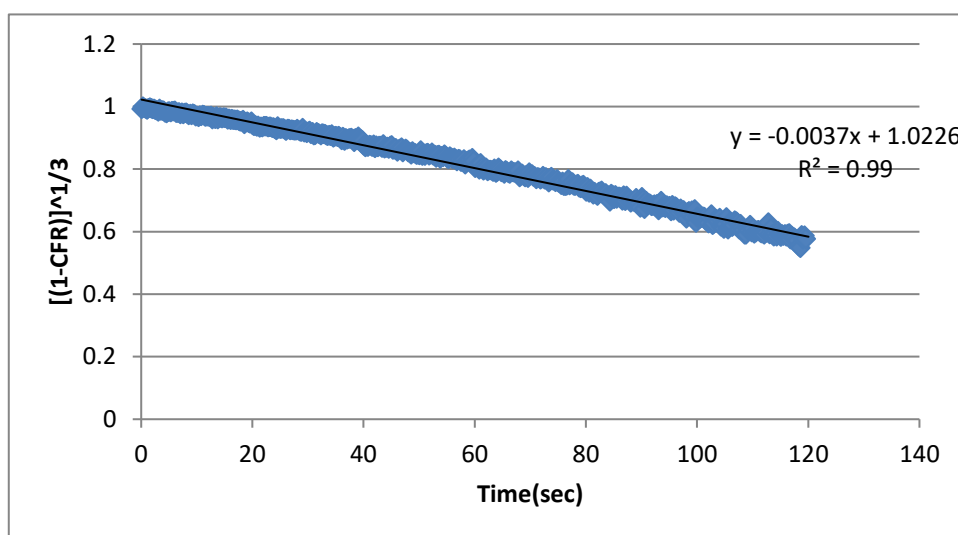
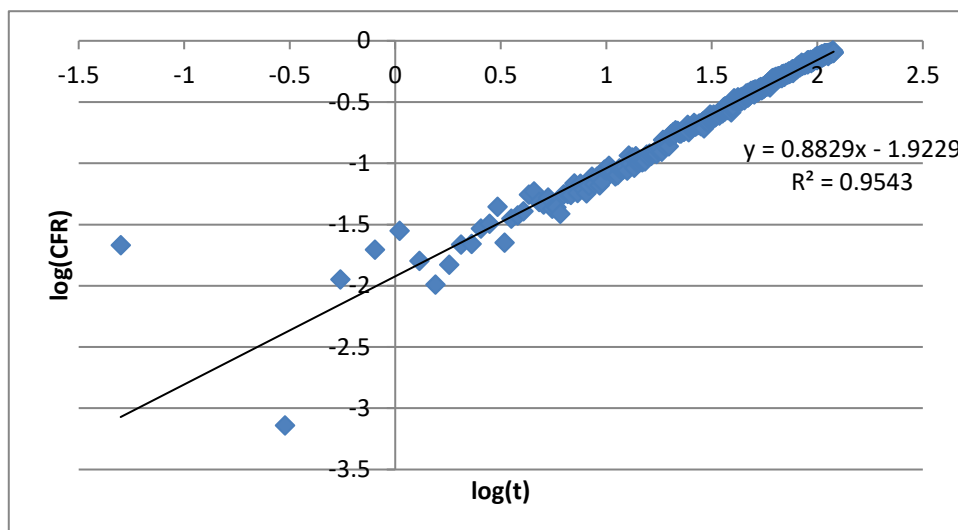


Figure 81: Korsmeyer-Peppas (top), Hixson-Crowell (middle), and Baker-Lonsdale (bottom) model fitting of DOX release from Tf-targeted liposomes at 9.85 mW/cm² (Batch 3)

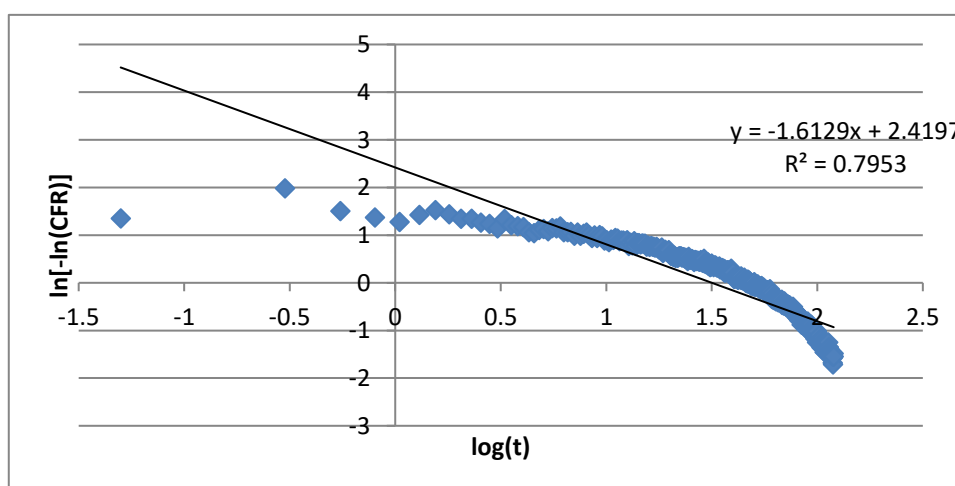
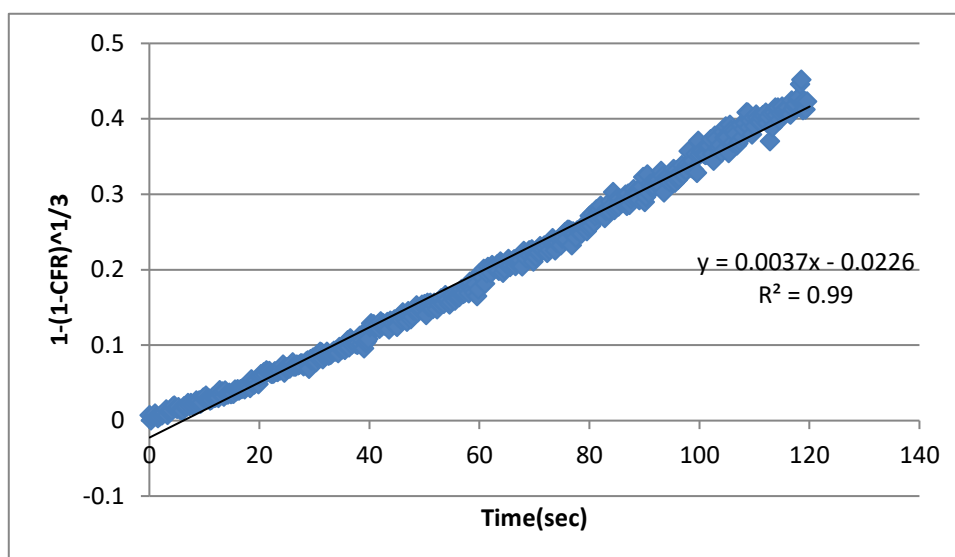
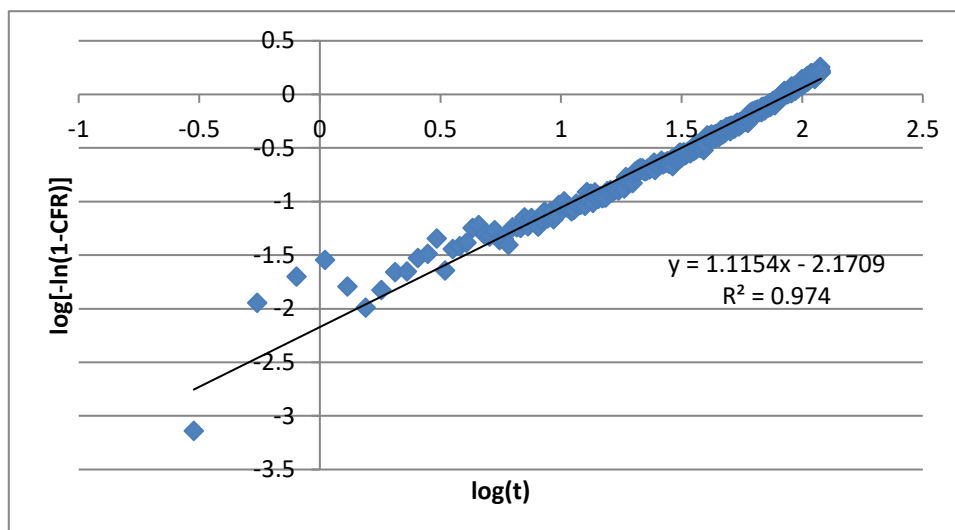


Figure 82: Weibull (top), Hopfenberg (middle), and Gompertz (bottom) model fitting of DOX release from Tf-targeted liposomes at 9.85 mW/cm² (Batch 3)

Appendix F: Plots of Kinetic Models of Tf-Liposomes at 17.31 mW/cm²

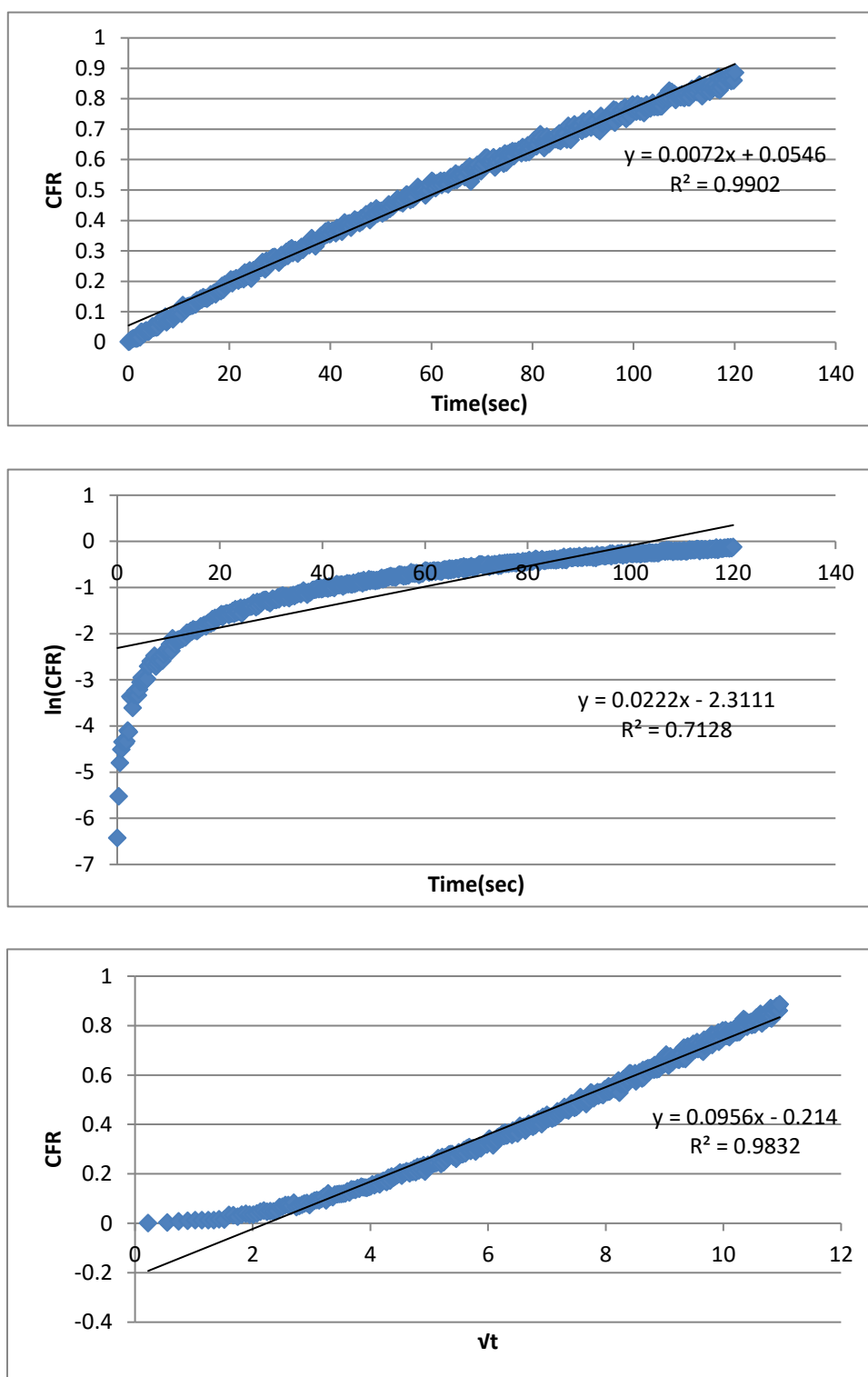


Figure 83: Zero-order (top), First-order (middle), and Higuchi (bottom) model fitting of DOX release from Tf-targeted liposomes at 17.31 mW/cm² (Batch 1)

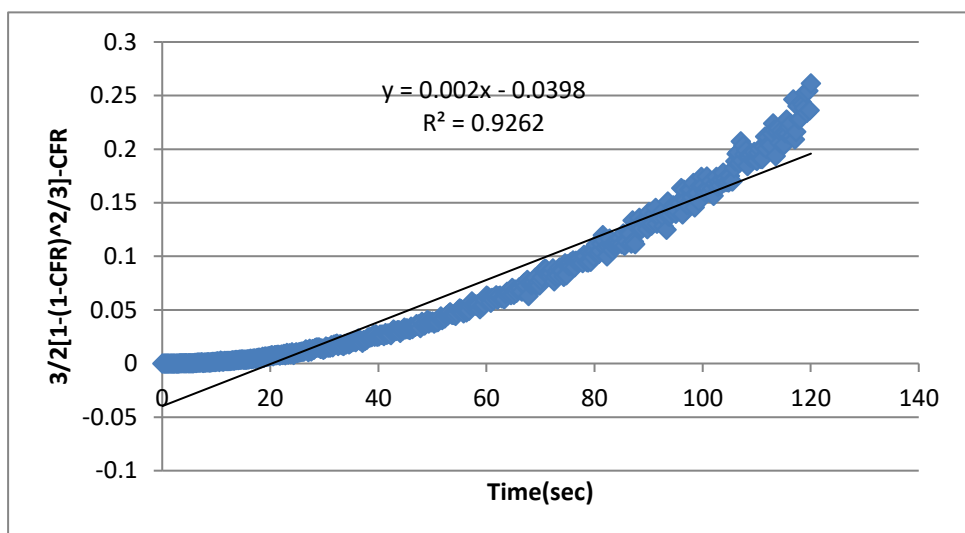
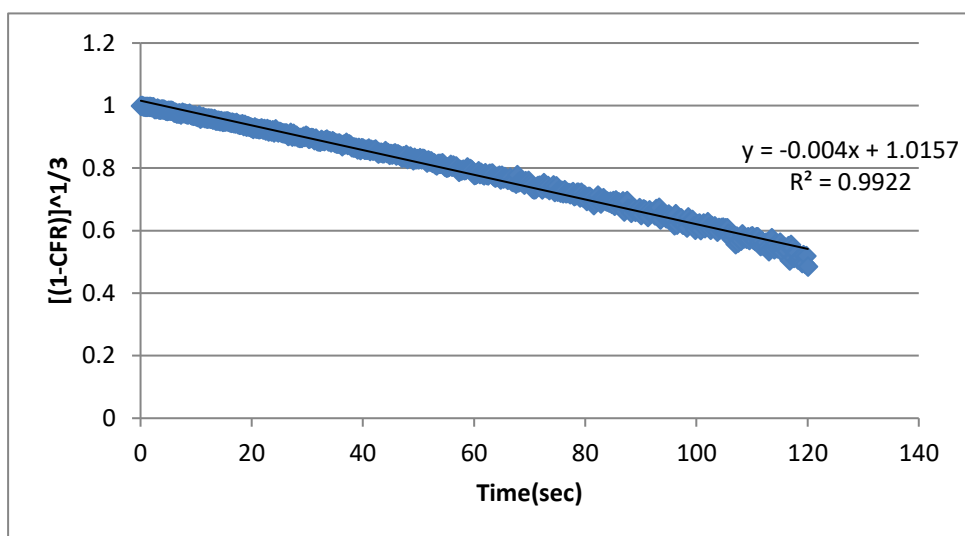
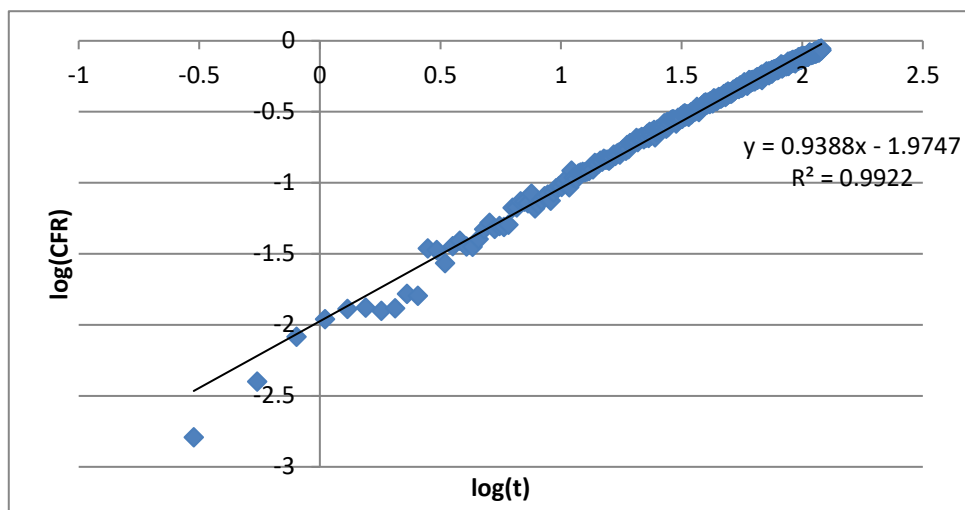


Figure 84: Korsmeyer-Peppas (top), Hixson-Crowell (middle), and Baker-Lonsdale (bottom) model fitting of DOX release from Tf-targeted liposomes at 17.31 mW/cm² (Batch 1)

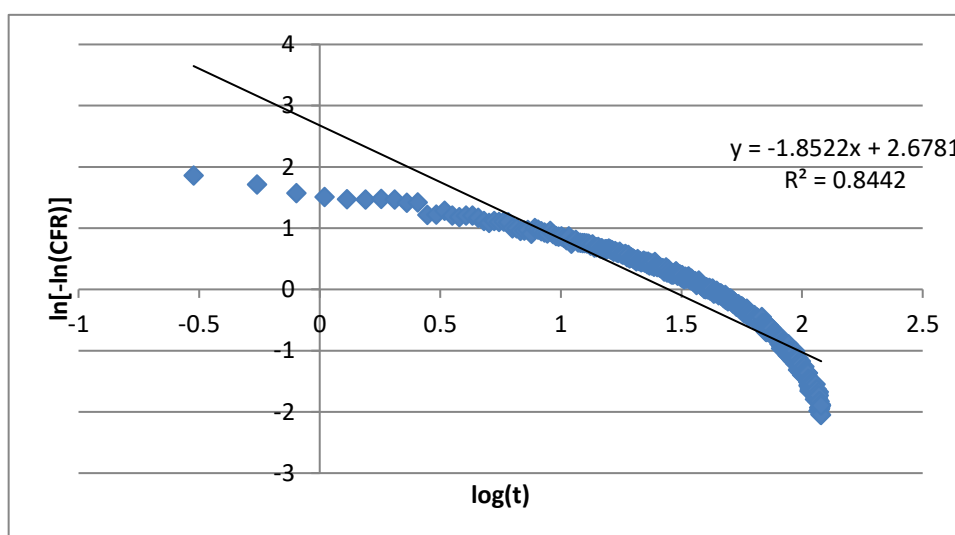
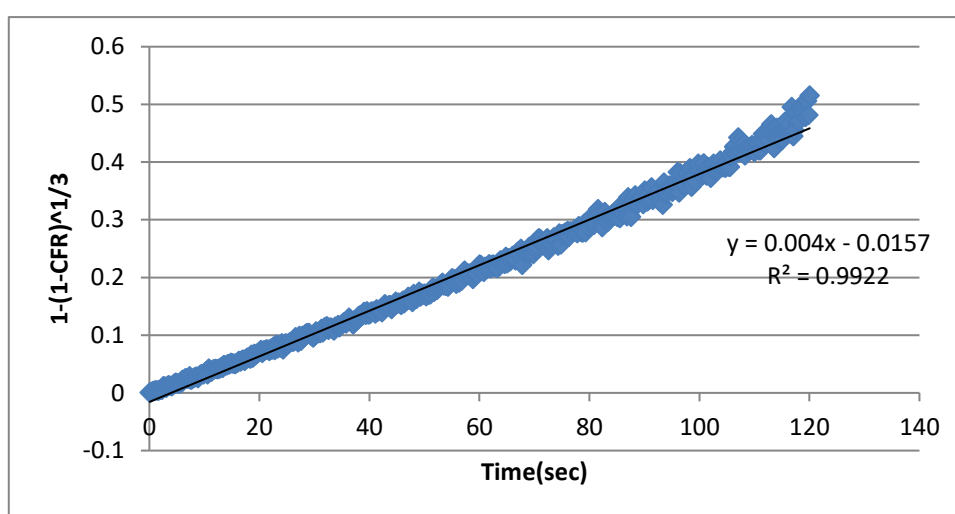
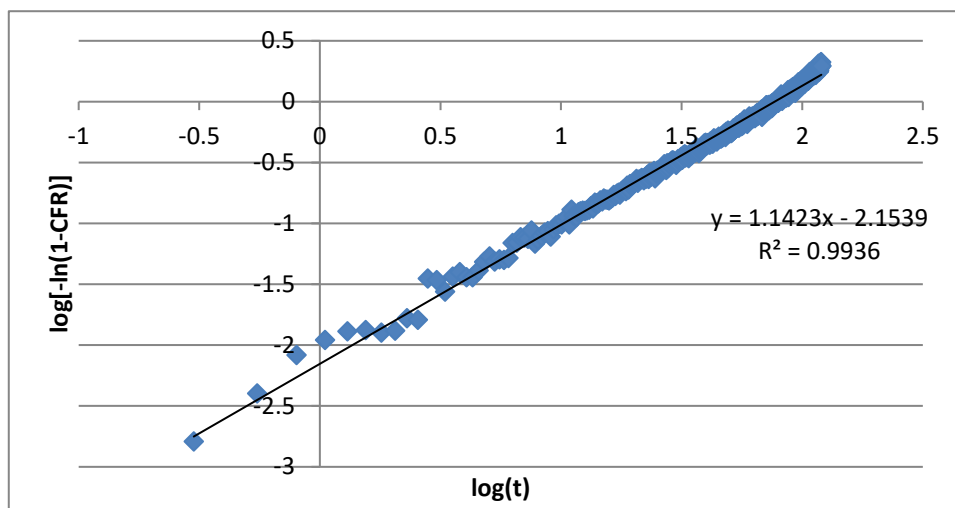


Figure 85: Weibull (top), Hopfenberg (middle), and Gompertz (bottom) model fitting of DOX release from Tf-targeted liposomes at 17.31 mW/cm² (Batch 1)

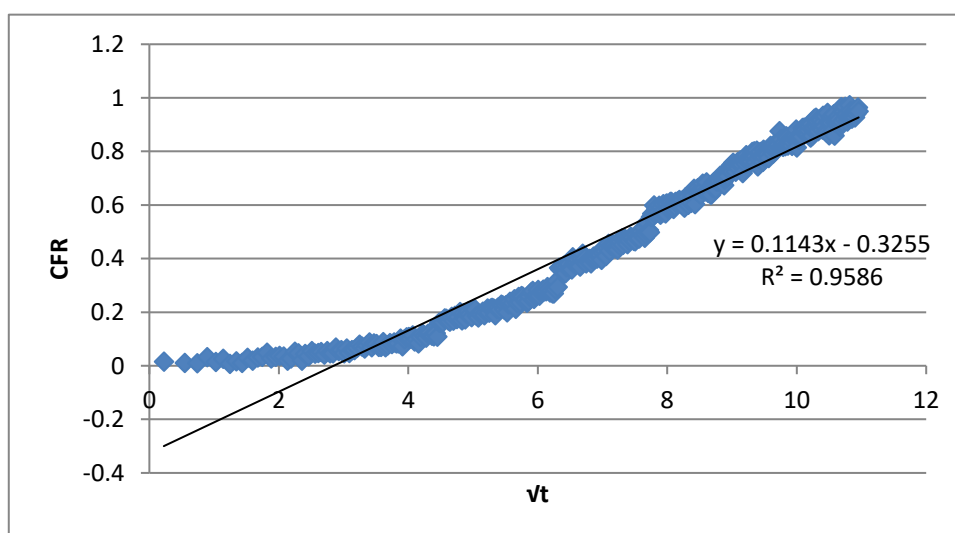
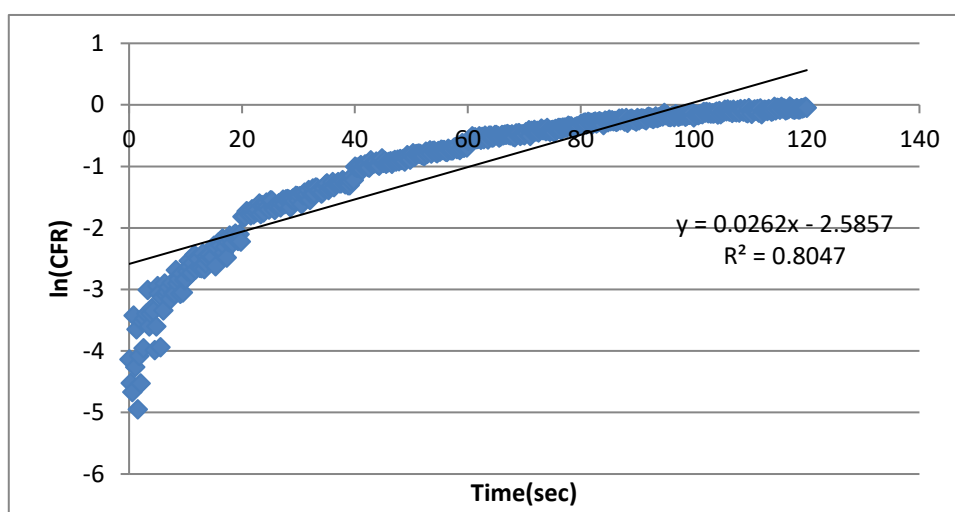
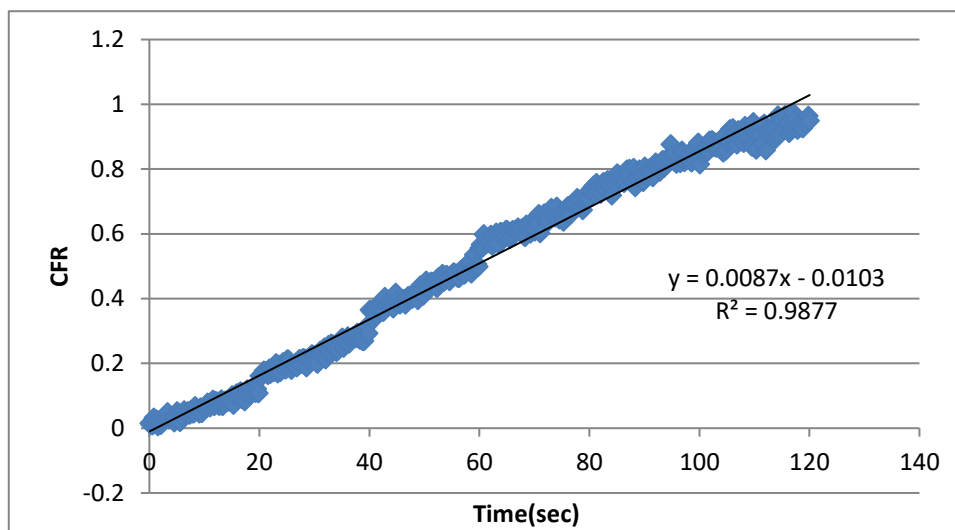


Figure 86: Zero-order (top), First-order (middle), and Higuchi (bottom) model fitting of DOX release from Tf-targeted liposomes at 17.31 mW/cm² (Batch 2)

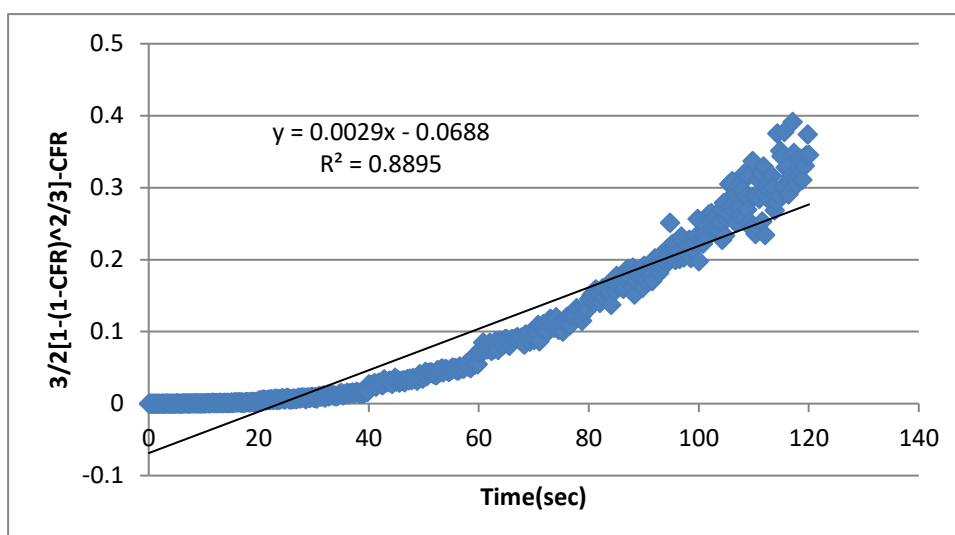
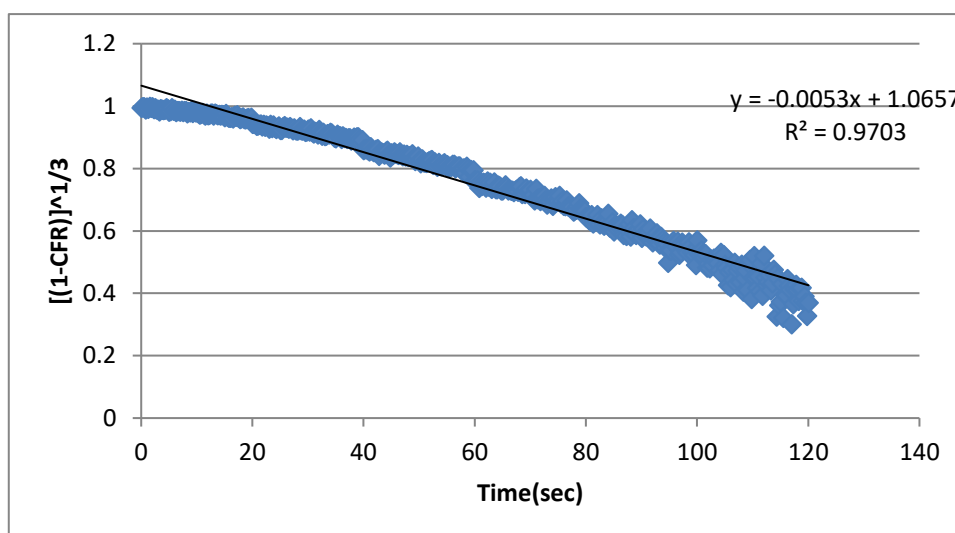
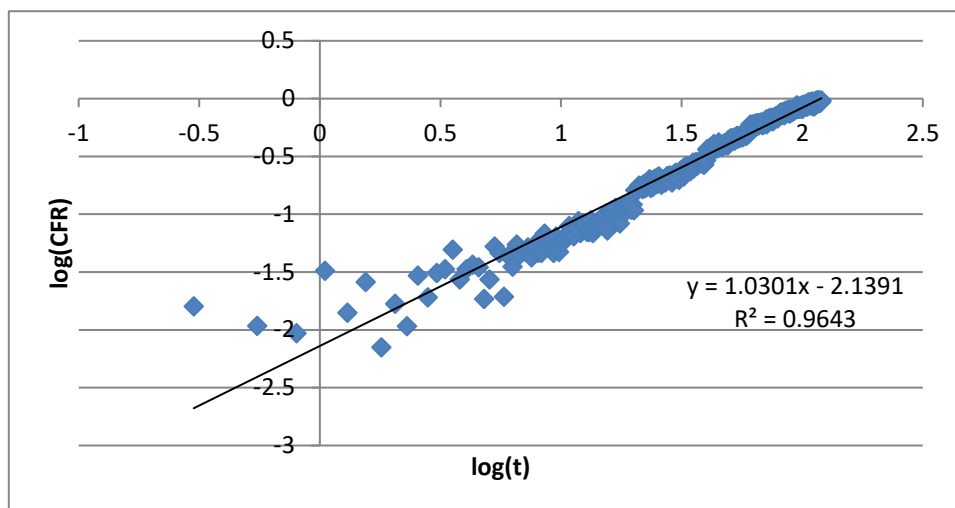


Figure 87: Korsmeyer-Peppas (top), Hixson-Crowell (middle), and Baker-Lonsdale (bottom) model fitting of DOX release from Tf-targeted liposomes at 17.31 mW/cm² (Batch 2)

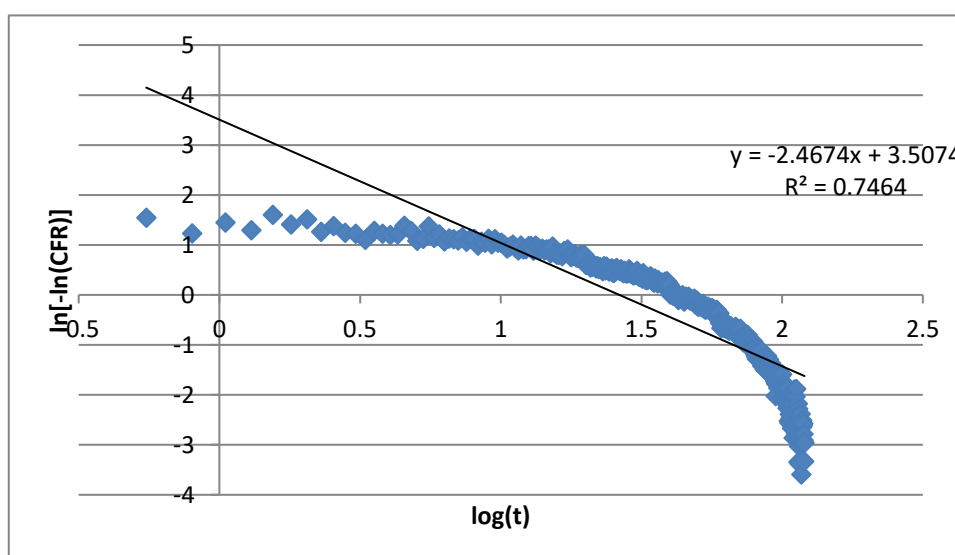
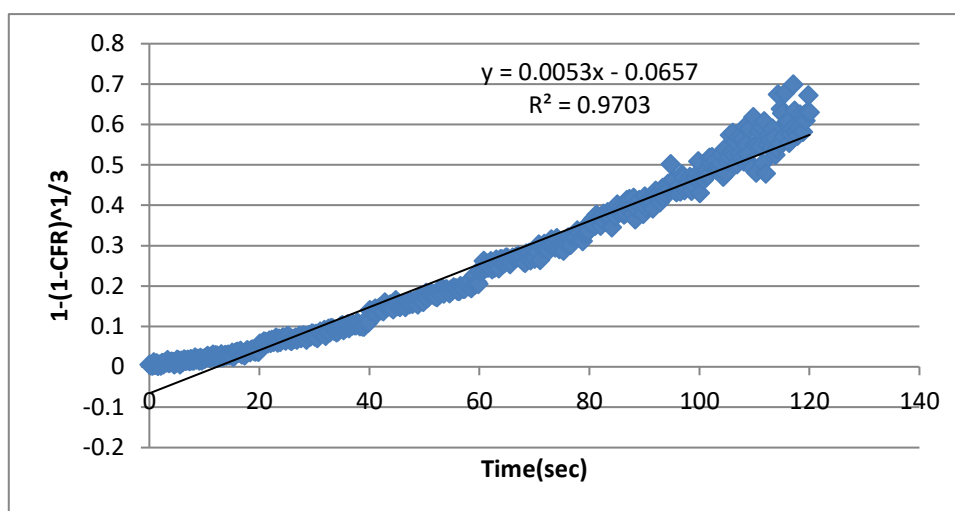
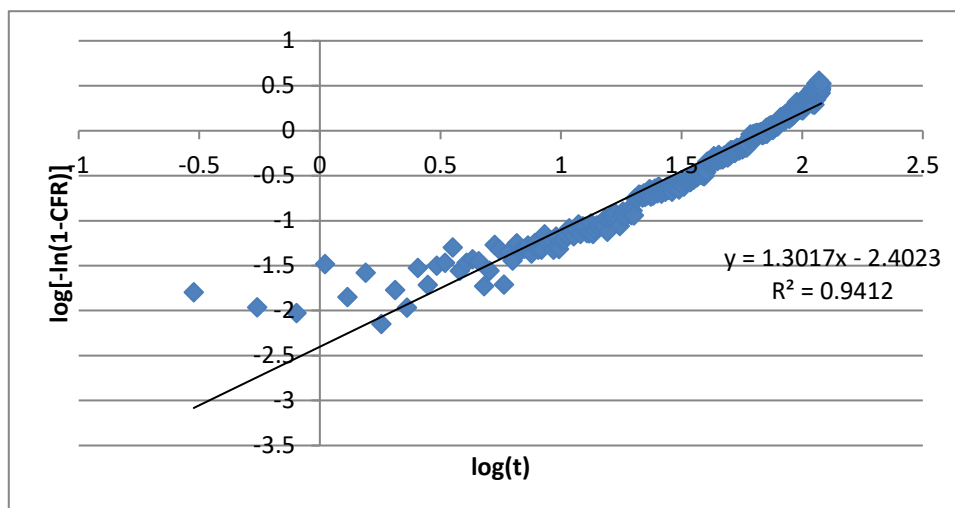


Figure 88: Weibull (top), Hopfenberg (middle), and Gompertz (bottom) model fitting of DOX release from Tf-targeted liposomes at 17.31 mW/cm² (Batch 2)

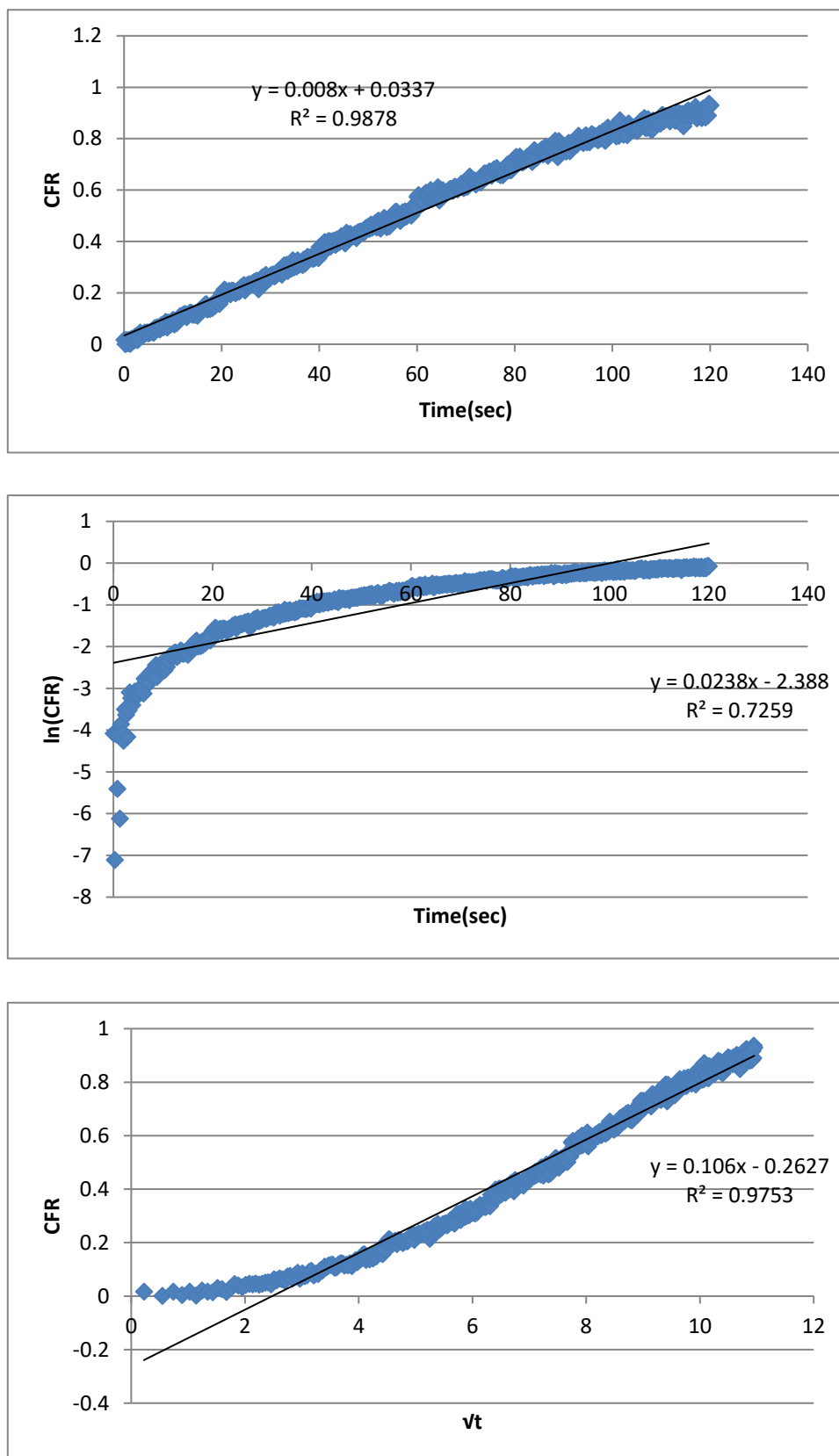


Figure 89: Zero-order (top), First-order (middle), and Higuchi (bottom) model fitting of DOX release from Tf-targeted liposomes at 17.31 mW/cm² (Batch 3)

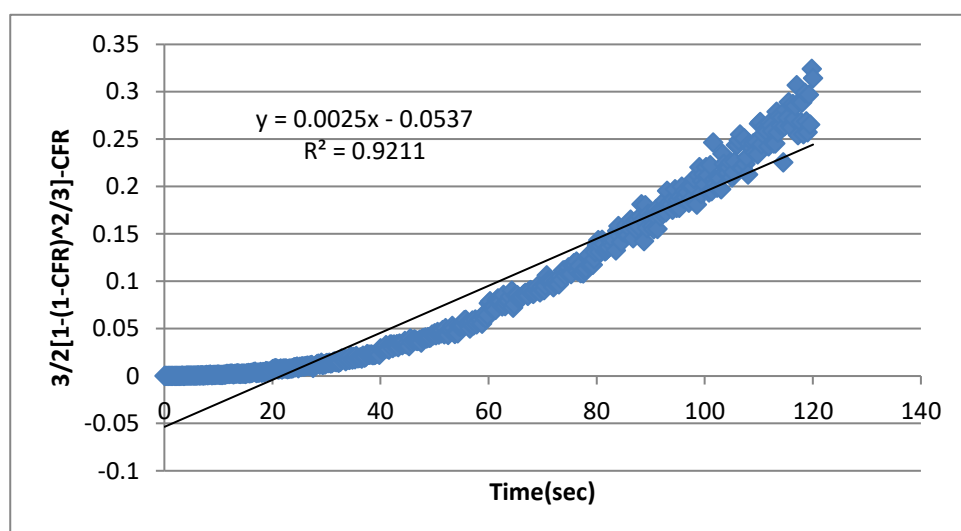
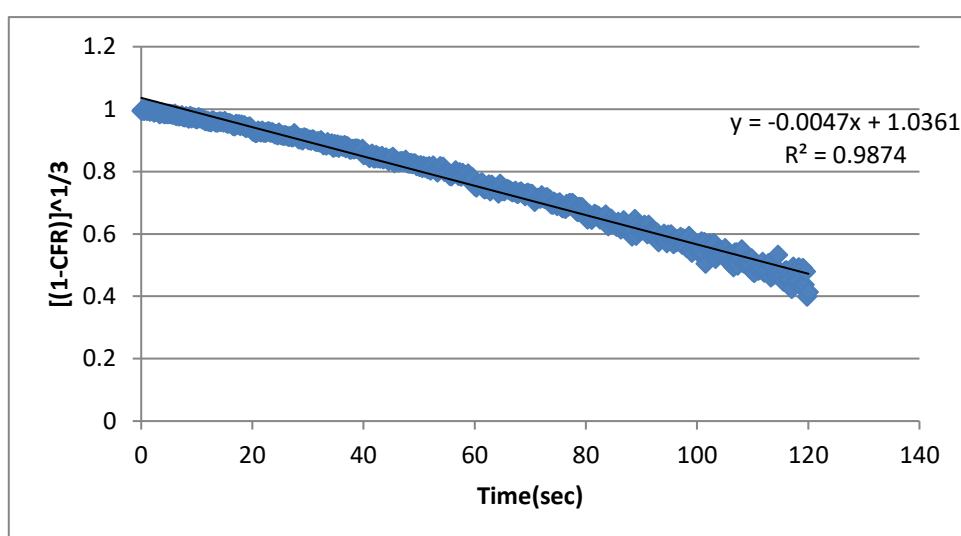
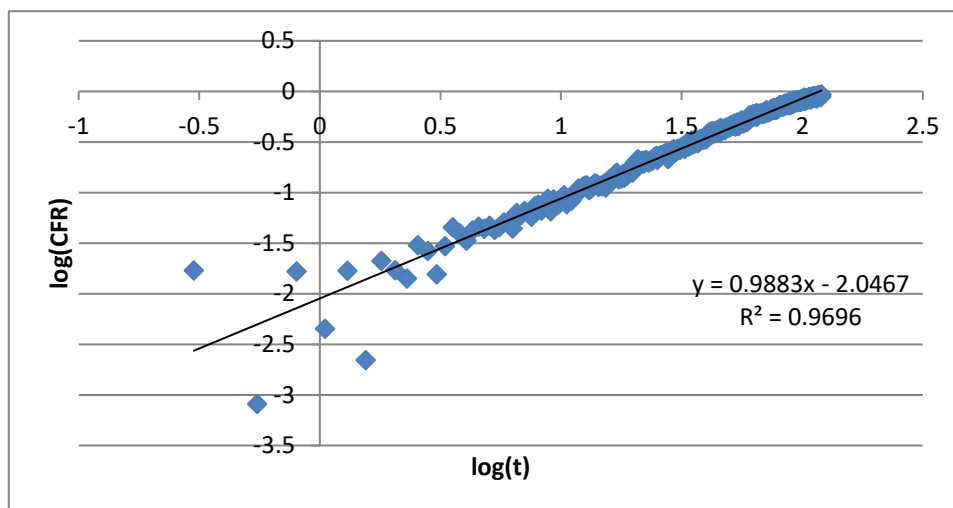


Figure 90: Korsmeyer-Peppas (top), Hixson-Crowell (middle), and Baker-Lonsdale (bottom) model fitting of DOX release from Tf-targeted liposomes at 17.31 mW/cm² (Batch 3)

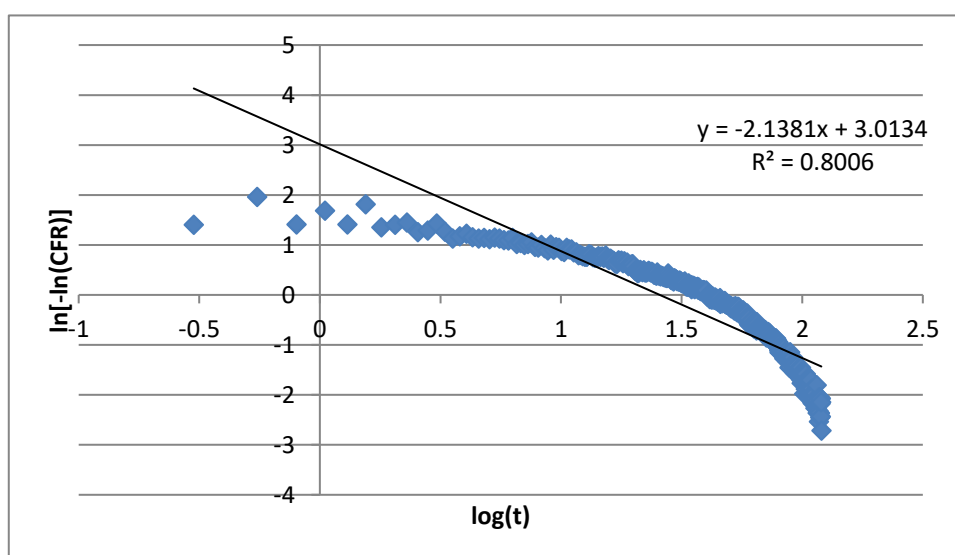
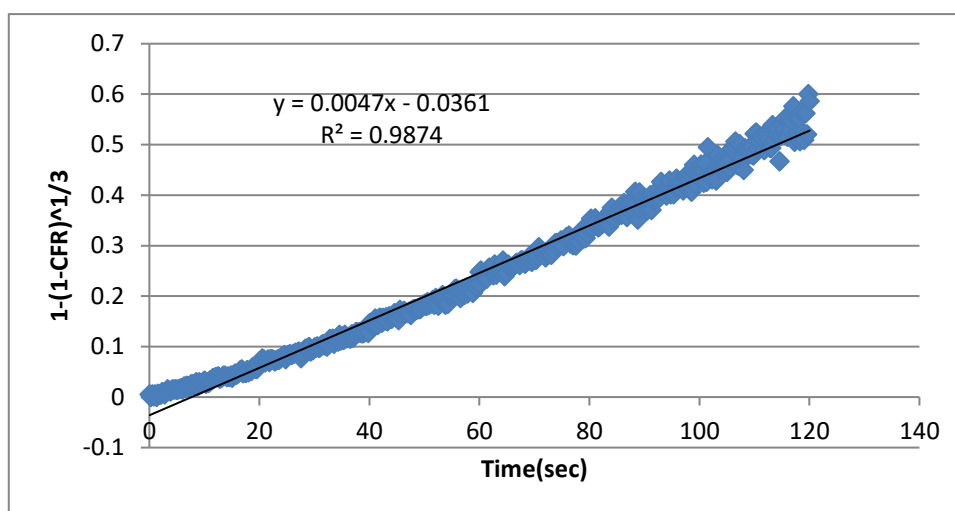
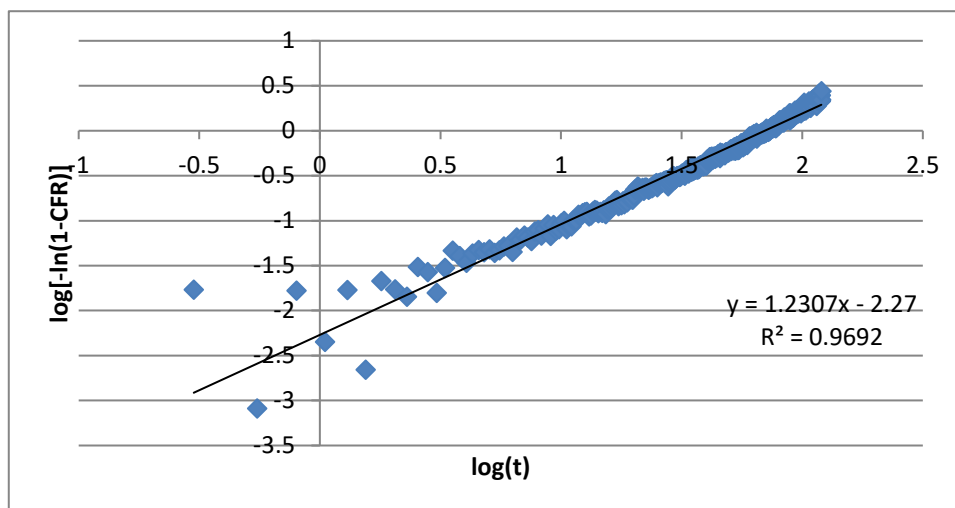


Figure 91: Weibull (top), Hopfenberg (middle), and Gompertz (bottom) model fitting of DOX release from Tf-targeted liposomes at 17.31 mW/cm² (Batch 3)

Vita

Paul Said Kawak was born in Muscat, Sultanate of Oman in the year 1995. He received his elementary education from Rosary School in Sharjah, United Arab Emirates. He received his secondary education from Sharjah British School and Al Ma'arifa International Private School in Sharjah, UAE. He joined the American University of Sharjah (AUS) in 2013 and completed an internship in Lubrex FZC in Sharjah, UAE. He obtained his B.Sc degree in Chemical Engineering from AUS in 2017. He joined the Chemical Engineering master's program at AUS in 2018. He was awarded a graduate assistantship that allowed him to work as a graduate teaching assistant from 2018 till 2020. His research and thesis focused on the delivery of drugs using nanoparticles and effectively triggering them at the desired location using ultrasound. He joined the Ultrasound in Drug Delivery group in AUS in 2015.